To the Graduate Council:

I am submitting herewith a thesis written by Kelly Lee Ausbrooks entitled "Non-Destructive Assay of Drum Packaged Radioactive Waste Utilizing Tomographic Gamma Scanning." I have examined the final copy of this thesis for form and content and recommend that it be accepted in partial fulfillment of the requirements for the degree of Master of Science, with a major in Nuclear Engineering.

Laurence F. Miller

Dr. Laurence F. Miller, Major Professor

We have read this thesis and recommend it acceptance:

Peter Groer

Dr. Peter Groer, Nuclear Engineering

Lawrence W. Townsend

Dr. Lawrence Townsend, Nuclear Engineering

Accepted for the Council:

Associate Vice Chancellor and
Dean of the Graduate School

Non-Destructive Assay of Drum Package Radioactive Wastes Utilizing Tomographic Gamma Scanning

A Thesis

Presented for the

Master of Science

Degree

The University of Tennessee, Knoxville

Kelly L. Ausbrooks

May, 1996

Dedication

I would like to dedicate this work to my father and mother, Pete and Ann Ausbrooks, whose love, devotion, and sacrifice has made this possible. I cannot begin to thank you for the inspiration and encouragement you have given me in my pursuit of this goal. For all the times I have not told you, I love you.

Acknowledgements

I wish to thank my major professor, Dr. Larry Miller, for his encouragement and guidance over the last several years. I am also grateful to the other committee members, Dr. Peter Groer and Dr. Lawrence Townsend, for their assistance and valuable comments. I would also like to thank Mr. Atsuto Ohashi, visiting researcher from the Ship Research Institute of Tokyo, Japan. His experience and knowledge of the MCNP transport code was invaluable and without which, a large portion of this thesis would not be possible. Also, thanks to Dr. Robert Estep, Los Alamos National Laboratory, for his help in the initial stages of this work. As a fortunate recipient of the United States Department of Energy Applied Health Physics Fellowship, I would like to thank my fellowship administrators, Mr. Tom Richmond and Mrs. Rose Etta Cox, Oak Ridge Institute for Science and Education, for their eternal patience and understanding. I have tried to serve the program with distinction and I feel honored to have received this award. Also, special thanks to Dr. Keith Eckerman at the Oak Ridge National Laboratory for his advice, support, and for granting me an internship. It was truly an honor to have worked with him. Lastly, I would like to express my thanks and love to my parents, whose faith and support have been an unwavering source of motivation.

This research was performed under appointment to the Applied Health Physics Fellowship Program, administered by the Oak Ridge Institute for Science and Education for the U.S. Department of Energy.

Abstract

A methodology for non-destructive assay (NDA) of drum packaged radioactive waste materials is investigated using Emission Computed Tomography (ECT) procedures. This method is suitable for mapping the activity distribution of point sources encased within typical 208 liter drums containing a primarily homogeneous medium. A requirement of this method is accurate gamma attenuation correction. This is accomplished by the use of a constant density distribution for the drum content, thereby requiring the need for a homogeneous medium. The current predominant NDA technique is the use of the Segmented Gamma Scanner (SGS). Tomographic Gamma Scanning (TGS) improves upon this method by providing a low-resolution, three-dimensional image of the source distribution, yielding both spatial and activity information. Reconstruction of the source distribution is accomplished by utilization of algebraic techniques with a nine (9) by six (6) voxel model with detector information gathered over scanning intevals of ninety (90) degrees. Construction of a linear system to describe the scenario was accomplished using a point-source response function (PSRF) methodology, where a 54x120 matrix contained the projected detector responses for each source-detector geometry. Entries in this matrix were calculated using the point-kernal shielding code QAD-CGGP. Validation was performed using the MCNP photon transport code. Solutions to the linear system were determined using two distinct least squares procedures, the Non-Negative Least Squares (NNLS) algorithm and the LSMOD algorithm. Both function as subroutines, each called from a user-written FORTRAN program. A series of four (4) scans were performed, each reconstructing the source distribution of a mock-up waste package containing a single 73 mCi ^{137}Cs point source. For each scan, the source was located in a different location. Results of the reconstruction routines accurately predict the location and activity of the source. The range of activity calculated using the NNLS routine is 0.2681 mCi with an average value of 77.7995 mCi. The range of values calcuated using LSMOD is 5.1843 mCi with an average of 72.8018 mCi.

Table of Contents

List of Tables

List of Figures

List of Acronyms

ANL	Argonne National Laboratory
ASCII	American Standard Code for Information Interchange
BPC	Bechtel Power Corporation
CFR	Code of Federal Regulations
CG	Combinatorial Geometry
CH	Contact Handled
CT	Computed Tomography
DOE	Department of Energy (United States)
ECT	Emission Computed Tomography
FORTRAN	Formula Translator
GP	Geometric Progression
HPGe	High Purity Germanium
HRGS	High Resolution Gamma Scanning
HVPS	High Voltage Power Supply
IBM	International Business Systems, Inc.
IBM-PC	Personal Computer Manufactured by IBM, Inc.
JAERI	Japan Atomic Energy Research Institute
LANL	Los Alamos National Laboratory
LINAC	Linear Accelerator

LLRW	Low Level Radioactive Waste
LSMOD	Least Squares Model
MCA	Multi-Channel Analyzer
MDA	Minimum Detectable Activity
MS-DOS	Microsoft Disk Operating System
MTF	Modulation Transfer Function
NaI(Tl)	Thallium Activated Sodium Iodide Crystal
NASA	National Aeronautics and Space Administration (United States)
NDA	Non-Destructive Assay
NIST	National Institute for Standards and Testing
NNLS	Non-Negative Least Squares
NRC	Nuclear Regulatory Commission (United States)
ORNL	Oak Ridge National Laboratory
PAN	Passive/Active Neutron
PMT	Photomultiplier Tube
PSRF	Point Source Response Function
RH	Remote Handled
RSIC	Radiation Shielding Information Center
RTR	Real Time Radiography
SGS	Segmented Gamma Scanning
SNM	Special Nuclear Material
TCT	Transmission Computed Tomography

TGS	Tomographic Gamma Scanning
TRU	Transuranic
WIPP	Waste Isolation Pilot Plant

Chapter 1

Introduction

Prior to the shipment of packaged low-level radioactive waste (LLRW) materials for disposal, the physical and chemical characteristics of the container and its contents must be determined (Kawasaki, 1990). Data gathered from these operations include the identification of radionuclides, the activity of the radionuclides, the physical and chemical form of the isotope, the spatial distribution of the activity, and the physical and chemical characteristics of the non-radioactive package contents.

1.1 Review of LLRW Classifications

The identity and quantities of the radionuclides present in a waste package and a determination of their waste form are requirements of federal law, as specified in 10CRF61, *United States Nuclear Regulatory Commission Regulations for Land Disposal of Low-Level Radioactive Wastes* (Moghissi, 1992). These characteristics are critical parameters used in the classification of the waste package. Classifications of radioactive wastes generated by non-Department of Energy (DOE) institutions are generally made according to federal law set forth in the Code of Federal Regulations (CFR). However, the Nuclear Regulatory Commission (NRC) has intentionally established broad classification requirements and, as such, many institutions have created site-specific classifications that correspond to the content and form of the waste in which they generate (Moghissi, 1992).

1.1.1 Class A Radioactive Wastes

Currently, federal law specifies three general classifications for LLRW. As outlined in 10CFR61, these classifications are based upon waste form and activity concentrations (Moghissi, 1992). The first classification, Class A, can only be applied to the lowest activity wastes. Therefore, waste form criteria, such as stability and containment, are at a minimum. These requirements include the packaging of wastes in containers fabricated from material other than cardboard or fiberboard, the solidification of liquid wastes or provisions for an absorbent material with a capacity twice the volume of liquid in the package, and the containment or elimination of freestanding liquids that exceed one (1) percent of the package volume. Also, Class A wastes are typically segregated from other wastes packages at the disposal facility (State of Tennessee, 1986).

1.1.2 Class B Radioactive Wastes

Class B wastes have activities greater than Class A materials. Because of this higher activity, packaging and containment requirements must meet more stringent standards than those of their Class A counterparts. These requirements specify that the waste package must meet the Class A criteria in addition to requirements that insure structural stability and minimization of waste degradation. Typically, these requirements include a high-strength container/package that will maintain its physical dimensions and integrity under a variety of conditions, such as compaction, moisture intrusion, microbial activity, internal radiation effects, and chemical changes. Also, liquid wastes must be converted to a stable form such that freestanding liquids remain in quantities no larger that 0.5 percent of the package volume following processing. Lastly, any void spaces in the package must be eliminated or reduced to a reasonably achievable degree (State of Tennessee, 1986).

1.1.3 Class C Radioactive Wastes

Wastes classified as Class C are those which exceed the activity limits of Class B materials. Typically, wastes of this type must meet the packaging and waste form requirements set forth for Class B materials. It is the disposal requirements that provide the largest distinction between Class C and Class B materials. Class C materials require the construction of an intruder barrier following disposal. This barrier is intended to reduce the possibility of inadvertent intrusion after loss of institutional control over the disposal facility. Concrete vaults and burial to a depth of at least five (5) meters are examples of a suitable intruder barrier. Wastes having activities greater than those of Class C are typically unsuitable for near-surface burial (Moghissi, 1992).

1.2 Overview of Current NDA Methods

Current non-destructive methods used to characterize the radionuclide content of waste packages prior to shipment for disposal include gross gamma counting, segmented gamma scanning (SGS), passive/active neutron scanning (PAN), X-ray real-time radiography (RTR), and traditional gamma spectroscopy. PAN systems have traditionally been used in the assessment of trans-uranic (TRU) wastes and special nuclear material (SNM). TRU wastes, as defined by DOE Order 5820.2A, are those wastes which contain alpha emitting trans-uranium radionuclides with half-lives greater than twenty (20) years and concentrations greater than 100 nCi/g (Canberra Industries, 1995). The term SNM, in this context, is used to refer to plutonium, uranium enriched in the isotopes ^{233}U or ^{235}U, or any materials which are artificially enriched in these isotopes (Moghissi, 1992).

1.2.1 Passive/Active Neutron Systems

Currently, there is great interest in the development of PAN systems to assay TRU waste packages containing activity sufficient to warrant remote handling (RH). The need to assay DOE RH TRU wastes prior to shipment to the Waste Isolation Pilot Plant (WIPP) has fueled much of the latest research into non-destructive assay (NDA) techniques (Bauer, 1992). Debate exists over which technique should be used to perform assays of TRU material. However, current philosophy has stipulated that passive neutron and gamma scanning systems are appropriate for determining the plutonium content of a TRU package (Canberra Industries, 1995). When examining very active RH TRU materials, i.e. those emitting neutrons at rates greater than 10^7 neutrons per second, linear accelerator (LINAC) based active neutron interrogation systems are being investigated. Researchers at the Oak Ridge National Laboratory (ORNL) have performed many of the early investigations into the feasibility of this technology (Vourvopoulos, 1992).

1.2.2 Tomographic Gamma Scanning

Researchers at the Los Alamos National Laboratory (LANL) have developed a tomographic gamma scanning (TGS) system to assay contact-handled (CH) TRU wastes and SNM which is packaged in 208 liter (55 gallon) drums. TGS seeks to overcome the shortcomings of traditional gamma spectroscopy and SGS. Both gamma spectroscopy and SGS determine the activity of gamma-emitting isotopes within a waste package by utilizing the full-energy response. However, this measurement is dependent upon the density distribution within the package. In the case where the density is high, Compton scattering and gamma attenuation increase the buildup of the spectrum continuum, which serves to reduce the signal-to-noise ratio of the full-energy measurement. TGS is able to compensate for this reduction in signal by utilizing computed tomographic (CT) methods to estimate the density distribution within a waste package prior to performing the activity estimate. Also, in order to accurately determine the identification the isotopes present in the SNM, the TGS system utilizes only high-purity germanium (HPGe) detectors. The increased resolution provided by these detectors is vital when performing assays of plutonium and uranium. TGS is, therefore, able to determine the identity of radionuclides within a waste package, their activities, their location, and evaluate the physical condition of the non-radioactive contents, i.e. search for free-liquids or compressed gas cylinders (Estep, 1994).

While the LANL TGS system was designed from the outset to investigate CH TRU wastes and SNM, parallel research has been conducted by both the Toshiba Corporation (Goto, 1992) and the Hitachi Energy Research Laboratory (Kawasaki, 1990). Here, researchers have adapted CT procedures to perform assays of typical LLRW as generated by nuclear power plants. The radionuclides of concern in these cases, generally, are ^{137}Cs and ^{60}Co. The distinctive photopeaks generated by the 0.662 MeV and 1.173 MeV, 1.333 MeV photons, respectfully, simplify identification of these isotopes. As such, high-resolution gamma spectroscopy (HRGS) equipment need not be placed within the scanning system. Therefore, arrays of thallium activated sodium iodide (NaI(Tl)) detectors can be utilized (Kawasaki, 1990).

1.3 Focus of This Study

Characterization of LLRW prior to shipment for disposal is a requirement of federal and state law. While current techniques are adequate, the criteria imposed by future waste disposal operations will no doubt call for more detailed information concerning the content of waste packages. It is for this reason that new NDA techniques have been developed.

This study investigates the feasibility of employing CT techniques in order to assay LLRW packages. Using the work discussed in Section 1.2.2 as a basis, research was performed using mock-up waste packages containing ^{137}Cs point sources. Investigations were conducted using traditional gamma detection equipment to determine the activity distribution within 208 liter (55 gallon) drums containing a homogeneous attenuating media. Each experiment was performed utilizing an emission CT methodology, with solutions provided by an algebraic reconstruction algorithm. Further, examinations of two (2) reconstruction routines were performed to evaluate least squares solution routines appropriate for tomographic examination of waste packages.

1.4 Structure of this Report

This report is divided into five (5) chapters. Chapter Two (2) provides an overview of the mathematics involved in CT procedures. A discussion of the relationship between the object and the image using Fourier methodology is provided. Further, a discussion of CT as it applies to waste scanning using algebraic solution techniques is also provided. Chapter Three (3) gives a discussion of the experimental procedures undertaken during this research. A description of the equipment and the methods in which they are utilized is included. Chapter Four (4) relates the results obtained for each experiment, with comparisons of the results generated by each algebraic reconstruction routine. Chapter Five (5) provides a summary of the information given in Chapter Four (4) and a series of conclusions which can be drawn from these results.

Chapter 2

Theoretical Methodology

Presented in this section is a discussion of the theoretical concepts and mathematics associated with the application of computed tomographic sampling and reconstruction procedures utilized in support of LLRW scanning

2.1 Comparison of Theoretical Constructs

Presently, there are two (2) general methodologies for reconstruction of images stemming from computed tomography (CT) procedures. The earliest research involving the reconstruction of images by use of projections utilized the convolution and backprojection method, as theorized by Radon in publications dating to 1917. This method utilizes Fourier transforms and frequency domain filters to generate an image set, given a set of projection data. It is interesting to note that, although the mathematics have been known for many years, this theory was not placed into practical use until the early 1970's. This is, in part, due to the need for vast computational resources, as the mathematics of reconstruction are quite cumbersome (Webb, 1993).

The second methodology for CT image reconstruction involves the use of systems of linear equations which are solved by use of iterative techniques. The application of this method has seen a resurgence over the past several years, mainly due to the abundance of inexpensive high-speed computational equipment. While mathematically simpler to implement than their Fourier counterparts, algebraic solution techniques generally require a large number of iterations before convergence. Therefore, reconstruction using large systems of linear equations is usually considered too computationally intense for medical applications. The increase in speed associated with the convolution and backprojection methodology are a prime factor in the medical industry's continued use of this reconstruction technique in CT imaging. However, when analyzing somewhat smaller data sets with poor statistics in a non-medical setting, iterative procedures are preferred (Webb, 1993). This is discussed further in following sections.

2.1.1 Image and Object Constructs

Given a measurement of some object located in three-dimensional space, it is possible to reconstruct an image of that measurement, which likewise is oriented in three-dimensional space. This measurement is to be regarded as the best approximation of the object distribution. For mathematical ease, convention has represented the object distribution as f and the image distribution as g. Experimentation is required to determine the appropriate relationship which describes the association of f and g. Both f and g are three-dimensional in the description of their appropriate distributions. Note that these distributions are constant with respect to time. However, tomography is based upon the ability to construct a three-dimensional image given a set of continuous two-dimensional descriptors. This has led to a simplification of the mathematics involved with reconstruction, thereby allowing a better understanding of the properties of a three-dimensional distribution. As such, only two dimensions are commonly included in the mathematical presentation of CT reconstruction methods using Fourier techniques, in most cases (Webb, 1993).

2.1.1.1 Image and Object Distributions

We begin our discussion of image and object distributions by representing the object distribution by $f(\alpha, \beta)$. This distribution is contained entirely within the plane of the object. The image distribution is represented by $g(x, y)$ and, similarly, is contained entirely within the plane of the image. Note, that because of experimental uncertainties present within the system, no direct 1:1 relationship exists between f and g. To provide a basis for the mathematics, it is assumed that the primary contribution of the image at location (x', y') is attributed to the object distribution located at point (α', β'). However, the neighborhood principle states that the contribution to the image at some point (x', y') is due to the object point (α', β') and the points in an infinite neighborhood surrounding the object point. The contribution to the image point diminishes rapidly as one moves away from the primary object point. This concept can quantitatively be described by use of point source response functions (PSRF) (Webb, 1993).

2.1.1.2 Non-Negativity Constraints

A basic premise of CT image reconstruction is that the image must be non-negative. Therefore, the activity of the sample, neglecting statistical fluctuations, must be non-negative. Mathematically, this can be stated as

$$f(\alpha,\beta) \geq 0 \quad \text{and} \quad g(x,y) \geq 0 \tag{2.1}$$

We now construct a function $h(x, y, \alpha, \beta)$ which models the spatial dependence of the above point process. Given that the object is only non-zero at (α', β'), the image can be interpreted as

$$g'(x,y) = h(x,y,\alpha',\beta',f(\alpha',\beta')) \tag{2.2}$$

We now assume that a second signal has been generated from the same object point, giving rise to a second image described by

$$g''(x,y) = h(x,y,\alpha',\beta',f'(\alpha',\beta')) \tag{2.3}$$

The superposition principle states that energies due to radiation are additive in nature and, as a result, the following non-linear equation is yielded

$$g'(x,y) + g''(x,y) = h(x,y,\alpha,\beta',f(\alpha',\beta')) + h(x,y,\alpha',\beta',f'(\alpha',\beta')) \tag{2.4}$$

This, therefore, states that additive components in the plane of the object do not yield additive results in the plane of the image. This is an undesirable characteristic of imaging systems, and as a result, mathematical interpretations of the object-image relationship are often assumed to be linear for convenience (Webb, 1993).

2.1.1.3 System Linearity

Assuming a object and image system that is linear in nature, Equation (2.2) becomes

$$g'(x,y) = h(x,y,\alpha',\beta')f'(\alpha',\beta') \tag{2.5}$$

and Equation (2.3) becomes

$$g''(x,y) = h(x,y,\alpha',\beta')f'(\alpha',\beta') \tag{2.6}$$

Combining the results for the image using the linear equations described above yields the following

$$g'(x',y') + g''(x',y') = h(x,y,\alpha',\beta')[f'(\alpha',\beta') + f''(\alpha',\beta')] \tag{2.7}$$

Equation (2.7) unlike (2.4) is linear, as the sum of two linear equations results in a linear equation and, in this case, yields a result which depends only on a single use of the transformation function h (Webb, 1993). This is referred to as linear superpositioning (Sorenson, 1987). It is for this reason that the assumption of linearity is made in most all CT reconstruction.

2.1.1.4 Point Source Response Functions

Once the linearity of the system has been established, the distribution of the image can be stated as a superpostion of a finite set of points (Sorenson, 1987). Integration over these points provides the reconstructed image, as shown below

$$g(x,y) = \iint h(x,y,\alpha,\beta)f(\alpha,\beta)d\alpha d\beta \tag{2.8}$$

The function h is now known as the point source response function (PSRF). The PSRF in the above example is dependent upon four (4) parameters. As such, it is known as a space-variant PSRF. However, if it is the case where the PSRF is constant for all points in the object plane, the function is referred to as the space-invariant PSRF. In this case, the function depends only upon the difference in the image and object points. This stems from the functional dependence upon the relative distance between interplaner points. The space-invariant linear system can be described by the following

$$g(x,y) = \iint h(x-\alpha,y-\beta)f(\alpha,\beta)d\alpha d\beta \tag{2.9}$$

This equation is often referred to as the convolution integral. The image is merely the object which has been convoluted through the PSRF. Therefore, the PSRF embodies the associated errors and uncertainties of the system. The attempt to remove these discrepancies from the system is referred to as deconvolution. Hence the name given to this methodology (Webb, 1993).

2.1.2 Fourier Deconvolution and Reconstruction

Assuming a linear space-invariant model, we have shown that f and g are related by convolution. Let us symbolically demonstrate this by developing the following equation

$$g(i,j) = h(i,j) \otimes f(i,j) \tag{2.10}$$

where the symbol $\otimes$ signifies convolution. We have used the parameters i and j to represent the appropriate 2-D coordinates for the system. When examined in Fourier space, convolution is transformed into simple multiplication; as such, Equation (2.10) becomes

$$G(u,v) = H(u,v) * F(u,v) \tag{2.11}$$

with spatial frequencies u in the i direction and v in the j direction. At this point, it is wise to reflect upon the Fourier representations of the image and object distributions. These representations are mathematically joined in Fourier space by the following equations

$$F(u,v) = \iint f(i,j) \exp[-2i\pi(ui + vj)]didj \tag{2.12}$$

and

$$f(i,j) = \iint F(u,v) \exp[+2i\pi(ui + vj)]dudv \tag{2.13}$$

Equation (2.12) exhibits how an object f can be transformed into its associated component spatial frequencies and Equation (2.13) demonstrates how the object is reconstructed from this distribution of frequencies (Webb, 1993).

2.1.2.1 Modulation Transfer Functions

Reviewing Equation (2.11), the 2-D Fourier transform of the PSRF, h, is often called the modulation transfer function, MTF (Sorenson, 1987). The MTF is denoted H by convention. The fraction of the object distribution at frequency (u, v) that is transferred to the image distribution via the Fourier transform is given by the value of the MTF. Thus, for a perfect imaging system, where no spatial frequency information was lost or deformed, the MTF would equal one (1). However, this is never the case. For all imaging systems, the PSRF is known to possess a finite width, thus the MTF, likewise, has a finite width (Webb, 1993). The PSRF can be measured by imaging a point source (Sorenson, 1987). In this case, $f = 1$ and $g = h$, or the image is the measure of the PSRF. Note, that the

PSRF is in this case approximated by a Gaussian function. As the Fourier transform of a Gaussian function is a Gaussian function, then the MTF, H, is Gaussian in shape as well. Therefore, G = H (Webb, 1993)

2.1.2.2 Discrete Data Sets in Fourier Space

In order to introduce convience into the solution, both the object and image are assumed to be discrete in nature. This is obviously incorrect, as all objects are composed of matter in a continuous fashion. However, this simplification leads to the replacement of the Fourier 2-D integrals with summations, allowing the display of image and object data in matrix format. Therefore, the transformation of the object into the frequency distribution, Equation (2.12), becomes

$$F(u,v) = \frac{1}{n} \sum_{i=0}^{N-1} \sum_{j=0}^{N-1} f(i,j) exp[-2ip(ui + vj) \quad N] \tag{2.14}$$

where N is the number of sampling points and i, j, u, v are discrete parameters determined at those sampling points. Analysis of the above equation is performed by the following method. The function is separable due to the exponential and a transform in the i direction can be made, thus yielding $F(u,j)$. A group of 1-D transforms are then used to determine $F(u,v)$. This solution method is referred to as the Cooley-Tukey algorithm, or more commonly as the fast Fourier transform (FFT). It is interesting to note that with use of the FFT, computation time increases as $N^2 lnN$, as opposed to linearly with increasing N as one might expect (Webb, 1993).

A discrete distribution for the image f is given by reversing Equation 2.14,

$$f(i,j) = \frac{1}{N}\sum_{u=0}^{N-1}\sum_{v=0}^{N-1} F(u,v)\exp[+2i\pi(ui+uj)/N] \qquad (2.15)$$

Processing of the image can be performed by placing a function $T(u,v)$ within the summation. This function serves as a filter or a modulator, as it is multiplied with the Fourier distribution F. It is here where this technique gets another piece of its name, that being filtered deconvolution (Webb, 1993).

2.1.2.3 Image Processing

Using operator notation, where $H\{\ \}$ denotes a real-space operation, the most basic equation for imaging can be written as

$$g = H\{f\} \qquad (2.16)$$

Functions f and g are generally 1-D arrays of information, while the operator H is a 2-D matrix. In this notation, the imaging equation can be written as

$$\vec{g} = [H]\vec{f} + \vec{n} \qquad (2.17)$$

where $\vec{n}$ denotes a noise vector (Webb, 1993). There are many techniques for reconstruction of a object distribution given a set of image data. Most medical applications utilize filtered deconvolution, evaluating the systems in Fourier space (Sorenson, 1987). However, this technique is unnecessarily cumbersome for barrel scanning applications. Also, the lack of a need for millimeter resolution leads to a reduction in sampling frequency. As such, the projection data sets may be ill-conditioned which can result in gross errors within the object reconstruction when using Fourier techniques. This frequency requirement is referred to as the Nyquist condition, and states that adjacent measurements need to be taken at intervals approximately equal to half the width of the detector (Sorenson, 1987). Many tomographic barrel scanning units do not meet this requirement, and as such, Fourier techniques do not provide a reliable means of reconstruction. As such, algebraic or iterative methods have become the norm (Estep, 1994).

2.1.3 Algebraic Reconstruction Techniques

In many implementations of tomographic methodology, it may not be possible to meet all the criteria required for FFT-based reconstruction techniques. Namely, it may not be possible to generate a large number of image projections, or the projections may be taken at unequal intervals over one-hundred eighty (180) or three-hundred sixty (360) degrees. Examples of these implementations include geologic characterization and waste assay applications. In these cases, object reconstruction is performed under the premise that an image cross-section or slice exists as an array of unknowns, describing systems of algebraic equations relating the projection data. Iterative solution techniques are normally employed to solve for the object distribution. These operations are performed in real-space, neglecting the need for Fourier transformations (Kak, 1988).

2.1.3.1 Principles of Algebraic Reconstruction Methods

In typical algebraic methods, a square grid is superimposed on the unknown image projection. In each cell, the value of the image is assumed constant. The grid spacing is directly related to the resolution of the system, as a finer mesh leads to enhanced resolution. In Figure 2.1, an image denoted $g(x, y)$, is partitioned according to a square grid having N cells. We let f_j denote the constant value for the image in the jth cell. A ray is now drawn through the gridplane, each ray having finite width r. The ray width is approximately equal to the width of each cell. We let p_i equal the ray sum along the path through the grid. A general relationship can be developed between the f_j and p_i terms, and is stated as

$$p_i = \sum_{j=1}^{N} w_{ij} f_i \tag{2.18}$$

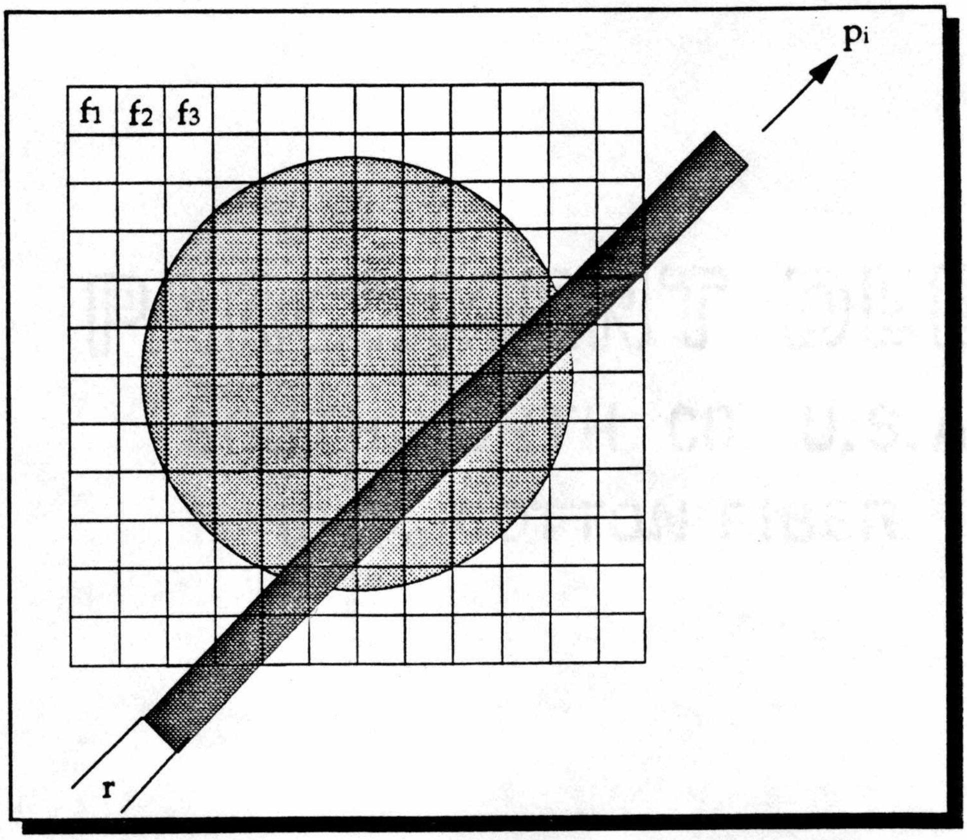

Figure 2.1. Representation of Tomographic Principles (Kak, 1988).

where w_{ij} is the weighing factor that represents the contribution of the *jth* cell to the integral of the *ith* ray. The weighing factors are equal to the fractional area of the *j*th image cell that is intercepted by the *i*th ray. Usually, most of the w_{ij}'s are of mean zero (0), as only a small portion of the image cells contribute to the sum of the ray. The above representations yield large systems of equations which are solved algebraically to determine the values of the image projections in each grid cell (Kak, 1988).

2.1.3.2 Solution Techniques for Algebraic Reconstruction Methods

During the early development of algebraic reconstruction theory for use in support of diagnostic nuclear medicine, it was realized that an inherent problem was the need to solve large systems of equations. Note, that typical matrix sizes for the w_{ij} matrix can be on the order of 10^5 x 10^5. As such, simple least squares techniques are impractical due to the large amount of computational time required to perform matrix operations on these large systems. Many other algorithms have therefore been developed, most based on Kaczmarz's "method of projections" (Kak, 1988).

However, we have previously stated that many tomographic imaging systems utilizing algebraic reconstruction techniques have relatively small data sets. These are generally on the order of 10^3 x 10^3 in size (Estep, 1994). Waste assay systems provide data sets having sizes which fall within this order of magnitude. As such, reconstruction of object data sets can be performed efficiently by use of iterative least squares techniques. There are an abundance of solution algorithms utilizing least squares protocols, and two have been selected for this project.

2.2 Waste Package Scanning

In the previous section, a discussion of the general mathematical interpretation of image processing was undertaken. This section is intended to provide an more specific usage of the mathematics in yielding a basis for waste package tomographic imaging.

2.2.1 Package Partioning

We begin our discussion by assuming a barrel contains a single radionuclide emitting a mono-chromatic gamma ray with constant intensity. Further, the barrel is partitioned into equi-volume units referred to as voxels. For the purposes of this discussion, the number of voxels is unimportant. The activity in the drum is partitioned by the voxels, of which there are N_d (Kawasaki, 1990). The activity distribution within the drum is synonymous with the object distribution referred to earlier.

2.2.2 Emission Computed Tomography

The determination of the activity distribution within a waste package requires the measurement of gamma rays emitted from radionuclide decay within the package by use of an external detection system (Goto, 1992). The measurement of these gamma rays and the techniques used to produce a reconstructed activity distribution from this data set is commonly refered to as emission computed tomography (ECT) (Kawasaki, 1990).

2.2.2.1 Photon Count Rate

By convention, the activity in voxel i is denoted A_i. Using a detector positioned outside the drum, the count rate at the detector, located in position j, is denoted as C_j. Figure 2.2 provides a schematic of ECT barrel scanning principles. An equation for the count rate can be derived from the above principles. Assuming that there are N_v imaginary voxels in the drum

$$C_j = \sum_{i=1}^{N_v} R_{i,j} A_i, j = 1, \ldots, N_d \qquad (2.19)$$

R_{μ} is an element of the PSRF matrix and N_d is the number of detector positions. C_j is the count rate of gamma photons with energy E_{ECT} which stike the detector located at position d. One can see that the PSRF provides an estimate of the photon attenuation within the voxel elements along the pathlength of the ray extending from the activity voxel A_i (Kawasaki, 1990).

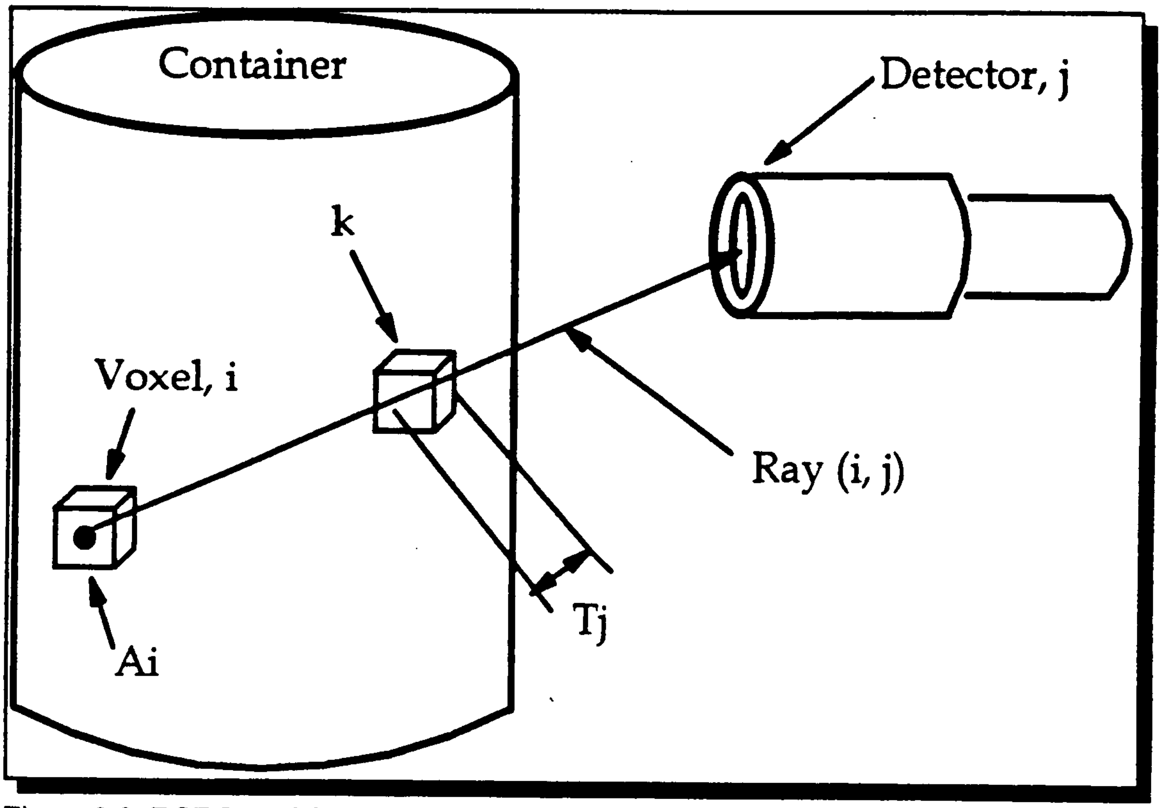

Figure 2.2 ECT Barrel Scanning Representation (Kawasaki, 1990)

2.2.2.2 PSRF Determination

Extrapolating from the discussion of general image processing, the PSRF is a matrix which has elements corresponding to the *j*th detector's count rate caused by a normalized activity located in voxel *i*. As such, the PSRF matrix is of size *j* by *i*. The units for the PSRF matrix vary, according to the normalization constant used for the reconstruction algorithm. A multi-parameter mathematical expression of the response elements is given by the function

$$R_{i,j} = \varepsilon\, G_{i,j} \exp\left[-\sum_k \mu(E_{ECT}) t_k\right] \tag{2.20}$$

where ε is the gamma emission efficiency, $G_{i,j}$ relates the geometric efficiency, t_k is the path length of ray (i,j) in voxel k, and $\mu(E_{ECT})$ is the linear attenuation coefficient with voxel k for gamma rays of energy E_{ECT}. The parameters ε, $G_{i,j}$, and t_k can be calculated directly for each voxel and detector position. The attenuation fraction must be determined by experiment. In the instance where the attenuating matrix is known and homogeneous, a direct calculation can be made (Kawasaki, 1990). This is the case assumed in this research, as the PSRF matrix was determined by use of several computational routines. A summary of the results of these codes is given in the following chapter.

2.2.3 Transmission Computed Tomography

In most cases, the contents of drum-packaged radioactive wastes are not homogeneous and the composition of the attenuating media is not known. It is for this reason that a method of determining the distribution of densities within the container must be utilized. The preferred technique for accomplishing this task is transmission computed tomography (TCT) (Estep, 1994).

TCT was the first application of Radon's original reconstruction hypothesis. In this case, an external source emits photons with a known energy and intensity. The source may either emit high-energy X-rays or gamma rays. In medical applications, X-rays are generally preferred for this procedure (Webb, 1993). This is in part due to the reduction in personnel risk due to the ability to deactivate the beam. Radionuclides do not offer this feature, as regardless of shielding, the decay of the nuclide is continuous, therefore a finite risk of unnecessary exposure exists. Also, complexity of the scanning apparatus is somewhat simplified, thereby reducing the possibility of equipment malfunction and construction cost.

2.2.3.1 Photon Count Rate

Having established the need for a TCT scan in order to determine the density distribution of a typical waste package, the mathematical formulation needed to establish the density matrix are deduced in a manner similar to the ECT case. Figure 2.3, illustrates the count rate of the detector located in position *j*, which is found as

$$P_j = P_{0j} \exp\left[\sum_k \mu_k(E_{ECT}) t_k\right] \tag{2.21}$$

where P_{0j} is the unattenuated count rate, *s* denotes the source position, $\mu_k(TCT)$ denotes the linear attenuation coefficient in the *k*th voxel, and t_k is the path length of the ray in the *k*th voxel (Kawasaki, 1990).

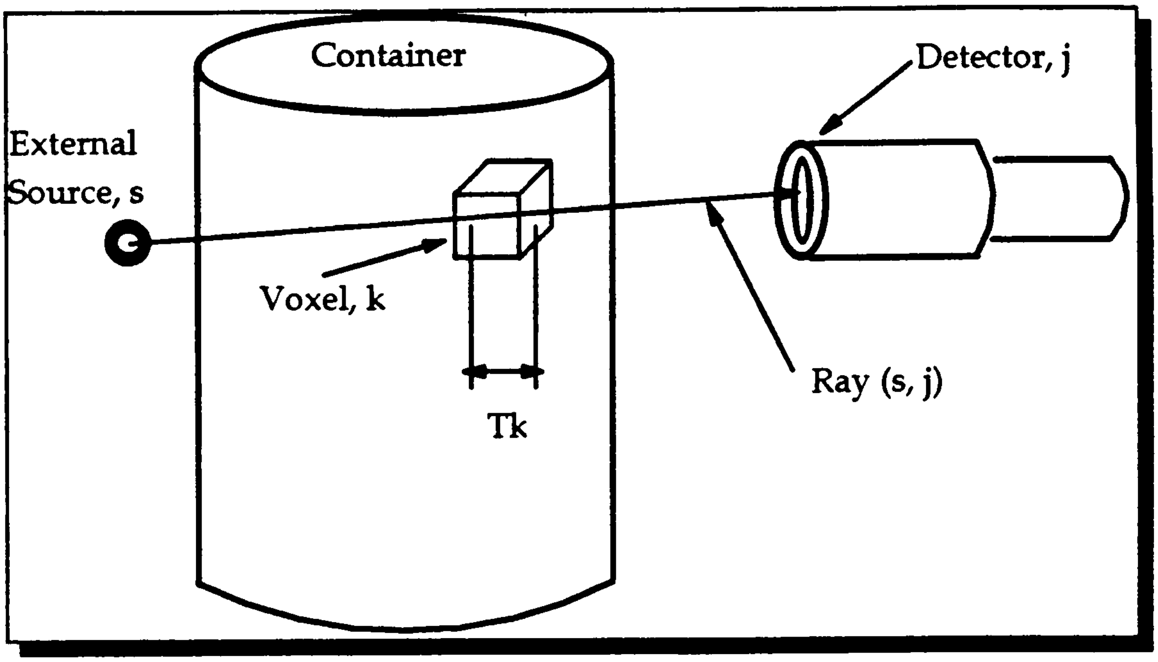

Figure 2.3 TCT Barrel Scanning Representation (Kawasaki, 1990)

2.2.3.2 Determining Attenuation Coefficients

By dividing Equation 2.21 by P_{oj} and taking the logarithm of both sides to eliminate the exponential term, an equation for the net attenuation, which is similar to Equation 2.19, is stated as

$$Y = \ln(P_j / P_{0j}) = \sum_{k=1}^{N_d} F_m \mu_k \tag{2.22}$$

where μ_k is the linear attenuation coefficient in the kth voxel and

$$F_m = \begin{bmatrix} t_k, & k \in ray(s, j) \\ 0, & k \notin ray(s, j) \end{bmatrix} \tag{2.23}$$

The function describing the distribution of the attenuation coefficients is based upon a summation of weighting factors and measured values and is given by

$$Z_{TCT} = \sum_{j-1}^{N_d} W_j^Y (Y_j^{\alpha x} - Y_j)^2 \qquad (2.24)$$

where

$$Y_j^{\alpha x} = \ln(P_j^{cx} / P_{0j}^{\alpha x}) \qquad (2.25)$$

The distribution is obtained by minimizing Equation 2.24 with the constraints

$$\mu_k \geq 0, \quad k = 1, \ldots, N_k \qquad (2.26)$$

Note, the distribution of densities is synonymous with the distribution of linear attenuation coefficients. The weighing factor, W_j^Y, which appears in Equation 2.23, is usually set to equal the reciprocal of the variance of Y_j^{0x} (Kawasaki, 1990).

The object of our assessment, radioactive waste packages, emits photons which can strike the detector and influence the measurements of densities within the drum (Goto, 1992). For that reason, typically, photons with energies different than those typically associated with radioactive waste are selected for use in TCT scanning. However, a finite probability for interference exists and for that reason, the value of P^{cx} in Equation 2.25 is calculated as

$$P_j^{\alpha x} = P_j^0 - P_j^c \qquad (2.26)$$

where the superscripts "o" stipulates that the external beam is active and the "c" stipulates that the beam is inactive (Kawasaki, 1990).

2.2.4 Relating TCT and ECT

Having established the main mathematical principles behind TCT scanning, the discussion of ECT can be completed. Solving for the attenuation coefficient distribution allows one to make a substitution into Equation 2.20 for each discrete ECT linear attenuation coefficient by the relation

$$\mu_i(E_{ECT}) = \mu_i(E_{TCT})\mu_m(E_{ECT})/\mu_m(E_{TCT}) \tag{2.27}$$

where μ_m is the mass attenuation coefficient for the specified gamma energy. It is interesting to note that for gamma rays of energy greater than 300 keV, the mass attenuation coefficient ratio in Equation 2.27 is approximately constant. There is a slight dependence upon waste package contents however for μ_i. Table 2.1 outlines several attenuation coefficients (Kawasaki, 1990).

Calculations of the elements composing the PSRF matrix are made utilizing Equation 2.20 and assuming a point source of known activity is located in the center of each voxel. The linear attenuation coefficient is assumed constant within the voxel. Methods used to make these calculations will be discussed in following chapters.

Having constructed the proper PSRF matrix, it is now possible to determine a solution for the activity distribution. Not unlike the minimization required in the TCT methodology, the equation

Table 2.1. Mass Attenuation Coefficients for Typical Waste Materials and Computed
Ratios with Respect to 0.66 MeV, (Kawasaki, 1990).

	μ_m (cm^2/g)			
Material	0.66 MeV	0.83 Mev	1.17 MeV	1.33 Mev
Aluminum	0.0744	0.0668	0.0567	0.0531
	1.0000	0.8980	0.7620	0.7140
Iron	0.0727	0.0652	0.0551	0.0517
	1.0000	0.8970	0.7580	0.7110
Copper	0.0717	0.0642	0.0542	0.0508
	1.0000	0.8950	0.7560	0.7090
Concrete	0.0772	0.0695	0.0588	0.0552
	1.0000	0.9000	0.7620	0.7150
Water	0.0856	0.0771	0.0653	0.0611
	1.0000	0.9010	0.7630	0.7140

$$Z_{ECT} = \sum_{j=1}^{n_d} W_j^c (C_j^{cx} - C_j)^2 \tag{2.28}$$

is reduced under the constraints

$$A_i \geq 0, \quad i = 1, \ldots, N_p \tag{2.29}$$

The measured count rate, C_j^{cx}, of the detector is found for each position j (Kawasaki, 1990). The rate is determined from a summation of peak counts followed by subtraction of the Compton continuum (Estep, 1994). This method is discussed in Chapter 3, entitled "Experimental Methodology". The net peak counts is then divided by the total count time at position j to yield C_j^{0x}. The weighting factor, W_j^c, as was the case with TCT, is usually set to equal the reciprocal of the variance of C_j^{0x} (Kawasaki, 1990).

2.2.5 Methods of Solution

The minimizations described for both TCT and ECT methodologies are commonly grouped under the heading of constrained least squares problems. There are several techniques in existence which provided solutions, several of them being (1) the Hansen and Lawson Non-Negative Least Squares (NNLS) algorithm (Lawson, 1974), (2) the Maximum Likelihood Expectation Maximization (MLEM) algorithm (Estep, 1994), and (3) the LSMOD package developed by Argonne National Laboratories (ANL) (Smith, 1993). Normally, least squares solution routines provide a unique solution for an over-determined system of equations based upon a minimization of chi squared (χ^2) (Smith, 1993).

The solution set yielded by the least squares technique yields the approximate activities for each voxel in the container. Therefore, to determine the total activity in the drum, a summation of these individual activities over the total number of voxels must be performed. Mathematically, this can be written as

$$A_t = \sum_{i=1}^{N_v} A_i \tag{2.30}$$

2.3 Solutions by Least Squares Procedures

Introduced by Gauss more that one-hundred (100) years ago, the method of least squares has for many years been an important technique for the calculation of experimental parameters (Stallman, 1981). Given a set of data and some prior information concerning the parameters, a set of best-estimate parameters can be determined (Smith, 1993). There are numerous algorithms which employ a variety of least squares techniques. In this research, two (2) such algorithms were utilized, each routine using unique formulations of Gauss's procedure.

2.3.1 The LSMOD Methodology

The LSMOD least squares algorithm, developed by the Engineering Physics Division at ANL to provide solutions to simple least squares problems, can be used to provide estimates of the parameters sought in this research. Typically, a judgement as to the accuracy of these estimates is made by some property of the solution. An example of such a property is minimum variance. The formulation of the LSMOD methodology involves the use of conditional probability and Bayesian statistics; each providing a basis onto which the algorithm can be constructed (Smith, 1993).

2.3.1.1 Conditional Probability

Assume E is a set of events collected by some sampling procedure. X and Y are non-trivial events which are contained within the set E. The symbol P represents probability. The conditional probability of X given Y has occurred is denoted as $P(X\,|\,Y)$. Note that $P(X)$ is the unconditional probability of X, which is equal to $P(X\,|\,E)$. The probability is normalized by setting $P(E) = 1$, and therefore $P(X)\leq 1$ and $P(X\,|\,Y)\leq 1$. We now introduce a set of non-trivial independent events which are contained within E. This set is denoted A_k, where $k = 1, ..., n$. If we now assume that E is formed by the union of all the elements of A, the events A_k are referred to as a partition of E. There are many partitions of E, each having the same properties. If we introduce another non-trivial event belonging to E, the conditional probability of A_k given D can be expressed as

$$P(A_k|D) = \frac{P(D|A_k)P(A_k)}{\sum_{j=1,n}\left[P(D|A_j)P(A_j)\right]} \tag{2.31}$$

The above formula in known as Bayes theorem (Smith, 1993).

2.3.1.2 Bayesian Probability

Examining Equation 2.31 using the Bayesian interpretation, A_k is referred to as the hypothesis. D is the experimental data set. $P(A_k\,|\,D)$ is the posterior conditional probability that A_k is true given set D. $P(D | A_k)$ is the conditional probability that data set D would be generated if A_k were true. This probability is referred to as the likelihood. The probability $P(A_k)$ is the unconditional probability that A_k is true. Note that the probability is normalized as $P(E | D) = 1$ (Smith, 1993).

When working with large data sets, equation 2.31 is not appropriate. We can reformulate this equation using probability density functions, denoted p. Bayes theorem then becomes

$$p(\mathbf{p}|D) = \frac{L(D|\mathbf{p})p_a(\mathbf{p})}{\int L(D|\mathbf{p}')p_a(\mathbf{p}')d\mathbf{p}'} \tag{2.32}$$

In Equation 2.32, **p** is the collection of parameters. Therefore, $p(\mathbf{p} | D)$ is the posterior probability density for **p** given that data set D is true, $L(D | \mathbf{p})$ is the likelihood that set **p** would yield data set D, and $p_a(\mathbf{p})$ is the unconditional probability density function for **p**. We can restate Equation 2.32, taking advantage of the likelihood function, as

$$p(\mathbf{p}|D) = CL(D|\mathbf{p})p_a(\mathbf{p}) \tag{2.32}$$

where C is the normalization constant determined by the integration (Smith, 1993).

The unconditional probability density function encompasses prior knowledge of the statistical situation in question. Following performance of an experiment, the probability density function must be revised with the data gathered during the experiment. Equation 2.33 can be used for this refinement process. Thus, a refinement can be made for each data set that is gathered. It is this iterative Bayesian approach which provides the algorithm for this computation using probability distributions (Smith, 1993).

However, many times, we are not concerned with the probability distributions, but rather, the best estimates of experimental parameters. If a probability distribution describes a set of parameters, classical statistics states that the best estimates of those parameters are the expected values. This can be stated as

$$<p_k> = \int p(\mathbf{p}'|D) p_k d\mathbf{p}' \quad (k = 1, \ldots, m) \tag{2.34}$$

The uncertainties and their correlations of these parameters can be obtained from the covariance matrix $\mathbf{V}_p$, whose elements are found using the equation

$$(\mathbf{V}_p)_{kq} = <(p_k - <p_k>)(p_q - <p_q>)> = \int (p_k - <p_k>)(p_q - <p_q>) p(\mathbf{p}'|D) d\mathbf{p}' \tag{2.35}$$

where k, q = 1, ..., m. This is a completely rigorous approach, and when the number of parameters is quite large, Equations 2.34 and 2.35 can become quite involved. We, therefore, investigate use of the likelihood function (Smith, 1993).

Suppose the data set D is represented as a collection of values denoted $\boldsymbol{y}$. The covariance matrix for these values is given by $\mathbf{V}_y$. We now let **f** represent a series of the function f_i, where $f_i(\mathbf{p}) = y_i$, given the parameter set **p**. Using the principle of maximum entropy, the likelihood, L, can be expressed as

$$L(D|\mathbf{p}) \propto \exp\left\{\left(\frac{-1}{2}\right)[\mathbf{y}-\mathbf{f}(\mathbf{p})]^{+}\mathbf{V}_{y}^{-1}[\mathbf{y}-\mathbf{f}(\mathbf{p})]\right\} \tag{2.36}$$

where the symbol "+" represents matrix transposition and $\mathbf{V}_y^{-1}$ is the inverse of the covariance matrix. Equation 2.36 suggests that knowledge of a data set and the associated covariance matrix provides a likelihood function which takes the form of a normal distribution. However, the form of the likelihood function is directly related to the functions **f**. Therefore, the likelihood function may or may not be normal in the parameters **p** (Smith, 1993).

2.3.1.3 Formulation of the LSMOD Algorithm

Combining equations 2.33 and 2.36 nets an expression for the probability density function, given as

$$p(\mathbf{p}|D) = C\exp\left\{\left(\frac{-1}{2}\right)[\mathbf{y}-\mathbf{f}(\mathbf{p})]^{+}\mathbf{V}_{y}^{-1}[\mathbf{y}-\mathbf{f}(\mathbf{p})]\right\}p_a(\mathbf{p}) \tag{2.36}$$

where C is the required normalization constant. Note that the likelihood function, L, has been included. However, as the LSMOD routine is appropriate for problems where little or no information of the prior parameters, the prior density function, p_a, must be a non-informative prior probability function. Therefore, it can be thought of a constant, independent of **p**. Assuming $p_a(\mathbf{p}) = 1$, we can restate Equation 2.37 as

$$p(\mathbf{p}|D) = C\exp\left\{\left(\frac{-1}{2}\right)[\mathbf{y}-\mathbf{f}(\mathbf{p})]^{+}\mathbf{V}_y^{-1}[\mathbf{y}-\mathbf{f}(\mathbf{p})]\right\} \tag{2.38}$$

The matrix $\mathbf{V}_y$ must be positive definite so as to represent reasonable physical uncertainties in the data set. It also follows from the definition of positive definite that the inverse is positive definite, and therefore, the quantity located within the exponential in Equation 2.38 is always a negative scalar (Smith, 1993).

Using the principle of maximum likelihood, the best choice of the set **p** is one which maximizes the posterior probability. This requirement can be met by the equation

$$[\mathbf{y}-\mathbf{f}(\mathbf{p})]^{+}\mathbf{V}_y^{-1}[\mathbf{y}-\mathbf{f}(\mathbf{p})] = \text{minimum} \tag{2.39}$$

Assuming that the model which relates the parameters **p** to the data **y** is linear, Equation 2.39 can be restated as

$$[\mathbf{y}-\mathbf{A}\mathbf{p}]^{+}\mathbf{V}_y^{-1}[\mathbf{y}-\mathbf{A}\mathbf{p}] = \text{minimum} \tag{2.40}$$

where **A** is defined as a matrix of fixed constants which relates the data **y** to the parameters **p**. **A** is referred to as the design matrix. Since the data **y** are approximated by **f(p)**, a simple expression can be used to denote the relationship of the system as

$$\mathbf{y} \approx \mathbf{A}\mathbf{p} \tag{2.41}$$

Minimizing equation 2.39 yields the following equations

$$\mathbf{p} = \mathbf{V}_p \mathbf{A}^{+} \mathbf{V}_y^{-1} \mathbf{y} \tag{2.41}$$

$$\mathbf{V}_p = (\mathbf{A}^{+} \mathbf{V}_y^{-1} \mathbf{A})^{-1} \tag{2.42}$$

$$\chi^2 = (\mathbf{y} - \mathbf{A}\mathbf{p})^{+} \mathbf{V}_y^{-1} (\mathbf{y} - \mathbf{A}\mathbf{p}) \tag{2.43}$$

Equations 2.41, 2.42, and 2.43 are used in all least squares calculations. The matrix $\mathbf{V}_p$ serves as the covariance matrix for the parameters **p**. χ^2 is a scalar used determine the accuracy of the estimates (Smith, 1993)

2.3.2 The NNLS Methodology

The derivation of the NNLS solution routine is quite different from that of the LSMOD package. Using the assumption that all of the elements of the solution set are equal to or greater than zero (0), the conditions under which a solution is derived is given by the Kuhn-Tucker theorem (Lawson, 1974). This theorem is described in subsequent sections.

2.3.2.1 The Kuhn-Tucker Theorem

An n-vector $\mathbf{x}$ *is a solution for the constrained least squares problem if and only if there exists an m-vector* $\mathbf{y}$ *and a partitioning of the integers one (1) through m into subsets* ε *and* δ *such that*

$$G^T y = E^T(Ex - f) \quad (2.45)$$

$$r_i = 0 \quad for\ i \in \varepsilon \quad (2.46)$$

$$r_i > 0 \quad for\ i \in \delta \quad (2.47)$$

$$y_i = 0 \quad for\ i \in \varepsilon \quad (2.48)$$

$$y_i > 0 \quad for\ i \in \delta \quad (2.49)$$

where

$$r = Gx - h \quad (2.50)$$

In the above, **G** is an *m* x *n* matrix, **h** is an *m*-vector. ***E*** is an *m* x *n* matrix, where f is an *m*-vector. The Kuhn-Tucker theorem can be interpreted in the following manner. Let g_i^T denote the ith row vector of the matrix *G*. The *i*th constraint, $g_i^T x \geq h_i$, defines a feasible half-space, $(x: g_i^T x \geq h_i)$. The vector g_i is orthogonal to the bounding hyperplane of this defining halfspace and is directed inward toward the halfspace. The point x is interior with respect to the halfspaces which are indexed by δ. The point x is on the boundary of the halfspaces which are indexed by ε (Lawson, 1974).

A gradient vector of the equation

$$\varphi(x) = \tfrac{1}{2}\|Ex - f\|^2 \quad at\ x = x \quad (2.51)$$

can be defined as the vector

$$p = E^T(Ex - f) \quad (2.52)$$

As y_i=0 for $i \notin \varepsilon$, Equation 2.45 can be rewritten as the following

$$\sum_{i\in\epsilon} y_i(-g_i) = -p \tag{2.53}$$

stating that the negative gradient vector can be expressed as a non-negative linear combination of outward-pointing orthogonal vectors. Using a geometric interpretation, this can be explained by stating that the negative gradient vector lies in the convex cone based at the point x and generated outward by the orthogonal vectors (Lawson, 1974).

Any perturbation u of the point x such that $x+u$ remains possible must satisfy the inequality $u^T g_i \geq 0$ for all $i \in \delta$. Multiplying Equation 2.53 by the vector u^T and using the constraint $y_i \geq 0$, it can be shown that u satisfies the inequality $u^T p \geq 0$. Utilizing the identity

$$\varphi(x+u) = \varphi(x) + u^T p + \|Eu\|^2 / 2 \tag{2.54}$$

it can be shown that there exists no feasible perturbation u which can reduce the value of φ (Lawson, 1974).

2.3.2.2 Formulation of the NNLS Algorithm

The NNLS algorithm is designed to calculate a solution vector, x, of the constrained least squares problem $Ex \cong f$, where E is the $m \times n$ design matrix and f is a vector of length m which describes the relationship of E and x. Working vectors of length m are defined as w and z. P and Z are defined as index sets and are modified in the algorithms execution. Variables indexed by Z are held to the value of zero (0), while those indexed within P can take other non-zero values. If the value of the variable is negative, the algorithm will set the variable to a positive value or set it to zero (0) and move it to the set Z (Lawson, 1974).

The following is a logical description of the processes utilized to complete the NNLS algorithm. This description is as described by Lawson in the text Solving Least Squares Problems, 1974.

Step 1 *Set P = Null, $Z = \{1,2,..., n\}$, and $x = 0$.*

Step 2 *Compute the n-vector $w = E^T(f - Ex)$.*

Step 3 *If the set Z is empty or if $w_j \leq 0$ for all $j \in Z$, go to Step 12.*

Step 4 *Find an index $t \in Z$ such that $w_t = max \{wj : j \in Z\}$.*

Step 5 *Move the index t from set Z to set P.*

Step 6 *Let E_P denote the m x n matrix defined by*

$$Column\ j\ of\ E_P = \begin{cases} column\ j\ of\ E\ if\ j \in P \\ 0\ if\ j \in Z \end{cases}$$

Compute the n-vector z as a solution of the least squares problem $E_P z \cong f$. Note that only the components z_j, $j \in P$, are determined by this problem. Define $z = 0$ for all $j \in Z$.

Step 7 *If $z_j > 0$ for all $j \in P$, set $x = z$ and go to Step 2.*

Step 8 *Find an index $q \in P$ such that $x_q / (x_q - z_q) = min\ x / (x_j - z_j)$: $z_j \leq 0, j \in P\}$.*

Step 9 *Set $\alpha = x_q / (x_q - z_q)$.*

Step 10 *Set $x = x + \alpha(z - x)$.*

Step 11 *Move from set P to set Z all indices $j \in P$ for which $x_j = 0$. Go to Step 6.*

Step 12 *Comment: The computation is complete.*

Upon completion of the algorithm, vector x contains the solution and w is the dual vector. Further discussion of this algorithm can be found in Lawson (1974).

2.4 Minimum Detectable Activity

In order to accurately determine the minimum detectable activity (MDA) for a tomographic gamma scanning system, one must consider each orientation and geometric configuration of the system. For each of these, a unique detection efficiency exists. The variation in efficiencies makes determination of a system MDA an extremely complex calculation.

However, reasonable approximations of the system MDA can be determined for a point source located in a known source position. In this fashion, the efficiency is assumed constant, with the detector position being that which provides the shortest path length from the source to the detector face. Note that the efficencies correspond to the elements of the PSRF matrix. Having made the assumption that this result provides a suitable approximation of the system MDA, a statistical analysis can be undertaken.

Using the methodology set forth in the paper *Statistical Measures of the Lower Limit of Detection of a Radioactivity Counter* (Altshuler, 1963) as a guide, a series of calculations and assumptions must be set forth. First, the term *minimum detectable true activity* is used to describe the smallest amount of activity present which results in measurement which predicts the presence of activity with a certain degree of confidence. This term is synonymous with MDA. The risk of error in the determination of activity, or the degree of confidence, can be discussed using two (2) types of errors. The reporting of activity when, in fact, there is none present is referred to as a Type One (1) error. The second error, a Type Two (2), occurs when an active sample is reported as having no activity. For each, a probability of error must be assigned. The probability of a Type One (1) error is referred to by the variable α while that of a Type Two (2) error is referred to as β. These probabilities are then used to determine the values of k_α and k_β using tables for the standardized normal distribution (Altshuler, 1963).

A final requirement of the calculation is the determination of an accurate background count. For this experiment, a sufficiently long background count was made. The number of counts in the region of interest was then summed and scaled to the appropriate time factor. This scaled value is now referred to as the background count for the system, B. The MDA can be directly calculated using the equations set forth by Altshuler and Pasternack (1963), where

$$MDA = \gamma\sqrt{B}\left[k_\alpha + k_\beta\sqrt{\left(1+\frac{k_\alpha}{\sqrt{B}}+\frac{k_\beta^2}{4B}\right)}+\frac{k_\beta^2}{2\sqrt{B}}\right] \tag{2.55}$$

Note that γ is the calibration constant, or the corresponding element of the PSRF matrix. An approximation of this equation can be made which greatly simplifies the calculation of the MDA. The approximation is given as

$$MDA \cong \gamma\left(k_\alpha + k_\beta\right)\sqrt{B} \tag{2.56}$$

The above equations are only appropriate when the background is accurately known and is subject to only statistical fluctuations, i.e. constant mean value (Altshuler, 1963). Under these assumptions, Equation 2.56 provides an approximate estimate for the system MDA.

Chapter 3

Experimental Methodology

3.1 Experimental Apparatus

ECT measurements were conducted using a typical radioactive waste package containing gamma emitting point sources. The equipment used in this experiment consisted of off-the-shelf hardware and custom-fabricated devices. An outline of the system is given in the following sections.

3.1.1 Radioactive Waste Container

The container chosen for this research was a standard 208 liter (55 gallon) steel drum with a removable band-constricted lid. The wall thickness of the drum was 2.54 millimeters (0.100 inches). The drum was 28.8 centimeters (11.3 inches) in radius and 85.6 centimeters (33.7 inches) in height. The lid was removed and a clear acrylic plastic fixture installed to facilitate placement of the source within the drum. Neglecting the presence of air, the drum contained no attenuating media.

As previously discussed, a requirement of ECT scanning is the need to measure the gamma flux at several angular positions about the drum. To facilitate these measurements, the drum is placed on a carousel unit, allowing the drum to rotate about its central axis. Four (4) angular positions were chosen with the drum being rotated clockwise at 90° intervals.

3.1.2 Detector Positioning Apparatus

To position the detector and collimator at the appropriate measurement locations, a fixture was constructed. Figure 3.1 provides an illustration of the positioning apparatus. The detector and collimator are placed upon a central platform which provides movement in the z-direction. Measurements are taken at six (6) z-direction intervals of 14.2 centimeters (5.6 inches). Total movement of the detector in the z-director is 101.6 centimeters (40.0 inches).

The detector and collimator are mounted upon a wheeled trolley located upon the central platform. The trolley provides movement in the x-direction. There are five (5) x-director positions. Measurements are taken at five (5) intervals of 11.4 centimeters (4.4 inches). Total movement of the detector in the x-director is 76.2 centimeters (30.0 inches). Figure 3.2 is a schematic of the platform.

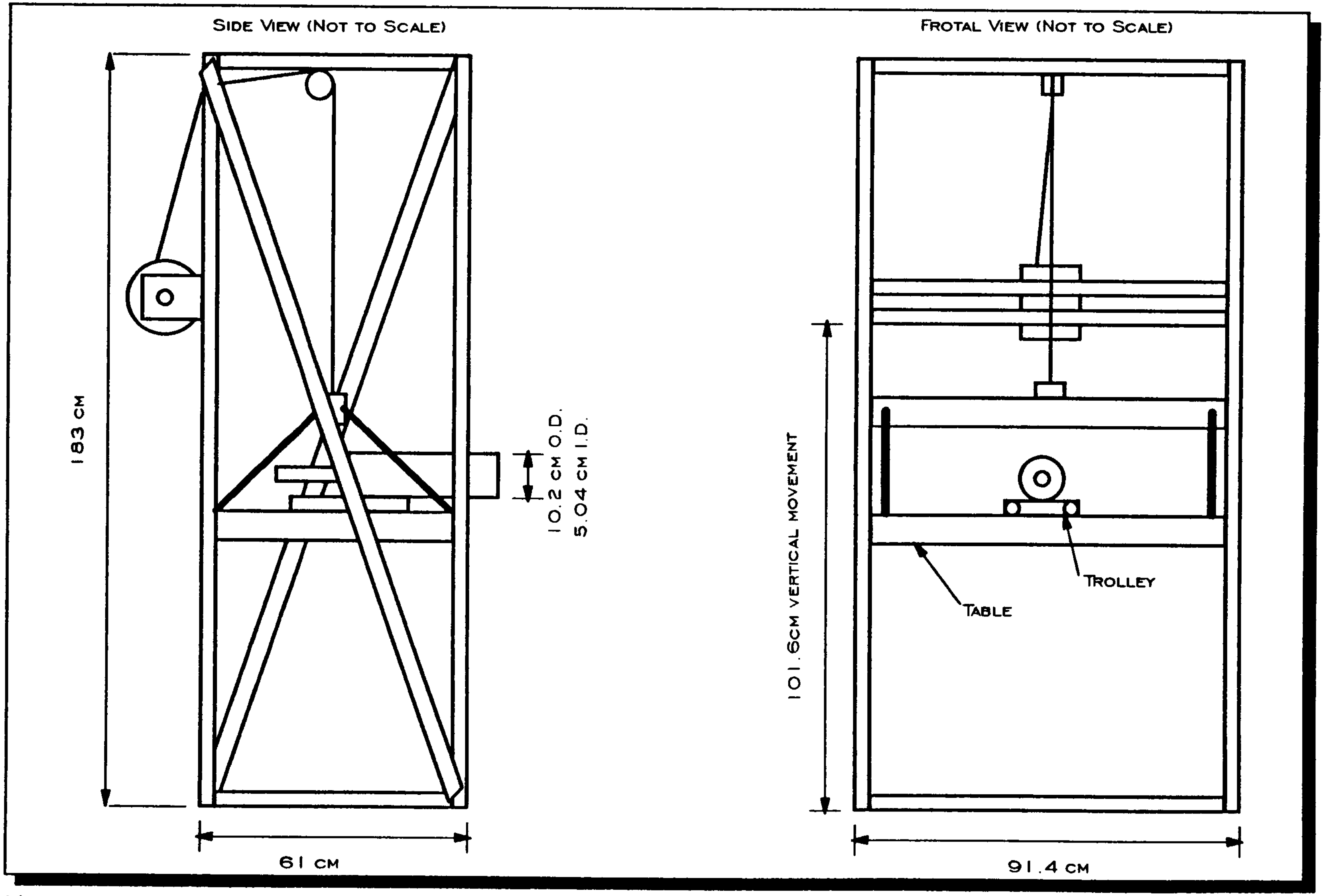

Figure 3.1 Schematic of Detector Positioning Apparatus

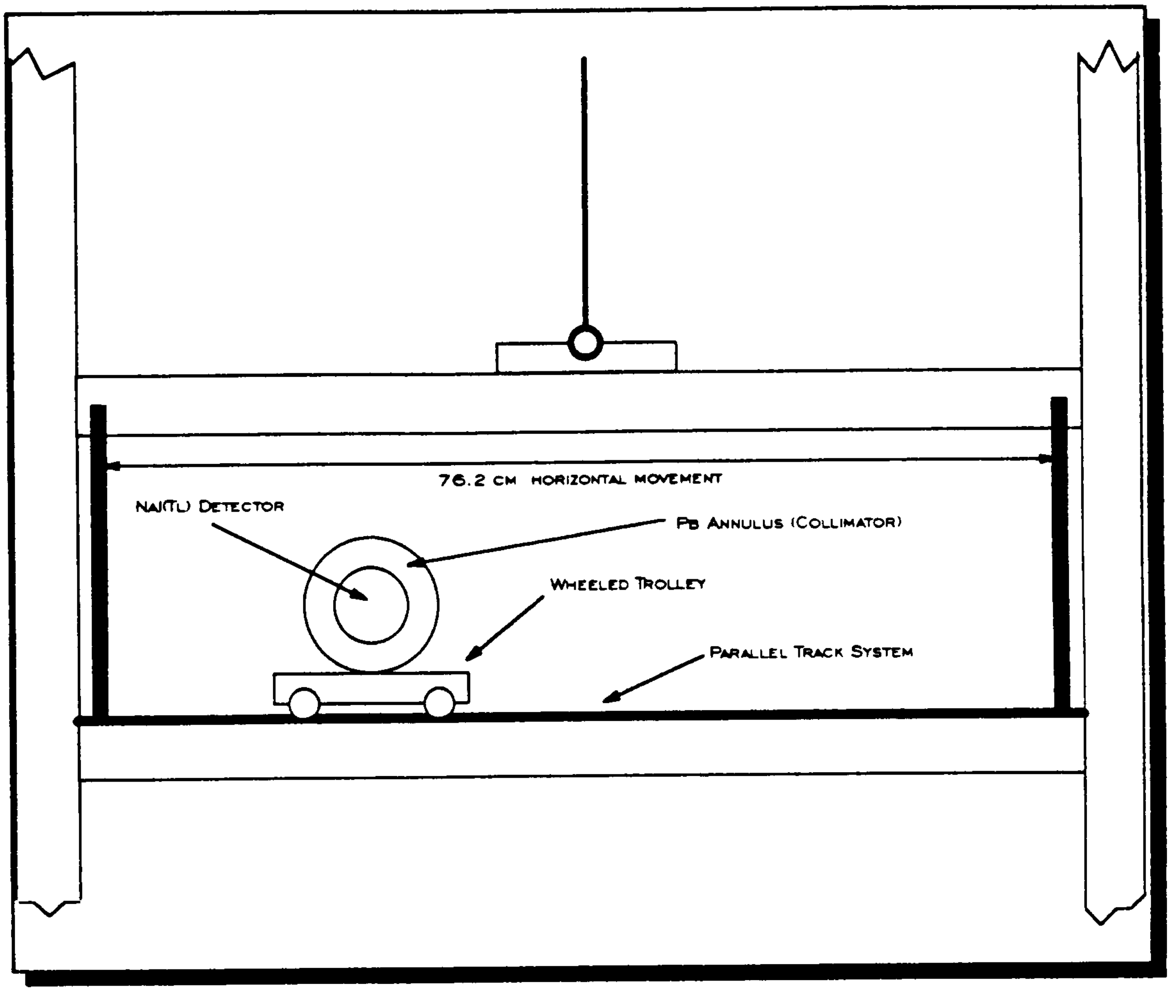

Figure 3.2 Schematic of central platform and detector trolley.

Movement of the platform is controlled by a manually operated winch having a ratio of 31:1. The winch is wound with 0.48 centimeter (0.19 inch) diameter steel cable which is attached to the central platform. Manually operated spring clamps retain the platform once it is in position. Figure 1, Appendix A contains a photograph of the apparatus and drum as used in this research.

3.1.3 Radioactive Sources

The isotope chosen for use in this research was ^{137}Cs. Selected for its commonality in typical LLRW streams and its monoenergtic 662 keV gamma, two point sources of different activity were utilized. The first source, with 180 μCi activity, is National Institute of Standards and Testing (NIST) "traceable" and is encased within a polymer resin. Fabricated by DuPont, Inc., the vial size is approximately 1.9 centimeters (0.75 inches) in diameter and 5.0 centimeters (2.0 inches) in height. The source was affixed to a movable rod which was then used to locate the source in the center of selected voxels within the drum.

A second ^{137}Cs source was also utilized. Initial measurements with the 180μCi source required a long count time at each detector position in order to achieve suitable statistics. In an effort to shorten the time period required to complete a barrel scan, a 73mCi ^{137}Cs source was procured. Fabricated by ICN, Inc., the source is encased by a stainless steel cladding and is affixed to a handling rod. Due to the high dose rate associated by this source (30 mR per hour unshielded at 1 meter), regulations dictated the construction of additional shielding and implementation of ALARA procedures to protect research personnel. Measured dose rates at the surface of the drum are approximately 10 mR per hour, while dose rates behind the restricted access perimeter are below 2 mR per hour. The cumulative dose to the researcher during the experimental period was measured as less than 60 mR, whole body. Use of the source served to reduce count time by a factor of approximately ten (10), while providing improved photon counting statistics.

3.1.4 Collimation System

To improve system resolution and reduce crosstalk between detector positions, a lead (Pb) collimator was fabricated for the detector. The collimator was formed by rolling 3.18 millimeter (0.125 inch) Pb sheeting around a 5.04 centimeter (2.0 inch) pipe. This was continued until a thickness of 2.54 centimeters (1.0 inch) was achieved. Following the rolling process, the collimator was tightly banded to reduce void space between the layers. It was then aligned and attached to the central trolley.

Figure 3.3 provides a schematic of the collimator and detector arrangement. As seen from the figure, the outside diameter is 10.2 centimeters (4.0 inches), the inside diameter is 5.04 centimeters (2.0 inches), and the overall length is 25.5 centimeters (10.0 inches). The detector is inserted 10.2 centimeters (4.0 inches) into the collimator. The detector has a conic field of vision with a vertex angle of 36.87 degrees.

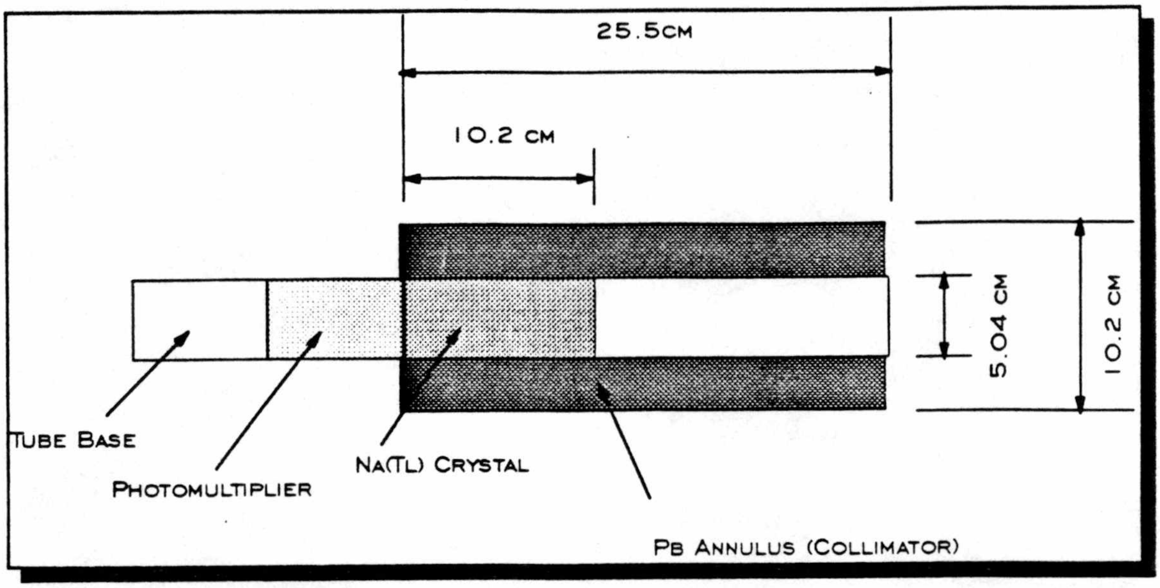

Figure 3.3 Schematic of detector collimator with dimensions.

Two problems have arisen with respect to the collimator. The first is related to the rolling procedure used in the fabrication process, which has caused an asymmetric condition. This problem is due to the wrapping of an additional layer of Pb over part of the collimator. This preferred method by which to eliminate this asymmetry is by the construction of a proper mold and the casting of a new collimator.

The second problem involves the large amount of Pb used in the collimator. While increasing resolution for the ECT scanning system, there are also a great deal of Pb X-rays, resulting from photoelectric gamma interactions and the subsequent ejection of K and L shell electrons. As the vacancies are filled, energy surplus is lost via creation of a characteristic X-ray. Due to the size and geometry of the collimator, a large number of Pb X-rays are created at certain source - detector orientations. The result is a large number of low energy interactions within the detector crystal. This serves to increase dead time in the system, thereby reducing overall system efficiency. To combat this problem, a copper (Cu) liner should be placed between the detector and the Pb collimator, as Cu has a large absorption coefficient for low energy photons. While it too produces characteristic X-rays due to photoelectric interactions, they are of much lower energy that those of Pb. As such, Cu has been used for many years in X-ray shielding fixtures (Eckerman, 1995).

3.1.5 Photon Detection Electronics

The detection system used in this experiment was composed of standard off-the-shelf research grade electronics. Figure 3.4 provides a schematic of the electronics and their orientations. Appendix A, Figure 2 provides a photograph of the electronics as they were used in this research.

3.1.5.1 Detector

A Bicron model 2m2/2 thallium-activated sodium iodide detector (NaI(Tl)) was utilized. This detector has a circular active crystal that is 5.04 centimeters (2.0 inches) in diameter and 5.04 centimeters (2.0 inches) in length. The crystal and

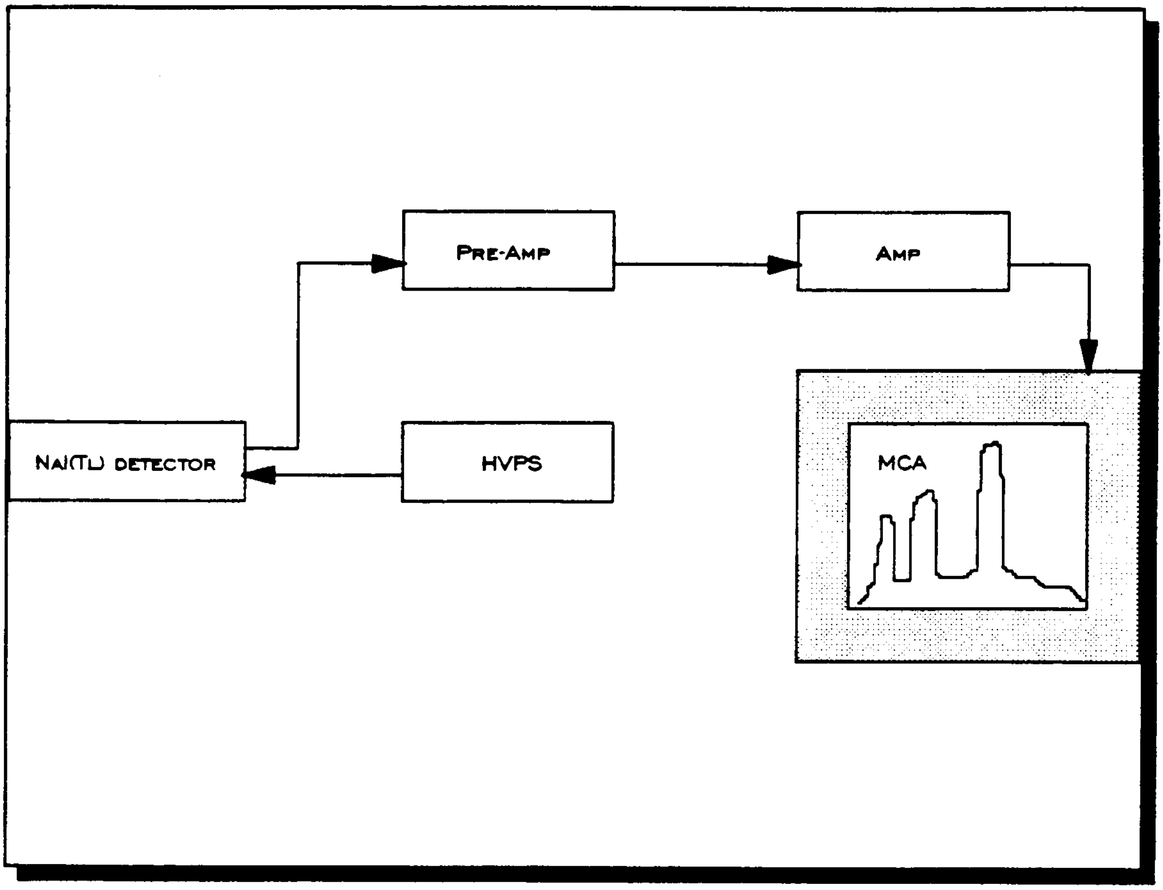

Figure 3.4 Schematic of research electronics.

photomultiplier tube (PMT) is encased within a stainless steel cladding. The detector was secured into a model TC-155 twelve (12) pin tube base.

3.1.5.2 Multi-Channel Analyzer

A PCA-II multi-channel analyzer (MCA) was used for data collection. Constructed by The Nucleus Company (now a subsidiary of Oxford Instruments, Inc.), the collection system consists of a data acquisition board, which is inserted into a IBM type personal computer, and a MS-DOS based software package. A

Zenith IBM-PC clone with an 80386 processor was host for the MCA system. The data was collected using 8096 channels, with the photopeak voltage adjusted to place the peak channel in channel 4000, approximately.

3.1.5.3 Support Electronics

Power for the PMT and pre-amp was supplied by a digital model TC-952 high voltage power supply (HVPS) manufactured by Tennelec, Inc. Voltage was nominally set for 940 volts, positive DC in all cases. The detector signal was collected at the PMT anode and routed to a Tennelec model TC-174 pre-amplifier. Capacitance was held fixed at 200 pF. Further signal processing was performed by an EG&G Ortec model 451 spectroscopy amplifier. The signal was shaped via bi-modal processor and routed to the MCA. A Tektronix model 2235 oscilloscope was placed in-line, following amplification, for voltage and shape monitoring of the PMT signal.

3.2 Experimental Procedure

Several experiments were conducted with the source located at various positions within the drum. System parameters were held constant to provide consistency in the results. This section outlines the laboratory procedures utilized during data collection and activity distribution reconstruction.

3.2.1 Source Positioning

As stated earlier, the drum was originally fabricated with a band-compressed lid. This was removed from the drum and a clear acrylic plastic cover fabricated. The cover has provisions for suspending retaining rod, which allows the source to be located in the geometric center of any voxel. Source positions, chosen at random, are listed in Table 3.1.

Table 3.1 Source Locations for Selected Experiment Number.

Experiment Number	Region Number (1-9)	Layer (A-F)
1	1	B
2	9	C
3	7	D
4	3	D

3.2.2 Detector Positioning

Positioning of the detector in the xy-plane is accomplished by moving the trolley to each of five (5) established positions along a fixed interval perpendicular to the y-axis. The interval is divided by five (5) so as to create a symmetric condition about the y-axis. The spacing between the detector centerlines, along the interval, is 11.4 centimeters (4.5 inches). Detector position one (1) is located at the x = -22.9 centimeter (-9.0 inch) position. Figure 3.5 provides a schematic of the detector positions and voxel arrangements in the xy-plane. Note that the geometric center of the drum serves as the center of the reference system governing the experiment.

In the yz-plane, the drum is divided into six (6) layers along the z-axis, each having a thickness of 14.0 centimeters (5.5 inches). The detector is placed in the center of these layers, with five (5) collection points for each layer; thus, yielding thirty (30) detector positions. The spacing between detector centerlines in the yz-plane is 14.0 centimeters (4.5 inches). Detector position A is located at the z = -35.45 centimeter (-14.0 inch) position. Figure 3.6 provides a schematic of the detector positions and voxel arrangements in the yz-plane.

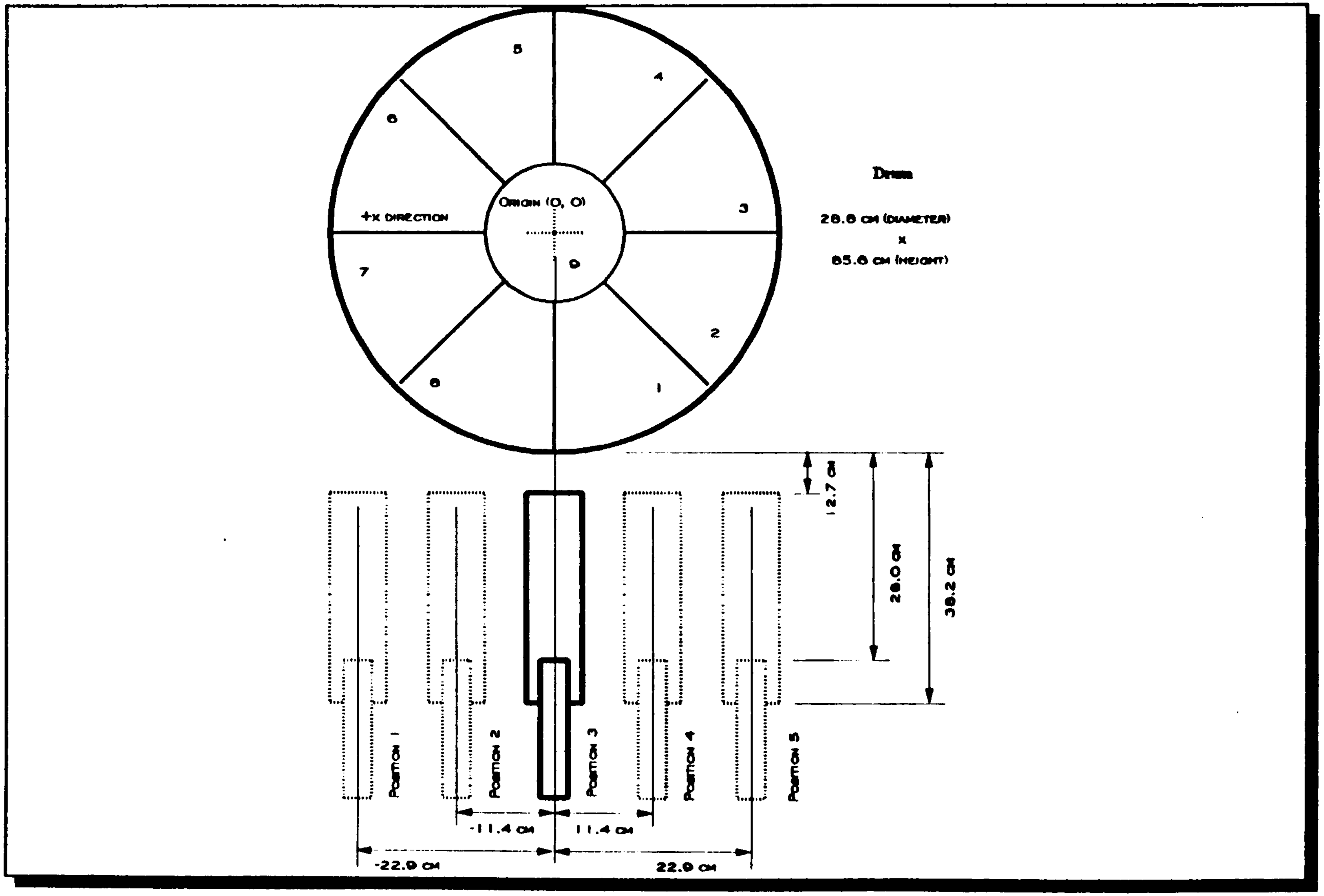

Figure 3.5 Detector Positioning in the XY- Plane

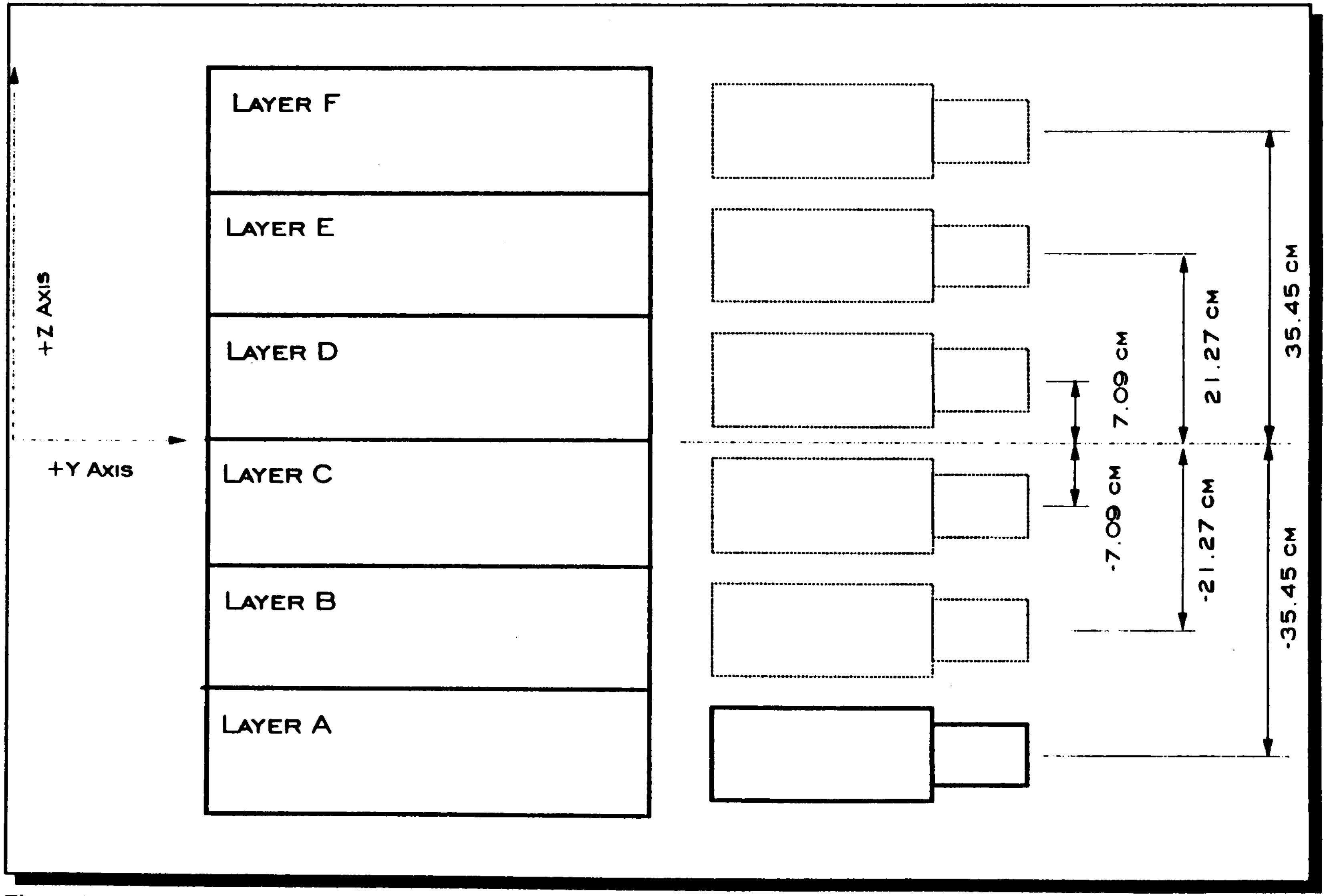

Figure 3.6 Detector Positioning in YZ-Plane.

3.2.3 Drum Positioning

The drum is placed upon the carousel and rotated so as to align the common side of voxel area eight (8) and area one (1) in a position which is perpendicular to the y-axis. Areas one (1) and eight (8) should be closest to the detector. The detector centerline when in position three (3), corresponding to x = 0.0, should be oriented along the area eight (8) and area one (1) divider. This alignment causes the vertex of the drum to intersect the y-axis of the system, thereby establishing a symmetric condition about the y-axis. The distance from the collimator to the edge of the barrel is 12.7 centimeters (5.0 inches). The distance from the detector face to the edge of the barrel is 28.0 centimeters (11 inches). These measurements were made to the outside drum surface, along the y-axis.

A series of thirty (30) measurements are made in this first orientation. This is referred to as the zero (0) degrees orientation. Once measurements have been made and recorded at each detector position, the drum is rotated on the carousel clockwise, orienting the drum with the area eight (8) and area one (1) divider lying perpendicular to the y-axis. This is the ninety (90) degree position. A series of thirty (30) measurements are taken at this position. The barrel is again rotated clockwise on the carousel an additional ninety (90) degrees and measurements taken at the one-hundred eighty (180) degree position. This is repeated for the two-hundred seventy (270) degree position.

3.2.4 Counting Times

Counting times at each detector position, using the 73 mCi source, were set at one (1) minute. This value provides a reasonably rapid total scanning time and improved photon statistics. Formerly, when the 180 μCi source had been used, counting times were set at ten (10) minutes. However, there were several locations where the number of counts under the full-energy peak was impossible to determine. Following background and Compton subtraction, the net count at these positions would be equal to or less than zero (0). It was determined that the 180 μCi source was below the system MDA. By using the 73 mCi source, which is approximately four-hundred (400) times more active than the 180μCi emitter, a reduction in count time by a factor of ten (10) was achieved while simultaneously providing an increase in the number of photons striking the detector by a factor of approximately forty (40).

3.2.5 Determination of Background Radiation

With the apparatus and barrel in position, a sufficiently long background count was made with the source out of the drum. The count time was 151,362 seconds (42.045 hours). The net number of counts in each bin was divided by the appropriate scaling factor and a background count normalized to one minute computed. This count is to be subtracted from each spectra, yielding a net count for the drum with the source located at some specified location. A long count time was chosen so as to reduce the standard deviation in the count rate according to general error propagation theory. The formula for the standard deviation of the count rate (σ_R), as stated by Turner (1992), is given by

$$\sigma_R = \sigma_C / t , \quad \textit{where } \sigma_C = \sqrt{\textit{total count}} \tag{3.1}$$

where the count rate is defined as the number of counts divided by the counting time (t).

3.2.6 Data Handling

The spectra were collected using the computer-based PCA-II MCA and software. The spectra files, in binary format, were then written to disks and transferred to another IBM-PC clone for processing. This new machine, manufactured by Quantex Microsystems, utilizes a 486-DX/2 processor operating at 66 megahertz. The spectra files are written to the hard-drive and then accessed by FORTRAN routines written by the author.

Two reconstruction routines were written. The first utilizes the NNLS solution package to provided solutions for the source distribution. The second uses the LSMOD package. Both are similar in design, handling data conversion and matrix creation in a similar manner. However, the input to each solution routine dictates a deviation in the latter sections of each code. Both programs can be found in Appendix B.

3.2.6.1 File Conversion

Initial operations performed by both reconstruction routines involve conversion of all spectra files from binary format to ASCII data sets. To do this, the reconstruction program reads an input file which contains the spectra filenames, new ASCII filenames, count time, and peak window. An example of this input file is found Appendix C. Conversion to ASCII format is by a standard reformatting algorithm, deleting all header information from the binary file. The output is placed into both an array and an external file.

3.2.6.2 Background Subtraction

Subtraction of the well-known background takes place during the file conversion process. For each channel within a certain spectrum, the binary data is converted to a set of ASCII integers, containing both the channel number and count in that channel. This is performed on a channel by channel basis and is implemented by an indexed loop. When the gross count in any channel is reformatted to ASCII, the background count for that channel is subtracted. This is done prior to writing any data to an output file or array. The conversion of the background count file is the first process undertaken and the ASCII values are placed into an array. It is this array, indexed inside the loop, which is subtracted from the gross count values, to yield the net count for any channel.

3.2.6.3 Subtraction of Compton Continuum

As previously stated, due to the large amount of Pb present in the collimator, there are a large number of counts attributed to both Pb K- or L-shell X-rays and Compton scattering. The result of the large amount of scattering associated with the collimator is a full-energy photopeak that is superimposed on top of a large Compton continuum. This is illustrated by Figure 3.7 which provides a plot of a selected data set in which the photopeak is obscured by the continuum. To combat this problem, a Compton continuum subtraction algorithm was incorporated into both reconstruction routines. The subtraction model, developed for ECT scanning at the Los Alamos National Laboratory (LANL), places a window on both sides of the full-energy photopeak. The net number of counts is found by

$$a = b - cx \tag{3.2}$$

where b is the gross number of counts in the full-energy photopeak, c is the sum of the counts in both continuum windows, and x is the ratio of the number of photopeak channels to the number of channels in the continuum windows.

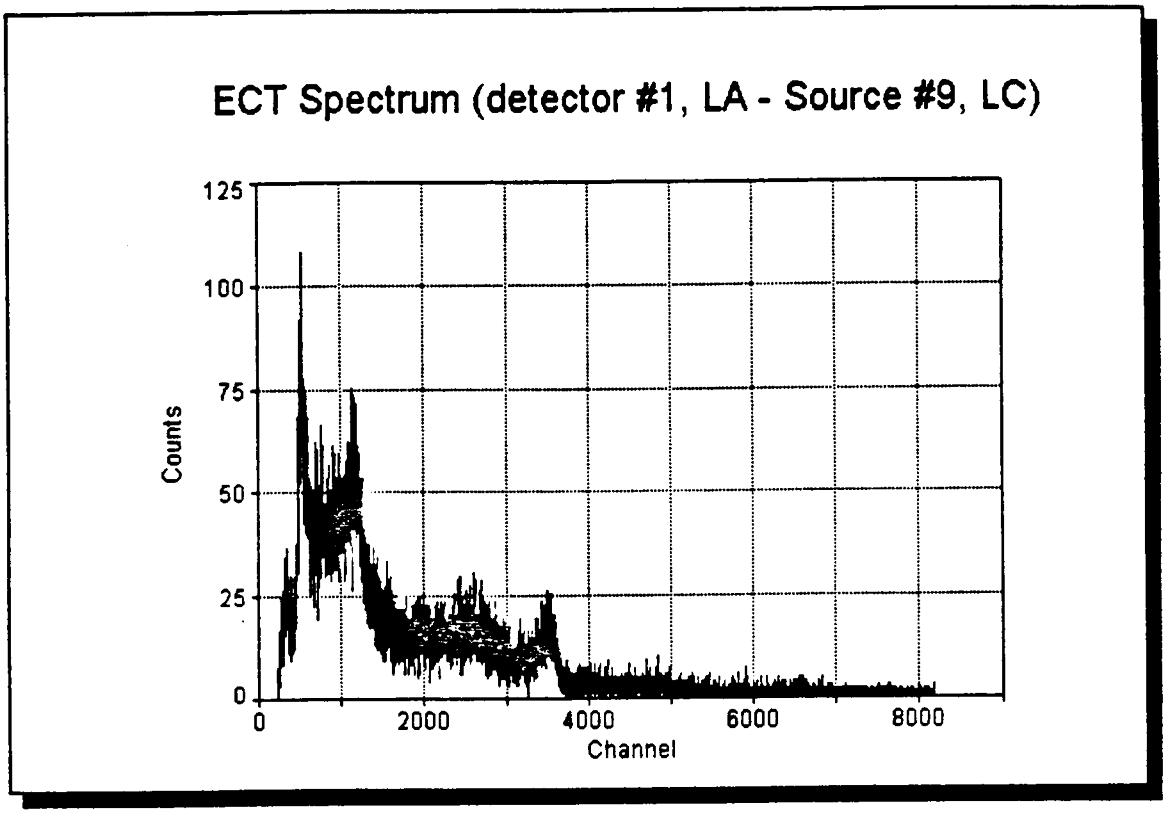

Figure 3.7 Plot of ECT Spectrum.

The use of this "symmetric" subtraction model provides results which are quite accurate. As such, the method of continuum subtraction is often used in assays of special nuclear materials (Estep, 1994) The net counts in each photopeak window, with width specified in the input file, is placed into an ASCII formatted output file.

3.2.6.4 Using the NNLS Algorithm

After performing the file conversion, background subtraction, and continuum subtraction, the reconstruction routine reads the net count values from a fixed-format ASCII data file. These values are multiplied by an experimentally determined calibration factor, whose value has been determined to be 60.0. This determination was made by performing several runs with the system, and computing the difference in the actual source activity and those values predicted by the algorithm. It is interesting to note that this factor is different when the LSMOD algorithm is utilized.

Following the scaling the data set by the experimentally determined calibration factor, the values are placed into an array. The data file containing the PSRF data file is then read and the values placed into a 2-D array. These, along with various other input parameters, are passed to the NNLS subroutine. Solutions to the linear system are determined within several seconds. Total run time for the routine is approximately 4 minutes, with a vast majority of that time being consumed with the input/output requirements of the conversion of some 120 data files, each having 8192 lines of data.

Once the NNLS subroutine has reconstructed the source distribution, the output is placed into an array and passed back to the main routine. The computed values for the activity are displayed in list form on the screen and placed into a data file. Values for the activity in each voxel are shown, with the sum for each layer being computed and displayed. Also, the total activity for the drum is calculated and shown at the end of both the screen display and data file. Output files for each experimental run using the NNLS-based reconstruction routine are located in Appendix D.

3.2.6.5 Using the LSMOD Algorithm

In a manner similar to the NNLS-based routine, the net count values are read from the data file. Likewise, they are scaled by division of a calibration factor, determined in the same manner as discussed in the previous section. However, the calibration factor utilized in this routine was calculated to be 15.0.

The LSMOD routine requires a covariance matrix as part of the input stream. As each count is independent, the covariance matrix takes the form of a diagonalized matrix, with the count variance being placed along the diagonal. Using Gaussian statistics, the variance of the count, or the square of the standard deviation, is just the count itself. The matrix is created by use of a compound loop, placing the count values along the diagonal and zeros (0) in all other positions. The covariance matrix, 120 x 120 in size, along with the data array, PSRF matrix, and array sizes, is passed to the LSMOD subroutine. The LSMOD subroutine returned a solution after a run time of approximately 10 minutes. Total run time of the reconstruction routine was approximately 14 minutes. This is a vast increase over that required to implement the NNLS algorithm. The iterative routines within the LSMOD algorithm, as discussed in Chapter 2, have been determined as the cause of the delay. The LSMOD, in its original form, was designed as a stand-alone routine which provides solutions to somewhat smaller systems of linear equations. The author modified the LSMOD code to function as a subroutine capable of providing solutions to the large linear systems utilized in the reconstruction of the source distribution within the drum.

Output is formatted in exactly the same manner as the NNLS-based routine. Data arrays containing the computed activity values for each voxel are written to both an external file and the screen. Similarly, the activity for each layer and the drum total are calculated and displayed as well. Output files for each experimental run using the LSMOD-based reconstruction routine can be found in Appendix E.

3.3 Modeling Procedures

In order to compute the PSRF matrix, the detector response was calculated for each source-detector location. These calculations were discussed in previous chapters. Several procedures were used in these calculations, for both response determination and validation. The responses were calculated by the point-kernal shielding algorithm, QAD-CGGP. Validation was performed with data calculated using the MCNP monte-carlo gamma ray and neutron transport code.

3.3.1 QAD-CGGP

QAD consists of a series of point-kernal shielding codes which were originally developed by researchers at LANL, the National Aeronautics and Space

Administration (NASA) Lewis Research Center, Brown Engineering, and ORNL. Over the years, the original series has spawned many use-specific versions. Recently, a combinatorial geometry (CG) version was added to the series. Adapted by researchers from the Bechtel Power Corporation (BPC), QAD-CGGP is based upon the QAD-5A version. Further modification and development was performed by researchers from the Japan Atomic Energy Research Institute (JAERI). The latest versions of the series, adapted for use with an IBM-PC, is distributed by the Radiation Shielding Information Center (RSIC) located at ORNL (RSIC, 1994).

3.3.1.1. Method of Solution

Written in FORTRAN 77, QAD-CGGP is a point-kernal shielding code which calculates the fast-neutron and gamma-ray penetration through various shielding configurations defined by the CG inputs. QAD-CGGP uses a point-kernal ray-tracing technique for photon calculations. Either an Albert-Welton kernal or kernals obtained from the moments solution method of the Boltzman transport equation is used for neutron transport calculations. A geometric progression (GP) fitting function is also included to calculate the photon buildup factor (RSIC, 1994).

3.3.1.2. Input Specifications

As previously mentioned, the specifications of each scenario are input via CG. CG is the process in which material configurations are described as unions, intersections, or differences of three-dimensional geometric bodies. Thus, the problem space is divided into geometric zones, each zone being geometrically described as a box, sphere, cylinder, cone, or other simple body. By joining each body with the appropriate logical connective, a complex problem can modeled (RSIC, 1994).

For this scenario, the drum was specified as the difference of two (2) right circular cylinders, as was the collimator. As the central axis of the system was located in the center of the drum, and due to the symmetric orientation of the voxel partitioning system, only 150 orientations were modeled, allowing for the completion of the PSRF matrix. A PSRF matrix outlining the problem symmetry is included in Appendix F. For each distinct source-detector orientation, a separate input file was written.

In order to validate the results obtained from QAD-CGGP, several calculations were performed using test data sets. The geometry of these test sets approximate the actual system geometry, however, the collimator was eliminated from the input file specifications for convenience. Examples of both the actual and validation QAD-CGGP input files are located in Appendix G.

3.3.1.3. Output Specifications

The QAD-CGGP code was implemented on a IBM-PC clone operating with an 80486 DX2/66 processor. Typical run times were less that one minute. Output is listed in a multi-page output file, examples of which are located in Appendix H. The QAD-CGGP code calculates the photon fluence at the detector location in units of mega electron volts per square centimeter per second (Mev/cm^2•sec). Note that this is the fluence of uncollided photons, as the energy discriminator for the program was set for a 0.002 Mev window with 0.662 MeV as the centroid.

The values for uncollided fluence rates were then used to determine the number of 0.662 MeV photons that strike the detector face per second, N_d. An equation for N_d can be stated as

$$N_d = f\left(\frac{MeV}{cm^2 \cdot sec}\right) \bullet a\left(cm^2\right) \bullet \mu\left(\frac{photons}{MeV}\right) \bullet \gamma \tag{3.3}$$

where f is the uncollided fluence rate, a is the surface area of the detector (20.27 cm^2), μ is the number of photons emitted per MeV (1/0.662), and *gamma* is the emission efficiency (0.85 for ^{137}Cs). In performing the fluence rate calculations, a source strength of 1 Curie (Ci) was assumed. The responses can be used in this normalized fashion, as a fluence rate per Ci, or scaled to a smaller activity unit. In this research, the values were stipulated as fluence rates per millicurie (mCi). The data for each detector - source position was then placed into a matrix and saved to a data file. It is this matrix which comprises the PSRF for the reconstruction algorithm. The PSRF matrix, in units of photons per mCi, is listed in Appendix I.

3.3.2 MCNP

In order to validate the PSRF matrix computed by QAD-CGGP, MCNP was used to model several detector - source positions. Calculations were performed by Atsuto Ohashi, visiting researcher from the Ship Research Institute, located in Tokyo, Japan. The calculations were performed using a Sun SparcStation 20 workstation and MCNP version 4A. A series of test data was computed using random source-detector positions, modeling the detector response under conditions similar to those used with the QAD-CGGP simulations. For convenience, the collimator geomery was not included in these calculations. The input file used for these calculations can be found in Appendix J.

Chapter 4

Experimental Results

This section contains a presentation of the results stemming from both the PSRF matrix determination calculations and the ECT scanning procedures. The PSRF matrix data is presented in tabular form along with a quantitative analysis, using the MCNP calculations as a basis. Further, the detector response, as calculated by the QAD-CGGP modeling procedure, is compared to the experimentally determined values. Additionally, an approximate minimum detectable activity (MDA) has been determined for the system using a one (1) minute sampling time at each detector location.

4.1 Results of the PSRF Calculations

Data used to complete the PSRF matrix was calculated using the QAD-CGGP photon transport code. Input specifications were given in the previous chapter. The QAD-CGGP values using several test data sets were compared to those responses obtained using the MCNP transport code to quantitatively determine the accuracy of the QAD-CGGP results. The QAD-CGGP responses used to construct the PSRF matrix were then compared to those values obtained experimentally. The experimental response values, which characterize both the asymmetry in the detection system and the inherent system noise function that is present at all source-detector locations, were used to condition the PSRF matrix.

4.1.1 QAD-CGGP Output

As discussed in the previous chapter, 150 distinct QAD-CGGP runs were required to determine the PSRF matrix. Each of these runs modeled a unique source-detector location and required a unique input file to specify the input geometry. Output for the QAD-CGGP code is in the form of a multi-page ASCII text file, with results for the direct beam flux having units of MeV/(cm^2·sec) per mCi ^{137}Cs. Examples of the output files are given in Appendix H.

The results were tabulated and the PSRF matrix constructed. Tables 4.1 through 4.6 provide a segment of the PSRF matrix, giving those values for the zero (0) degrees orientation. Note that these values have undergone units conversion to express the response in units of photons/sec per mCi ^{137}Cs. The entire PSRF matrix has been tabulated and is located in Appendix I. Figure 4.1 provides a contour plot of the PSRF matrix for source voxels 0 through 54 and detector positions A1 through E6. A more detailed analysis of selected detector responses is given in Figures 4.2 through 4.7. One would expect the response functions to be Gaussian in shape for

Table 4.1 QAD-CGGP Computed Detector Responses for Layer A at 0 Degrees. (photons/sec/mCi)

Detector	Voxel Number								
Number	1	2	3	4	5	6	7	8	9
a1	3967.6	2769.3	840.8	68.86	5761.0	331220.0	559710.0	220.48	113.54
b1	672.18	1047.1	1845.7	413.36	254990.0	332860.0	551010.0	924550.0	17874.0
c1	131410.0	60.69	174.72	254200.0	254200.0	174.72	60.69	131410.0	443470.0
d1	924550.0	551010.0	332860.0	254990.0	413.36	1845.7	1047.1	672.18	17874.0
e1	220.48	559710.0	331220.0	5761.0	68.86	840.8	2769.3	3967.6	113.54
a2	4860.6	3108.6	1014.9	127.99	98.09	1317.2	89.08	1196.7	302.41
b2	1855.1	1526.4	324.62	275.48	12777.0	928.96	65.49	152.31	40.02
c2	258.7	315.28	33.62	3861.9	3861.9	33.62	315.28	258.7	801.47
d2	152.31	65.49	928.96	12777.0	275.48	324.62	1526.4	1855.1	40.02
e2	1196.7	89.08	1317.2	98.09	127.99	1014.9	3108.6	4860.6	302.41
a3	6408.6	3767.0	1484.3	379.4	104.42	167.3	995.28	4626.4	1123.8
b3	4960.8	2735.6	832.41	141.9	47.37	176.09	1012.3	3470.3	563.0
c3	3638.2	1651.1	371.0	55.43	55.43	371.0	1651.1	3638.2	393.08
d3	3470.3	1012.3	176.09	47.37	141.9	832.41	2735.6	4960.8	563.0
e3	4626.4	995.28	167.3	104.42	379.4	1484.3	3767.0	6408.6	1123.8
a4	6944.4	3801.3	2044.5	855.26	528.94	944.79	2969.5	6834.1	2305.7
b4	6735.0	3801.3	1591.2	589.02	423.83	963.96	2946.2	6497.7	1893.5
c4	6478.9	3287.3	1195.0	443.16	443.16	1195.0	3287.3	6478.9	1737.6
d4	6497.7	2946.2	963.96	423.83	589.02	1591.2	3801.3	6735.0	1893.5
e4	6834.1	2969.5	944.79	528.94	855.26	2044.5	3801.3	6944.4	2305.7
a5	6395.2	4258.0	2450.2	1372.0	1127.4	1815.0	3984.8	6850.4	3097.5
b5	6650.4	4158.6	2215.3	1183.0	1047.4	184.03	3926.5	6748.2	2922.7
c5	6660.2	4008.8	1989.0	1066.6	1066.6	1989.0	4008.8	6660.2	2853.1
d5	6748.2	3926.5	184.03	1047.4	1183.0	2215.3	4158.6	6650.4	2922.7
e5	6850.4	3984.8	1815.0	1127.4	1372.0	2450.2	4258.0	6395.2	3097.5
a6	5401.2	3937.1	2605.3	1739.1	1593.5	2290.8	4006.0	5836.1	3320.4
b6	5581.2	3945.3	2509.1	1638.3	1556.1	2320.5	3933.5	5811.9	3272.2
c6	5716.7	3923.2	2402.5	1571.7	1571.7	2402.5	3923.2	5716.7	3251.3
d6	5811.9	3933.5	2320.5	1556.1	1638.3	2509.1	3945.3	5581.2	3272.2
e6	5836.1	4006.0	2290.8	1593.5	1739.1	2605.3	3937.1	5401.2	3320.4

Table 4.2 QAD-CGGP Computed Detector Responses for Layer B at 0 Degrees. (photons/sec/mCi)

Detector	Voxel Number								
Number	10	11	12	13	14	15	16	17	18
a1	4860.6	3108.6	1014.9	127.99	98.09	1317.2	89.08	1196.7	302.41
b1	1855.1	1526.4	324.62	275.48	12777.0	928.96	65.49	152.31	40.02
c1	258.7	315.28	33.62	3861.9	3861.9	33.62	315.28	258.7	801.47
d1	152.31	65.49	928.96	12777.0	275.48	324.62	1526.4	1855.1	40.02
e1	1196.7	89.08	1317.2	98.09	127.99	1014.9	3108.6	4860.6	302.41
a2	3967.6	2769.3	840.8	68.86	5761.0	331220.0	559710.0	220.48	113.54
b2	672.18	1047.1	1845.7	413.36	254990.0	332860.0	551010.0	924550.0	17874.0
c2	131410.0	60.69	174.72	254200.0	254200.0	174.72	60.69	131410.0	443470.0
d2	924550.0	551010.0	332860.0	254990.0	413.36	1845.7	1047.1	672.18	17874.0
e2	220.48	559710.0	331220.0	5761.0	68.86	840.8	2769.3	3967.6	113.54
a3	4860.6	3108.6	1014.9	127.99	98.09	1317.2	89.08	1196.7	302.41
b3	1855.1	1526.4	324.62	275.48	12777.0	928.96	65.49	152.31	40.02
c3	258.7	315.28	33.62	3861.9	3861.9	33.62	315.28	258.7	801.47
d3	152.31	65.49	928.96	12777.0	275.48	324.62	1526.4	1855.1	40.02
e3	1196.7	89.08	1317.2	98.09	127.99	1014.9	3108.6	4860.6	302.41
a4	6408.6	3767.0	1484.3	379.4	104.42	167.3	995.28	4626.4	1123.8
b4	4960.8	2735.6	832.41	141.9	47.37	176.09	1012.3	3470.3	563.0
c4	3638.2	1651.1	371.0	55.43	55.43	371.0	1651.1	3638.2	393.08
d4	3470.3	1012.3	176.09	47.37	141.9	832.41	2735.6	4960.8	563.0
e4	4626.4	995.28	167.3	104.42	379.4	1484.3	3767.0	6408.6	1123.8
a5	6944.4	3801.3	2044.5	855.26	528.94	944.79	2969.5	6834.1	2305.7
b5	6735.0	3801.3	1591.2	589.02	423.83	963.96	2946.2	6497.7	1893.5
c5	6478.9	3287.3	1195.0	443.16	443.16	1195.0	3287.3	6478.9	1737.6
d5	6497.7	2946.2	963.96	423.83	589.02	1591.2	3801.3	6735.0	1893.5
e5	6834.1	2969.5	944.79	528.94	855.26	2044.5	3801.3	6944.4	2305.7
a6	6395.2	4258.0	2450.2	1372.0	1127.4	1815.0	3984.8	6850.4	3097.5
b6	6650.4	4158.6	2215.3	1183.0	1047.4	184.03	3926.5	6748.2	2922.7
c6	6660.2	4008.8	1989.0	1066.6	1066.6	1989.0	4008.8	6660.2	2853.1
d6	6748.2	3926.5	184.03	1047.4	1183.0	2215.3	4158.6	6650.4	2922.7
e6	6850.4	3984.8	1815.0	1127.4	1372.0	2450.2	4258.0	6395.2	3097.5

Table 4.3 QAD-CGGP Computed Detector Responses for Layer C at 0 Degrees. (photons/sec/mCi)

Detector	Voxel Number								
Number	19	20	21	22	23	24	25	26	27
a1	6408.6	3767.0	1484.3	379.4	104.42	167.3	995.28	4626.4	1123.8
b1	4960.8	2735.6	832.41	141.9	47.37	176.09	1012.3	3470.3	563.0
c1	3638.2	1651.1	371.0	55.43	55.43	371.0	1651.1	3638.2	393.08
d1	3470.3	1012.3	176.09	47.37	141.9	832.41	2735.6	4960.8	563.0
e1	4626.4	995.28	167.3	104.42	379.4	1484.3	3767.0	6408.6	1123.8
a2	4860.6	3108.6	1014.9	127.99	98.09	1317.2	89.08	1196.7	302.41
b2	1855.1	1526.4	324.62	275.48	12777.0	928.96	65.49	152.31	40.02
c2	258.7	315.28	33.62	3861.9	3861.9	33.62	315.28	258.7	801.47
d2	152.31	65.49	928.96	12777.0	275.48	324.62	1526.4	1855.1	40.02
e2	1196.7	89.08	1317.2	98.09	127.99	1014.9	3108.6	4860.6	302.41
a3	3967.6	2769.3	840.8	68.86	5761.0	331220.0	559710.0	220.48	113.54
b3	672.18	1047.1	1845.7	413.36	254990.0	332860.0	551010.0	924550.0	17874.0
c3	131410.0	60.69	174.72	254200.0	254200.0	174.72	60.69	131410.0	443470.0
d3	924550.0	551010.0	332860.0	254990.0	413.36	1845.7	1047.1	672.18	17874.0
e3	220.48	559710.0	331220.0	5761.0	68.86	840.8	2769.3	3967.6	113.54
a4	4860.6	3108.6	1014.9	127.99	98.09	1317.2	89.08	1196.7	302.41
b4	1855.1	1526.4	324.62	275.48	12777.0	928.96	65.49	152.31	40.02
c4	258.7	315.28	33.62	3861.9	3861.9	33.62	315.28	258.7	801.47
d4	152.31	65.49	928.96	12777.0	275.48	324.62	1526.4	1855.1	40.02
e4	1196.7	89.08	1317.2	98.09	127.99	1014.9	3108.6	4860.6	302.41
a5	6408.6	3767.0	1484.3	379.4	104.42	167.3	995.28	4626.4	1123.8
b5	4960.8	2735.6	832.41	141.9	47.37	176.09	1012.3	3470.3	563.0
c5	3638.2	1651.1	371.0	55.43	55.43	371.0	1651.1	3638.2	393.08
d5	3470.3	1012.3	176.09	47.37	141.9	832.41	2735.6	4960.8	563.0
e5	4626.4	995.28	167.3	104.42	379.4	1484.3	3767.0	6408.6	1123.8
a6	6944.4	3801.3	2044.5	855.26	528.94	944.79	2969.5	6834.1	2305.7
b6	6735.0	3801.3	1591.2	589.02	423.83	963.96	2946.2	6497.7	1893.5
c6	6478.9	3287.3	1195.0	443.16	443.16	1195.0	3287.3	6478.9	1737.6
d6	6497.7	2946.2	963.96	423.83	589.02	1591.2	3801.3	6735.0	1893.5
e6	6834.1	2969.5	944.79	528.94	855.26	2044.5	3801.3	6944.4	2305.7

Table 4.4 QAD-CGGP Computed Detector Responses for Layer D at 0 Degrees. (photons/sec/mCi)

Detector	Voxel Number								
Number	28	29	30	31	32	33	34	35	36
a1	6944.4	3801.3	2044.5	855.26	528.94	944.79	2969.5	6834.1	2305.7
b1	6735.0	3801.3	1591.2	589.02	423.83	963.96	2946.2	6497.7	1893.5
c1	6478.9	3287.3	1195.0	443.16	443.16	1195.0	3287.3	6478.9	1737.6
d1	6497.7	2946.2	963.96	423.83	589.02	1591.2	3801.3	6735.0	1893.5
e1	6834.1	2969.5	944.79	528.94	855.26	2044.5	3801.3	6944.4	2305.7
a2	6408.6	3767.0	1484.3	379.4	104.42	167.3	995.28	4626.4	1123.8
b2	4960.8	2735.6	832.41	141.9	47.37	176.09	1012.3	3470.3	563.0
c2	3638.2	1651.1	371.0	55.43	55.43	371.0	1651.1	3638.2	393.08
d2	3470.3	1012.3	176.09	47.37	141.9	832.41	2735.6	4960.8	563.0
e2	4626.4	995.28	167.3	104.42	379.4	1484.3	3767.0	6408.6	1123.8
a3	4860.6	3108.6	1014.9	127.99	98.09	1317.2	89.08	1196.7	302.41
b3	1855.1	1526.4	324.62	275.48	12777.0	928.96	65.49	152.31	40.02
c3	258.7	315.28	33.62	3861.9	3861.9	33.62	315.28	258.7	801.47
d3	152.31	65.49	928.96	12777.0	275.48	324.62	1526.4	1855.1	40.02
e3	1196.7	89.08	1317.2	98.09	127.99	1014.9	3108.6	4860.6	302.41
a4	3967.6	2769.3	840.8	68.86	5761.0	331220.0	559710.0	220.48	113.54
b4	672.18	1047.1	1845.7	413.36	254990.0	332860.0	551010.0	924550.0	17874.0
c4	131410.0	60.69	174.72	254200.0	254200.0	174.72	60.69	131410.0	443470.0
d4	924550.0	551010.0	332860.0	254990.0	413.36	1845.7	1047.1	672.18	17874.0
e4	220.48	559710.0	331220.0	5761.0	68.86	840.8	2769.3	3967.6	113.54
a5	4860.6	3108.6	1014.9	127.99	98.09	1317.2	89.08	1196.7	302.41
b5	1855.1	1526.4	324.62	275.48	12777.0	928.96	65.49	152.31	40.02
c5	258.7	315.28	33.62	3861.9	3861.9	33.62	315.28	258.7	801.47
d5	152.31	65.49	928.96	12777.0	275.48	324.62	1526.4	1855.1	40.02
e5	1196.7	89.08	1317.2	98.09	127.99	1014.9	3108.6	4860.6	302.41
a6	6408.6	3767.0	1484.3	379.4	104.42	167.3	995.28	4626.4	1123.8
b6	4960.8	2735.6	832.41	141.9	47.37	176.09	1012.3	3470.3	563.0
c6	3638.2	1651.1	371.0	55.43	55.43	371.0	1651.1	3638.2	393.08
d6	3470.3	1012.3	176.09	47.37	141.9	832.41	2735.6	4960.8	563.0
e6	4626.4	995.28	167.3	104.42	379.4	1484.3	3767.0	6408.6	1123.8

Table 4.5 QAD-CGGP Computed Detector Responses for Layer E at 0 Degrees. (photons/sec/mCi)

Detector	Voxel Number								
Number	37	38	39	40	41	42	43	44	45
a1	6395.2	4258.0	2450.2	1372.0	1127.4	1815.0	3984.8	6850.4	3097.5
b1	6650.4	4158.6	2215.3	1183.0	1047.4	184.03	3926.5	6748.2	2922.7
c1	6660.2	4008.8	1989.0	1066.6	1066.6	1989.0	4008.8	6660.2	2853.1
d1	6748.2	3926.5	184.03	1047.4	1183.0	2215.3	4158.6	6650.4	2922.7
e1	6850.4	3984.8	1815.0	1127.4	1372.0	2450.2	4258.0	6395.2	3097.5
a2	6944.4	3801.3	2044.5	855.26	528.94	944.79	2969.5	6834.1	2305.7
b2	6735.0	3801.3	1591.2	589.02	423.83	963.96	2946.2	6497.7	1893.5
c2	6478.9	3287.3	1195.0	443.16	443.16	1195.0	3287.3	6478.9	1737.6
d2	6497.7	2946.2	963.96	423.83	589.02	1591.2	3801.3	6735.0	1893.5
e2	6834.1	2969.5	944.79	528.94	855.26	2044.5	3801.3	6944.4	2305.7
a3	6408.6	3767.0	1484.3	379.4	104.42	167.3	995.28	4626.4	1123.8
b3	4960.8	2735.6	832.41	141.9	47.37	176.09	1012.3	3470.3	563.0
c3	3638.2	1651.1	371.0	55.43	55.43	371.0	1651.1	3638.2	393.08
d3	3470.3	1012.3	176.09	47.37	141.9	832.41	2735.6	4960.8	563.0
e3	4626.4	995.28	167.3	104.42	379.4	1484.3	3767.0	6408.6	1123.8
a4	4860.6	3108.6	1014.9	127.99	98.09	1317.2	89.08	1196.7	302.41
b4	1855.1	1526.4	324.62	275.48	12777.0	928.96	65.49	152.31	40.02
c4	258.7	315.28	33.62	3861.9	3861.9	33.62	315.28	258.7	801.47
d4	152.31	65.49	928.96	12777.0	275.48	324.62	1526.4	1855.1	40.02
e4	1196.7	89.08	1317.2	98.09	127.99	1014.9	3108.6	4860.6	302.41
a5	3967.6	2769.3	840.8	68.86	5761.0	331220.0	559710.0	220.48	113.54
b5	672.18	1047.1	1845.7	413.36	254990.0	332860.0	551010.0	924550.0	17874.0
c5	131410.0	60.69	174.72	254200.0	254200.0	174.72	60.69	131410.0	443470.0
d5	924550.0	60.69	332860.0	254990.0	413.36	1845.7	1047.1	672.18	17874.0
e5	220.48	559710.0	331220.0	5761.0	68.86	840.8	2769.3	3967.6	113.54
a6	4860.6	3108.6	1014.9	127.99	98.09	1317.2	89.08	1196.7	302.41
b6	1855.1	1526.4	324.62	275.48	12777.0	928.96	65.49	152.31	40.02
c6	258.7	315.28	33.62	3861.9	3861.9	33.627.0	315.28	258.7	801.47
d6	152.31	65.49	928.96	12777.0	275.48	324.62.0	1526.4	1855.1	40.02
e6	1196.7	89.08	1317.2	98.09	127.99	1014.9	3108.6	4860.6	302.41

Table 4.6 QAD-CGGP Computed Detector Responses for Layer F at 0 Degrees. (photons/sec/mCi)

Detector	Voxel Number								
Number	46	47	48	49	50	51	52	53	54
a1	5401.2	3937.1	2605.3	1739.1	1593.5	2290.8	4006.0	5836.1	3320.4
b1	5581.2	3945.3	2509.1	1638.3	1556.1	2320.5	3933.5	5811.9	3272.2
c1	5716.7	3923.2	2402.5	1571.7	1571.7	2402.5	3923.2	5716.7	3251.3
d1	5811.9	3933.5	2320.5	1556.1	1638.3	2509.1	3945.3	5581.2	3272.2
e1	5836.1	4006.0	2290.8	1593.5	1739.1	2605.3	3937.1	5401.2	3320.4
a2	6395.2	4258.0	2450.2	1372.0	1127.4	1815.0	3984.8	6850.4	3097.5
b2	6650.4	4158.6	2215.3	1183.0	1047.4	184.03	3926.5	6748.2	2922.7
c2	6660.2	4008.8	1989.0	1066.6	1066.6	1989.0	4008.8	6660.2	2853.1
d2	6748.2	3926.5	184.03	1047.4	1183.0	2215.3	4158.6	6650.4	2922.7
e2	6850.4	3984.8	1815.0	1127.4	1372.0	2450.2	4258.0	6395.2	3097.5
a3	6944.4	3801.3	2044.5	855.26	528.94	944.79	2969.5	6834.1	2305.7
b3	6735.0	3801.3	1591.2	589.02	423.83	963.96	2946.2	6497.7	1893.5
c3	6478.9	3287.3	1195.0	443.16	443.16	1195.0	3287.3	6478.9	1737.6
d3	6497.7	2946.2	963.96	423.83	589.02	1591.2	3801.3	6735.0	1893.5
e3	6834.1	2969.5	944.79	528.94	855.26	2044.5	3801.3	6944.4	2305.7
a4	6408.6	3767.0	1484.3	379.4	104.42	167.3	995.28	4626.4	1123.8
b4	4960.8	2735.6	832.41	141.9	47.37	176.09	1012.3	3470.3	563.0
c4	3638.2	1651.1	371.0	55.43	55.43	371.0	1651.1	3638.2	393.08
d4	3470.3	1012.3	176.09	47.37	141.9	832.41	2735.6	4960.8	563.0
e4	4626.4	995.28	167.3	104.42	379.4	1484.3	3767.0	6408.6	1123.8
a5	4860.6	3108.6	1014.9	127.99	98.09	1317.2	89.08	1196.7	302.41
b5	1855.1	1526.4	324.62	275.48	12777.0	928.96	65.49	152.31	40.02
c5	258.7	315.28	33.62	3861.9	3861.9	33.62	315.28	258.7	801.47
d5	152.31	65.49	928.96	12777.0	275.48	324.62	1526.4	1855.1	40.02
e5	1196.7	89.08	1317.2	98.09	127.99	1014.9	3108.6	4860.6	302.41
a6	3967.6	2769.3	840.8	68.86	5761.0	331220.0	559710.0	220.48	113.54
b6	672.18	1047.1	1845.7	413.36	254990.0	332860.0	551010.0	924550.0	17874.0
c6	131410.0	60.69	174.72	254200.0	254200.0	174.72	60.69	131410.0	443470.0
d6	924550.0	551010.0	332860.0	254990.0	413.36	1845.7	1047.1	672.18	17874.0
e6	220.48	559710.0	331220.0	5761.0	68.86	840.8	2769.3	3967.6	113.54

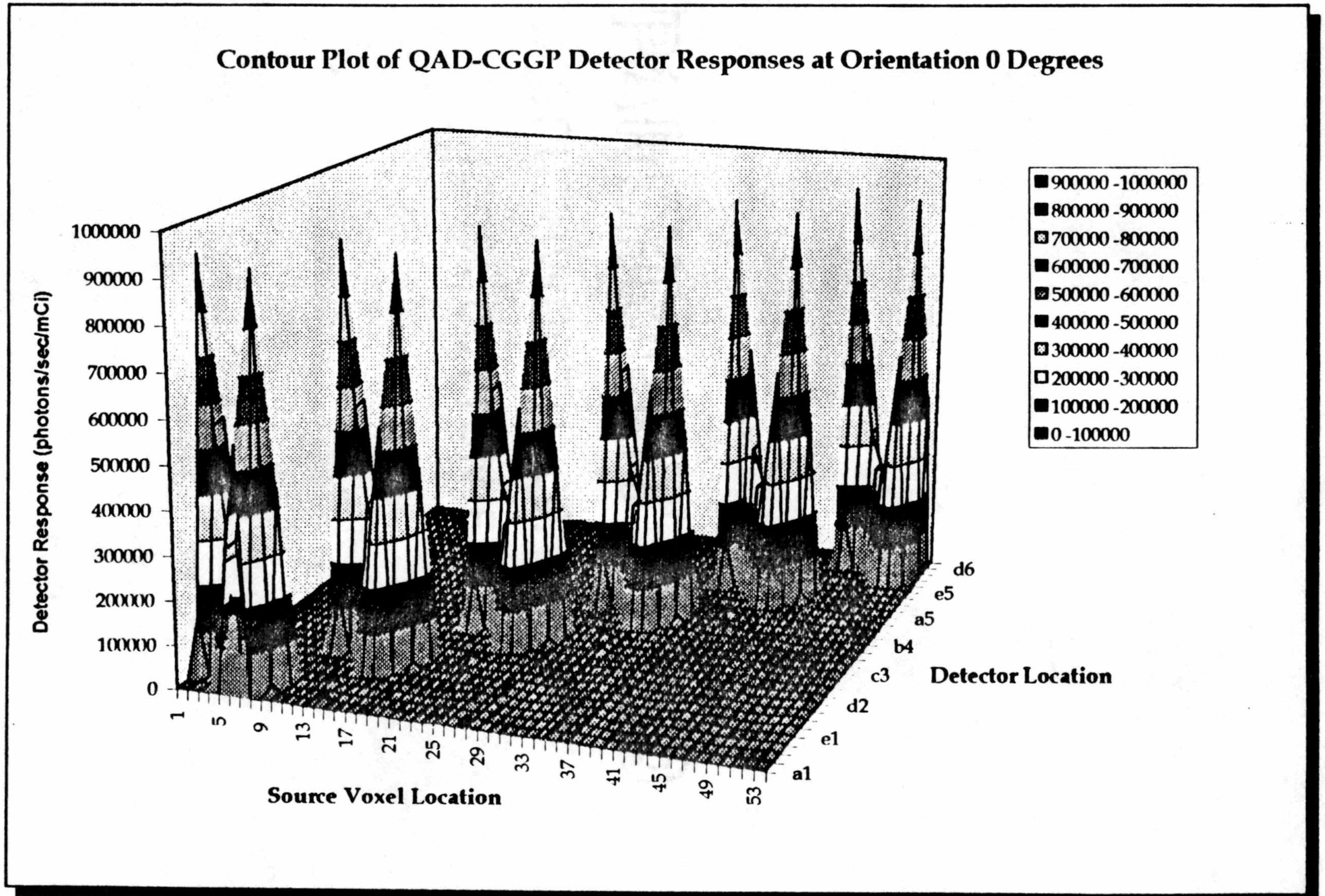

Figure 4.1 Contour Plot of Detector Response at 0 Degrees Orientation.

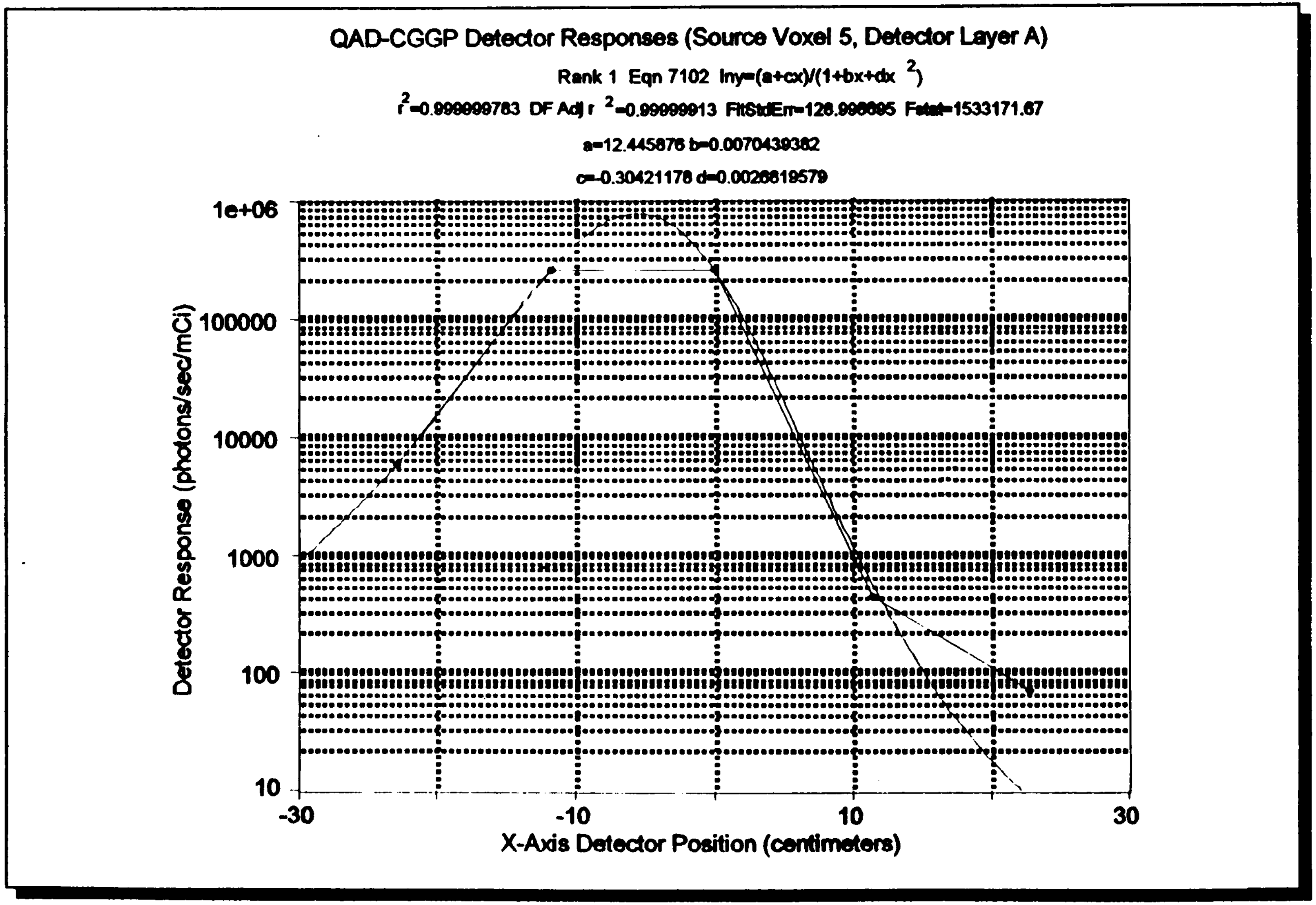

Figure 4.2 QAD-CGGP Detector Responses for Source Voxel 5, Detector Layer A.

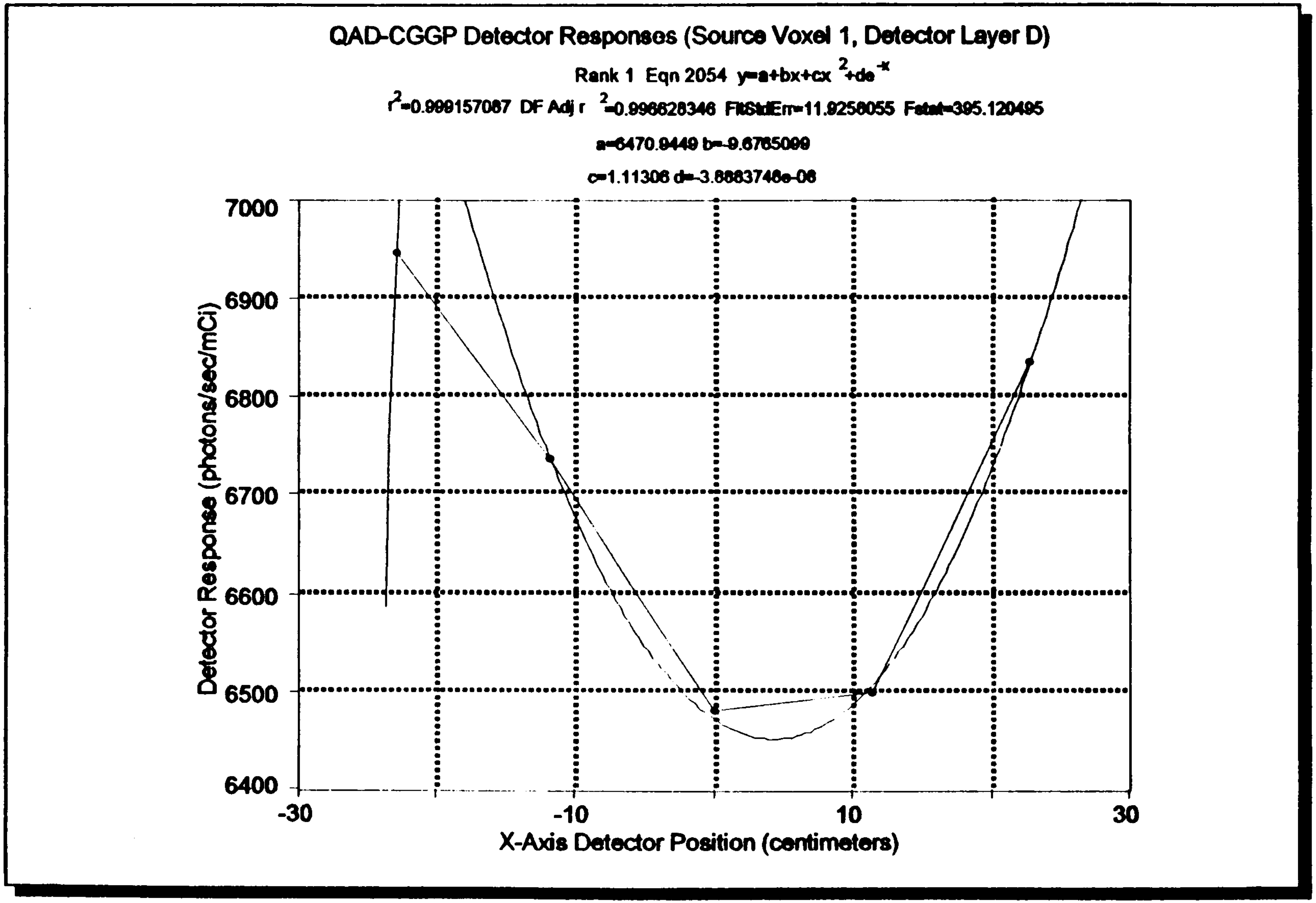

Figure 4.3 QAD-CGGP Detector Responses for Source Voxel 1, Detector Layer D.

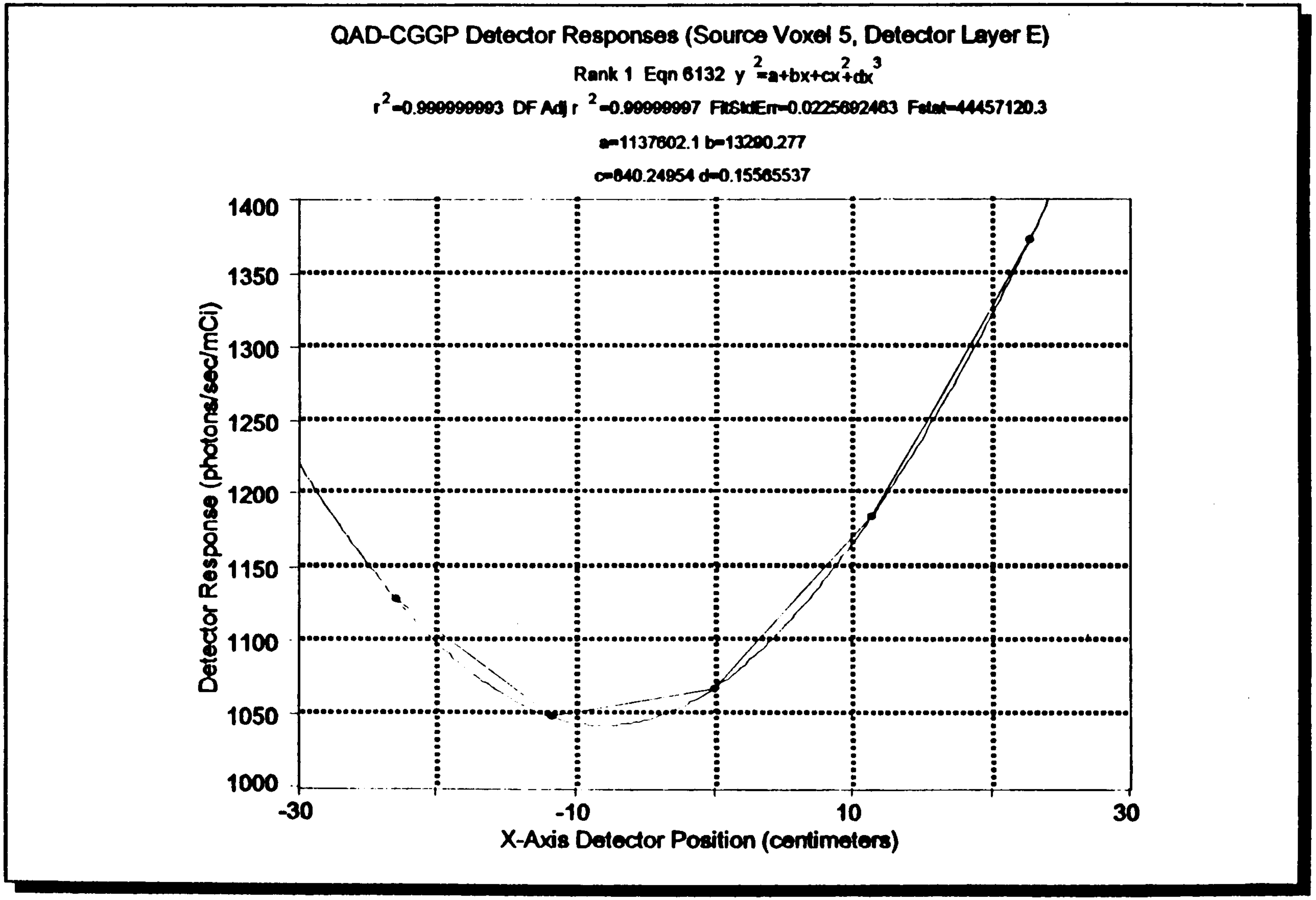

Figure 4.4 QAD-CGGP Detector Responses for Source Voxel 5, Detector Layer E.

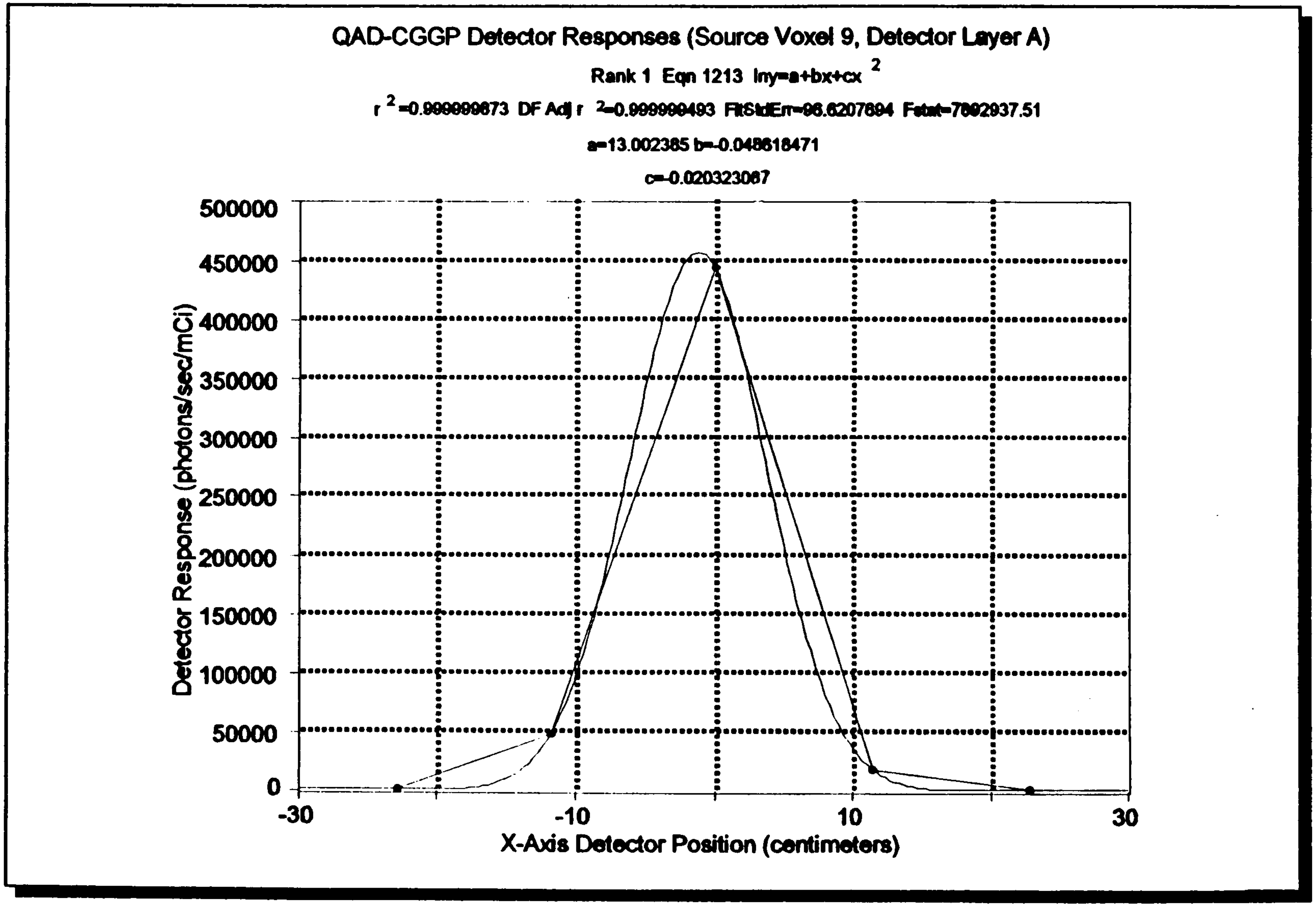

Figure 4.5 QAD-CGGP Detector Responses for Source Voxel 9, Detector Layer A.

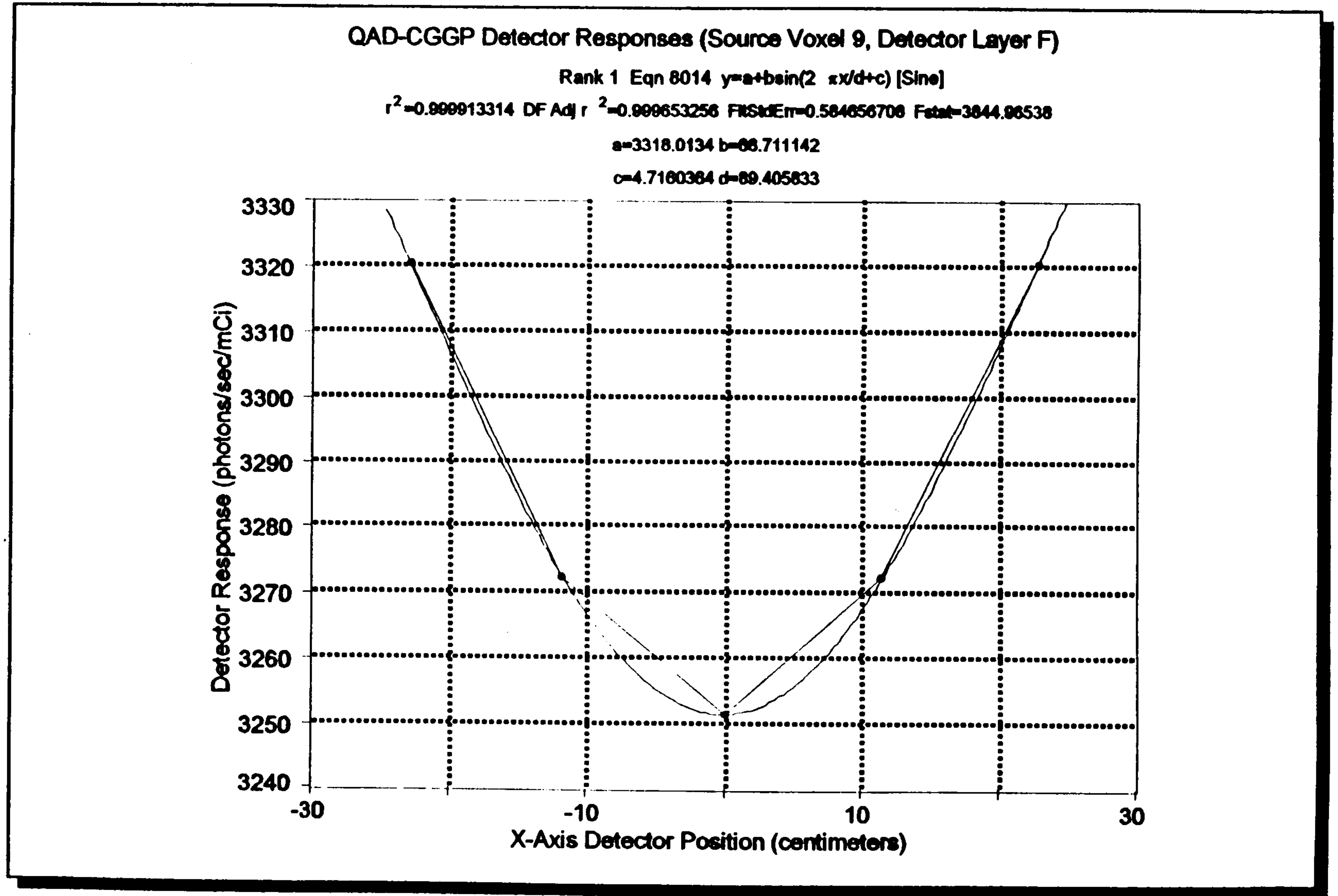

Figure 4.6 QAD-CGGP Detector Responses for Voxel 9, Detector Layer F.

all cases. However, the collimator, or more specifically, the orientation of the collimator, causes the response functions to abandon their Gaussian appearance. This is due to the path length the photon travels within the collimator.

A geometric examination of each source-detector location validates the predicted values, as the response is directly proportional to the path-length. Note, each plot has been fitted to an appropriate function using the Jandel Scientific TableCurve version 1.11 scientific analysis software.

4.1.2 MCNP Output

MCNP was used to model several test source-detector locations as a method of verification. Locations were chosen at random and calculations performed assuming an uncollimated geometry. The geometry used in the model corresponds to the test data used for the QAD-CGGP validation calculations. The output of the MCNP calculations is given in Table 4.7. Calculations were made using the non-collimated models with an energy bin of 0.661-0.663 MeV. The small bin window allows for only full-energy interactions within the crystal region to be included in the estimation of pulse height. Note that for all cases, the source is located at coordinates (0, 0, 0) centimeters. Also, note the units for the pulse height estimator are counts or pulses per source photon.

Table 4.7 Results of MCNP Calculations Utilized for Verification

Detector X (cm)	Detector Z (cm)	Pulse Height Estimator (Pulses per source photon)	Fractional Standard Deviation (PHE)	Track Length Estimator (Particles per cm^2 per source photon)	Fractional Standard Deviation (TLE)
0.0	0.0	1.62900E-4	0.0124	1.19803E-5	0.0088
0.0	16.256	1.55275E-4	0.0127	1.15713E-5	0.0086
0.0	32.512	1.22500E-4	0.0143	9.45342E-6	0.0092
11.176	0.0	1.57950E-4	0.0126	1.20277E-5	0.0086
11.176	16.256	1.53275E-4	0.0128	1.12209E-5	0.0086
11.176	32.512	1.22275E-4	0.0143	9.20289E-6	0.0093
22.352	0.0	1.46275E-4	0.0131	1.10343E-5	0.0087
22.352	16.256	1.36175E-4	0.0135	1.04343E-5	0.0088
22.352	32.512	1.12450E-4	0.0149	8.57503E-6	0.0097

4.1.3 Validation of the QAD-CGGP Data

Validation of the QAD-CGGP computer model as used to determine the PSRF matrix values was performed by quantitative comparison of data at selected data points. Table 4.8 provides a list of data as determined by QAD-CGGP with geometry specifications similar to that modeled by MCNP. Note, the source is located at position (0, 0, 0) centimeters for all test calculations.

A comparison of the QAD-CGGP and MCNP results show that the QAD-CGGP values are more than a factor of two (2) greater than those obtained by MCNP. This is shown in both Table 4.9 and Figure 4.1. Analysis of the causes for the deviation in calculated fluences have lead to the following conclusion. QAD-CGGP calculates the uncollided fluence at some specified point in space. Therefore, the values calculated by QAD-CGGP stipulate the number of photons which are present at this point in space each second, given one (1) curie of activity. This corresponds to a detector efficiency of one hundred (100) percent. The results given by MCNP calculate the number of full-energy interactions within the crystal region, namely, those photons which are transported to the crystal, interact, and deposit all energy within the region. MCNP, due to the small energy window set for the problem, will not count those photons which pass through the crystal without interacting or those that deposit only a partial amount of their energy. QAD-CGGP does not make this distinction. Therefore, over-estimation of the photon fluence, as predicted by QAD-CGGP, was anticipated. Further, it is important for one to

Table 4.8 QAD-CGGP Responses Using Test Input Specifications

Detector X (cm)	Detector Z (cm)	Direct Beam Flux (MeV/(cm^2·sec))	Converted Flux (Photons/sec)
0.0	0.0	5.0113E+5	4.1467E-4
0.0	16.256	4.5543E+5	3.7685E-4
0.0	32.512	3.5611E+5	2.9467E-4
11.176	0.0	4.8001E+5	3.9719E-4
11.176	16.256	4.3791E+5	3.6236E-4
11.176	32.512	3.4537E+5	2.8578E-4
22.352	0.0	4.2609E+5	3.5258E-4
22.352	16.256	3.9260E+5	3.2486E-4
22.352	32.512	3.1667E+5	2.6203E-4

Table 4.9 Comparison of Selected Response Data

Detector X (cm)	Detector Z (cm)	QAD-CGGP Fluence*	MCNP Fluence*	Ratio (QAD/MCNP)
0.0	0.0	4.1467E-4	1.62900E-4	2.5455
0.0	16.256	3.7685E-4	1.55275E-4	2.4386
0.0	32.512	2.9467E-4	1.22500E-4	2.4055
11.176	0.0	3.9719E-4	1.57950E-4	2.5147
11.176	16.256	3.6236E-4	1.53275E-4	2.3641
11.176	32.512	2.8578E-4	1.22275E-4	2.3372
22.352	0.0	3.5258E-4	1.46275E-4	2.4103
22.352	16.256	3.2486E-4	1.36175E-4	2.3856
22.352	32.512	2.6203E-4	1.12450E-4	2.3302

* (Photons/Sec/Source Photon)

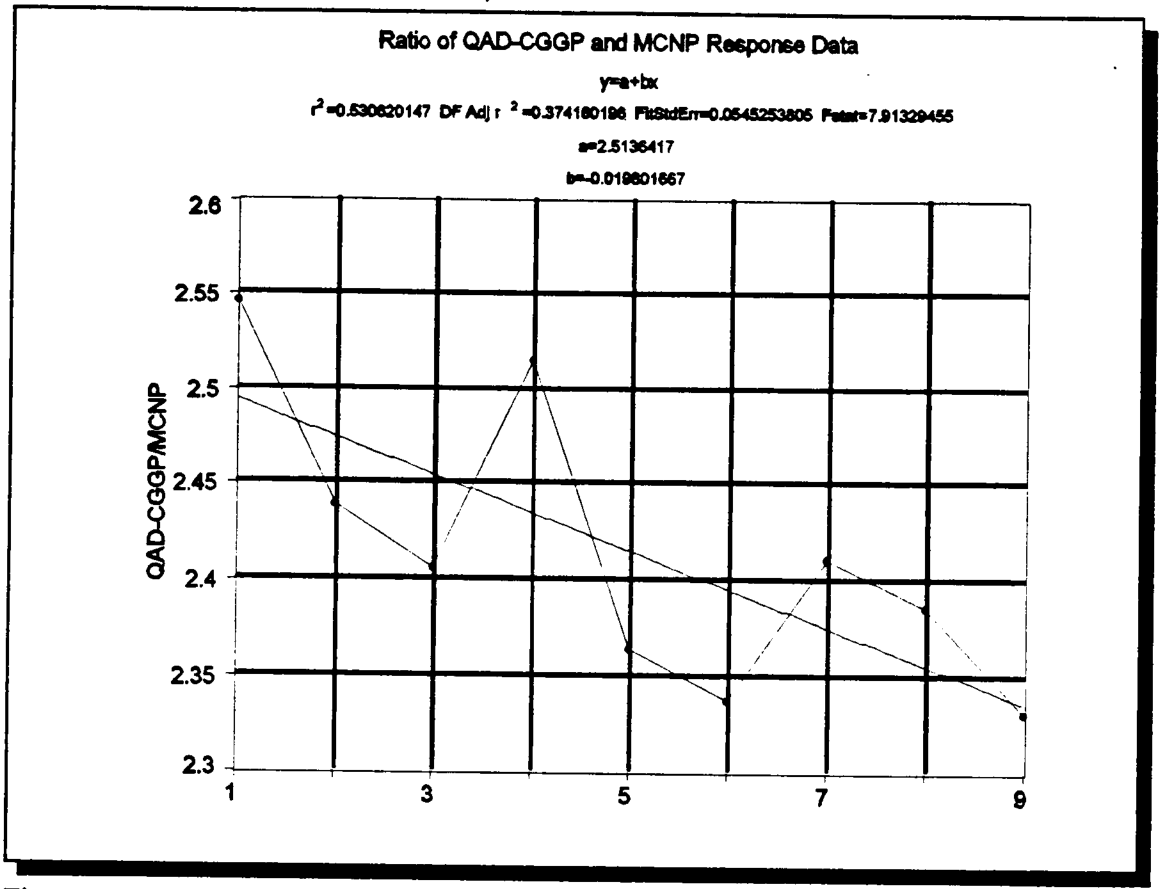

Figure 4.7 Ratio of QAD-CGGP to MCNP Data.

consider that the response matrix has only to characterize the shape of the PSRF, as the system is calibrated experimentally.

As seen in both Table 4.9 and Figure 4.7, the ratios of the QAD-CGGP to MCNP response predictions is in the range (2.5455, 2.3302). These ratios were judged consistent and served to verify the validity of the QAD-CGGP predictions. Based upon this fact, the QAD-CGGP modeling procedure was deemed appropriate and used to calculate detector responses for the PSRF matrix.

4.1.4 Conditioning of the PSRF Matrix

The PSRF matrix, having been constructed using data from the QAD-CGGP transport code, provides a series of detector responses assuming exact, ideal conditions. In the laboratory setting, this is not the case. There are many parameters that corrupt the data, which cannot be accurately modeled. The primary inaccuracy being caused by the asymmetry of the detector collimator. However, statistical fluctuations and electronic noise also serve to create inaccuracy. To combat this problem, the PSRF matrix underwent a conditioning process, in which the responses were calibrated according to experimental data. In this process, the experimental responses were used to scale the computer generated data. This was done by computing the ratio of the modeling responses to those obtained experimentally. The appropriate column of the PSRF matrix, corresponding to the voxel containing the source, was then multiplied by these ratios. Therefore, a complete PSRF calibration would require 54 experimental runs. In this research, four (4) columns of the matrix were conditioned.

Comparisons have been made using the unconditioned QAD-CGGP calculated responses and those acquired by experiment. This comparison is presented in Tables 4.10 through 4.13. Note, the experimental response has been normalized to give the number of interactions per second per mCi. Activity distributions were solved using both the unconditioned and conditioned matrices.

Table 4.10 Comparison of QAD-CGGP and Experimental Responses for Orientation 0 Degrees (photons/sec/mCi).

Detector	Voxel 10		Voxel 12		Voxel 25		Voxel 27	
Number	QAD-CGGP	Trial	QAD-CGGP	Trial	QAD-CGGP	Trial	QAD-CGGP	Trial
a1	4860.6	2553	1014.9	413.65	995.28	683.09	1123.8	410.75
b1	1855.1	820.56	324.62	104.78	1012.3	891.43	563.0	236.54
c1	258.7	106.08	33.62	19.54	1651.1	1602.7	393.08	244.64
d1	152.31	119.9	928.96	260.98	2735.6	2678.3	563.0	435.17
e1	1196.7	844.78	1317.2	239.21	3767	3754.2	1123.8	897.32
a2	3967.6	1663.82	840.8	282.89	89.08	37.41	302.41	43.46
b2	672.18	184.04	1845.7	37.61	65.47	46.91	40.02	92.86
c2	131410	5030.74	174.72	375.79	315.28	395.76	801.47	386.52
d2	924550	8879.26	332860	3856.9	1526.4	1738.7	40.02	34.50
e2	220.48	123.19	331220	3708	3108.6	3230.8	302.41	224.32
a3	4860.6	2088.6	1014.9	309.05	559710	6902.2	113.54	5.71
b3	1855.1	542.79	324.62	55.61	551010	3771.1	17874.0	2076.4
c3	258.7	36.3	33.62	46.28	60.69	153.54	443470.0	4812.5
d3	152.31	16.39	928.96	1217.8	1047.1	1392.8	17874.0	1196.1
e3	1196.7	249.12	1317.2	1125.5	2769.3	3016	113.54	61.53
a4	6408.6	3371.3	1484.3	554.54	89.08	513.54	302.41	44.31
b4	4960.8	2232.7	832.41	209.04	65.49	124.43	40.02	259.53
c4	3638.2	1322	371	57.31	315.28	298.8	801.47	1225.4
d4	3470.3	1301.2	176.09	17.95	1526.4	1620.4	40.02	83.87
e4	4626.4	2667.3	167.3	30.43	3108.6	3014.6	302.41	153.46
a5	6944.4	3931.4	2044.5	876.27	995.28	245.16	1123.8	284.45
b5	6735	3532	1591.2	578.95	1012.3	378.06	563.0	86.32
c5	6478.9	3229.3	1195	366.31	1651.1	1092	393.08	56.64
d5	6497.7	3402.5	963.96	275.65	2735.6	2435.6	563.0	193.31
e5	6834.1	4281	944.79	332.04	3767	3410.9	1123.8	587.97
a6	6395.2	3957.9	2450.2	577.62	2969.5	1331.2	2305.7	950.63
b6	6650.4	3892.4	2215.3	559.01	2946.2	1595.3	1893.5	545.27
c6	6660.2	3830.4	1989	483.54	3287.3	2353.9	1737.6	531.45
d6	6748.2	4039.1	184.03	453.42	3801.3	3098.2	1893.5	794.71
e6	6850.4	4502	1815	534.53	3801.3	3648.8	2305.7	1253.01

Table 4.11 Comparison of QAD-CGGP and Experimental Responses for Orientation 90 Degrees (photons/sec/mCi).

Detector Number	Voxel 10		Voxel 12		Voxel 25		Voxel 27	
	QAD-CGGP	Trial	QAD-CGGP	Trial	QAD-CGGP	Trial	QAD-CGGP	Trial
a1	89.08	55.53	4860.6	2615.3	104.42	44.34	1123.8	528.57
b1	65.49	61.23	1855.1	870.68	47.37	36.54	563.0	308.42
c1	315.28	422.5	258.7	183.15	55.43	67.83	393.08	282.91
d1	1526.4	1697.6	152.31	261.63	141.9	169.98	563.3	473.12
e1	3108.6	3156.3	1196.7	1398.6	379.4	397.79	1123.8	942.2
a2	559710.0	6844.1	3967.6	1524.8	98.09	229.89	302.41	95.61
b2	551010.0	3435.8	672.18	110.65	12777.0	688.94	40.02	27.98
c2	60.69	93.91	131410.0	6505.7	3861.9	260.46	801.47	369.41
d2	1047.1	1168.5	924550.0	6315.3	275.48	29.28	40.02	60.75
e2	2769.3	2884.9	220.48	256.15	127.99	157.46	302.41	194.36
a3	89.08	461.04	4860.6	1884.7	5761.0	1573.3	113.54	17.18
b3	65.49	93.68	1855.1	376.79	254990.0	3062.9	17874.0	1292.8
c3	315.28	308.41	258.7	25.39	254200.0	1534.0	443470.0	5134.6
d3	1526.4	1539.0	152.31	43.53	413.36	115.36	17874.0	2127.4
e3	3108.6	3017.9	1196.7	747.30	68.86	115.36	113.54	39.10
a4	995.28	277.28	6408.6	3191.2	98.09	545.15	302.41	59.28
b4	1012.3	408.50	4960.8	1930.9	12777.0	1509.3	40.02	97.28
c4	1651.1	1193.5	3638.2	1015.1	3861.9	812.76	801.47	1141.8
d4	2735.6	2440.5	3470.3	1301.3	275.48	29.80	40.02	107.19
e4	3767.0	3430.1	4626.4	2990.0	127.99	107.63	302.41	115.43
a5	2969.5	1384.1	6944.4	3286.3	104.42	10.21	1123.8	365.35
b5	2946.2	1642.3	6735.0	2959.1	47.37	11.60	563.0	127.20
c5	3287.3	2374.6	6478.9	2801.7	55.43	17.72	393.08	62.97
d5	3801.3	3092.1	6497.7	3206.7	141.9	76.64	563.0	177.57
e5	3801.3	3691.3	6834.1	4185.8	379.4	258.38	1123.8	554.91
a6	3984.8	2266.1	6395.2	3918.8	528.94	118.23	2305.7	900.87
b6	3926.5	2497.6	6650.4	3768.3	423.83	93.12	1893.5	640.67
c6	4008.8	2905.3	6660.2	3641.9	443.83	143.45	1737.6	560.35
d6	4158.6	3355.0	6748.2	3654.6	589.02	298.19	1893.5	766.30
e6	4258.0	3630.8	6850.4	3615.6	855.26	564.89	2305.7	1245.6

Table 4.12 Comparison of QAD-CGGP and Experimental Responses for Orientation 180 Degrees (photons/sec/mCi).

Detector	Voxel 10		Voxel 12		Voxel 25		Voxel 27	
Number	QAD-CGGP	Trial	QAD-CGGP	Trial	QAD-CGGP	Trial	QAD-CGGP	Trial
a1	98.09	142.10	89.08	43.06	1484.3	573.83	1123.8	522.60
b1	1277.0	679.01	65.49	67.20	832.41	294.68	563.0	323.21
c1	3861.9	489.45	315.28	558.83	371.0	145.91	393.08	310.72
d1	275.48	29.65	1526.4	1863.1	176.09	106.47	563.0	545.24
e1	127.99	102.16	3108.6	3221.8	167.3	148.79	1123.8	1105.7
a2	5761.0	1098.3	559710.0	6415.3	1014.9	285.39	302.41	94.056
b2	254990.0	3130.5	551010.0	3713.5	324.62	60.89	40.02	43.50
c2	254200.0	2277.9	60.69	99.53	33.62	22.32	801.47	323.75
d2	413.36	179.19	1047.1	1175.8	928.96	455.67	40.02	43.35
e2	68.86	53.75	2769.3	2708.9	1317.2	329.28	302.47	294.52
a3	98.09	324.34	89.08	973.34	840.8	178.54	113.54	13.46
b3	1277.0	133.27	65.49	169.50	1845.7	20.84	17874.0	21.76.6
c3	3861.9	841.15	315.28	247.02	174.72	745.21	443470.0	5470.0
d3	275.48	40.09	1526.4	1427.9	332860.0	3962.1	17874.0	1473.7
e3	127.99	76.69	3108.6	2789.1	331220.0	3165.0	113.54	99.64
a4	104.42	13.28	995.28	128.69	1014.9	287.34	302.41	73.93
b4	47.37	11.69	1012.3	281.30	324.62	66.54	40.02	85.23
c4	55.43	14.38	1651.1	887.93	33.62	39.49	801.47	1084.7
d4	414.9	55.73	2735.6	2159.3	928.96	1082.0	40.02	44.35
e4	379.4	191.79	3767.0	3249.1	1317.2	972.08	302.41	203.98
a5	528.94	104.60	2969.5	1084.5	1484.3	517.80	1123.8	344.36
b5	423.83	77.71	2946.2	1365.3	832.41	214.45	563.0	142.62
c5	443.83	109.32	3287.3	2049.7	371.0	69.04	393.08	80.13
d5	589.02	223.27	3801.3	2817.0	176.09	24.38	563.0	207.84
e5	855.26	441.10	3801.3	3482.4	167.3	29.97	1123.8	717.67
a6	1127.4	337.32	3984.8	1972.9	2044.5	800.49	2305.7	1049.6
b6	1047.4	294.82	3926.5	2219.0	1591.2	531.15	1893.5	734.49
c6	1066.6	341.72	4008.8	2671.1	1195.0	343.21	1737.6	685.0
d6	1183.0	510.38	4158.6	3040.3	963.96	239.94	1893.5	959.84
e6	1372.0	697.35	4258.0	3413.2	944.79	305.09	2305.7	1581.2

Table 4.13 Comparison of QAD-CGGP and Experimental Responses for Orientation 270 Degrees (photons/sec/mCi).

Detector	Voxel 10		Voxel 12		Voxel 25		Voxel 27	
Number	QAD-CGGP	Trial	QAD-CGGP	Trial	QAD-CGGP	Trial	QAD-CGGP	Trial
a1	1014.9	368.95	98.09	161.06	6408.6	1030.6	1123.8	501.39
b1	324.62	78.43	12777.0	593.54	4960.8	1657.4	563.0	319.71
c1	33.62	23.05	3861.9	242.23	3638.2	1793.3	393.08	322.63
d1	928.96	433.63	275.48	27.28	3470.3	2541.7	563.0	573.90
e1	1317.2	323.97	127.99	147.82	4626.4	4096.2	1123.8	1209.89
a2	840.8	368.95	5761.0	1252.4	4860.6	3199.7	302.41	373.69
b2	1845.7	37.12	254990.0	3145.2	1855.1	745.60	40.02	74.49
c2	174.72	559.35	254200.0	1931.6	258.7	118.52	801.47	373.73
d2	332860.0	4122.2	413.36	141.90	152.31	129.61	40.02	47.52
e2	331220.0	3468.0	68.86	76.00	1196.7	899.43	302.41	253.35
a3	1014.9	348.76	98.09	506.20	3967.6	1852.6	113.54	14.05
b3	324.62	64.04	12777.0	1652.2	672.18	202.90	17874.0	2712.8
c3	33.62	21.60	3861.9	843.05	131410.0	3514.5	443470.0	5439.0
d3	928.96	946.28	275.48	31.60	924550.0	8122.6	17874.0	1208.5
e3	1317.2	1002.8	127.99	92.06	220.48	78.32	113.54	122.19
a4	1484.3	553.60	104.42	11.21	4860.6	2226.8	302.41	51.39
b4	832.41	246.80	47.37	20.91	1855.1	556.68	40.02	153.68
c4	371.0	74.19	55.43	14.65	258.7	40.98	801.47	1098.0
d4	176.09	20.67	141.9	55.47	152.31	36.58	40.02	31.72
e4	167.3	23.34	379.4	206.23	1196.7	658.69	302.41	208.56
a5	2044.5	886.53	528.94	100.75	6408.6	3309.3	1123.8	317.01
b5	1591.2	602.38	423.83	79.41	4960.8	2190.6	563.0	117.0
c5	1195.0	380.91	443.16	118.34	3638.2	1228.4	393.08	78.41
d5	963.96	274.76	589.02	260.12	3470.3	1262.1	563.0	224.21
e5	944.79	291.47	855.26	487.27	4626.4	2597.2	1123.8	426.24
a6	2450.2	1180.1	1127.4	346.90	6944.4	3952.2	2305.7	915.30
b6	2215.3	996.63	1047.4	318.67	6735.0	3596.8	1893.5	680.12
c6	1989.0	838.12	1066.6	374.31	6478.9	3201.9	1737.6	641.10
d6	184.03	738.41	1183.0	542.78	6497.7	3386.7	1893.5	962.68
e6	1815.0	778.28	1372.0	777.0	6834.1	4248.6	2305.7	1509.0

4.2 Determination of Source Distribution

The source distribution was reconstructed using the scenarios listed in Chapter 3. For each of these, the solution algorithm was implemented using both the conditioned and unconditioned PSRF matrix and both the NNLS- and LSMOD-based subroutines. The distribution data calculated using the conditioned PSRF matrix is expressed in a graphical form which relates the activity per voxel per layer. The distributions calculated using the unconditioned PSRF matrix are listed in tabular form in the later stages of this chapter.

4.2.1 NNLS Reconstruction Using a 73mCi ^{137}Cs Source

A total of four (4) experiments were performed with the source in various positions. The data collected from each experiment was then analyzed using both the NNLS- and LSMOD-based reconstruction algorithms. This section relates the computed activity distributions calculated using the NNLS subroutine. The computed activity for each source voxel has been entered into a schematic which depicts each layer of the drum. Figures 4.8 through 4.11 provide these renderings. The output, as written by the reconstruction program, is listed in Appendix D. Note, the sum for each layer is given along with the sum for the entire drum.

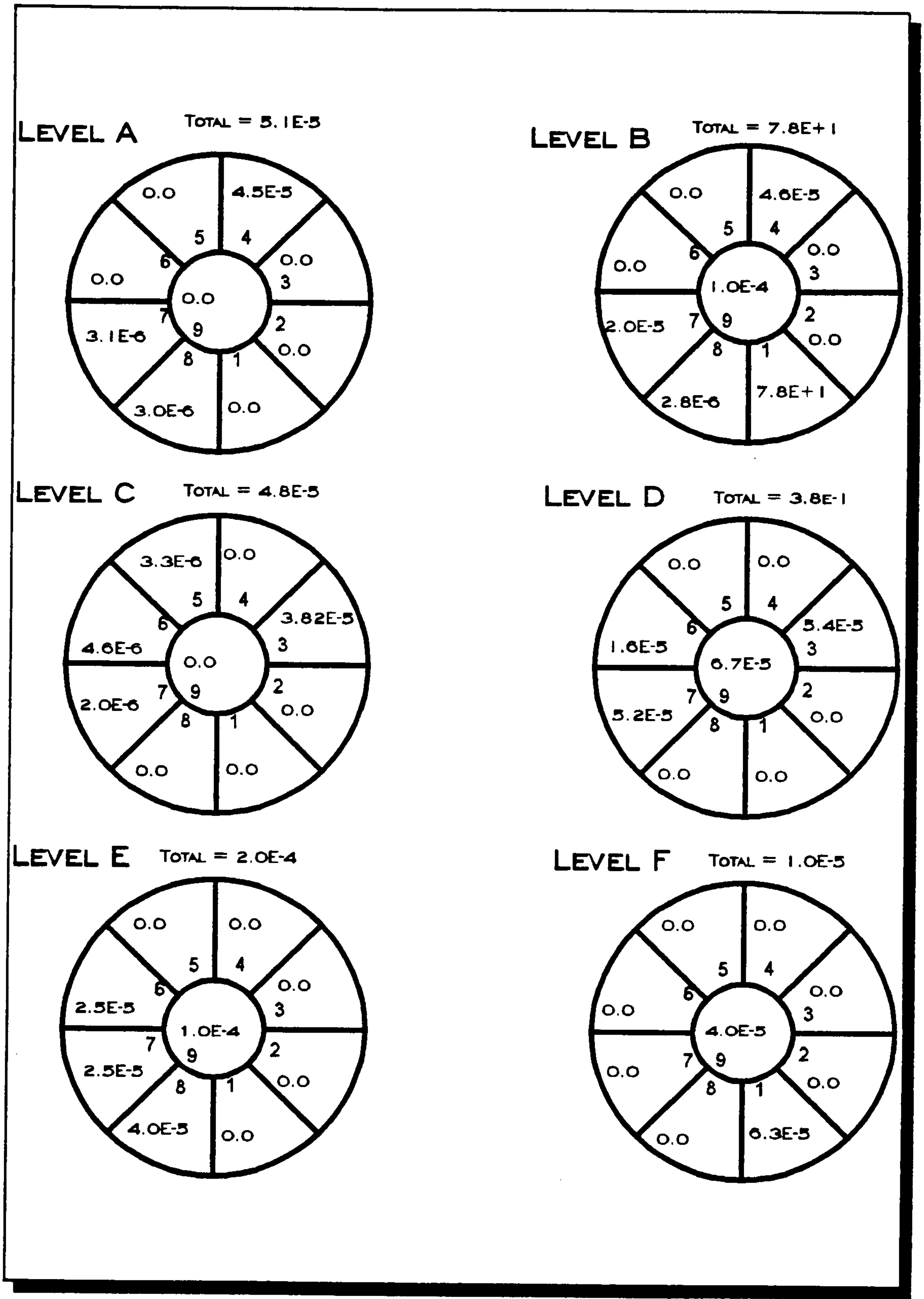

Figure 4.8 Computed Activity Using NNLS Subroutine for Run 1 (mCi).

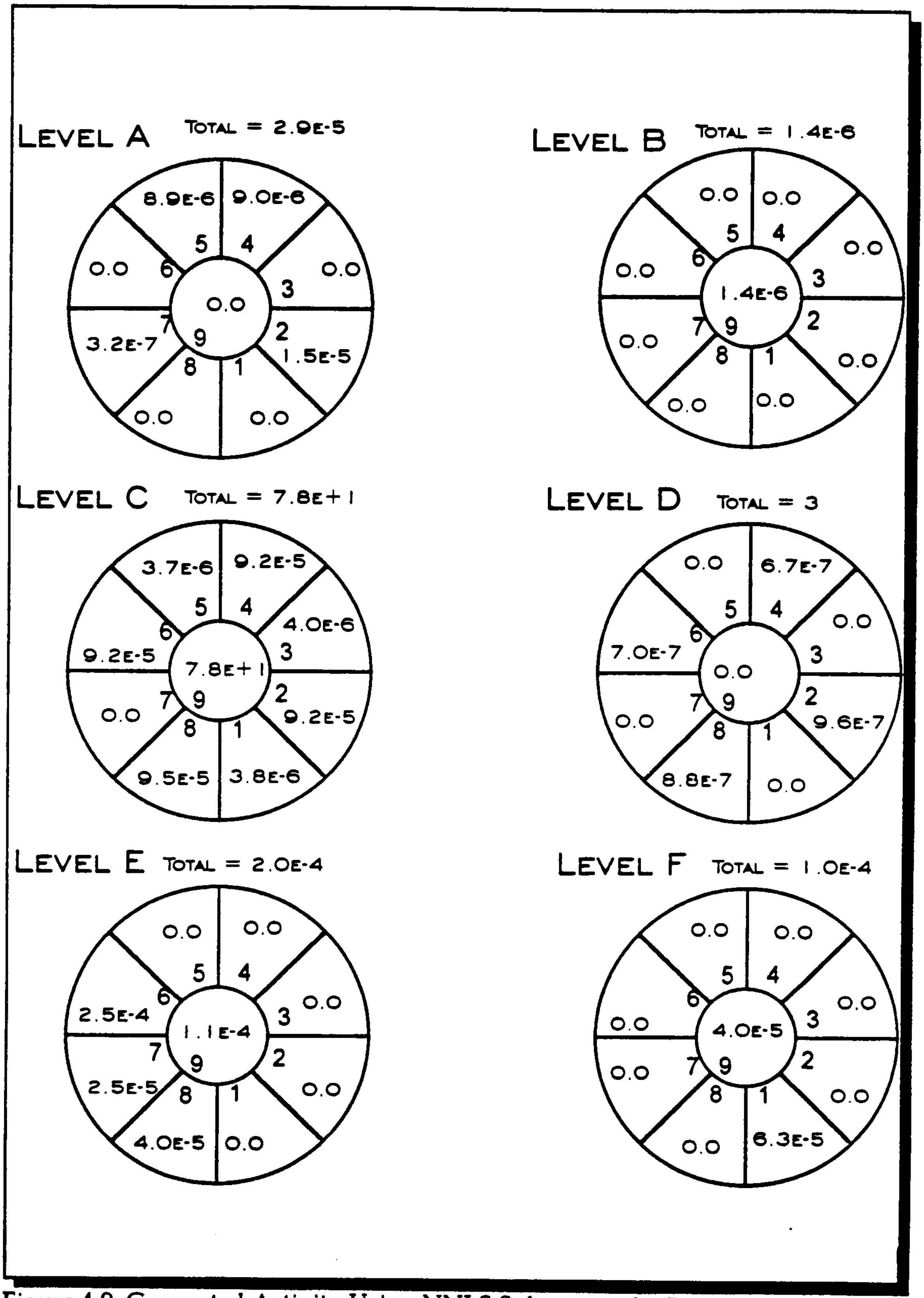

Figure 4.9 Computed Activity Using NNLS Subroutine for Run 2 (mCi).

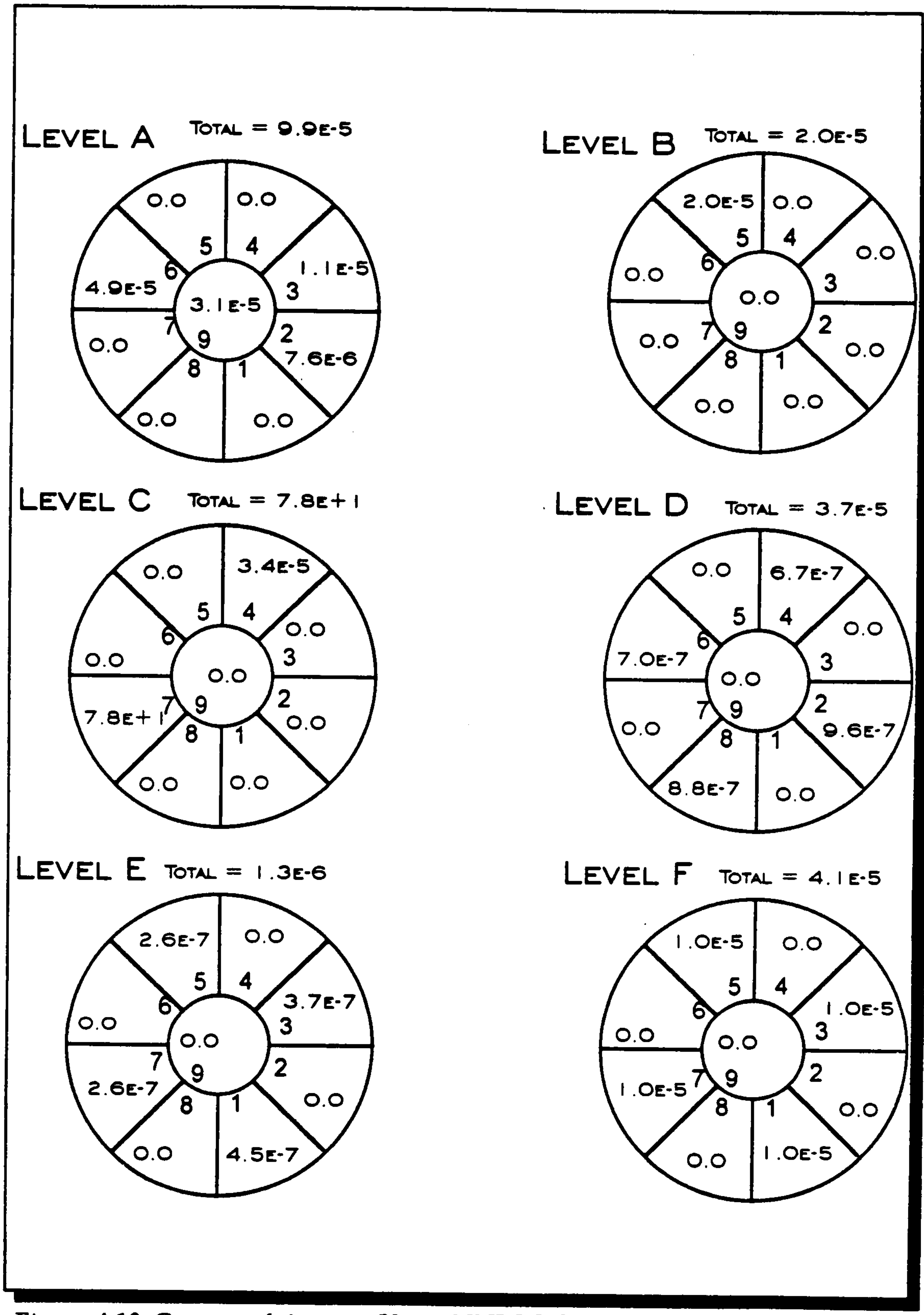

Figure 4.10 Computed Activity Using NNLS Subroutine for Run 3 (mCi).

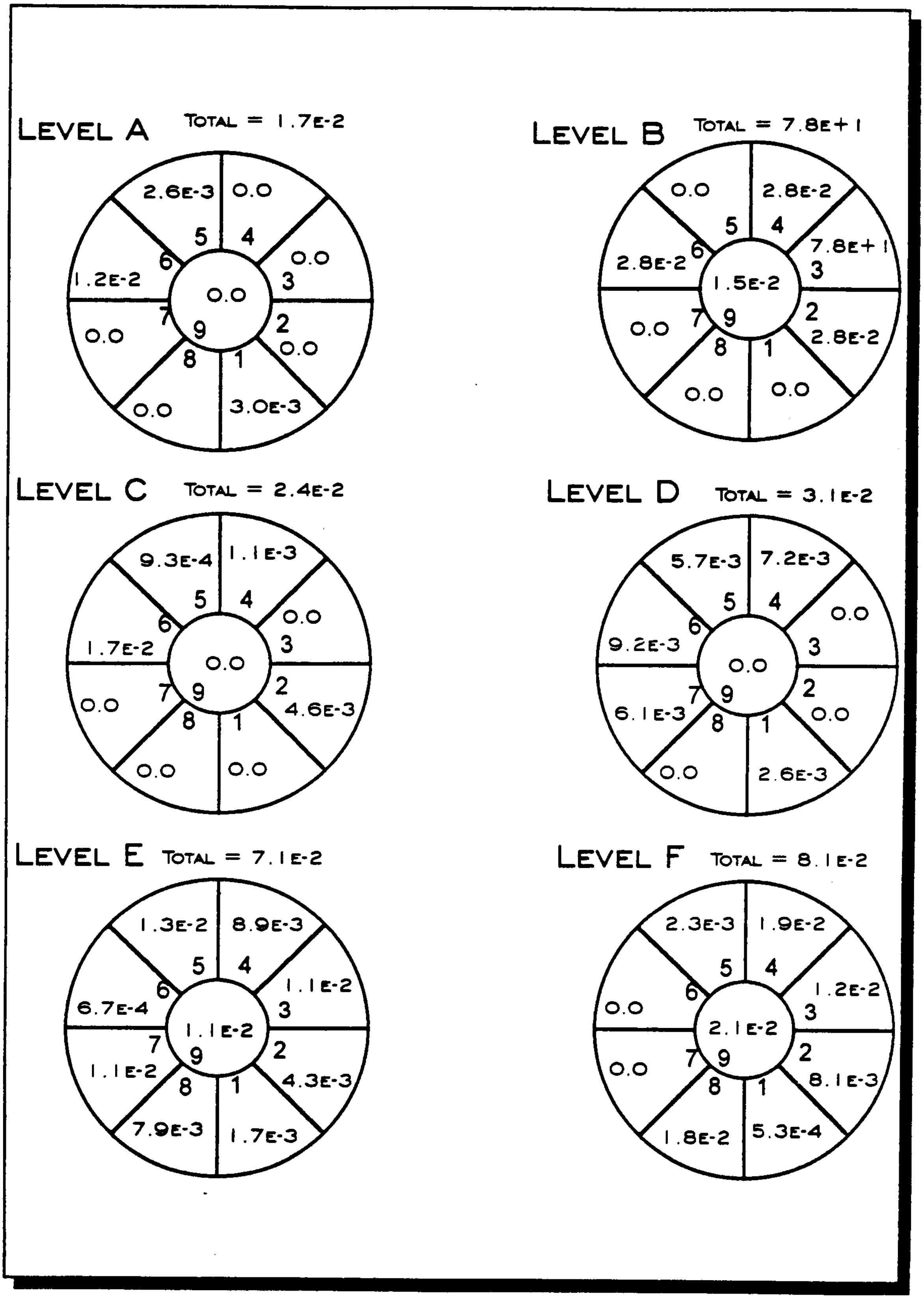

Figure 4.11 Computed Activity Using NNLS Subroutine for Run 4 (mCi).

The activities computed by the NNLS-based algorithm using the conditioned PSRF matrix accurately predicted the location and activity of the point source. Also, the predictions for the other voxels in the system have either been calculated as zero (0) or at least four (4) orders of magnitude less than that of the primary source activity. The primary source activity is the 73mCi ^{137}Cs point source. Further, note that the computed value of the primary source activity is quite precise. The average value for the computed primary source activity is 77.7995 mCi, with a minimum activity of 77.5985 mCi and a maximum activity of 77.8666 mCi. This corresponds to a range of 0.2681 mCi. Further calibration of the reconstruction algorithm would provide computed activities approximately equal to 73mCi.

The spurious calculated activities, for voxels other than those which contain the primary source, is attributed to statistical uncertainties in the detection system, PSRF matrix, solution package, and nuclide decay. No uncertainty analysis has been performed to determine the dominant causation of the uncertainty. Initial observations do lead one to consider the system uncertainty *(i.e. detector positioning and collimator geometry fluctuations)* as the primary cause for the spurious activities. However, uncertainties are always present in the imaging system. As noted in Chapter 2, the image set is composed of the object set plus an unknown noise vector. The uncertainties described above can be considered as functional parameters describing the noise vector.

4.2.2 LSMOD Reconstruction of a 73mCi ^{137}Cs Source

The LSMOD-based algorithm was used to provide computed activities in a manner similar to the NNLS-based routine. The computed value for these activities has also been entered into the same schematic as used in the previous section. Figures 4.12 through 4.15 provide these renderings. The output files written by the reconstruction routine are included in Appendix E.

It is interesting to note that, when compared to the NNLS-generated data, the LSMOD routine calculates a larger number of spurious activities. These can be thought of a Type One (1) errors, stating that activity is present in voxels when, in fact, there is none. Also, while the NNLS-routine produced a number of these spurious activities, those calculated by the LSMOD-routine are, in general, three (3) to four (4) orders of magnitude larger than those of NNLS.

The mean primary source activity, calculated by averaging the individual computed primary activities for each run, is 72.8018 mCi. The range of computed primary activities is 5.1843 mCi, with a minimum of 69.7299 mCi and a maximum of 74.9142 mCi. Note, that the calibration of the solution routine is such that the mean computed primary activity is approximately equal to the actual source activity, however, the range of the LSMOD values, and the sum of the total drum activity, is much larger than those generated by the NNLS-routine.

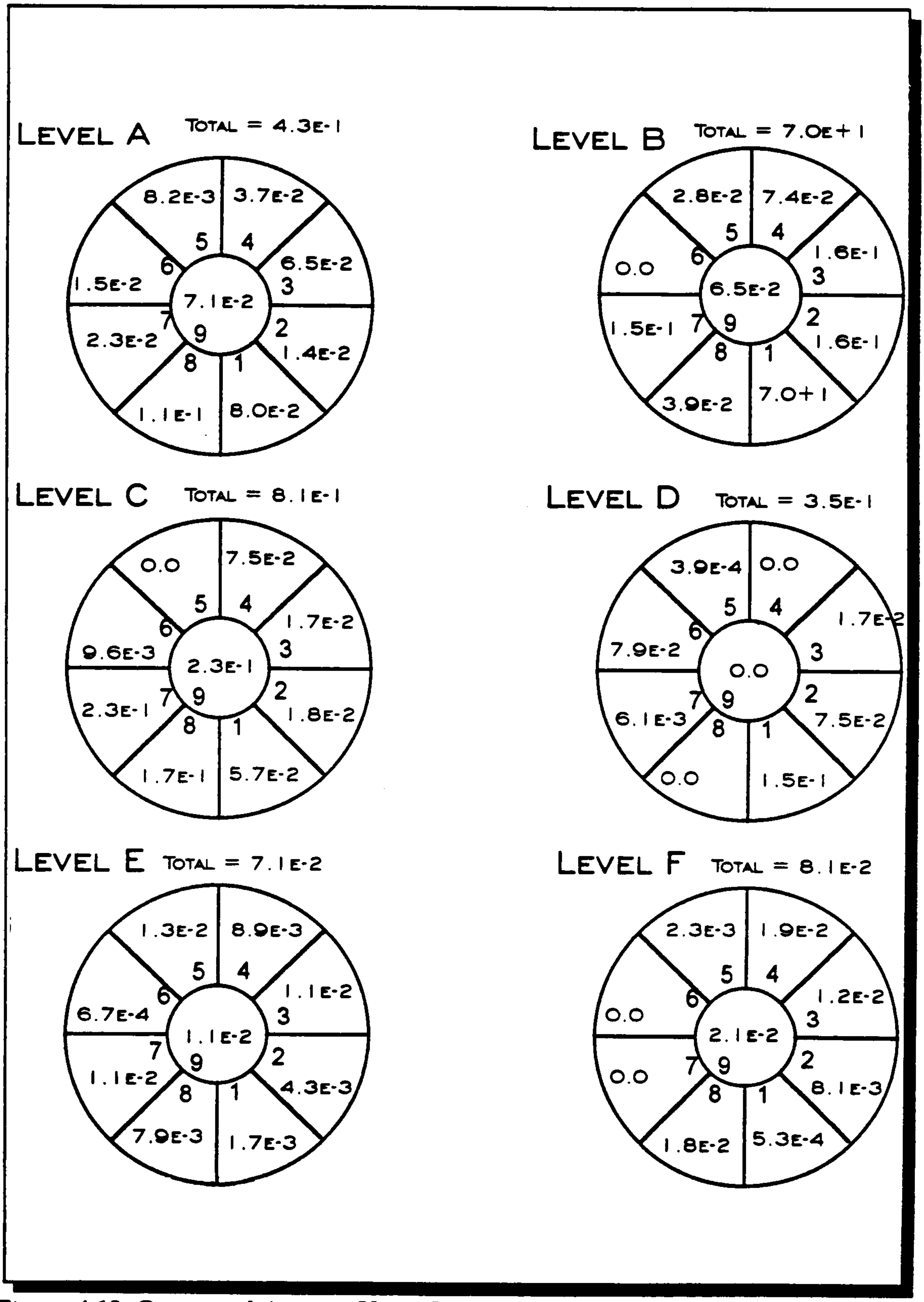

Figure 4.12 Computed Activity Using LSMOD Subroutine for Run 1 (mCi).

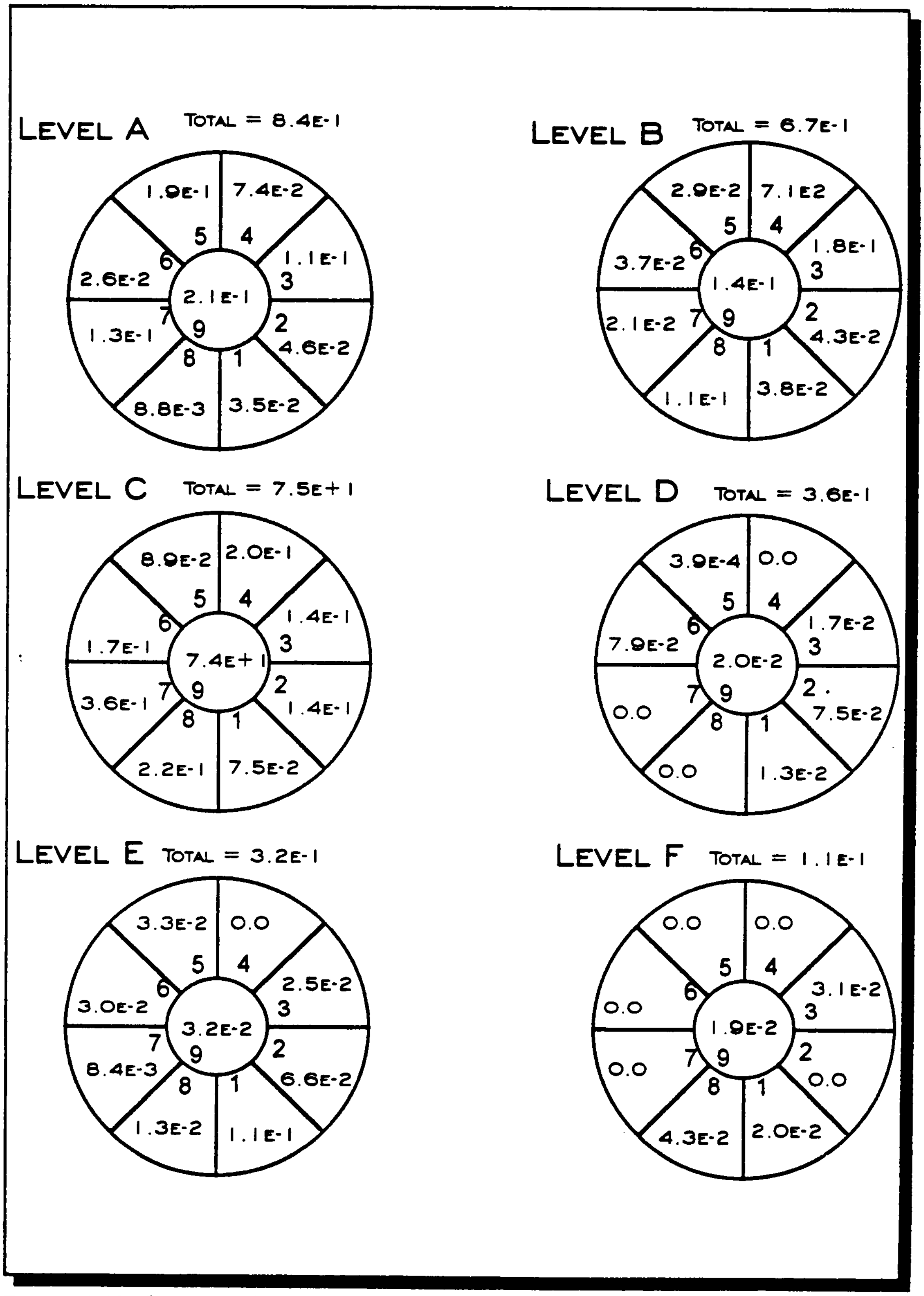

Figure 4.13 Computed Activity Using LSMOD Subroutine for Run 2 (mCi).

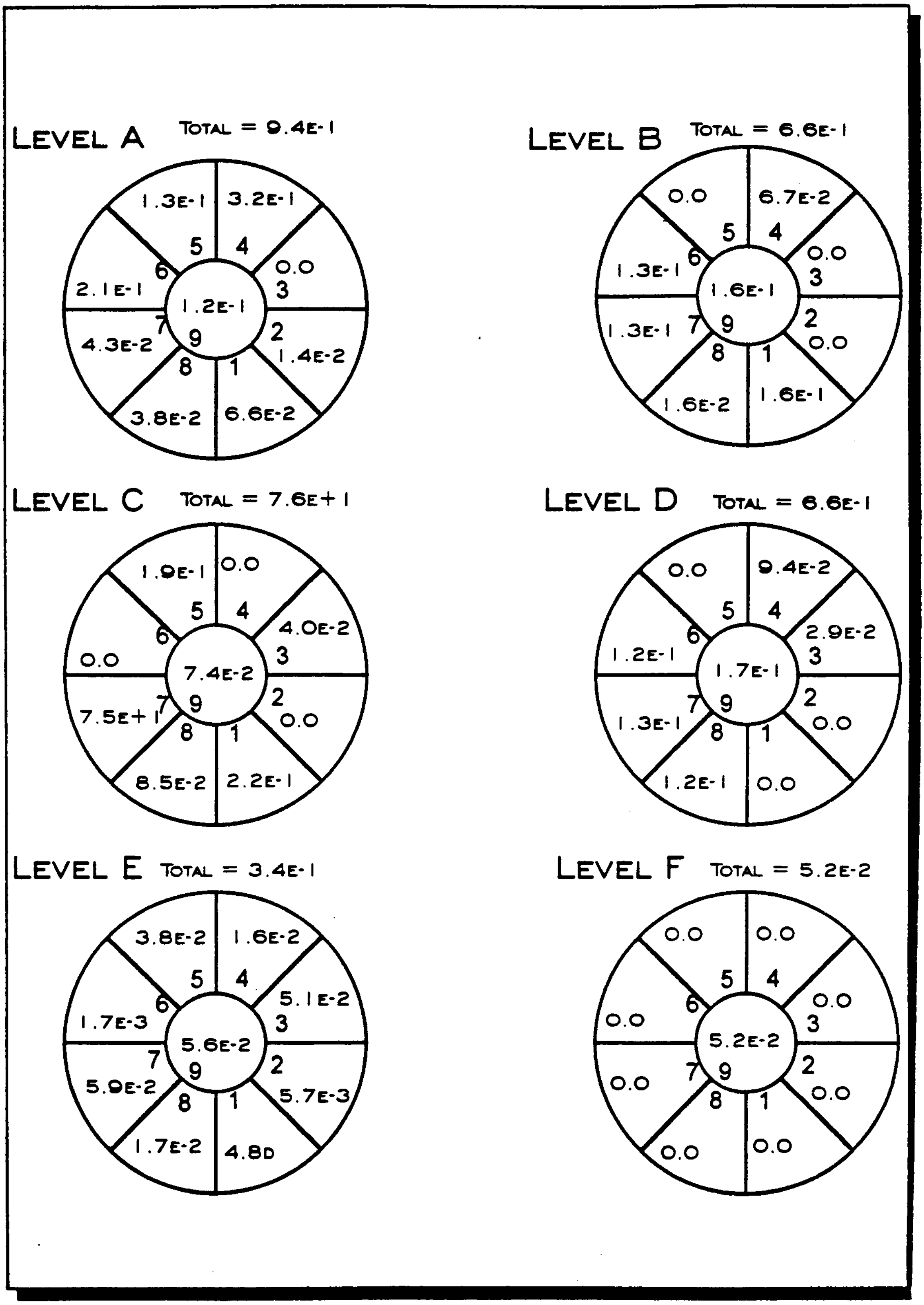

Figure 4.14 Computed Activity Using LSMOD Subroutine for Run 3 (mCi).

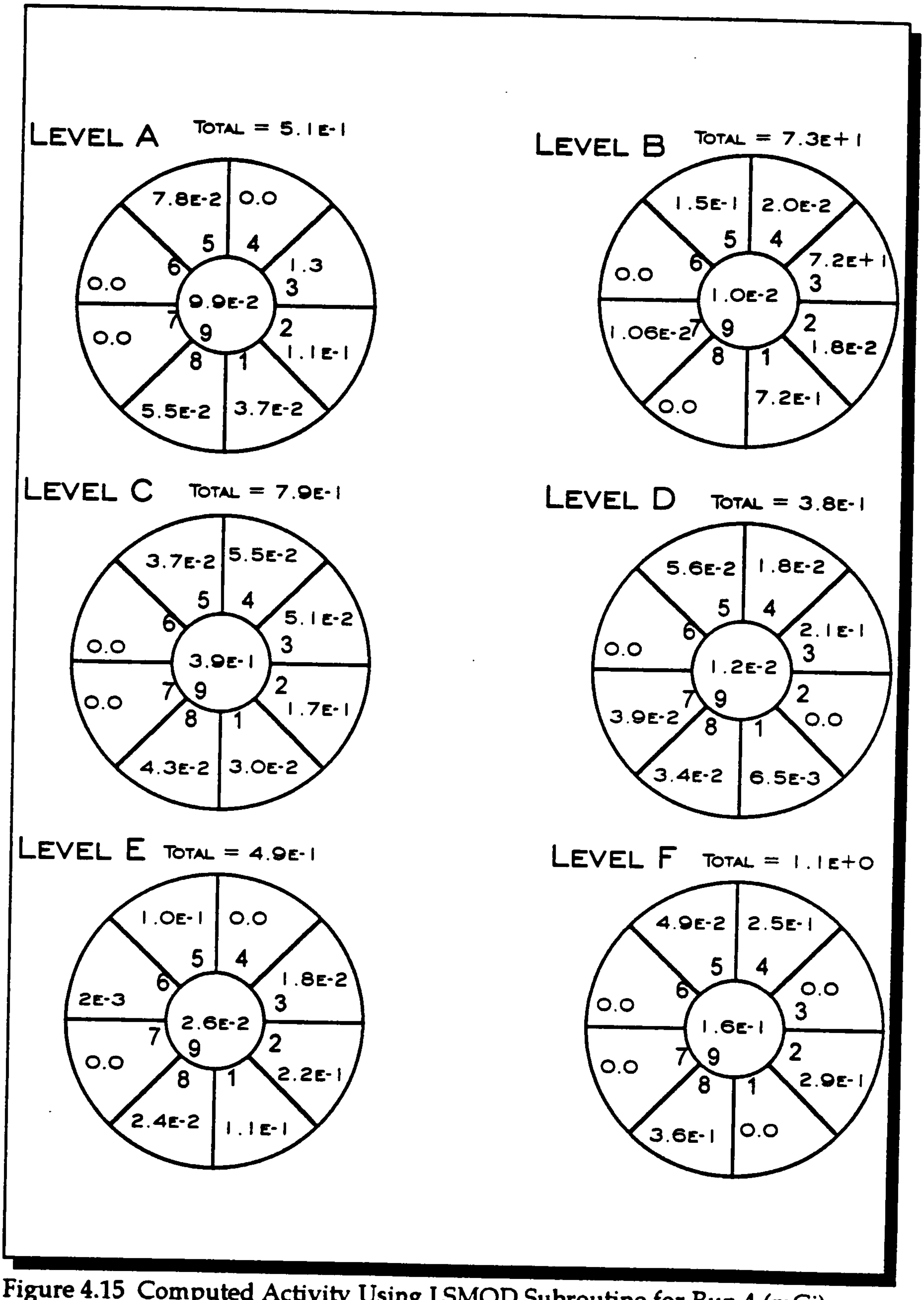

Figure 4.15 Computed Activity Using LSMOD Subroutine for Run 4 (mCi).

4.3 Evaluation of Matrix Conditioning

The computed values for activity using both the NNLS- and LSMOD-routines were determined by using a PSRF matrix which was conditioned or scaled to compensate for inherent system discrepancies not described by the QAD-CGGP modeling procedure. This section presents the computed activities using both routines when the unconditioned PSRF matrix was utilized by the solution algorithm. This data is presented in Tables 4.14 through 4.17. Note, the calculated primary source activity is, in all cases, less than the actual source activity. Further, the values for the spurious activities are, in general, much larger that those predicted when using the conditioned matrix.

Upon examination, the unconditioned matrix's inability to predict the responses due to the collimation asymmetry can be observed. The large activity values calculated for voxels in the upper regions of the drum indicate this asymmetry. The geometry of the collimator is such that the data gathered from the upper layers is affected to a larger degree by cross talk than data which is gathered from the lower layers.

In the following tables, note the over-estimation of the computed activities when using the unconditioned PSRF matrix. This is due to QAD-CGGP's inability to calculate the number of full-energy interactions within the crystal region. Thus, the PSRF matrix as calculated by QAD-CGGP assumes a detection efficiency of one

Table 4.14 Results of Reconstruction Algorithms Using a 73mCi Source Located in Voxel 10 (mCi)

Source Voxel	NNLS Conditioned	NNLS Condit'd	LSMOD Conditioned	LSMOD Uncondit'd
01(1A)	0.0000e+00	0.0000e+00	8.0300e-02	0.0000e+00
02(2A)	0.0000e+00	0.0000e+00	1.4400e-02	0.0000e+00
03(3A)	0.0000e+00	0.0000e+00	6.5500e-02	1.0700e+00
04(4A)	4.4503e-05	4.2900e+00	3.7000e-02	2.2000e+00
05(5A)	0.0000e+00	0.0000e+00	8.2000e-03	0.0000e+00
06(6A)	0.0000e+00	0.0000e+00	1.4500e-02	0.0000e+00
07(7A)	3.0635e-06	2.8600e+00	2.3000e-02	1.4300e+00
08(8A)	2.9914e-06	0.0000e+00	1.1800e-01	1.2500e+00
09(9A)	0.0000e+00	0.0000e+00	7.1000e-02	0.0000e+00
Layer Total	5.0558e-05	7.1500e+00	4.3200e-01	5.9600e+00
10(1B)	7.7867e+01	2.2900e+01	6.9700e+01	2.2200e+01
11(2B)	0.0000e+00	0.0000e+00	1.5700e-01	0.0000e+00
12(3B)	0.0000e+00	0.0000e+00	1.6300e-01	3.0500e+00
13(4B)	4.5716e-05	4.8100e+00	7.4100e-02	2.2200e+00
14(5B)	0.0000e+00	1.1800e-01	2.7600e-02	6.1500e-01
15(6B)	0.0000e+00	0.0000e+00	0.0000e+00	0.0000e+00
16(7B)	2.0460e-05	1.1900e+00	1.5300e-01	3.6400e+00
17(8B)	2.7660e-06	6.6900e-01	3.9300e-02	0.0000e+00
18(9B)	1.0285e-04	4.3800e+00	6.4500e-02	7.2300e-02
Layer Total	7.7867e+01	3.4100e+01	7.0400e+01	3.1800e+01
19(1C)	0.0000e+00	0.0000e+00	5.6600e-02	0.0000e+00
20(2C)	0.0000e+00	0.0000e+00	1.7900e-02	0.0000e+00
21(3C)	3.8225e-05	0.0000e+00	1.6900e-02	1.7700e+00
22(4C)	0.0000e+00	5.0000e+00	7.5400e-02	2.8000e+00
23(5C)	3.3251e-06	0.0000e+00	0.0000e+00	0.0000e+00
24(6C)	4.6009e-06	0.0000e+00	9.6400e-03	0.0000e+00
25(7C)	2.0021e-06	2.5700e+00	2.3000e-01	2.2800e+00
26(8C)	0.0000e+00	7.2000e-01	1.7300e-01	1.8000e+00
27(9C)	0.0000e+00	0.0000e+00	2.2900e-01	0.0000e+00
Layer Total	4.8153e-05	8.3000e+00	8.0900e-01	8.6500e+00

Table 4.14 (Continued) Results of Reconstruction Algorithms Using a 73mCi Source Located in Voxel 10 (mCi).

Source Voxel	NNLS Conditioned	NNLS Uncondit'd	LSMOD Conditioned	LSMOD Uncondit'd
28(1D)	0.0000e+00	0.0000e+00	1.5400e-01	7.8100e-01
29(2D)	0.0000e+00	6.1400e-01	7.5200e-02	5.9400e-01
30(3D)	5.3945e-05	1.9600e+00	1.6600e-02	0.0000e+00
31(4D)	0.0000e+00	3.4500e+00	0.0000e+00	0.0000e+00
32(5D)	0.0000e+00	1.1300e+00	3.8700e-04	0.0000e+00
33(6D)	1.5778e-05	0.0000e+00	7.9100e-02	8.8300e-01
34(7D)	5.2472e-05	4.0700e+00	0.0000e+00	0.0000e+00
35(8D)	0.0000e+00	0.0000e+00	0.0000e+00	0.0000e+00
36(9D)	6.6620e-05	8.6700e-01	2.0200e-02	1.2400e-01
Layer Total	1.8881e-04	1.2100e+01	3.4600e-01	2.3800e+00
37(1E)	0.0000e+00	2.5400e+00	1.0800e-01	2.4400e+00
38(2E)	0.0000e+00	9.9100e-01	6.6200e-02	1.0600e+00
39(3E)	0.0000e+00	4.8700e+00	2.5400e-02	4.1100e-01
40(4E)	0.0000e+00	1.9200e+00	0.0000e+00	0.0000e+00
41(5E)	0.0000e+00	1.6100e+00	3.3300e-02	8.7300e-01
42(6E)	2.4946e-05	1.9300e+00	2.9700e-02	2.4700e+00
43(7E)	2.5452e-05	3.6400e+00	8.4400e-03	1.3500e-01
44(8E)	3.9511e-05	3.4800e+00	1.3400e-02	6.2200e-01
45(9E)	1.1142e-04	3.6400e+00	3.2500e-02	5.2900e-02
Layer Total	2.0132e-04	2.4600e+01	3.1700e-01	8.0700e+00
46(1F)	6.3248e-05	2.8000e+00	2.0400e-02	3.3400e+00
47(2F)	0.0000e+00	4.5600e+00	0.0000e+00	2.8600e+00
48(3F)	0.0000e+00	2.9100e+00	3.0800e-02	6.1900e-01
49(4F)	0.0000e+00	3.2000e+00	0.0000e+00	0.0000e+00
50(5F)	0.0000e+00	2.3600e+00	0.0000e+00	9.1700e-01
51(6F)	0.0000e+00	1.5500e+00	0.0000e+00	2.3900e+00
52(7F)	0.0000e+00	3.5200e+00	0.0000e+00	6.3400e-01
53(8F)	0.0000e+00	2.5500e+00	4.3100e-02	8.8500e-01
54(9F)	4.0121e-05	5.6300e+00	1.9300e-02	1.7500e+00
Layer Total	1.0337e-04	2.9100e+01	1.1400e-01	1.3400e+01

Table 4.15 Results of Reconstruction Algorithms Using a 73mCi Source Located in Voxel 12 (mCi).

Source Voxel	NNLS Conditioned	NNLS Condit'd	LSMOD Conditioned	LSMOD Uncondit'd
01(1A)	2.9600e-03	2.3800e+00	3.7000e-02	9.8400e-01
02(2A)	0.0000e+00	0.0000e+00	1.1200e-01	1.0200e+00
03(3A)	0.0000e+00	0.0000e+00	1.3000e-01	0.0000e+00
04(4A)	0.0000e+00	0.0000e+00	0.0000e+00	0.0000e+00
05(5A)	2.5600e-03	7.3800e-01	7.8000e-02	1.0100e+00
06(6A)	1.1900e-02	4.0200e+00	0.0000e+00	2.1100e+00
07(7A)	0.0000e+00	0.0000e+00	0.0000e+00	0.0000e+00
08(8A)	0.0000e+00	0.0000e+00	5.5400e-02	0.0000e+00
09(9A)	0.0000e+00	0.0000e+00	9.8700e-02	0.0000e+00
Layer Total	1.7500e-02	7.5900e+00	5.1100e-01	5.1300e+00
10(1B)	0.0000e+00	7.6300e-02	7.1600e-01	3.4700e+00
11(2B)	2.7600e-02	3.1400e-01	1.8100e-02	0.0000e+00
12(3B)	7.7600e+01	1.8500e+01	7.2500e+01	1.9800e+01
13(4B)	2.8500e-02	0.0000e+00	2.0400e-02	0.0000e+00
14(5B)	0.0000e+00	0.0000e+00	1.4700e-01	2.7300e+00
15(6B)	2.8100e-02	5.3100e+00	0.0000e+00	2.4100e+00
16(7B)	0.0000e+00	0.0000e+00	1.6300e-02	4.2300e-01
17(8B)	0.0000e+00	0.0000e+00	0.0000e+00	0.0000e+00
18(9B)	1.5300e-02	6.3400e+00	9.9800e-03	0.0000e+00
Layer Total	7.7700e+01	3.3400e+01	7.3400e+01	2.8900e+01
19(1C)	0.0000e+00	2.3400e+00	3.0200e-02	2.6400e+00
20(2C)	4.5600e-03	1.2100e+00	1.7400e-01	1.4000e+00
21(3C)	0.0000e+00	8.9600e-02	5.1400e-02	0.0000e+00
22(4C)	1.0600e-03	0.0000e+00	5.4800e-01	0.0000e+00
23(5C)	9.2900e-04	2.8700e-01	3.6600e-02	2.0100e+00
24(6C)	1.6600e-02	4.9600e+00	0.0000e+00	3.0000e+00
25(7C)	0.0000e+00	0.0000e+00	0.0000e+00	0.0000e+00
26(8C)	0.0000e+00	0.0000e+00	4.3500e-02	0.0000e+00
27(9C)	0.0000e+00	0.0000e+00	3.9200e-01	0.0000e+00
Layer Total	2.3200e-02	8.8800e+00	7.8200e-01	9.0500e+00

Table 4.15 (Continued) Results of Reconstruction Algorithms Using a 73mCi Source Located in Voxel 12 (mCi).

Source Voxel	NNLS Conditioned	NNLS Uncondit'd	LSMOD Conditioned	LSMOD Uncondit'd
28(1D)	2.6400e-03	3.5200e+00	6.5200e-03	0.0000e+00
29(2D)	0.0000e+00	0.0000e+00	0.0000e+00	0.0000e+00
30(3D)	0.0000e+00	0.0000e+00	2.1400e-01	5.2800e-01
31(4D)	7.1600e-03	1.0500e+00	1.8200e-02	4.3900e-01
32(5D)	5.7200e-03	1.8900e+00	5.6400e-02	0.0000e+00
33(6D)	9.1800e-03	3.0500e+00	0.0000e+00	2.8800e-02
34(7D)	6.1000e-03	1.1100e+00	2.8800e-02	0.0000e+00
35(8D)	0.0000e+00	0.0000e+00	3.4500e-02	7.6900e-01
36(9D)	0.0000e+00	1.0600e-01	1.2400e-02	1.4500e-01
Layer Total	3.0800e-02	1.0700e+01	3.8100e+00	1.9100e+00
37(1E)	1.7300e-03	2.9600e+00	1.0700e-01	3.7500e-01
38(2E)	4.5300e-03	2.7000e+00	2.1600e-01	9.0500e-01
39(3E)	1.1400e-02	2.4000e+00	1.8400e-02	2.2900e+00
40(4E)	8.8900e-03	1.1600e+00	0.0000e+00	7.0100e-01
41(5E)	1.3500e-02	4.5100e+00	1.0200e-01	5.8800e-01
42(6E)	6.6500e-04	1.7400e+00	2.0000e-03	0.0000e+00
43(7E)	1.1400e-02	1.8100e+00	0.0000e+00	8.8600e-01
44(8E)	7.9400e-03	1.6000e+00	2.3900e-02	2.3900e+00
45(9E)	1.1400e-02	3.0500e+00	2.6000e-02	1.4500e-01
Layer Total	7.1200e-02	2.1900e+01	4.9500e-01	8.2800e+00
46(1F)	5.2800e-04	3.5200e+00	0.0000e+00	5.3500e-01
47(2F)	8.1100e-03	2.5000e+00	2.8600e-01	7.2400e-01
48(3F)	1.1600e-02	2.7100e+00	0.0000e+00	3.3100e+00
49(4F)	1.8700e-02	3.2500e+00	2.5100e-01	2.5100e+00
50(5F)	2.3500e-03	2.6100e+00	4.9500e-02	7.7800e-01
51(6F)	0.0000e+00	3.1000e+00	0.0000e+00	0.0000e+00
52(7F)	0.0000e+00	6.5800e-01	0.0000e+00	1.2100e+00
53(8F)	1.8000e-02	2.0700e+00	3.5900e-01	2.0000e+00
54(9F)	2.1500e-02	5.2800e+00	1.6100e-01	1.8400e+00
Layer Total	8.0700e-02	2.5700e+01	1.1000e+00	1.2900e+01

Table 4.16 Results of Reconstruction Algorithms Using a 73mCi Source Located in Voxel 25 (mCi).

Source Voxel	NNLS Conditioned	NNLS Uncondit'd	LSMOD Conditioned	LSMOD Uncondit'd
01(1A)	0.0000e+00	2.1900e+00	6.5600e-02	0.0000e+00
02(2A)	7.6300e-06	2.8200e+00	1.4400e-02	0.0000e+00
03(3A)	1.0700e-05	2.2100e+00	0.0000e+00	4.7300e-01
04(4A)	0.0000e+00	0.0000e+00	3.2100e-01	1.2300e+00
05(5A)	0.0000e+00	1.8400e-01	1.2800e-01	0.0000e+00
06(6A)	4.9200e-05	1.0700e+00	2.1000e-01	0.0000e+00
07(7A)	0.0000e+00	0.0000e+00	4.3000e-02	2.0400e+00
08(8A)	0.0000e+00	4.2400e+00	3.7900e-02	1.2600e+00
09(9A)	3.1100e-05	1.9100e+00	1.2500e-01	2.5300e-01
Layer Total	9.8700e-05	1.4600e+01	9.4500e-01	5.2600e+00
10(1B)	0.0000e+00	1.9900e-01	1.6200e-01	1.4600e+00
11(2B)	0.0000e+00	4.3700e+00	0.0000e+00	2.1800e+00
12(3B)	0.0000e+00	0.0000e+00	0.0000e+00	0.0000e+00
13(4B)	0.0000e+00	0.0000e+00	6.6800e-02	0.0000e+00
14(5B)	2.0100e-05	3.4500e+00	0.0000e+00	1.7300e+00
15(6B)	0.0000e+00	0.0000e+00	1.2500e-01	1.1700e+00
16(7B)	0.0000e+00	0.0000e+00	1.3000e-01	0.0000e+00
17(8B)	0.0000e+00	0.0000e+00	1.5600e-02	0.0000e+00
18(9B)	0.0000e+00	0.0000e+00	1.5700e-01	0.0000e+00
Layer Total	2.0100e-05	8.0200e+00	6.5600e-01	6.5500e+00
19(1C)	0.0000e+00	7.7400e-01	2.2400e-01	4.5000e+00
20(2C)	0.0000e+00	4.3200e+00	0.0000e+00	1.6600e+00
21(3C)	0.0000e+00	0.0000e+00	4.0400e-02	2.0000e-01
22(4C)	3.4000e-05	0.0000e+00	0.0000e+00	0.0000e+00
23(5C)	0.0000e+00	2.3500e+00	1.8700e-01	4.4400e+00
24(6C)	0.0000e+00	1.7900e-01	0.0000e+00	0.0000e+00
25(7C)	7.7900e+01	2.1800e+00	7.4900e+01	2.2400e+01
26(8C)	0.0000e+00	0.0000e+00	8.5200e-02	0.0000e+00
27(9C)	0.0000e+00	1.7300e+00	7.4100e-02	0.0000e+00
Layer Total	7.7900e+01	3.1100e+01	7.5500e+01	3.3200e+01

Table 4.16 (Continued) Results of Reconstruction Algorithms Using a 73 mCi Source Located in Voxel 25 (mCi).

Source Voxel	NNLS Conditioned	NNLS Uncondit'd	LSMOD Conditioned	LSMOD Uncondit'd
28(1D)	0.0000e+00	3.1500e-01	0.0000e+00	2.3200e+00
29(2D)	0.0000e+00	5.1500e+00	0.0000e+00	3.0200e+00
30(3D)	0.0000e+00	0.0000e+00	2.9100e-02	0.0000e+00
31(4D)	0.0000e+00	0.0000e+00	9.3900e-02	0.0000e+00
32(5D)	9.0700e-07	3.0500e+00	0.0000e+00	2.6200e+00
33(6D)	2.2000e-05	5.7200e-01	1.1900e-01	2.0000e+00
34(7D)	2.1100e-06	0.0000e+00	1.3300e-01	0.0000e+00
35(8D)	1.2400e-05	0.0000e+00	1.1700e-01	0.0000e+00
36(9D)	0.0000e+00	0.0000e+00	1.6600e-01	0.0000e+00
Layer Total	3.7400e-05	9.0900e+00	6.5800e-01	9.9600e+00
37(1E)	0.0000e+00	3.4900e+00	4.8300e-02	1.1400e-01
38(2E)	0.0000e+00	2.0600e+00	0.0000e+00	0.0000e+00
39(3E)	0.0000e+00	9.4800e-01	3.5900e-02	3.5100e-01
40(4E)	1.9000e-05	9.7000e-01	2.1100e-02	1.0400e+00
41(5E)	1.3600e-05	3.2300e-01	0.0000e+00	0.0000e+00
42(6E)	0.0000e+00	1.7100e+00	6.8900e-03	1.1000e-01
43(7E)	0.0000e+00	0.0000e+00	1.5400e-01	5.3400e-01
44(8E)	0.0000e+00	0.0000e+00	5.4400e-02	1.9100e-01
45(9E)	0.0000e+00	3.0900e-01	1.8000e-02	2.3200e-03
Layer Total	3.2600e-05	1.2700e+01	3.3900e-01	2.3400e+00
46(1F)	0.0000e+00	2.5900e+00	3.2700e-02	0.0000e+00
47(2F)	0.0000e+00	3.4700e+00	0.0000e+00	0.0000e+00
48(3F)	2.3800e-05	1.8200e+00	0.0000e+00	6.9400e-01
49(4F)	0.0000e+00	9.2200e-01	0.0000e+00	1.8900e+00
50(5F)	0.0000e+00	3.7400e+00	0.0000e+00	0.0000e+00
51(6F)	1.5900e-05	1.7100e+00	4.5900e-02	0.0000e+00
52(7F)	0.0000e+00	9.5100e-01	8.2800e-02	2.5700e+00
53(8F)	0.0000e+00	3.7500e+00	2.0900e-02	2.0500e+00
54(9F)	0.0000e+00	3.9900e+00	2.6200e-02	7.1100e-01
Layer Total	3.9700e-05	2.2900e+01	2.0800e-01	7.9200e+00

Table 4.17 Results of Reconstruction Algorithm Using a 73mCi Source Located in Voxel 27 (mCi).

Source Voxel	NNLS Conditioned	NNLS Uncondit'd	LSMOD Conditioned	LSMOD Uncondit'd
01(1A)	0.0000e+00	6.5700e-01	3.5200e-02	1.3400e+00
02(2A)	1.0600e-05	1.1200e+00	4.6200e-02	1.7100e+02
03(3A)	0.0000e+00	6.2500e-01	1.0900e-01	1.3400e+00
04(4A)	9.0500e-06	1.1000e+00	7.4200e-02	1.7600e-01
05(5A)	8.8500e-06	5.7200e-01	1.9100e-01	1.3400e+00
06(6A)	0.0000e+00	1.0500e+00	2.6300e-02	1.7400e-01
07(7A)	3.2600e-07	6.0700e-01	1.3400e-01	1.3500e+00
08(8A)	0.0000e+00	1.0600e+00	8.7700e-03	1.6700e-01
09(9A)	0.0000e+00	2.7800e-01	2.1100e-01	8.1800e-01
Layer Total	2.8800e-05	7.0700e+00	8.3600e-01	6.8700e+00
10(1B)	0.0000e+00	0.0000e+00	3.8300e-02	0.0000e+00
11(2B)	0.0000e+00	2.1300e-01	4.2500e-02	2.8600e-01
12(3B)	0.0000e+00	0.0000e+00	1.8000e-01	0.0000e+00
13(4B)	0.0000e+00	2.6000e-01	7.0900e-02	3.2300e-01
14(5B)	0.0000e+00	2.6800e-01	2.9500e-02	2.7800e-02
15(6B)	0.0000e+00	3.4100e-02	3.7100e-02	1.9500e-01
16(7B)	0.0000e+00	0.0000e+00	2.0700e-02	0.0000e+00
17(8B)	0.0000e+00	1.1000e-01	1.0600e-01	2.5400e-01
18(9B)	1.3800e-06	1.7400e+00	1.4400e-01	1.9000e+00
Layer Total	1.3800e-06	2.6200e+00	6.6900e-01	2.9800e+00
19(1C)	3.7000e-06	0.0000e+00	7.5000e-02	0.0000e+00
20(2C)	9.1600e-05	3.8100e+00	1.4500e-01	2.3000e+00
21(3C)	3.9700e-06	0.0000e+00	1.4200e-01	0.0000e+00
22(4C)	9.2000e-05	3.8100e+00	2.0200e-01	2.3000e+00
23(5C)	3.6900e-06	0.0000e+00	8.8600e-02	0.0000e+00
24(6C)	9.2100e-06	3.8100e+00	1.7500e-01	2.3000e+00
25(7C)	0.0000e+00	0.0000e+00	3.6200e-01	0.0000e+00
26(8C)	9.5100e-05	3.8100e+00	2.0200e-01	2.3000e+00
27(9C)	7.7900e+01	2.7900e+01	7.4000e+01	3.0700e+00
Layer Total	7.7900e+01	4.3100e+01	7.5500e+01	3.9900e+01

Table 4.17 (Continued) Results of Reconstruction Algorithms Using a 73mCi Source Located in Voxel 27 (mCi).

Source Voxel	NNLS Conditioned	NNLS Uncondit'd	LSMOD Conditioned	LSMOD Uncondit'd
28(1D)	0.0000e+00	0.0000e+00	1.2600e-02	0.0000e+00
29(2D)	9.5800e+01	1.7700e-01	5.7500e-02	5.7200e-01
30(3D)	0.0000e+00	0.0000e+00	3.7200e-02	0.0000e+00
31(4D)	6.7100e-07	1.7400e-01	7.4600e-02	5.7300e-01
32(5D)	0.0000e+00	0.0000e+00	4.4900e-03	0.0000e+00
33(6D)	7.0000e-07	1.7400e-01	6.5500e-02	5.7300e-01
34(7D)	0.0000e+00	0.0000e+00	3.5700e-02	0.0000e+00
35(8D)	8.7900e-07	1.7800e-01	7.7400e-02	5.7300e-01
36(9D)	0.0000e+00	5.9800e+00	0.0000e+00	5.5900e+00
Layer Total	3.2100e-06	6.6800e+00	3.6500e-01	7.8800e+00
37(1E)	4.5300e-07	3.1900e-01	3.4800e-02	5.0700e-01
38(2E)	0.0000e+00	4.7700e-01	5.7100e-03	3.6800e-02
39(3E)	3.7200e-07	3.1700e-01	5.0600e-02	5.0600e-01
40(4E)	0.0000e+00	4.7400e-01	1.6100e-02	3.6900e-02
41(5E)	2.6000e-07	3.1500e-01	3.7600e-02	5.0500e-01
42(6E)	0.0000e+00	4.7700e-01	1.7200e-03	3.8900e-02
43(7E)	2.6200e-07	3.1600e-01	5.9400e-02	5.0700e-01
44(8E)	0.0000e+00	4.7800e-01	1.6900e-02	3.7500e-02
45(9E)	0.0000e+00	0.0000e+00	5.6200e-02	0.0000e+00
Layer Total	1.3500e-06	3.1700e+00	2.7900e-01	2.1800e+00
46(1F)	1.0400e-05	1.2300e+00	0.0000e+00	1.6600e+00
47(2F)	0.0000e+00	1.3900e+00	0.0000e+00	5.7800e-01
48(3F)	1.0500e-05	1.2300e+00	0.0000e+00	1.6500e+00
49(4F)	0.0000e+00	1.3800e+00	0.0000e+00	5.7900e-01
50(5F)	1.0100e-05	1.2300e+00	0.0000e+00	1.6500e+00
51(6F)	0.0000e+00	1.3900e+00	0.0000e+00	5.8200e-01
52(7F)	1.0400e-05	1.2300e+00	0.0000e+00	1.6600e+00
53(8F)	0.0000e+00	1.0390e+01	0.0000e+00	5.7900e-01
54(9F)	0.0000e+00	9.7300e-01	5.2000e-02	1.3200e+00
Layer Total	4.1400e-05	1.1400e+01	5.2000e-02	1.0200e+01

hundred (100) percent. This is false of course and, as such, the conditioning of the matrix provides a method of correcting the responses for the much lower detector and system efficiencies.

4.4 System MDA

As discussed in Chapter 2, the calculation of a system MDA for an ECT scanner can be quite intensive. However, a reasonable approximation can be made by calculating the MDA for a point source using the following assumptions. First, the source must be located in the center of a voxel, preferably a central voxel. Second, the detector is located in position three (3) lying along the y-axis and in direct view of the source located in the central voxel. Using these assumptions, an approximation of the MDA can be made using standard counting statistics.

For this experiment, Equation 2.56 was used to calculate the approximate MDA. Parameters included a ninety-five (95) percent confidence interval for both Type One (1) and Type Two (2) errors, a sufficiently long background count (151,362 seconds), and a efficiency of 0.01517 mCi per count. A count time of one (1) minute was chosen and all data scaled to this value. The background count was determined by summing over the region of interest which contained the 0.662 MeV photopeak. This was then normalized to a background count per minute, or 0.258 counts per minute. Complying with the assumptions listed above, the source is assumed to be located in a central voxel and a detector position directly in line with this voxel is chosen. Experimentally, this corresponds to source position 27 and detector position C3. This source position was used in a reconstruction experiment. The efficiency, determined experimentally, stipulates that 0.01517 mCi yields one count per minute. Using the formula derived by Altshuler (1963), the MDA as calculated by Equation 2.56 is given as 30.20 μCi for a one (1) minute count time.

Chapter 5

Summary and Conclusions

In this paper, the ECT methodology has been used to determine the activity distribution of a mock-up waste package containing a single 73mCi ^{137}Cs point source. Reconstruction of the distribution was performed using algebraic techniques with the detector responses being described by the PSRF. The distribution is simply the solution of the linear system which relates the response matrix and source distribution to the data gathered by the detection system. In this case, a 2x2 inch NaI(Tl) detector was used to provide data at each of 120 sampling points. The source distribution, the unknown in the linear system, was then calculated to provide information for each of the fifty-four (54) active voxels of the container. Solutions to the system were calculated using two (2) least squares packages, Hansen and Lawson's Non-Negative Least Squares and ANL's LSMOD.

Reconstructions were performed using both solution packages for four (4) experiments. In each, the source was located in the center of a random voxel. In all cases, the distributions calculated using the NNLS package provided superior approximations of the actual source distribution. The range of calculated values using the NNLS-based routine was 0.2681 mCi with an average of 77.7995 mCi. The

LSMOD routine was noted as providing a larger number of spurious activities than the NNLS routine, which leads to an over-estimation of the packages total activity. In most cases, these over-estimations were two (2) or more orders of magnitude larger than their NNLS counterparts. Further, the range of solutions provided by LSMOD for the primary source activity was vastly larger than that generated by the NNLS-based algorithm. The range was determined to be 5.1843 mCi, with an average computed source activity of 72.8018 mCi. Therefore, the NNLS-routine, as employed in the solution program, provides results which are more precise and when properly calibrated, accurate than those of the LSMOD routine.

In summary, the use of ECT scanning to determine the source distribution of mock-up LLRW waste packages is a viable and appropriate procedure. Further, analysis of the results of this research has led to the following conclusions.

- ECT has produced accurate and precise results when imaging point sources in a homogeneous attenuating media.
- Initial determination of the PSRF matrix by use of the point-kernal code QAD-CGGP provided consistent results when compared to data calculated by MCNP using a similar test geometric model.
- Conditioning of the PSRF matrix is a viable method of compensating for asymmetric conditions associated with the scanning system.
- The NNLS-based solution algorithm determines the primary source activity with high precision, the results having a range much less than those results obtained by the LSMOD-routine.
- The LSMOD-based solution algorithm over-estimates the total package activity due to the large number of spurious activities provided in the solution set.
- An approximation of system MDA, using standard counting statistics, yields a value of 30.20 μCi.

Further research in this area, in the laboratory setting, would include completion of the PSRF calibration with experimental data and the addition of a device to insure exact duplication of detector positioning along the x-axis. Expanding upon this methodology into an industrial climate, one would need to institute major changes. Of these, the addition of a automated positioning system, perhaps governed by a programmable logic controller, would provide help to provide the vast increase in scan time required. Also, the creation of a software package which interprets the data gathered by the MCA and relays it to the reconstruction package, eliminating another tedious operation. However, in order for this system to provide consistent and accurate results in industry, the addition of a TCT system must be included. The most important determination made by the CT scanning system is the calculation of the attenuation coefficients of each voxel. In a homogeneous case, these are know before hand, and a modeling routine or experimental data can be use to complete the PSRF matrix. However, in a industrial setting, scanning packages prior to disposal, the composition of the contents is not known. It is for this reason that the TCT option must be included.

Little doubt can be cast upon the future of the ECT/TCT scanning methodology for LLRW waste packages, as systems are currently under development which employ this technology. This research has shown that the implementation of a CT methodology to perform assays of LLRW is a feasible and advantageous alternative to current NDA methods.

Bibliography

Bibliography

Altshuler, B. and Pasternack, B., *Statistical Measures of the Lower Limit of Detection of a Radioactivity Counter*, Health Physics, vol. 9, 1963.

Bauer, M., Schultz, F., and Vourvoupoulos, G., *LINAC-Based Transuranic Waste Characterization System: Intern Project Report (draft)*, Oak Ridge National Laboratory, October, 1992.

Canberra Industries, Inc., *Waste Measurement Systems*, Meridian, Connecticut, July, 1995.

Eckerman, K., Oak Ridge National Laboratory, personal conversation, July, 1995.

Estep, R., *A Preliminary Design Study for Improving Performance in Tomographic Assays* (LA-12727-MS), Los Alamos National Laboratory, March, 1994.

Goto, T., and Hiroaki, K., *A Radioactivity Assay Method Using Computed Tomography*, Nuclear Technology, vol. 100, December 1992, 322-330.

Kak, A. C. and Slaney, M., Principles of Computerized Tomographic Imaging, IEEE Engineering in Medicine and Biology Society, IEEE Press, 1986.

Kawasaki, S., Kondo, M., Izumi, S., and Kikuchi, M., *Radioactivity Measurement of Drum Package Waste by a Computed-Tomography Technique*, Applied Radiation and Isotopes, vol. 41, October/November 1990, 983-987.

Lawson, C. L. and Hanson, R. J., Solving Least Squares Problems, Prentice-Hall, Englewood Cliffs, 1974.

Moghissi, A. A., Godbee, H. W., and Hobart, S. A., eds., Radioactive Waste Technology, American Society of Mechanical Engineers, 1992.

Radiation Shielding Information Center, *QAD Point-Kernel General Purpose Shielding Codes: QAD-IV, QAD-P5, QAD-B, QAD-V, QAD-INT, QAD-HD, QAD-5K, QAD-BR, and QAD-P5A* (CCC-48), Oak Ridge National Laboratory, February 1980.

Radiation Shielding Information Center, *QAD-CGGP A Combinatorial Geometry Version of QAD-P5A, A Point Kernel Code System for Neutron and Gamma-Ray Shielding Calculations Using the GP Buildup Factor* (CCC-493), Oak Ridge National Laboratory, May 1994.

Smith, D. L., *A Least-Squares Computational "Tool Kit"* (ANL/NDM-128), Argonne National Laboratory, 1993.

Sorenson, J. A., and Phelps, M. E., Physics in Nuclear Medicine, W. B. Saunders Co., Philadelphia, 1987.

Stallman, F. W., *Theory and Practice of General Adjustment and Model Fitting Parameters* (NUREG/CR-2222), Oak Ridge National Laboratory, December 1981.

State of Tennessee, Tennessee Department of Health and Environment, *State Regulations for Protection Against Radiation* (Tennessee Annotated Code Chapter 1200-2), May 1986.

Turner, J. E., Atoms, Radiation, and Radiation Protection, McGraw-Hill, New York, 1992.

United States. *The Atomic Energy Act of 1954* (Public Law 83-703, 88 Stat. 1233, 42 U.S.C Chapter 23), 1954.

Webb, S., The Physics of Medical Imaging, Institute of Physics Publishing, Philadelphia, 1988.

Vourvoupoulos, G., *The Use of an Electron LINAC for Waste Assay: Feasibility Study,* Unpublished Report, September 1992.

Appendices

Appendix A

Photographs of Experimental Apparatus

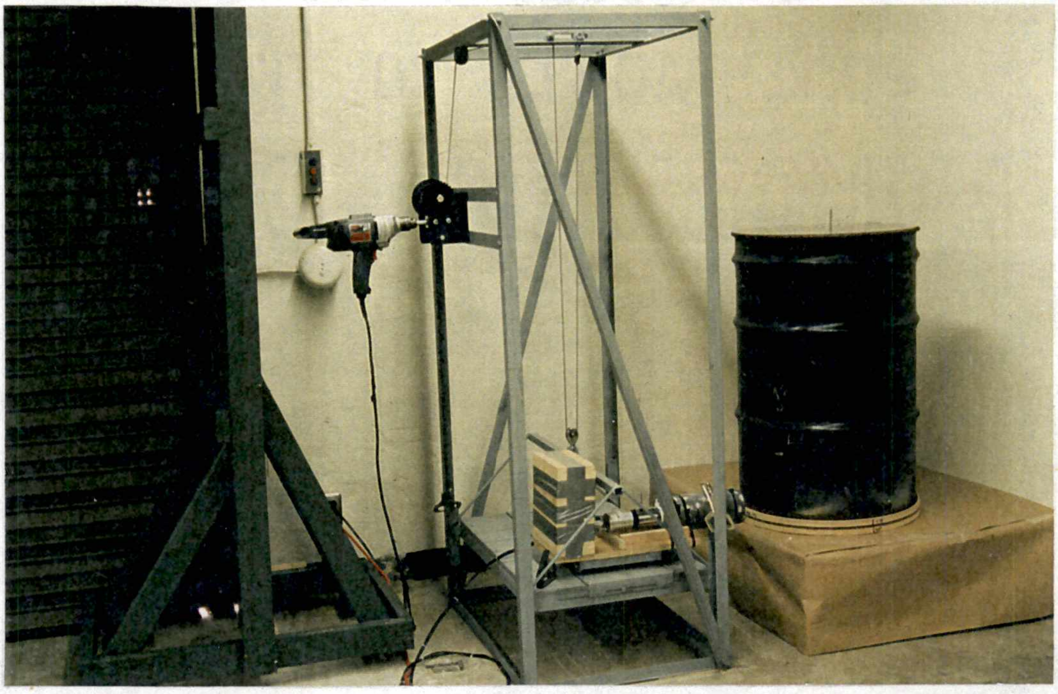

Figure A.1 Photograph of Detector and Drum Positioning Apparatus.

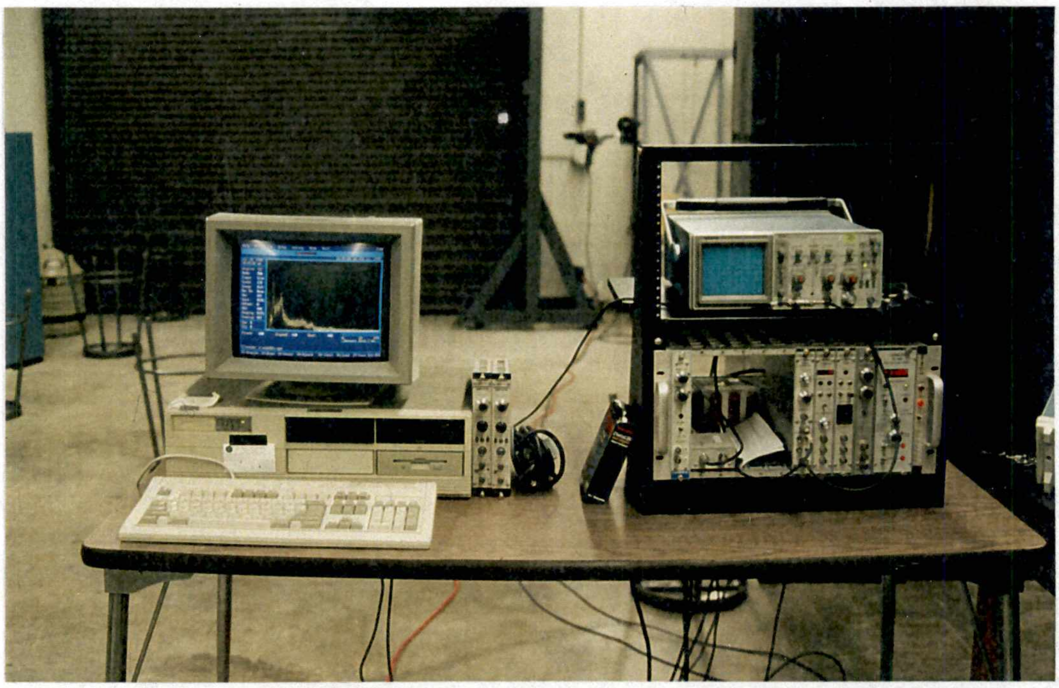

Figure A.2 Photograph of Experimental Electronics.

Appendix B: FORTRAN Reconstruction Routines

Appendix B

FORTRAN Reconstruction Routines

This appendix contains the FORTRAN programs for both the NNLS- and LSMOD-based reconstruction routines. For each, the main program will be listed first, followed by the appropriate subroutine. Note that each is written in standard FORTRAN-77 and was compiled/run under Microsoft FORTRAN version 5.1.

Program 1 - Main NNLS Program

```
c       PROGRAM ECTSCANR.FOR
c       WRITTEN BY KELLY L. AUSBROOKS
c               THE UNIVERSITY OF TENNESSEE, KNOXVILLE
c               THE DEPARTMENT OF NUCLEAR ENGINEERING
c               12 JUNE, 1995
c
c       THIS PROGRAM COMPUTES THE ACTIVITY DISTRIBUTION WITHIN A STANDARD
c       55 GAL. RADIOACTIVE WASTE DRUM USING A NON-NEGATIVE LINEAR LEAST
c       SQUARES TECHNIQUE WITH DETECTOR DATA STEMMING FROM A 2" NAI DETECTOR
c       AND A NUCLEUS (OXFORD) PCA-II MCA.  THE DRUM IS PARTITIONED INTO 54
c       VOXELS EACH HAVING VOLUME OF APPROXIMATELY 1 GALLON.  COORDINATE
c       SYSTEM ORIENTATION HAS THE Z AXIS RUNNING ALONG THE VERTEX OF THE
c       DRUM WITH THE Y AXIS ORIENTED ALONG THE DETECTOR CENTERLINE.  THE
c       POINT SOURCE RESPONSE FUNCTION (PSRF) MATRIX USED FOR THIS PROGRAM
c       HAS BEEN ESTABLISHED USING THE QAD-CGGP POINT-KERNAL SHIELDING CODE.
c       THESE PSRF VALUES ARE DEPENDENT ON SPATIAL LOCATION AND ORIENTATION,
c       SOURCE TYPE, AND MEDIA WITHIN THE DRUM.  AS SUCH, THIS MATRIX IS USED
c       ONLY WITH THE EXPERIMENT DESCRIBED WITHIN THE THESIS WHICH THIS CODE
c       SUPPORTS.  FURTHER INFORMATION ABOUT THE IMPLEMENTATION OF THE CODE
c       CAN BE FOUND THERE.  THE REMAINING COMMENTS DISCUSS VARIABLE AND
c       PARAMETER IDENTIFICATION AND IS PROGRAM SPECIFIC.
c
c
c       VARIABLE IDENTIFICATION
```

```
C
C       ECTFILE = FILE CONTAINING PCA & ASCII FILE NAMES, TIMES, AND PEAK ROI.
C       PSFRFILE = NAME OF FILE CONTAINING M X N PSRF MATRIX.
C       PCAFILE = NAME OF PCA GROSS COUNT SPECTRUM FILE.
C       ASCFILE = NAME OF NEW ASCII NET COUNT SPECTRUM FILE.
C       PSRFUNIT = DERIVED ACTIVITY UNIT FOR PSRF MATRIX.
C       TIME = TIME OF GROSS COUNT.
C       PEAKA = BEGINNING CHANNEL OF PHOTOPEAK ROI.
C       PEAKB = ENDING CHANNEL OF PHOTOPEAK ROI.
C       INTCHL = INTERVAL BETWEEN ASCII CHANNELS. THIS SCENARIO 1.
C       BEGCHL = BEGINNING CHANNEL FOR ASCII CONVERSION. THIS SCENARIO 1.
C       ENDCHL = ENDING CHANNEL FOR ASCII CONVERSION. THIS SCENARIO 8192.
C       IDAT(10000) = ARRAY CONTAINING CONVERTED ASCII COUNT DATA/CHANNEL.
C       PEAKSUM = SUM OF COUNTS IN PEAK ROI. BETWEEN REGION PEAKA & PEAKB.
C       PEAKCHN = SUM OF CHANNELS IN PEAK ROI. PEAKB - PEAKA.
C       COMPBKGD = SUM OF COUNTS IN BOTH COMPTON ROI'S.
C       COMPCHN = SUM OF CHANNELS IN BOTH COMPTON ROI'S.
C       NETTIME = TIME OF NATURAL BACKGROUND COUNT.
C       IPOS = VARIABLE PRESENT IN ASCII CONVERSION.
C       MDA = VALUE OF M. PASSED TO NNLS AND USED TO SIZE AN ARRAY.
C       M = NUMBER OF ROWS IN THE PSRF MATRIX.
C       N = NUMBER OF COLUMNS IN THE PSRF MATRIX.
C       H = USED TO LOAD THE DETECTOR DATA INTO ARRAY B.
C       MODE = NNLS SOLUTION SUCCESS FLAG.
C       D = BEGINNING CHANNEL OF LEFT COMPTON ROI. PEAKA - 120.
C       E = ENDING CHANNEL OF LEFT COMPTON ROI. PEAKA - 20. 100 CHN WIDE.
C       F = BEGINNING CHANNEL OF RIGHT COMPTON ROI. PEAKB + 20.
C       G = ENDING CHANNEL OF RIGHT COMPTON ROI. PEAKB + 120. 100 CHN WIDE.
C       ARRAY(120, 54) = PSRF ARRAY PASSED TO NNLS SUBROUTINE.
C       B(120) = DETECTOR COUNT DATA PASSED TO NNLS SUBROUTINE.
C       X(54) = SOURCE SOLUTION DATA CALCULATED IN NNLS SUBROUTINE.
C       NETPEAK = NET COUNTS IN PHOTOPEAK AFTER COMPTON CONTINUUM SUBTRACTION.
C       SAL = SPECIFIC ACTIVITY IN EACH LAYER OF THE DRUM.
C       SAT = SPECIFIC ACTIVITY OF THE TOTAL DRUM.
C       SCALE = SCALING FACTOR FOR ACCURATE NNLS SOLUTION
C       COMPT = COMPTON CONTINUUM FACTOR BEFORE NINT CONVERSION
C
C       VARIABLE DECLARATION
C
$STORAGE:4
        CHARACTER*25 ECTFILE, PSRFFILE, PCAFILE, ASCFILE
        CHARACTER*8 PSRFUNIT
        CHARACTER*1 DCHR(40000)
        INTEGER*4 TIME, PEAKA, PEAKB, INTCHL, BEGCHL, ENDCHL, INTBKG
        INTEGER*4 IDAT(10000), PEAKSUM, PEAKCHN, COMPBKGD, COMPCHN
        INTEGER*4 NETTIME, IPOS, MDA, M, N, H, MODE, D, E, F, G, L
        INTEGER*4 BKGDCNT(10000), NETPEAK, INDEX(54), XX
        REAL*4 ARRAY(120, 54), B(120), X(54), SCALE, COMPT
        REAL*4 ZZ(120), W(120), RNORM, SAL, SAT, Y(120), Q(120)
        EQUIVALENCE (IDAT(1), DCHR(1))
C
C       USER INPUT OF PROGRAM VARIABLES
C
        PRINT *, 'ENTER NAME OF FILENAME OF ECTSCANR DATA FILE.'
        READ '(A)', ECTFILE
        PRINT *, 'ENTER NAME OF PSRF DATA FILE.'
        READ '(A)', PSRFFILE
        PRINT *, 'ENTER UNITS DEFINED BY PSRF FILE (BQ OR MCI).'
```

```
      READ '(A)', PSRFUNIT
C
C     BINARY TO ASCII CONVERSION ROUTINE W/ NATURAL BACKGROUND SUBTRACTION
C
      PRINT *, 'BEGINNING BINARY (PCA-II) TO ASCII CONVERSION.'
      OPEN (01, FILE = 'DETARAY.ASC', STATUS = 'NEW')
      OPEN (11, FILE = ECTFILE, STATUS = 'OLD')
      DO WHILE (.TRUE.)
            READ (11, 8000, END = 500)PCAFILE,ASCFILE,TIME,PEAKA,PEAKB
            OPEN (21, FILE = PCAFILE, STATUS = 'OLD', FORM = 'BINARY')
            OPEN (31, FILE = ASCFILE, STATUS = 'NEW', FORM = 'FORMATTED')
            PRINT *, 'CONVERTING FILE',PCAFILE
            INTCHL = 1
            BEGCHL = 1
            ENDCHL = 8192
            READ (21)(IDAT(K), K = 1, 128)
            READ (21)(IDAT(K), K = 129, 8320)
C          ISUM = 1
C          DO 100 A = 1, 23
C100              ISUM = ISUM + 2**A
C          WRITE(*, 2000)
            WRITE(31, 2000)
            L = BEGCHL
            DO 300 C = (129+BEGCHL), (129+ENDCHL), INTCHL
                  IPOS = 512 + (C - 128)*4
                  DCHR(IPOS) = ' '
                  IDAT(C) = IDAT(C) - 5.36870912E08
                  IF (PEAKA.EQ.O) THEN
                        P = IDAT(C)
                        BKGDCNT(C) = P
                        NETTIME = TIME
                  END IF
                  IF (PEAKA.NE.O) THEN
                        INTBKG = NINT(BKGDCNT(C)*(TIME/NETTIME))
                        IDAT(C) = IDAT(C) - INTBKG
                  END IF
C               WRITE (*, 4000)L, IDAT(C)
                  WRITE (31, 4000)L, IDAT(C)
C
C     SUBTRACTING COMPTOM CONTINUUM BACKGROUND
C
                  IF (PEAKA.LT.200) GO TO 299
                  D = PEAKA - 110
                  E = PEAKA - 10
                  F = PEAKB + 10
                  G = PEAKB + 110
                  IF (L.GE.D .AND. L.LE.E) THEN
                        COMPBKGD = COMPBKGD + IDAT(C)
                        COMPCHN = COMPCHN + 1
                  END IF
                  IF (L.GE.PEAKA .AND. L.LE.PEAKB) THEN
                        PEAKSUM = PEAKSUM + IDAT(C)
                        PEAKCHN = PEAKB - PEAKA
                  END IF
                  IF (L.GE.F .AND. L.LE.G) THEN
                        COMPBKGD = COMPBKGD + IDAT(C)
                        COMPCHN = COMPCHN + 1
                  END IF
```

```
299             L = L + INTCHL
300          END DO
             IF (PEAKA.NE.0) THEN
             COMPT = (COMPBKGD*(PEAKCHN/COMPCHN))
             NETPEAK = PEAKSUM - NINT(COMPT)
             PRINT *, 'GROSS COUNTS IN PHOTOPEAK =',PEAKSUM
             PRINT *, 'COUNTS IN COMPTON ROIS * RATIO',COMPT
             PRINT *, 'NET NUMBER OF COUNTS IN PHOTOPEAK WINDOW =',NETPEAK
             IF (NETPEAK.LT. 0) THEN
                    XX = 0
                    NETPEAK = XX
             END IF
             WRITE (01, 5000)NETPEAK
             COMPBKGD = 0
             COMPCHN = 0
             PEAKSUM = 0
             END IF
      END DO
500   CONTINUE
      CLOSE (01)
C
C     CALLING NNLS SOLVER ROUTINE AND WRITES SOLUTION ARRAY
C
      OPEN(02, FILE = 'DETARAY.ASC', STATUS = 'OLD')
C     OPEN(03, FILE = 'FACTOR1.TXT', STATUS = 'OLD')
      PRINT *, 'CALLING NNLS SOLVER'
      MDA = 120
      M = 120
      N = 54
      H = 1
      SCALE = 60
      DO WHILE (.TRUE.)
             READ (02,*, END = 600)Y(H)
C          READ (03,*)Q(H)
C          B(H) = Y(H)/Q(H)
             B(H) = Y(H)*SCALE
             H = H + 1
C          PRINT *, B(H)
      END DO
600   CONTINUE
      OPEN (41, FILE = 'ECTOUT.ASC', STATUS = 'NEW')
      OPEN (51, FILE = PSRFFILE, STATUS = 'OLD')
      DO ROW = 1, M
             READ(51, *) (ARRAY(ROW, COL), COL = 1,N)
             DO COL = 1, N
             ARRAY(ROW, COL) = ARRAY(ROW, COL)*(60/3.2)
             END DO
C          PRINT *, (ARRAY(ROW, COL), COL = 1, N)
      END DO
      CALL NNLS(ARRAY, MDA, M, N, B, X, RNORM, W, ZZ, INDEX, MODE)
C
C     PRINTING AND WRITING RESULTS.
C
      SAL = 0.0
      SAT = 0.0
      DO I = 1, N
             WRITE(41, 9000) X(I)
             PRINT *, X(I)
```

```
                SAL = SAL + X(I)
                SAT = SAT + X(I)
                IF (MOD(I*6, 54).EQ.0) THEN
                        PRINT *, 'ACTIVITY IN LAYER',I/9,'=',SAL,PSRFUNIT
                        WRITE(41, 6000)SAL, PSRFUNIT
                        SAL = 0.0
                END IF
        END DO
        WRITE(41, 7000)SAT, PSRFUNIT
        PRINT *, 'TOTAL ACTIVITY IN DRUM =',SAT,PSRFUNIT
        PRINT *, 'SUCCESS-FAIL FLAG'
        PRINT *, '1 - THE SOLUTION HAS BEEN COMPUTED SUCCESSFULLY.'
        PRINT *, '2 - THE DIMENSIONS OF THE PROBLEM ARE BAD.'
        PRINT *, '3 - ITERATION COUNT EXCEEDED.  > 3*N ITERATIONS.'
        PRINT *, 'FLAG NUMBER =',MODE
C
C       FORMAT STATEMENTS
C
2000    FORMAT(' CHANNEL', 4X, 'COUNTS')
4000    FORMAT(' ', I4, ' ', I8)
5000    FORMAT(I10)
6000    FORMAT('ACTIVITY IN LAYER =', 1P, E12.5,A6)
7000    FORMAT('TOTAL DRUM ACTIVITY =', 1P, E12.5,A6)
8000    FORMAT(1X, A12, 1X, A12, 1X, I6, 1X, I5, 1X, I5)
9000    FORMAT(1P, E12.5)
C
C       CLOSING ALL DATA FILES
C
        CLOSE (02)
C       CLOSE (03)
        CLOSE (11)
        CLOSE (21)
        CLOSE (31)
        CLOSE (41)
        CLOSE (51)
C
C       PROGRAM TERMINATED
C
        STOP
        END
```

Subprogram 1 - NNLS Subroutine

```
C------------------------------------------------------------
C
C       SUBROUTINE NNLS
C
C       FROM C.L.LAWSON AND R.J.HANSON,
C       SOLVING LEAST SQUARES PROBLEMS,
C       PAGES 304-308
C
C       TYPED IN BY R. ESTEP, 10-31-88
C       (SEE REFERENCE FOR COMMENTS, USAGE)
C
C       GIVEN AN M BY N MATIX, A, AND AN M-VECTOR, B, COMPUTE AN
C       N-VECTOR, X, WHICH SOLVES THE LEAST SQUARES PROBLEM
C
C               A * X = B  SUBJECT TO  X .GE. 0
C
C       A(),MDA,M,N     MDA IS THE FIRST DIMENSIONING PARAMETER FOR THE
C                       ARRAY, A(). ON ENTRY A() CONTAINS THE M BY N
C                       MATRIX, A.  ON EXIT A() CONTAINS
C                       THE PRODUCT MATRIX, Q*A, WHERE Q IS AN M BY M ORTHOGONAL
C                       MATRIX GENERATED IMPLICITLY BY
C                       THIS SUBROUTINE.
C       B()     ON ENTRY B() CONTAINS THE M-VECTOR, B.  ON EXIT B() CONTAINS
C               Q*B
C       X()     ON ENTRY X() IS UNINITIALIZED. ON EXIT X() WILL
C               CONTAIN THE SOLUTION VECTOR
C       RNORM   ON EXIT RNORM CONTAINS THE EUCLIDEAN NORM OF THE RESIDUAL
C               VECTOR
C       W()     AN N-ARRAY OF WORKING SPACE. ON EXIT W() WILL CONTAIN
C               THE DUAL SOLUTION VECTOR. W WILL SATISFY W(I) = 0.
C               FOR ALL I IN SET P AND W(I) .LE. 0 FOR ALL I IN SET Z
C       ZZ()    AN M-ARRAY OF WORKING SPACE
C       INDEX()         AN INTEGER WORKING ARRAY OF LENGTH AT LEAST N.
C                       ON EXIT THE CONTENTS OF THIS ARRAY DEFINE THE SETS
C                       P AND Z AS FOLLOWS:
C
C                       INDEX(1) THRU INDEX(NSETP) = SET P
C                       INDEX(IZ1) THRU INDEX(IZ2) = SET Z
C                       IZ1 = NSETP + 1 = NPP1
C                       IZ2 = N
C       MODE    THIS IS A SUCCESS-FAILURE FLAG WITH THE FOLLOWING
C               MEANINGS.
C               1       THE SOLUTION HAS BEEN COMPUTED SUCCESSFULLY
C               2       THE DIMENSIONS OF THE PROBLEM ARE BAD
C               3       ITERATION COUNT EXCEEDED. MORE THAN 3*N ITERATIONS.
C
C
C
        SUBROUTINE NNLS (A,MDA,M,N,B,X,RNORM,W,ZZ,INDEX,MODE)
        IMPLICIT REAL*4 (A-H)
        IMPLICIT REAL*4 (O-Z)
        IMPLICIT INTEGER*4 (I-N)
        REAL*4 A(MDA,N), B(M), X(N), W(N), ZZ(M)
```

```
      INTEGER*4 INDEX(N)
      ZERO=0.
      ONE=1.
      TWO=2.
      FACTOR=0.01
C
      MODE=1
      IF (M.GT.0.AND.N.GT.0) GO TO 10
      MODE=2
      RETURN
10    ITER=0
      ITMAX=3*N
C
C           INITIALIZE THE ARRAYS INDEX() AND X().
C
      DO 20 I=1,N
      X(I)=ZERO
20    INDEX(I)=I
C
      IZ2=N
      IZ1=1
      NSETP=0
      NPP1=1
C
C.....................................................................
C                                               PAGE 305
C           *****  MAIN LOOP BEGINS HERE  *****
30    CONTINUE
C           QUIT IF ALL COEFFICIENTS ARE ALREADY IN THE SOLUTION.
C                   OR IF M COLS OF A HAVE BEEN TRIANGULARIZED
C
      IF (IZ1.GT.IZ2.OR.NSETP.GE.M) GO TO 350
C
C           COMPUTE COMPONENTS OF THE DUAL (NEGATIVE GRADIENT) VECTOR W().
C
            DO 50 IZ=IZ1,IZ2
            J=INDEX(IZ)
            SM=ZERO
                  DO 40 L=NPP1,M
40                SM=SM+A(L,J)*B(L)
50          W(J)=SM
60    WMAX=ZERO
            DO 70 IZ=IZ1,IZ2
            J=INDEX(IZ)
            IF(W(J).LE.WMAX) GO TO 70
            WMAX=W(J)
            IZMAX=IZ
70          CONTINUE
C
C                 IF WMAX .LE. 0 GO TO TERMINATION
C                 THIS INDICATES SATISFACTION OF THE KUHN-TUCKER CONDITION
S
C
      IF (WMAX) 350, 350, 80
80    IZ=IZMAX
      J=INDEX(IZ)
C
C     THE SIGN OF W(J) IS OK FOR J TO BE MOVED TO SET P.
```

```
C       BEGIN THE TRANSFORMATION AND CHECK NEW DIAGONAL ELEMENT TO AVOID
C       NEAR LINEAR DEPENDENCE.
C
        ASAVE=A(NPP1,J)
        CALL H12 (1,NPP1,NPP1+1,M,A(1,J),1,UP,DUMMY,1,1,0)
        UNORM=ZERO
        IF(NSETP.EQ.0) GO TO 100
                DO 90 L=1,NSETP
90              UNORM=UNORM+A(L,J)**2
100     UNORM=SQRT(UNORM)
        IF(DIFF(UNORM+ABS(A(NPP1,J))*FACTOR,UNORM)) 130, 130, 110
C
C       COL J IS SUFFICIEANTLY INDEPENDENT. COPY B INTO ZZ, UPDATE ZZ AND
C       SOLVE FOR ZTEST ( = PROPOSED NEW VALUE FOR X(J)).
C
110             DO 120 L=1,M
120             ZZ(L)=B(L)
        CALL H12 (2,NPP1,NPP1+1,M,A(1,J),1,UP,ZZ,1,1,1)
        ZTEST=ZZ(NPP1)/A(NPP1,J)
C
C               SEE IF ZTEST IS POSITIVE
C
        IF (ZTEST) 130, 130, 140
C
C       REJECT J AS A CANDIDATE TO BE MOVED FROM SET Z TO SET P.
C       RESTORE A(NPP1,J), SET W(J)=0., AND LOOP BACK TO TEST DUAL
C       COEFFS AGAIN.
C
130     A(NPP1,J)=ASAVE
        W(J)=0
        GO TO 60
C..................................................................
C                                               PAGE 306
C
C       THE INDEX J=INDEX(IZ) HAS BEEN SELECTED TO BE MOVED FROM
C       SET Z TO SET P.  UPDATE B, UPDATE INDICES, APPLY HOUSEHOLDER
C       TRANSFORMATIONS TO COLS IN NEW SET Z, ZERO SUBDIAGONAL ELTS IN
C       COL J,  SET W(J)=0
C
140     DO 150 L=1,M
150     B(L)=ZZ(L)
C
        INDEX(IZ)=INDEX(IZ1)
        INDEX(IZ1)=J
        IZ1=IZ1+1
c       WRITE(*,1000)J
1000    FORMAT(' ADDING ELEMENT ',I3,' TO MODEL')
        NSETP=NPP1
        NPP1=NPP1+1
C
        IF (IZ1.GT.IZ2) GO TO 170
                DO 160 JZ=IZ1,IZ2
                JJ=INDEX(JZ)
160             CALL H12 (2,NSETP,NPP1,M,A(1,J),1,UP,A(1,JJ),1,MDA,1)
170     CONTINUE
C
        IF(NSETP.EQ.M) GO TO 190
                DO 180 L=NPP1,M
```

```
180        A(L,J)=ZERO
190   CONTINUE
C
      W(J)=0
C                         SOLVE THE TRIANGULAR SYSTEM
C                         STORE THE SOLUTION TEMPORARILY IN ZZ().
      ASSIGN 200 TO NEXT
      GO TO 400
200   CONTINUE
C
C                  ****  SECONDARY LOOP BEGINS HERE   *****
C
C                                 ITERATION COUNTER
C
210   ITER=ITER+1
      IF (ITER.LE.ITMAX) GO TO 220
      MODE = 3
      WRITE(*,440)
      GO TO 350
220   CONTINUE
C
C                         SEE IF ALL NEW CONSTRAINED COEFFS ARE FEASIBLE
C                         IF NOT, COMPUTE ALPHA
C
      ALPHA=2
         DO 240 IP=1,NSETP
         L=INDEX(IP)
         IF (ZZ(IP)) 230,230,240
C
230      T=-X(L)/(ZZ(IP)-X(L))
         IF (ALPHA.LE.T) GO TO 240
         ALPHA=T
         JJ=IP
240      CONTINUE
C
C       IF ALL NEW CONSTRAINED COEFFS ARE FEASIBLE THEN ALPHA WILL
C     STILL = 2.  IF SO, EXIT FROM SECONDARY LOOP TO MAIN LOOP
C
        IF (ALPHA.EQ.TWO)  GO TO 330
C
C                  OTHERWISE USE ALPHA WHICH WILL BE BETWEEN 0. AND 1. TO
C                  INTERPOLATE BETWEEN THE OLD X AND THE NEW ZZ
C
         DO 250 IP=1,NSETP
         L=INDEX(IP)
250      X(L)=X(L)+ALPHA*(ZZ(IP)-X(L))
C
C.....................................................................
C                                          PAGE 307
C
C        MODIFY A AND B AND THE INDEX ARRAYS TO MOVE COEFFICIENT I
C        FROM SET P TO SET Z
C
      I=INDEX(JJ)
260   X(I)=0
c     WRITE(*,1001)I
1001  FORMAT(' DELETING ELEMENT ',I3,' FROM MODEL')
C
```

```
      IF (JJ.EQ.NSETP) GO TO 290
      JJ=JJ+1
            DO 280 J=JJ,NSETP
            II=INDEX(J)
            INDEX(J-1)=II
            CALL G1 (A(J-1,II),A(J,II),CC,SS,A(J-1,II))
            A(J,II)=0
                  DO 270 L=1,N
         IF (L.NE.II) CALL G2(CC,SS,A(J-1,L),A(J,L))
270               CONTINUE
280         CALL G2 (CC,SS,B(J-1),B(J))
290   NPP1=NSETP
      NSETP=NSETP-1
      IZ1=IZ1-1
      INDEX(IZ1)=I
C
C           SEE IF THRE REMAINING COEFFICIENTS IN SET P ARE FEASIBLE. THEY S
HOULD
C           BE BECAUSE OF THE WAY ALPHA WAS DETERMINED.
C           IF ANY ARE INFEASIBLE IT IS DUE TO ROUND-OFF ERROR.  ANY
C           THAT ARE NON-POSITIVE WILL BE SET TO ZERO
C           AND MOVED FROM SET P TO SET Z
C
            DO 300 JJ=1,NSETP
            I=INDEX(JJ)
            IF (X(I))260,260,300
300         CONTINUE
C
C     .           COPY B() INTO ZZ(). THEN SOLVE AGAIN AND LOOP BACK.
C
            DO 310 I=1,M
310         ZZ(I)=B(I)
      ASSIGN 320 TO NEXT
      GO TO 400
320   CONTINUE
      GOTO 210
C                 *****   END OF SECONDARY LOOP   *****
C
330         DO 340 IP=1,NSETP
            I=INDEX(IP)
340         X(I)=ZZ(IP)
C                       ALL NEW COEFFS ARE POSITIVE.  LOOP BACK TO BEGIN
NING.
      GO TO 30
C
C                 ********   END OF MAIN LOOP   ********
C
C           COME TO HERE FOR TERMINATION.
C           COMPUTE THE NORM OF THE FINAL RESIDUAL VECTOR.
C
350   SM=ZERO
      IF (NPP1.GT.M) GO TO 370
            DO 360 I=NPP1,M
360         SM=SM+B(I)**2
      GO TO 390
370         DO 380 J=1,N
380         W(J)=ZERO
390   RNORM=SQRT(SM)
```

```
      RETURN
C
C     THE FOLLOWING BLOCK OF CODE IS USED AS AN INTERNAL SUBROUTINE
C     TO SOLVE THE TRIANGULAR SYSTEM, PUTTING THE SOLUTION IN ZZ().
C
400          DO 430 L=1,NSETP
             IP=NSETP+1-L
             IF (L.EQ.1) GO TO 420
                   DO 410 II=1,IP
410                ZZ(II)=ZZ(II)-A(II,JJ)*ZZ(IP+1)
420          JJ=INDEX(IP)
430          ZZ(IP)=ZZ(IP)/A(IP,JJ)
      GO TO NEXT, (200,320)
440   FORMAT(' NNLS QUITTING ON ITERATION COUNT.')
      END
C------------------------------------------------------------
C
C     SUBROUTINE H12 (MODE,LPIVOT,LI,M,U,IUE,UP,C,ICE,ICV,NCV)
C     C.L.LAWSON AND R.J.HANSON, JPL, 1973 JUN 12
C
C     FROM SOLVING LEAST SQARES PROBLEMS, PAGE 308
C
C     CONSTRUCTION AND/OR APPLICATION OF A SINGLE
C     HOUSEHOLDER TRASNSFORMATION.   Q = I + U*(U**T)/B
C
C     SEE BOOK FOR INSTRUCTIONS
C
      SUBROUTINE H12(MODE,LPIVOT,L1,M,U,IUE,UP,C,ICE,ICV,NCV)
      IMPLICIT REAL*4 (A-H)
      IMPLICIT REAL*4 (O-Z)
      IMPLICIT INTEGER*4 (I-N)
      REAL*4 U(IUE,M), C(1)
      REAL*8 SM,B
      ONE=1.
C
      IF (0.GE.LPIVOT.OR.LPIVOT.GE.L1.OR.L1.GT.M) RETURN
      CL=ABS(U(1,LPIVOT))
      IF (MODE.EQ.2) GO TO 60
C                  **** CONSTRUCT THE TRANSFORMATION  ****
             DO 10 J=L1,M
10           CL=AMAX1(ABS(U(1,J)),CL)
      IF (CL) 130,130,20
20    CLINV=ONE/CL
      SM=(DBLE(U(1,LPIVOT))*CLINV)**2
             DO 30 J=L1,M
30           SM=SM+(DBLE(U(1,J))*CLINV)**2
C                                     CONVERT DBLE. PREC. SM TO SNGL. PREC. SM
      SM1=SM
      CL=CL*SQRT(SM1)
      IF (U(1,LPIVOT))50,50,40
40    CL=-CL
50    UP=U(1,LPIVOT)-CL
      U(1,LPIVOT)=CL
      GO TO 70
C            **** APPLY THE TRANSFORMATION  I + U*(U**T)/B  TO  C ****
C
60    IF (CL) 130,130,70
70    IF (NCV.LE.0) RETURN
```

```
      B=DBLE(UP)*U(1,LPIVOT)
C             B MUST BE NONPOSITIVE HERE. IF B = 0. , RETURN
C
      IF (B) 80,130,130
80    B=ONE/B
      I2=1-ICV+ICE*(LPIVOT-1)
      INCR=ICE*(L1-LPIVOT)
            DO 120 J=1,NCV
            I2=I2+ICV
            I3=I2+INCR
            I4=I3
            SM=C(I2)*DBLE(UP)
                  DO 90 I=L1,M
                  SM=SM+C(I3)*DBLE(U(1,I))
90                I3=I3+ICE
            IF (SM) 100,120,100
100         SM=SM*B
            C(I2)=C(I2)+SM*DBLE(UP)
                  DO 110 I=L1,M
                  C(I4)=C(I4)+SM*DBLE(U(1,I))
110               I4=I4+ICE
120         CONTINUE
130   RETURN
      END
C-----------------------------------------------------------------
C
C     ALSO BY LAWSON AND HANSON, COMIPUTES ORTHOGONAL ROTATION MATRIX
C     PAGE 309
      SUBROUTINE G1 (A,B,COS,SIN,SIG)
      IMPLICIT REAL*4 (A-H)
      IMPLICIT REAL*4 (O-Z)
      IMPLICIT INTEGER*4 (I-N)
C
C
      ZERO=0.
      ONE=1.
      IF (ABS(A).LE.ABS(B)) GO TO 10
      XR=B/A
      YR=SQRT(ONE+XR**2)
      COS=SIGN(ONE/YR,A)
      SIN=COS*XR
      SIG=ABS(A)*YR
      RETURN
C
C
10    IF (B) 20,30,20
20    XR=A/B
      YR=SQRT(ONE+XR**2)
      SIN=SIGN(ONE/YR,B)
      COS=SIN*XR
      SIG=ABS(B)*YR
      RETURN
C
C
30    SIG=ZERO
      COS=ZERO
      SIN=1
      RETURN
```

```
      END
C-----------------------------------------------------------
C
C     ALSO FROM LAWSON AND HANSON, PAGE 309
C
      SUBROUTINE G2 (COS,SIN,X,Y)
      IMPLICIT REAL*4 (A-H)
      IMPLICIT REAL*4 (O-Z)
      IMPLICIT INTEGER*4 (I-N)
      XR=COS*X+SIN*Y
      Y=-SIN*X+COS*Y
      X=XR
      RETURN
      END
C-----------------------------------------------------------
C
C     ALSO FROM LAWSON AND HANSON, PAGE 311
C
      FUNCTION DIFF(X,Y)
      IMPLICIT REAL*4 (A-H)
      IMPLICIT REAL*4 (O-Z)
      IMPLICIT INTEGER*4 (I-N)
      DIFF=X-Y
      RETURN
      END
C-----------------------------------------------------------
C
C
C     SUBROUTINE HFTI, FROM C.LAWSON AND R.HANSON, 1974
C                      SOLVING LEAST SQUARES PROBLEMS
C                      PAGE 290
C                      CALL NO.519,L425S,C.14 LANL LIBRARY
C
C     USES HOUSEHOLDER TRANSFORMATION TO SOLVE
C     GENERAL LINEAR LEAST SQUARES PROBLEM
C
C     TYPED IN BY R. ESTEP, 11-23-88
C
      SUBROUTINE HFTI(A,MDA,M,N,B,MDB,NB,TAU,KRANK,RNORM,H,G,IP)
C
C
C
      IMPLICIT REAL*4 (A-H)
      IMPLICIT REAL*4 (O-Z)
      IMPLICIT INTEGER*4 (I-N)
      REAL*4 B(MDB,NB)
      REAL*4 A(MDA,N),H(N),G(N),RNORM(NB)
      INTEGER*4 IP(N),KP1,IONE,ITWO,I,II,J,K
      REAL*8 SM,DZERO
      SZERO=0.
      DZERO=0.D0
      FACTOR=.001
      IONE=1
      ITWO=2
C
      K=0
      LDIAG=MIN0(M,N)
      IF (LDIAG.LE.0)GO TO 270
```

```
      DO 80 J=1,LDIAG
      IF (J.EQ.1) GO TO 20
C
C     UPDATE SQUARED COLUMN LENGTHS AND FIND LMAX
C
      LMAX=J
        DO 10 L=J,N
        H(L)=H(L)-A(J-1,L)**2
        IF (H(L).GT.H(LMAX)) LMAX=L
10        CONTINUE
      IF(DIFF(HMAX+FACTOR*H(LMAX),HMAX)) 20,20,50
C
C     COMPUTE SQUARED COLUMN LENGTHS AND FIND LMAX
C
20      LMAX=J
        DO 40 L=J,N
        H(L)=0
          DO 30 I=J,M
30          H(L)=H(L)+A(I,L)**2
        IF (H(L).GT.H(LMAX)) LMAX=L
40        CONTINUE
      HMAX=H(LMAX)
C
C     LMAX HAS BEEN DETERMINED
C
C     DO COLUMN INTERCHANGES IF NEEDED
C
50      CONTINUE
      IP(J)=LMAX
      IF (IP(J).EQ.J) GO TO 70
        DO 60 I=1,M
        TMP=A(I,J)
        A(I,J)=A(I,LMAX)
60        A(I,LMAX)=TMP
      H(LMAX)=H(J)
C
C     COMPUTE THE JTH TRANSFORMATION AND APPLY IT TO A AND B
C
70     CALL H12 (IONE,J,J+1,M,A(1,J),IONE,H(J),A(1,J+1),IONE,MDA,N-J)
80     CALL H12 (ITWO,J,J+1,M,A(1,J),IONE,H(J),B,IONE,MDB,NB)
C
C     DETERMINE THE PSEUDORANK, K, USING THE TOLERANCE, TAU
C
      DO 90 J=1,LDIAG
      IF (ABS(A(J,J)).LE.TAU) GOTO 100
90      CONTINUE
     K=LDIAG
     GOTO 110
100   K=J-1
110   KP1=K+1
C
C     COMPUTE THE NORMS OF THE RESIDUAL VECTORS
C
     IF (NB.LE.0) GO TO 140
       DO 130 JB=1,NB
       TMP=SZERO
       IF (KP1.GT.M) GO TO 130
         DO 120 I=KP1,M
```

```
120           TMP=TMP+B(I,JB)**2
130        RNORM(JB)=SQRT(TMP)
140     CONTINUE
C                       SPECIAL FOR PSEUDORANK = O
      IF (K.GT.O) GO TO 160
      IF (NB.LE.O) GO TO 270
        DO 150 JB=1,NB
          DO 150 I=1,N
150         B(I,JB)=SZERO
      GO TO 270
C
C      IF THE PSEUDORANK IS LESS THAN N COMPUTE HOUSEHOLDER
C      DECOMPOSITION OF FIRST K ROWS.
C
160     IF (K.EQ.N) GO TO 180
        DO 170 II=1,K
        I=KP1-II
170     CALL H12 (IONE,I,KP1,N,A(I,1),MDA,G(I),A,MDA,IONE,I-1)
180     CONTINUE
C
C
      IF (NB.LE.O) GO TO 270
        DO 260 JB=1,NB
C
C      SOLVE THE K BY K TRIANGULAR SYSTEM
C
          DO 210 L=1,K
          SM=DZERO
          I=KP1-L
          IF (I.EQ.K) GO TO 200
          IP1=I+1
            DO 190 J=IP1,K
190           SM=SM+A(I,J)*DBLE(B(J,JB))
200         SM1=SM
210         B(I,JB)=(B(I,JB)-SM1)/A(I,I)
C
C      COMPLETE COMPUTATION OF SOLUTION VECTOR
C
        IF (K.EQ.N) GO TO 240
          DO 220 J=KP1,N
220         B(J,JB)=SZERO
          DO 230 I=1,K
230     CALL H12 (ITWO,I,KP1,N,A(I,1),MDA,G(I),B(1,JB),IONE,MDB,IONE)
C
C      RE-ORDER THE SOLUTION VECTOR TO COMPENSATE FOR THE
C      COLUMN INTERCHANGES
C
240         DO 250 JJ=1,LDIAG
          J=LDIAG+1-JJ
          IF (IP(J).EQ.J) GO TO 250
          L=IP(J)
          TMP=B(L,JB)
          B(L,JB)=B(J,JB)
          B(J,JB)=TMP
250         CONTINUE
260        CONTINUE
C
C      THE SOLUTION VECTORS, X, ARE NOW
```

```
C      IN THE FIRST N ROWS OF THE ARRAY B(,).
C
270     KRANK=K
      RETURN
      END
C--------------------------------------------------------
```

Program 2 - Main LSMOD Program

```
c       PROGRAM ECTLSMD.FOR
c       WRITTEN BY KELLY L. AUSBROOKS
c               THE UNIVERSITY OF TENNESSEE, KNOXVILLE
c               THE DEPARTMENT OF NUCLEAR ENGINEERING
c               17 JUNE, 1995
c
c       THIS PROGRAM COMPUTES THE ACTIVITY DISTRIBUTION WITHIN A STANDARD
c       55 GAL. RADIOACTIVE WASTE DRUM USING A SIMPLIFIED LINEAR LEAST
c       SQUARES TECHNIQUE WITH DETECTOR DATA STEMMING FROM A 2" NAI DETECTOR
c       AND A NUCLEUS (OXFORD) PCA-II MCA. THE DRUM IS PARTITIONED INTO 54
c       VOXELS EACH HAVING VOLUME OF APPROXIMATELY 1 GALLON. COORDINATE
c       SYSTEM ORIENTATION HAS THE Z AXIS RUNNING ALONG THE VERTEX OF THE
c       DRUM WITH THE Y AXIS ORIENTED ALONG THE DETECTOR CENTERLINE. THE
c       POINT SOURCE RESPONSE FUNCTION (PSRF) MATRIX USED FOR THIS PROGRAM
c       HAS BEEN ESTABLISHED USING THE QAD-CGGP POINT-KERNAL SHIELDING CODE.
c       THESE PSRF VALUES ARE DEPENDENT ON SPATIAL LOCATION AND ORIENTATION,
c       SOURCE TYPE, AND MEDIA WITHIN THE DRUM. AS SUCH, THIS MATRIX IS USED
c       ONLY WITH THE EXPERIMENT DESCRIBED WITHIN THE THESIS WHICH THIS CODE
c       SUPPORTS. FURTHER INFORMATION ABOUT THE IMPLEMENTATION OF THE CODE
c       CAN BE FOUND THERE. THE REMAINING COMMENTS DISCUSS VARIABLE AND
c       PARAMETER IDENTIFICATION AND IS PROGRAM SPECIFIC.
c
c
c       VARIABLE IDENTIFICATION
c
c       ECTFILE = FILE CONTAINING PCA & ASCII FILE NAMES, TIMES, AND PEAK ROI.
c       PSFRFILE = NAME OF FILE CONTAINING M X N PSRF MATRIX.
c       PCAFILE = NAME OF PCA GROSS COUNT SPECTRUM FILE.
c       ASCFILE = NAME OF NEW ASCII NET COUNT SPECTRUM FILE.
c       PSRFUNIT = DERIVED ACTIVITY UNIT FOR PSRF MATRIX.
c       TIME = TIME OF GROSS COUNT.
c       PEAKA = BEGINNING CHANNEL OF PHOTOPEAK ROI.
c       PEAKB = ENDING CHANNEL OF PHOTOPEAK ROI.
c       INTCHL = INTERVAL BETWEEN ASCII CHANNELS. THIS SCENARIO 1.
c       BEGCHL = BEGINNING CHANNEL FOR ASCII CONVERSION. THIS SCENARIO 1.
c       ENDCHL = ENDING CHANNEL FOR ASCII CONVERSION. THIS SCENARIO 8192.
c       IDAT(10000) = ARRAY CONTAINING CONVERTED ASCII COUNT DATA/CHANNEL.
c       PEAKSUM = SUM OF COUNTS IN PEAK ROI. BETWEEN REGION PEAKA & PEAKB.
c       PEAKCHN = SUM OF CHANNELS IN PEAK ROI. PEAKB - PEAKA.
c       COMPBKGD = SUM OF COUNTS IN BOTH COMPTON ROI'S.
c       COMPCHN = SUM OF CHANNELS IN BOTH COMPTON ROI'S.
c       NETTIME = TIME OF NATURAL BACKGROUND COUNT.
c       IPOS = VARIABLE PRESENT IN ASCII CONVERSION.
c       MDA = VALUE OF M. PASSED TO LSMOD AND USED TO SIZE AN ARRAY.
c       N = NUMBER OF ROWS IN THE PSRF MATRIX.
c       M = NUMBER OF COLUMNS IN THE PSRF MATRIX.
c       H = USED TO LOAD THE DETECTOR DATA INTO ARRAY B.
c       D = BEGINNING CHANNEL OF LEFT COMPTON ROI. PEAKA - 120.
c       E = ENDING CHANNEL OF LEFT COMPTON ROI. PEAKA - 20. 100 CHN WIDE.
c       F = BEGINNING CHANNEL OF RIGHT COMPTON ROI. PEAKB + 20.
c       G = ENDING CHANNEL OF RIGHT COMPTON ROI. PEAKB + 120. 100 CHN WIDE.
c       A(120, 54) = PSRF ARRAY PASSED TO LSMOD SUBROUTINE.
c       Y(120) = DETECTOR COUNT DATA PASSED TO LSMOD SUBROUTINE.
```

```
C       P(54) = SOURCE SOLUTION DATA CALCULATED IN LSMOD SUBROUTINE.
C       NETPEAK = NET COUNTS IN PHOTOPEAK AFTER COMPTON CONTINUUM SUBTRACTION.
C       SAL = SPECIFIC ACTIVITY IN EACH LAYER OF THE DRUM.
C       SAT = SPECIFIC ACTIVITY OF THE TOTAL DRUM.
C       SCALE = SCALING FACTOR FOR ACCURATE LSMOD SOLUTION
C       COMPT = COMPTON CONTINUUM FACTOR BEFORE NINT CONVERSION
C
C       VARIABLE DECLARATION
C
$STORAGE:4
        CHARACTER*25 ECTFILE, PSRFFILE, PCAFILE, ASCFILE, OUTFILE, LSFILE
        CHARACTER*8  PSRFUNIT
        CHARACTER*1 DCHR(40000)
        INTEGER*4 TIME, PEAKA, PEAKB, INTCHL, BEGCHL, ENDCHL, INTBKG
        INTEGER*4 IDAT(10000), PEAKSUM, PEAKCHN, COMPBKGD, COMPCHN
        INTEGER*4 NETTIME, IPOS, MDA, M, N, H, MODE, D, E, F, G, L, X
        INTEGER*4 BKGDCNT(10000), NETPEAK, INDEX(54), B(120), S, T,TEMP
        INTEGER*4 ROW, COL, ISUM, C
        REAL*4 A(120, 54), Y(120), P(54), SCALE, COMPT, VY(120, 120)
        REAL*4 SAL, SAT
        EQUIVALENCE (IDAT(1), DCHR(1))
C
C       USER INPUT OF PROGRAM VARIABLES
C
        PRINT *, 'ENTER NAME OF FILENAME OF ECTLSMD DATA FILE.'
        READ '(A)', ECTFILE
        PRINT *, 'ENTER NAME OF PSRF DATA FILE.'
        READ '(A)', PSRFFILE
        PRINT *, 'ENTER UNITS DEFINED BY PSRF FILE (BQ OR MCI).'
        READ '(A)', PSRFUNIT
C
C       BINARY TO ASCII CONVERSION ROUTINE W/ NATURAL BACKGROUND SUBTRACTION
C
        PRINT *, 'BEGINNING BINARY (PCA-II) TO ASCII CONVERSION.'
        OPEN (01, FILE = 'DETARAY.ASC', STATUS = 'NEW')
        OPEN (11, FILE = ECTFILE, STATUS = 'OLD')
        DO WHILE (.TRUE.)
                READ (11, 8000, END = 500)PCAFILE,ASCFILE,TIME,PEAKA,PEAKB
                OPEN (21, FILE = PCAFILE, STATUS = 'OLD', FORM = 'BINARY')
                OPEN (31, FILE = ASCFILE, STATUS = 'NEW', FORM = 'FORMATTED')
                PRINT *, 'CONVERTING FILE',PCAFILE
                INTCHL = 1
                BEGCHL = 1
                ENDCHL = 8192
                READ (21)(IDAT(K), K = 1, 128)
                READ (21)(IDAT(K), K = 129, 8320)
C             ISUM = 1
C             DO 100 A = 1, 23
C100                  ISUM = ISUM + 2**A
C             WRITE(*, 2000)
                WRITE(31, 2000)
                L = BEGCHL
                DO 300 C = (129+BEGCHL), (129+ENDCHL), INTCHL
                        IPOS = 512 + (C - 128)*4
                        DCHR(IPOS) = ''
                        IDAT(C) = IDAT(C) - 5.36870912E08
                        IF (PEAKA.EQ.0) THEN
                                X = IDAT(C)
```

```
                                BKGDCNT(C) = X
                                NETTIME = TIME
                        END IF
                        IF (PEAKA.NE.0) THEN
                                INTBKG = NINT(BKGDCNT(C)*(TIME/NETTIME))
                                IDAT(C) = IDAT(C) - INTBKG
                        END IF
C                   WRITE (*, 4000)L, IDAT(C)
                        WRITE (31, 4000)L, IDAT(C)
C
C       SUBTRACTING COMPTOM CONTINUUM BACKGROUND
C
                        IF (PEAKA.LT.110) GO TO 299
                        D = PEAKA - 110
                        E = PEAKA - 10
                        F = PEAKB + 10
                        G = PEAKB + 110
                        IF (L.GE.D .AND. L.LE.E) THEN
                                COMPBKGD = COMPBKGD + IDAT(C)
                                COMPCHN = COMPCHN + 1
                        END IF
                        IF (L.GE.PEAKA .AND. L.LE.PEAKB) THEN
                                PEAKSUM = PEAKSUM + IDAT(C)
                                PEAKCHN = PEAKB - PEAKA
                        END IF
                        IF (L.GE.F .AND. L.LE.G) THEN
                                COMPBKGD = COMPBKGD + IDAT(C)
                                COMPCHN = COMPCHN + 1
                        END IF
299                   L = L + INTCHL
300             END DO
                  IF (PEAKA.NE.0) THEN
C               COMPT = (COMPBKGD*(PEAKCHN/COMPCHN))
                  COMPT = 0.0
                  NETPEAK = PEAKSUM - NINT(COMPT)
                  PRINT *, 'GROSS COUNTS IN PHOTOPEAK =',PEAKSUM
                  PRINT *, 'COUNTS IN COMPTON ROIs',COMPBKGD
                  IF (NETPEAK.LT. 0) THEN
                        TEMP = 0
                        NETPEAK = TEMP
                  END IF
                  PRINT *, 'NET NUMBER OF COUNTS IN PHOTOPEAK WINDOW =',NETPEAK
                  WRITE (01, 5000)NETPEAK
                  COMPBKGD = 0
                  COMPCHN = 0
                  PEAKSUM = 0
                  END IF
        END DO
500     CONTINUE
        CLOSE (01)
C
C       CALLING LSMOD SOLVER ROUTINE AND WRITES SOLUTION ARRAY
C
        OPEN(02, FILE = 'DETARAY.ASC', STATUS = 'OLD')
        PRINT *, 'CALLING LSMOD SOLVER'
        MDA = 120
        N = 120
        M = 54
```

```
        H = 1
        SCALE = 15
        DO WHILE (.TRUE.)
                READ(02,*, END = 600)B(H)
                Y(H) = B(H)*SCALE
C             PRINT *, Y(H)
                H = H + 1
        END DO
600     CONTINUE
C
C      CREATING COVARIANCE MATRIX TO PASS TO LSMOD
C
        DO S = 1, N
                DO T = 1, N
                        IF (S .EQ. T) THEN
                                VY(S,T) = Y(S)
C                        PRINT *, VY(S,T)
                                GOTO 601
                        ELSE
                                VY(S,T) = 0
                        END IF
                END DO
601     CONTINUE
        END DO
C
C      CALLING LSMOD
C
        LSFILE = 'LSMDOUT.ASC'
        OUTFILE = 'ECTOUT.ASC'
        OPEN (41, FILE = OUTFILE, STATUS = 'NEW')
        OPEN (51, FILE = PSRFFILE, STATUS = 'OLD')
        DO ROW = 1, N
                READ(51, *) (A(ROW, COL), COL = 1, M)
                DO COL = 1,M
                        A(ROW,COL) = A(ROW,COL)*(60/3.2)
                END DO
        END DO
        CALL LSMD(A, VY, Y, N, M, LSFILE, P)
C
C      PRINTING AND WRITING RESULTS.
C
        DO I = 1, M
                IF (P(I).LT.0.0) P(I) = 0.0
                WRITE(41, 9000) P(I)
                SAL = SAL + P(I)
                SAT = SAT + SAL
                IF (MOD(I*6, 54).EQ.0) THEN
                        PRINT *, 'ACTIVITY IN LAYER',I/9,'=',SAL,PSRFUNIT
                        WRITE(41, 6000)SAL, PSRFUNIT
                        SAL = 0.0
                END IF
        END DO
        WRITE(41, 7000)SAT, PSRFUNIT
C
C      FORMAT STATEMENTS
C
2000    FORMAT(' CHANNEL', 4X, 'COUNTS')
4000    FORMAT(' ', I4, ' ', I8)
```

```
5000    FORMAT(I10)
6000    FORMAT('ACTIVITY IN LAYER =',1P, E12.5,A6)
7000    FORMAT('TOTAL DRUM ACTIVITY =',1P,E12.5,A6)
8000    FORMAT(1X, A12, 1X, A12, 1X, I6, 1X, I5, 1X, I5)
9000    FORMAT(1P,E12.5)
C
C      CLOSING ALL DATA FILES
C
        CLOSE (02)
        CLOSE (11)
        CLOSE (21)
        CLOSE (31)
        CLOSE (41)
        CLOSE (51)
C
C      PROGRAM TERMINATED
C
        STOP
        END
```

Subprogram 2 - LSMOD Subroutine

```
      SUBROUTINE LSMD(A, VY, Y, N, M, LSFILE, P)
C       SUBROUTINE LSMOD
C
C     IBM PC - D.L. SMITH AND R.T. MAINARDI - 17 JULY 1988
C
C     REVISED 12/18/92. ALTERED I/O AND LEAST-SQUARES ROUTINE.
C
C     ALTERED 17 JUNE, 1995 KELLY L. AUSBROOKS
C     CHANGED INPUT TO ALLOW USE AS A SUBROUTINE.  CALL PASSES ARRAYS
C     AND VALUES INSTEAD OF READING INPUT.
C
C
       REAL Y(120), EY(120), CY(120,120), VY(120,120), VYI(120,120)
       REAL P(54), EP(54), CP(54,54), VP(54,54), VPI(54,54), A(120,54)
       REAL QN(120), WN(120,121), QM(54), WM(54,55)
       INTEGER NTEST
       CHARACTER*25 LSFILE
C
C     INITIALIZATION AND CONTROL
C
      OPEN(5, FILE=LSFILE, STATUS= 'NEW')
 12    FORMAT (6E12.6)
C
C     ORDINARY LEAST-SQUARES ANALYSIS
C
      DO 1004 I=1,N
 1004 EY(I)=SQRT(VY(I,I))
      DO 1005 I=1,N
      DO 1005 J=1,N
 1005 CY(I,J)=VY(I,J)/EY(I)/EY(J)
      CALL MATINV(QN,VY,VYI,WN,NTEST,N,120,121)
      IF(NTEST.EQ.1) GO TO 1009
 1007 WRITE(*,1008)
 1008 FORMAT(' NO INV'/)
      STOP
 1009 DO 1010 I=1,M
      DO 1010 J=1,M
      VPI(I,J)=0.0
      DO 1010 K2=1,N
      DO 1010 K1=1,N
 1010 VPI(I,J)=VPI(I,J)+A(K2,I)*VYI(K2,K1)*A(K1,J)
      CALL MATINV(QM,VPI,VP,WM,NTEST,M,54,55)
      IF(NTEST.EQ.0) GO TO 1007
      DO 1011 I=1,M
      P(I)=0.0
      DO 1011 K3=1,M
      DO 1011 K2=1,N
      DO 1011 K1=1,N
 1011 P(I)=P(I)+VP(I,K3)*A(K2,K3)*VYI(K2,K1)*Y(K1)
      DO 1012 I=1,M
 1012 EP(I)=SQRT(VP(I,I))
      DO 1013 I=1,M
      DO 1013 J=1,M
```

```
 1013 CP(I,J)=VP(I,J)/EP(I)/EP(J)
      DO 1014 I=1,N
      QN(I)=Y(I)
      DO 1014 K1=1,M
 1014 QN(I)=QN(I)-A(I,K1)*P(K1)
      CHI2=0.0
      DO 1015 K2=1,N
      DO 1015 K1=1,N
 1015 CHI2=CHI2+QN(K2)*VYI(K2,K1)*QN(K1)
      CHI2NM=CHI2/FLOAT(N-M)
C
C      PRINT OUTPUT TO FILE (UNIT 5)
C
      WRITE(5,40)
   40 FORMAT(' Y')
   41 WRITE(5,12) (Y(I),I=1,N)
      WRITE(5,410)
  410 FORMAT(' EY')
      WRITE(5,12) (EY(I),I=1,N)
      WRITE(5,411)
  411 FORMAT(' VY')
      DO 412 I=1,N
  412 WRITE(5,12) (VY(I,J),J=1,I)
      WRITE(5,43)
   43 FORMAT(' CY')
      DO 44 I=1,N
   44 WRITE(5,12) (CY(I,J),J=1,I)
      WRITE(5,441)
  441 FORMAT(' A')
      DO 442 I=1,N
  442 WRITE(5,12) (A(I,J),J=1,M)
      WRITE (5,45)
   45 FORMAT(' P')
      WRITE(5,12) (P(I),I=1,M)
      WRITE(5,451)
  451 FORMAT(' EP')
      WRITE(5,12) (EP(I),I=1,M)
      WRITE(5,452)
  452 FORMAT(' VP')
      DO 453 I=1,M
  453 WRITE(5,12) (VP(I,J),J=1,I)
      WRITE(5,47)
   47 FORMAT(' CP')
      DO 48 I=1,M
   48 WRITE(5,12) (CP(I,J),J=1,I)
      WRITE(5,49)
   49 FORMAT(' CHI2,CHI2NM')
      WRITE(5,12) CHI2,CHI2NM
      RETURN
      CLOSE (5)
      END
C
      SUBROUTINE MATINV(B,D,Q,E,NTEST,NS,NARA,NMAX)
      DIMENSION B(NARA),D(NARA,NARA),Q(NARA,NARA),E(NARA,NMAX)
      IP=NS+1
      BIG=0.0
      DO 555 I=1,NS
      DO 555 J=1,NS
```

```
      ABD=ABS(D(I,J))
      IF(ABD-BIG) 555,555,554
  554 BIG=ABD
  555 CONTINUE
      FACT=SQRT(BIG)
      I=1
    1 IF(I-NS) 2,2,20
    2 J=1
    3 IF(J-NS) 4,4,8
    4 K=1
    5 IF(K-NS) 6,6,7
    6 E(J,K)=D(K,J)/FACT
      K=K+1
      GO TO 5
    7 J=J+1
      GO TO 3
    8 L=1
    9 IF(L-NS) 10,10,14
   10 IF(L-I) 11,13,11
   11 E(L,IP)=0.0
   12 L=L+1
      GO TO 9
   13 E(L,IP)=1.0
      GO TO 12
   14 CALL JORDAN(B,E,NTEST,NS,NARA,NMAX)
      IF(NTEST) 15,15,16
   15 RETURN
   16 M=1
   17 IF(M-NS) 18,18,19
   18 Q(I,M)=E(M,IP)/FACT
      M=M+1
      GO TO 17
   19 I=I+1
      GO TO 1
   20 RETURN
      END
C
      SUBROUTINE JORDAN(B,C,INDEX,N,NARA,NMAX)
C
C      SUBROUTINE JORDAN SOLVES A SYSTEM OF LINEAR NONHOMOGENEOUS
C      EQUATIONS BY THE METHOD OF GAUSS-JORDAN REDUCTION. IF THE SYSTEM
C      FAILS TO HAVE A SOLUTION, A FLAG IS SET WHICH SIGNALS THE MAIN
C      PROGRAM.
C
      DIMENSION B(NARA),C(NARA,NMAX)
      K=1
    1 IF(K-N) 2,2,22
    2 IF(C(K,K)) 10,3,10
    3 L=K+1
    4 IF(L-N) 5,5,21
    5 IF(C(L,K)) 7,6,7
    6 L=L+1
      GO TO 4
    7 M=1
    8 IF(M-N-1) 9,9,2
    9 B(M)=C(K,M)
      C(K,M)=C(L,M)
      C(L,M)=B(M)
```

```
   M=M+1
   GO TO 8
10 J=N+1
11 IF(J-K) 13,12,12
12 C(K,J)=C(K,J)/C(K,K)
   J=J-1
   GO TO 11
13 I=1
14 IF(I-N) 16,16,15
15 K=K+1
   GO TO 1
16 IF(I-K) 18,17,18
17 I=I+1
   GO TO 14
18 II=N+1
19 IF(II-K) 17,20,20
20 C(I,II)=C(I,II)-C(I,K)*C(K,II)
   II=II-1
   GO TO 19
21 INDEX=0
   GO TO 23
22 INDEX=1
23 RETURN
   END
```

Appendix C

Input Files for Reconstruction Routines

Appendix C: Input File for Reconstruction Routines

This section contains the input files used for both reconstruction routines. Each is a fixed-format ASCII file which is read in the initial stages of the programs. Note that both reconstruction routines utilize the same input file. Information contained within these files include: spectra file name, ASCII file name, peak window channels, and count time.

Input File for Run 1

```
 backgrd.spm  backgrd.asc 151362     0     0
run7d11a.spm r2000d1a.asc     60  3200  3800
run7d21a.spm r2000d2a.asc     60  3200  3800
run7d31a.spm r2000d3a.asc     60  3200  3800
run7d41a.spm r2000d4a.asc     60  3200  3800
run7d51a.spm r2000d5a.asc     60  3200  3800
run7d11b.spm r2000d1b.asc     60  3200  3800
run7d21b.spm r2000d2b.asc     60  3200  3800
run7d31b.spm r2000d3b.asc     60  3200  3800
run7d41b.spm r2000d4b.asc     60  3200  3800
run7d51b.spm r2000d5b.asc     60  3200  3800
run7d11c.spm r2000d1c.asc     60  3200  3800
run7d21c.spm r2000d2c.asc     60  3200  3800
run7d31c.spm r2000d3c.asc     60  3200  3800
run7d41c.spm r2000d4c.asc     60  3200  3800
run7d51c.spm r2000d5c.asc     60  3200  3800
run7d11d.spm r2000d1d.asc     60  3200  3800
run7d21d.spm r2000d2d.asc     60  3200  3800
run7d31d.spm r2000d3d.asc     60  3200  3800
run7d41d.spm r2000d4d.asc     60  3200  3800
run7d51d.spm r2000d5d.asc     60  3200  3800
run7d11e.spm r2000d1e.asc     60  3200  3800
run7d21e.spm r2000d2e.asc     60  3200  3800
run7d31e.spm r2000d3e.asc     60  3200  3800
run7d41e.spm r2000d4e.asc     60  3200  3800
run7d51e.spm r2000d5e.asc     60  3200  3800
run7d11f.spm r2000d1f.asc     60  3200  3800
run7d21f.spm r2000d2f.asc     60  3200  3800
run7d31f.spm r2000d3f.asc     60  3200  3800
run7d41f.spm r2000d4f.asc     60  3200  3800
run7d51f.spm r2000d5f.asc     60  3200  3800
run8d11a.spm r2090d1a.asc     60  3200  3800
run8d21a.spm r2090d2a.asc     60  3200  3800
run8d31a.spm r2090d3a.asc     60  3200  3800
run8d41a.spm r2090d4a.asc     60  3200  3800
run8d51a.spm r2090d5a.asc     60  3200  3800
run8d11b.spm r2900d1b.asc     60  3200  3800
run8d21b.spm r2090d2b.asc     60  3200  3800
run8d31b.spm r2090d3b.asc     60  3200  3800
run8d41b.spm r2090d4b.asc     60  3200  3800
run8d51b.spm r2090d5b.asc     60  3200  3800
run8d11c.spm r2090d1c.asc     60  3200  3800
run8d21c.spm r2090d2c.asc     60  3200  3800
run8d31c.spm r2090d3c.asc     60  3200  3800
run8d41c.spm r2090d4c.asc     60  3200  3800
run8d51c.spm r2090d5c.asc     60  3200  3800
run8d11d.spm r2090d1d.asc     60  3200  3800
run8d21d.spm r2090d2d.asc     60  3200  3800
```

run8d31d.spm	r2090d3d.asc	60	3200	3800
run8d41d.spm	r2090d4d.asc	60	3200	3800
run8d51d.spm	r2090d5d.asc	60	3200	3800
run8d11e.spm	r2090d1e.asc	60	3200	3800
run8d21e.spm	r2090d2e.asc	60	3200	3800
run8d31e.spm	r2090d3e.asc	60	3200	3800
run8d41e.spm	r2090d4e.asc	60	3200	3800
run8d51e.spm	r2090d5e.asc	60	3200	3800
run8d11f.spm	r2090d1f.asc	60	3200	3800
run8d21f.spm	r2090d2f.asc	60	3200	3800
run8d31f.spm	r2090d3f.asc	60	3200	3800
run8d41f.spm	r2090d4f.asc	60	3200	3800
run8d51f.spm	r2090d5f.asc	60	3200	3800
run9d11a.spm	r2180d1a.asc	60	3200	3800
run9d21a.spm	r2180d2a.asc	60	3200	3800
run9d31a.spm	r2180d3a.asc	60	3200	3800
run9d41a.spm	r2180d4a.asc	60	3200	3800
run9d51a.spm	r2180d5a.asc	60	3200	3800
run9d11b.spm	r2180d1b.asc	60	3200	3800
run9d21b.spm	r2180d2b.asc	60	3200	3800
run9d31b.spm	r2180d3b.asc	60	3200	3800
run9d41b.spm	r2180d4b.asc	60	3200	3800
run9d51b.spm	r2180d5b.asc	60	3200	3800
run9d11c.spm	r2180d1c.asc	60	3200	3800
run9d21c.spm	r2180d2c.asc	60	3200	3800
run9d31c.spm	r2180d3c.asc	60	3200	3800
run9d41c.spm	r2180d4c.asc	60	3200	3800
run9d51c.spm	r2180d5c.asc	60	3200	3800
run9d11d.spm	r2180d1d.asc	60	3200	3800
run9d21d.spm	r2180d2d.asc	60	3200	3800
run9d31d.spm	r2180d3d.asc	60	3200	3800
run9d41d.spm	r2180d4d.asc	60	3200	3800
run9d51d.spm	r2180d5d.asc	60	3200	3800
run9d11e.spm	r2180d1e.asc	60	3200	3800
run9d21e.spm	r2180d2e.asc	60	3200	3800
run9d31e.spm	r2180d3e.asc	60	3200	3800
run9d41e.spm	r2180d4e.asc	60	3200	3800
run9d51e.spm	r2180d5e.asc	60	3200	3800
run9d11f.spm	r2180d1f.asc	60	3200	3800
run9d21f.spm	r2180d2f.asc	60	3200	3800
run9d31f.spm	r2180d3f.asc	60	3200	3800
run9d41f.spm	r2180d4f.asc	60	3200	3800
run9d51f.spm	r2180d5f.asc	60	3200	3800
run10d1a.spm	r2270d1a.asc	60	3200	3800
run10d2a.spm	r2270d2a.asc	60	3200	3800
run10d3a.spm	r2270d3a.asc	60	3200	3800
run10d4a.spm	r2270d4a.asc	60	3200	3800
run10d5a.spm	r2270d5a.asc	60	3200	3800
run10d1a.spm	r2270d1b.asc	60	3200	3800
run10d2b.spm	r2270d2b.asc	60	3200	3800
run10d3b.spm	r2270d3b.asc	60	3200	3800
run10d4b.spm	r2270d4b.asc	60	3200	3800

run10d5b.spm	r2270d5b.asc	60	3200	3800
run10d1c.spm	r2270d1c.asc	60	3200	3800
run10d2c.spm	r2270d2c.asc	60	3200	3800
run10d3c.spm	r2270d3c.asc	60	3200	3800
run10d4c.spm	r2270d4c.asc	60	3200	3800
run10d5c.spm	r2270d5c.asc	60	3200	3800
run10d1d.spm	r2270d1d.asc	60	3200	3800
run10d2d.spm	r2270d2d.asc	60	3200	3800
run10d3d.spm	r2270d3d.asc	60	3200	3800
run10d4d.spm	r2270d4d.asc	60	3200	3800
run10d5d.spm	r2270d5d.asc	60	3200	3800
run10d1e.spm	r2270d1e.asc	60	3200	3800
run10d2e.spm	r2270d2e.asc	60	3200	3800
run10d3e.spm	r2270d3e.asc	60	3200	3800
run10d4e.spm	r2270d4e.asc	60	3200	3800
run10d5e.spm	r2270d5e.asc	60	3200	3800
run10d1f.spm	r2270d1f.asc	60	3200	3800
run10d2f.spm	r2270d2f.asc	60	3200	3800
run10d3f.spm	r2270d3f.asc	60	3200	3800
run10d4f.spm	r2270d4f.asc	60	3200	3800
run10d5f.spm	r2270d5f.asc	60	3200	3800

Input File for Run 2

```
 backgrd.spm  backgrd.asc 151462    0     0
runl4dla.spm r3000dla.asc     60  2800  3400
runl4d2a.spm r3000d2a.asc     60  2800  3400
runl4d3a.spm r3000d3a.asc     60  2800  3400
runl4d4a.spm r3000d4a.asc     60  2800  3400
runl4d5a.spm r3000d5a.asc     60  2800  3400
runl4dlb.spm r3000dlb.asc     60  3000  3600
runl4d2b.spm r3000d2b.asc     60  3000  3600
runl4d3b.spm r3000d3b.asc     60  3000  3600
runl4d4b.spm r3000d4b.asc     60  3000  3600
runl4d5b.spm r3000d5b.asc     60  3000  3600
runl4dlc.spm r3000dlc.asc     60  3000  3700
runl4d2c.spm r3000d2c.asc     60  3000  3700
runl4d3c.spm r3000d3c.asc     60  3000  3700
runl4d4c.spm r3000d4c.asc     60  3000  3700
runl4d5c.spm r3000d5c.asc     60  3000  3700
runl4dld.spm r3000dld.asc     60  3200  3800
runl4d2d.spm r3000d2d.asc     60  3200  3800
runl4d3d.spm r3000d3d.asc     60  3200  3800
runl4d4d.spm r3000d4d.asc     60  3200  3800
runl4d5d.spm r3000d5d.asc     60  3200  3800
runl4dle.spm r3000dle.asc     60  3200  3800
runl4d2e.spm r3000d2e.asc     60  3200  3800
runl4d3e.spm r3000d3e.asc     60  3200  3800
runl4d4e.spm r3000d4e.asc     60  3200  3800
runl4d5e.spm r3000d5e.asc     60  3200  3800
runl4dlf.spm r3000dlf.asc     60  3200  3800
runl4d2f.spm r3000d2f.asc     60  3200  3800
runl4d3f.spm r3000d3f.asc     60  3200  3800
runl4d4f.spm r3000d4f.asc     60  3200  3800
runl4d5f.spm r3000d5f.asc     60  3200  3800
runl4dla.spm r3090dla.asc     60  2800  3400
runl4d2a.spm r3090d2a.asc     60  2800  3400
runl4d3a.spm r3090d3a.asc     60  2800  3400
runl4d4a.spm r3090d4a.asc     60  2800  3400
runl4d5a.spm r3090d5a.asc     60  2800  3400
runl4dlb.spm r3900dlb.asc     60  3000  3600
runl4d2b.spm r3090d2b.asc     60  3000  3600
runl4d3b.spm r3090d3b.asc     60  3000  3600
runl4d4b.spm r3090d4b.asc     60  3000  3600
runl4d5b.spm r3090d5b.asc     60  3000  3600
runl4dlc.spm r3090dlc.asc     60  3000  3700
runl4d2c.spm r3090d2c.asc     60  3000  3700
runl4d3c.spm r3090d3c.asc     60  3000  3700
runl4d4c.spm r3090d4c.asc     60  3000  3700
runl4d5c.spm r3090d5c.asc     60  3000  3700
runl4dld.spm r3090dld.asc     60  3200  3800
runl4d2d.spm r3090d2d.asc     60  3200  3800
runl4d3d.spm r3090d3d.asc     60  3200  3800
```

run14d4d.spm	r3090d4d.asc	60	3200	3800
run14d5d.spm	r3090d5d.asc	60	3200	3800
run14d1e.spm	r3090d1e.asc	60	3200	3800
run14d2e.spm	r3090d2e.asc	60	3200	3800
run14d3e.spm	r3090d3e.asc	60	3200	3800
run14d4e.spm	r3090d4e.asc	60	3200	3800
run14d5e.spm	r3090d5e.asc	60	3200	3800
run14d1f.spm	r3090d1f.asc	60	3200	3800
run14d2f.spm	r3090d2f.asc	60	3200	3800
run14d3f.spm	r3090d3f.asc	60	3200	3800
run14d4f.spm	r3090d4f.asc	60	3200	3800
run14d5f.spm	r3090d5f.asc	60	3200	3800
run14d1a.spm	r3180d1a.asc	60	2800	3500
run14d2a.spm	r3180d2a.asc	60	2800	3500
run14d3a.spm	r3180d3a.asc	60	2800	3500
run14d4a.spm	r3180d4a.asc	60	2800	3500
run14d5a.spm	r3180d5a.asc	60	2800	3500
run14d1b.spm	r3180d1b.asc	60	3000	3600
run14d2b.spm	r3180d2b.asc	60	3000	3600
run14d3b.spm	r3180d3b.asc	60	3000	3600
run14d4b.spm	r3180d4b.asc	60	3000	3600
run14d5b.spm	r3180d5b.asc	60	3000	3600
run14d1c.spm	r3180d1c.asc	60	3000	3700
run14d2c.spm	r3180d2c.asc	60	3000	3700
run14d3c.spm	r3180d3c.asc	60	3000	3700
run14d4c.spm	r3180d4c.asc	60	3000	3700
run14d5c.spm	r3180d5c.asc	60	3000	3700
run14d1d.spm	r3180d1d.asc	60	3200	3800
run14d2d.spm	r3180d2d.asc	60	3200	3800
run14d3d.spm	r3180d3d.asc	60	3200	3800
run14d4d.spm	r3180d4d.asc	60	3200	3800
run14d5d.spm	r3180d5d.asc	60	3200	3800
run14d1e.spm	r3180d1e.asc	60	3200	3800
run14d2e.spm	r3180d2e.asc	60	3200	3800
run14d3e.spm	r3180d3e.asc	60	3200	3800
run14d4e.spm	r3180d4e.asc	60	3200	3800
run14d5e.spm	r3180d5e.asc	60	3200	3800
run14d1f.spm	r3180d1f.asc	60	3200	3800
run14d2f.spm	r3180d2f.asc	60	3200	3800
run14d3f.spm	r3180d3f.asc	60	3200	3800
run14d4f.spm	r3180d4f.asc	60	3200	3800
run14d5f.spm	r3180d5f.asc	60	3200	3800
run14d1a.spm	r3270d1a.asc	60	2800	3500
run14d2a.spm	r3270d2a.asc	60	2800	3500
run14d3a.spm	r3270d3a.asc	60	2800	3500
run14d4a.spm	r3270d4a.asc	60	2800	3500
run14d5a.spm	r3270d5a.asc	60	2800	3500
run14d1a.spm	r3270d1b.asc	60	3000	3600
run14d2b.spm	r3270d2b.asc	60	3000	3600
run14d3b.spm	r3270d3b.asc	60	3000	3600
run14d4b.spm	r3270d4b.asc	60	3000	3600
run14d5b.spm	r3270d5b.asc	60	3000	3700

run14d1c.spm	r3270d1c.asc	60	3000	3700
run14d2c.spm	r3270d2c.asc	60	3000	3700
run14d3c.spm	r3270d3c.asc	60	3000	3700
run14d4c.spm	r3270d4c.asc	60	3000	3700
run14d5c.spm	r3270d5c.asc	60	3000	3700
run14d1d.spm	r3270d1d.asc	60	3200	3800
run14d2d.spm	r3270d2d.asc	60	3200	3800
run14d3d.spm	r3270d3d.asc	60	3200	3800
run14d4d.spm	r3270d4d.asc	60	3200	3800
run14d5d.spm	r3270d5d.asc	60	3200	3800
run14d1e.spm	r3270d1e.asc	60	3200	3800
run14d2e.spm	r3270d2e.asc	60	3200	3800
run14d3e.spm	r3270d3e.asc	60	3200	3800
run14d4e.spm	r3270d4e.asc	60	3200	3800
run14d5e.spm	r3270d5e.asc	60	3200	3800
run14d1f.spm	r3270d1f.asc	60	3200	3800
run14d2f.spm	r3270d2f.asc	60	3200	3800
run14d3f.spm	r3270d3f.asc	60	3200	3800
run14d4f.spm	r3270d4f.asc	60	3200	3800
run14d5f.spm	r3270d5f.asc	60	3200	3800

Input File for Run 3

backgrd.spm	backgrd.asc	151362	0	0
run20d1a.spm	r4000d1a.asc	60	3600	4400
run20d2a.spm	r4000d2a.asc	60	3600	4400
run20d3a.spm	r4000d3a.asc	60	3600	4400
run20d4a.spm	r4000d4a.asc	60	3600	4400
run20d5a.spm	r4000d5a.asc	60	3600	4400
run20d1b.spm	r4000d1b.asc	60	4000	4800
run20d2b.spm	r4000d2b.asc	60	4000	4800
run20d3b.spm	r4000d3b.asc	60	4000	4800
run20d4b.spm	r4000d4b.asc	60	4000	4800
run20d5b.spm	r4000d5b.asc	60	4000	4800
run20d1c.spm	r4000d1c.asc	60	4000	4800
run20d2c.spm	r4000d2c.asc	60	4000	4800
run20d3c.spm	r4000d3c.asc	60	4000	4800
run20d4c.spm	r4000d4c.asc	60	4000	4800
run20d5c.spm	r4000d5c.asc	60	4000	4800
run20d1d.spm	r4000d1d.asc	60	4200	5000
run20d2d.spm	r4000d2d.asc	60	4200	5000
run20d3d.spm	r4000d3d.asc	60	4200	5000
run20d4d.spm	r4000d4d.asc	60	4200	5000
run20d5d.spm	r4000d5d.asc	60	4200	5000
run20d1e.spm	r4000d1e.asc	60	4200	5000
run20d2e.spm	r4000d2e.asc	60	4200	5000
run20d3e.spm	r4000d3e.asc	60	4200	5000
run20d4e.spm	r4000d4e.asc	60	4200	5000
run20d5e.spm	r4000d5e.asc	60	4200	5000
run20d1f.spm	r4000d1f.asc	60	4200	5000
run20d2f.spm	r4000d2f.asc	60	4200	5000
run20d3f.spm	r4000d3f.asc	60	4200	5000
run20d4f.spm	r4000d4f.asc	60	4200	5000
run20d5f.spm	r4000d5f.asc	60	4200	5000
run21d1a.spm	r4090d1a.asc	60	3600	4400
run21d2a.spm	r4090d2a.asc	60	3600	4400
run21d3a.spm	r4090d3a.asc	60	3600	4400
run21d4a.spm	r4090d4a.asc	60	3600	4400
run21d5a.spm	r4090d5a.asc	60	3600	4400
run21d1b.spm	r4090d1b.asc	60	4000	4800
run21d2b.spm	r4090d2b.asc	60	4000	4800
run21d3b.spm	r4090d3b.asc	60	4000	4800
run21d4b.spm	r4090d4b.asc	60	4000	4800
run21d5b.spm	r4090d5b.asc	60	4000	4800
run21d1c.spm	r4090d1c.asc	60	4000	4800
run21d2c.spm	r4090d2c.asc	60	4000	4800
run21d3c.spm	r4090d3c.asc	60	4000	4800
run21d4c.spm	r4090d4c.asc	60	4000	4800
run21d5c.spm	r4090d5c.asc	60	4000	4800
run21d1d.spm	r4090d1d.asc	60	4200	5000
run21d2d.spm	r4090d2d.asc	60	4200	5000
run21d3d.spm	r4090d3d.asc	60	4200	5000

run21d4d.spm	r4090d4d.asc	60	4200	5000
run21d5d.spm	r4090d5d.asc	60	4200	5000
run21d1e.spm	r4090d1e.asc	60	4200	5000
run21d2e.spm	r4090d2e.asc	60	4200	5000
run21d3e.spm	r4090d3e.asc	60	4200	5000
run21d4e.spm	r4090d4e.asc	60	4200	5000
run21d5e.spm	r4090d5e.asc	60	4200	5000
run21d1f.spm	r4090d1f.asc	60	4200	5000
run21d2f.spm	r4090d2f.asc	60	4200	5000
run21d3f.spm	r4090d3f.asc	60	4200	5000
run21d4f.spm	r4090d4f.asc	60	4200	5000
run21d5f.spm	r4090d5f.asc	60	4200	5000
run22d1a.spm	r4180d1a.asc	60	3600	4400
run22d2a.spm	r4180d2a.asc	60	3600	4400
run22d3a.spm	r4180d3a.asc	60	3600	4400
run22d4a.spm	r4180d4a.asc	60	3600	4400
run22d5a.spm	r4180d5a.asc	60	3600	4400
run22d1b.spm	r4180d1b.asc	60	4000	4800
run22d2b.spm	r4180d2b.asc	60	4000	4800
run22d3b.spm	r4180d3b.asc	60	4000	4800
run22d4b.spm	r4180d4b.asc	60	4000	4800
run22d5b.spm	r4180d5b.asc	60	4000	4800
run22d1c.spm	r4180d1c.asc	60	4200	5000
run22d2c.spm	r4180d2c.asc	60	4200	5000
run22d3c.spm	r4180d3c.asc	60	4200	5000
run22d4c.spm	r4180d4c.asc	60	4200	5000
run22d5c.spm	r4180d5c.asc	60	4200	5000
run22d1d.spm	r4180d1d.asc	60	4200	5000
run22d2d.spm	r4180d2d.asc	60	4200	5000
run22d3d.spm	r4180d3d.asc	60	4200	5000
run22d4d.spm	r4180d4d.asc	60	4200	5000
run22d5d.spm	r4180d5d.asc	60	4200	5000
run22d1e.spm	r4180d1e.asc	60	4200	5000
run22d2e.spm	r4180d2e.asc	60	4200	5000
run22d3e.spm	r4180d3e.asc	60	4200	5000
run22d4e.spm	r4180d4e.asc	60	4200	5000
run22d5e.spm	r4180d5e.asc	60	4200	5000
run22d1f.spm	r4180d1f.asc	60	4200	5000
run22d2f.spm	r4180d2f.asc	60	4200	5000
run22d3f.spm	r4180d3f.asc	60	4200	5000
run22d4f.spm	r4180d4f.asc	60	4200	5000
run22d5f.spm	r4180d5f.asc	60	4200	5000
run23d1a.spm	r4270d1a.asc	60	3600	4400
run23d2a.spm	r4270d2a.asc	60	3600	4400
run23d3a.spm	r4270d3a.asc	60	3600	4400
run23d4a.spm	r4270d4a.asc	60	3600	4400
run23d5a.spm	r4270d5a.asc	60	3600	4400
run23d1a.spm	r4270d1b.asc	60	4000	4800
run23d2b.spm	r4270d2b.asc	60	4000	4800
run23d3b.spm	r4270d3b.asc	60	4000	4800
run23d4b.spm	r4270d4b.asc	60	4000	4800
run23d5b.spm	r4270d5b.asc	60	4000	4800

run23d1c.spm	r4270d1c.asc	60	4200	5000
run23d2c.spm	r4270d2c.asc	60	4200	5000
run23d3c.spm	r4270d3c.asc	60	4200	5000
run23d4c.spm	r4270d4c.asc	60	4200	5000
run23d5c.spm	r4270d5c.asc	60	4200	5000
run23d1d.spm	r4270d1d.asc	60	4200	5000
run23d2d.spm	r4270d2d.asc	60	4200	5000
run23d3d.spm	r4270d3d.asc	60	4200	5000
run23d4d.spm	r4270d4d.asc	60	4200	5000
run23d5d.spm	r4270d5d.asc	60	4200	5000
run23d1e.spm	r4270d1e.asc	60	4200	5000
run23d2e.spm	r4270d2e.asc	60	4200	5000
run23d3e.spm	r4270d3e.asc	60	4200	5000
run23d4e.spm	r4270d4e.asc	60	4200	5000
run23d5e.spm	r4270d5e.asc	60	4200	5000
run23d1f.spm	r4270d1f.asc	60	4200	5000
run23d2f.spm	r4270d2f.asc	60	4200	5000
run23d3f.spm	r4270d3f.asc	60	4200	5000
run23d4f.spm	r4270d4f.asc	60	4200	5000
run23d5f.spm	r4270d5f.asc	60	4200	5000

Input File for Run 4

backgrd.spm	backgrd.asc	151362	0	0
run30d1a.spm	r5000d1a.asc	60	4300	5100
run30d2a.spm	r5000d2a.asc	60	4300	5100
run30d3a.spm	r5000d3a.asc	60	4300	5100
run30d4a.spm	r5000d4a.asc	60	4300	5100
run30d5a.spm	r5000d5a.asc	60	4300	5100
run30d1b.spm	r5000d1b.asc	60	4300	5100
run30d2b.spm	r5000d2b.asc	60	4300	5100
run30d3b.spm	r5000d3b.asc	60	4300	5100
run30d4b.spm	r5000d4b.asc	60	4300	5100
run30d5b.spm	r5000d5b.asc	60	4300	5100
run30d1c.spm	r5000d1c.asc	60	4300	5100
run30d2c.spm	r5000d2c.asc	60	4300	5100
run30d3c.spm	r5000d3c.asc	60	4300	5100
run30d4c.spm	r5000d4c.asc	60	4300	5100
run30d5c.spm	r5000d5c.asc	60	4300	5100
run30d1d.spm	r5000d1d.asc	60	4300	5100
run30d2d.spm	r5000d2d.asc	60	4300	5100
run30d3d.spm	r5000d3d.asc	60	4300	5100
run30d4d.spm	r5000d4d.asc	60	4300	5100
run30d5d.spm	r5000d5d.asc	60	4300	5100
run30d1e.spm	r5000d1e.asc	60	4200	5000
run30d2e.spm	r5000d2e.asc	60	4200	5000
run30d3e.spm	r5000d3e.asc	60	4200	5000
run30d4e.spm	r5000d4e.asc	60	4200	5000
run30d5e.spm	r5000d5e.asc	60	4200	5000
run30d1f.spm	r5000d1f.asc	60	4150	4950
run30d2f.spm	r5000d2f.asc	60	4100	4900
run30d3f.spm	r5000d3f.asc	60	4100	4900
run30d4f.spm	r5000d4f.asc	60	4100	4900
run30d5f.spm	r5000d5f.asc	60	4100	4900
run31d1a.spm	r5090d1a.asc	60	4300	5100
run31d2a.spm	r5090d2a.asc	60	4300	5100
run31d3a.spm	r5090d3a.asc	60	4300	5100
run31d4a.spm	r5090d4a.asc	60	4300	5100
run31d5a.spm	r5090d5a.asc	60	4300	5100
run31d1b.spm	r5900d1b.asc	60	4300	5100
run31d2b.spm	r5090d2b.asc	60	4300	5100
run31d3b.spm	r5090d3b.asc	60	4300	5100
run31d4b.spm	r5090d4b.asc	60	4300	5100
run31d5b.spm	r5090d5b.asc	60	4300	5100
run31d1c.spm	r5090d1c.asc	60	4300	5100
run31d2c.spm	r5090d2c.asc	60	4300	5100
run31d3c.spm	r5090d3c.asc	60	4300	5100
run31d4c.spm	r5090d4c.asc	60	4300	5100
run31d5c.spm	r5090d5c.asc	60	4300	5100
run31d1d.spm	r5090d1d.asc	60	4300	5100
run31d2d.spm	r5090d2d.asc	60	4300	5100
run31d3d.spm	r5090d3d.asc	60	4300	5100

run31d4d.spm	r5090d4d.asc	60	4300	5100
run31d5d.spm	r5090d5d.asc	60	4300	5100
run31d1e.spm	r5090d1e.asc	60	4200	4900
run31d2e.spm	r5090d2e.asc	60	4200	4900
run31d3e.spm	r5090d3e.asc	60	4200	4900
run31d4e.spm	r5090d4e.asc	60	4200	4900
run31d5e.spm	r5090d5e.asc	60	4200	4900
run31d1f.spm	r5090d1f.asc	60	4100	4900
run31d2f.spm	r5090d2f.asc	60	4100	4900
run31d3f.spm	r5090d3f.asc	60	4100	4900
run31d4f.spm	r5090d4f.asc	60	4100	4900
run31d5f.spm	r5090d5f.asc	60	4100	4900
run32d1a.spm	r5180d1a.asc	60	4300	5100
run32d2a.spm	r5180d2a.asc	60	4300	5100
run32d3a.spm	r5180d3a.asc	60	4300	5100
run32d4a.spm	r5180d4a.asc	60	4300	5100
run32d5a.spm	r5180d5a.asc	60	4300	5100
run32d1b.spm	r5180d1b.asc	60	4300	5100
run32d2b.spm	r5180d2b.asc	60	4300	5100
run32d3b.spm	r5180d3b.asc	60	4300	5100
run32d4b.spm	r5180d4b.asc	60	4300	5100
run32d5b.spm	r5180d5b.asc	60	4300	5100
run32d1c.spm	r5180d1c.asc	60	4300	5100
run32d2c.spm	r5180d2c.asc	60	4300	5100
run32d3c.spm	r5180d3c.asc	60	4300	5100
run32d4c.spm	r5180d4c.asc	60	4300	5100
run32d5c.spm	r5180d5c.asc	60	4300	5100
run32d1d.spm	r5180d1d.asc	60	4300	5100
run32d2d.spm	r5180d2d.asc	60	4300	5100
run32d3d.spm	r5180d3d.asc	60	4300	5100
run32d4d.spm	r5180d4d.asc	60	4300	5100
run32d5d.spm	r5180d5d.asc	60	4300	5100
run32d1e.spm	r5180d1e.asc	60	4200	5000
run32d2e.spm	r5180d2e.asc	60	4200	5000
run32d3e.spm	r5180d3e.asc	60	4200	5000
run32d4e.spm	r5180d4e.asc	60	4200	5000
run32d5e.spm	r5180d5e.asc	60	4200	5000
run32d1f.spm	r5180d1f.asc	60	4100	4900
run32d2f.spm	r5180d2f.asc	60	4100	4900
run32d3f.spm	r5180d3f.asc	60	4100	4900
run32d4f.spm	r5180d4f.asc	60	4100	4900
run32d5f.spm	r5180d5f.asc	60	4100	4900
run33d1a.spm	r5270d1a.asc	60	4300	5100
run33d2a.spm	r5270d2a.asc	60	4300	5100
run33d3a.spm	r5270d3a.asc	60	4300	5100
run33d4a.spm	r5270d4a.asc	60	4300	5100
run33d5a.spm	r5270d5a.asc	60	4300	5100
run33d1b.spm	r5270d1b.asc	60	4300	5100
run33d2b.spm	r5270d2b.asc	60	4300	5100
run33d3b.spm	r5270d3b.asc	60	4300	5100
run33d4b.spm	r5270d4b.asc	60	4300	5100
run33d5b.spm	r5270d5b.asc	60	4300	5100

run33d1c.spm	r5270d1c.asc	60	4300	5100
run33d2c.spm	r5270d2c.asc	60	4300	5100
run33d3c.spm	r5270d3c.asc	60	4300	5100
run33d4c.spm	r5270d4c.asc	60	4300	5100
run33d5c.spm	r5270d5c.asc	60	4300	5100
run33d1d.spm	r5270d1d.asc	60	4300	5100
run33d2d.spm	r5270d2d.asc	60	4300	5100
run33d3d.spm	r5270d3d.asc	60	4300	5100
run33d4d.spm	r5270d4d.asc	60	4300	5100
run33d5d.spm	r5270d5d.asc	60	4300	5100
run33d1e.spm	r5270d1e.asc	60	4200	5000
run33d2e.spm	r5270d2e.asc	60	4200	5000
run33d3e.spm	r5270d3e.asc	60	4200	5000
run33d4e.spm	r5270d4e.asc	60	4200	5000
run33d5e.spm	r5270d5e.asc	60	4200	5000
run33d1f.spm	r5270d1f.asc	60	4100	4900
run33d2f.spm	r5270d2f.asc	60	4100	4900
run33d3f.spm	r5270d3f.asc	60	4100	4900
run33d4f.spm	r5270d4f.asc	60	4100	4900
run33d5f.spm	r5270d5f.asc	60	4100	4900

Appendix D

Output Files - NNLS Routine

Appendix D: Output Files - NNLS Routine

This section contains the output files for run one (1) through four (4) as calculated by the NNLS-bases reconstruction routine. Note, totals for each layer and the entire drum are calculated. Activities for layer one (1), voxels one (1) through nine (9) heads the list, followed by layer 2, and so forth.

```
0.00000E+00
0.00000E+00
0.00000E+00
4.45029E-05
0.00000E+00
0.00000E+00
3.06345E-06
2.99135E-06
0.00000E+00
Activity in Layer = 5.05577E-05mCi
7.78665E+01
0.00000E+00
0.00000E+00
4.57155E-05
0.00000E+00
0.00000E+00
2.04603E-05
2.76604E-06
1.02852E-04
Activity in Layer = 7.78667E+01mCi
0.00000E+00
0.00000E+00
3.82248E-05
0.00000E+00
3.32514E-06
4.60094E-06
2.00211E-06
0.00000E+00
0.00000E+00
Activity in Layer = 4.81530E-05mCi
0.00000E+00
0.00000E+00
5.39448E-05
0.00000E+00
0.00000E+00
1.57783E-05
5.24719E-05
0.00000E+00
6.66195E-05
Activity in Layer = 1.88814E-04mCi
0.00000E+00
0.00000E+00
0.00000E+00
0.00000E+00
0.00000E+00
2.49455E-05
2.54515E-05
3.95110E-05
1.11416E-04
```

```
Activity in Layer = 2.01324E-04mCi
 6.32475E-05
 0.00000E+00
 0.00000E+00
 0.00000E+00
 0.00000E+00
 0.00000E+00
 0.00000E+00
 0.00000E+00
 4.01209E-05
Activity in Layer = 1.03368E-04mCi
Total Drum Activity = 7.78672E+01mCi
```

```
 0.00000E+00
 1.05902E-05
 0.00000E+00
 9.04809E-06
 8.85357E-06
 0.00000E+00
 3.26388E-07
 0.00000E+00
 0.00000E+00
Activity in Layer = 2.88183E-05mCi
 0.00000E+00
 0.00000E+00
 0.00000E+00
 0.00000E+00
 0.00000E+00
 0.00000E+00
 0.00000E+00
 0.00000E+00
 1.38012E-06
Activity in Layer = 1.38012E-06mCi
 3.75642E-06
 9.16249E-05
 3.97039E-06
 9.19940E-05
 3.69234E-06
 9.21446E-05
 0.00000E+00
 9.51021E-05
 7.78665E+01
Activity in Layer = 7.78669E+01mCi
 0.00000E+00
 9.57921E-07
 0.00000E+00
 6.70664E-07
 0.00000E+00
 6.99578E-07
 0.00000E+00
 8.79306E-07
 0.00000E+00
Activity in Layer = 3.20747E-06mCi
 4.53070E-07
 0.00000E+00
 3.71905E-07
 0.00000E+00
 2.60261E-07
 0.00000E+00
 2.62276E-07
 0.00000E+00
 0.00000E+00
```

```
Activity in Layer = 1.34751E-06mCi
 1.03590E-05
 0.00000E+00
 1.05157E-05
 0.00000E+00
 1.01396E-05
 0.00000E+00
 1.03588E-05
 0.00000E+00
 0.00000E+00
Activity in Layer = 4.13731E-05mCi
Total Drum Activity = 7.78669E+01mCi
```

```
 0.00000E+00
 7.63329E-06
 1.07188E-05
 0.00000E+00
 0.00000E+00
 4.91759E-05
 0.00000E+00
 0.00000E+00
 3.11432E-05
Activity in Layer = 9.86712E-05mCi
 0.00000E+00
 0.00000E+00
 0.00000E+00
 0.00000E+00
 2.01332E-05
 0.00000E+00
 0.00000E+00
 0.00000E+00
 0.00000E+00
Activity in Layer = 2.01332E-05mCi
 0.00000E+00
 0.00000E+00
 0.00000E+00
 3.39652E-05
 0.00000E+00
 0.00000E+00
 7.78666E+01
 0.00000E+00
 0.00000E+00
Activity in Layer = 7.78666E+01mCi
 0.00000E+00
 0.00000E+00
 0.00000E+00
 0.00000E+00
 9.07228E-07
 2.20108E-05
 2.10950E-06
 1.23496E-05
 0.00000E+00
Activity in Layer = 3.73771E-05mCi
 0.00000E+00
 0.00000E+00
 0.00000E+00
 1.90272E-05
 1.35784E-05
 0.00000E+00
 0.00000E+00
 0.00000E+00
 0.00000E+00
```

```
Activity in Layer = 3.26055E-05mCi
 0.00000E+00
 0.00000E+00
 2.38187E-05
 0.00000E+00
 0.00000E+00
 1.58561E-05
 0.00000E+00
 0.00000E+00
 0.00000E+00
Activity in Layer = 3.96749E-05mCi
Total Drum Activity = 7.78669E+01mCi
```

Output File for Run 4 Calculated Using NNLS

```
 2.96376E-03
 0.00000E+00
 0.00000E+00
 0.00000E+00
 2.55836E-03
 1.19420E-02
 0.00000E+00
 0.00000E+00
 0.00000E+00
Activity in Layer = 1.74641E-02mCi
 0.00000E+00
 2.75678E-02
 7.75985E+01
 2.85043E-02
 0.00000E+00
 2.80819E-02
 0.00000E+00
 0.00000E+00
 1.53437E-02
Activity in Layer = 7.76980E+01mCi
 0.00000E+00
 4.56060E-03
 0.00000E+00
 1.06443E-03
 9.28605E-04
 1.66411E-02
 0.00000E+00
 0.00000E+00
 0.00000E+00
Activity in Layer = 2.31948E-02mCi
 2.63738E-03
 0.00000E+00
 0.00000E+00
 7.15988E-03
 5.71942E-03
 9.17600E-03
 6.09580E-03
 0.00000E+00
 0.00000E+00
Activity in Layer = 3.07885E-02mCi
 1.73235E-03
 4.34519E-03
 1.13812E-02
 8.88587E-03
 1.34766E-02
 6.65073E-04
 1.13717E-02
 7.93508E-03
 1.13976E-02
```

```
Activity in Layer = 7.11906E-02mCi
 5.28194E-04
 8.11483E-03
 1.15659E-02
 1.87122E-02
 2.34961E-03
 0.00000E+00
 0.00000E+00
 1.79599E-02
 2.14807E-02
Activity in Layer = 8.07114E-02mCi
Total Drum Activity = 7.79214E+01mCi
```

Appendix E

Output Files - LSMOD Routine

Appendix E: Output Files - LSMOD Routine

This section contains output files for runs one (1) through four (4) as calculated by the LSMOD-based reconstruction routine. Note, totals for each layer and the entire drum are calculated. Activities for layer one (1), voxels one (1) through (9) head the list, followed by layer two (2), and so forth.

```
8.02889E-02
1.44001E-02
6.54610E-02
3.69527E-02
8.19557E-03
1.45265E-02
2.30058E-02
1.17797E-01
7.10011E-02
Activity in Layer = 4.31628E-01mCi
6.97299E+01
1.56692E-01
1.63488E-01
7.41258E-02
2.76005E-02
0.00000E+00
1.53460E-01
3.93453E-02
6.45258E-02
Activity in Layer = 7.04091E+01mCi
5.65914E-02
1.79104E-02
1.69487E-02
7.53560E-02
0.00000E+00
9.64213E-03
2.30320E-01
1.73177E-01
2.29128E-01
Activity in Layer = 8.09073E-01mCi
1.54127E-01
7.51576E-02
1.66489E-02
0.00000E+00
3.86997E-04
7.90789E-02
0.00000E+00
0.00000E+00
2.02208E-02
Activity in Layer = 3.45620E-01mCi
1.08325E-01
6.61819E-02
2.53684E-02
0.00000E+00
3.32698E-02
2.96814E-02
8.43692E-03
1.34044E-02
3.25143E-02
```

```
Activity in Layer = 3.17182E-01mCi
 2.04482E-02
 0.00000E+00
 3.08016E-02
 0.00000E+00
 0.00000E+00
 0.00000E+00
 0.00000E+00
 4.30721E-02
 1.93025E-02
Activity in Layer = 1.13624E-01mCi
Total Drum Activity = 6.40674E+02mCi
```

```
 3.51657E-02
 4.62259E-02
 1.09463E-01
 7.42427E-02
 1.90634E-01
 2.63038E-02
 1.33815E-01
 8.77210E-03
 2.11395E-01
Activity in Layer = 8.36016E-01mCi
 3.82662E-02
 4.25481E-02
 1.80451E-01
 7.09067E-02
 2.94693E-02
 3.71413E-02
 2.07232E-02
 1.05777E-01
 1.43560E-01
Activity in Layer = 6.68842E-01mCi
 7.49685E-02
 1.44557E-01
 1.42414E-01
 2.02406E-01
 8.86279E-02
 1.74923E-01
 3.61852E-01
 2.20263E-01
 7.40428E+01
Activity in Layer = 7.54528E+01mCi
 1.26126E-02
 5.74840E-02
 3.71681E-02
 7.46344E-02
 4.48837E-03
 6.54994E-02
 3.56764E-02
 7.73748E-02
 0.00000E+00
Activity in Layer = 3.64938E-01mCi
 3.48480E-02
 5.70989E-03
 5.05775E-02
 1.61332E-02
 3.75512E-02
 1.72186E-03
 5.93516E-02
 1.68521E-02
 5.61852E-02
```

```
Activity in Layer = 2.78931E-01mCi
 0.00000E+00
 0.00000E+00
 0.00000E+00
 0.00000E+00
 0.00000E+00
 0.00000E+00
 0.00000E+00
 0.00000E+00
 5.19932E-02
Activity in Layer = 5.19932E-02mCi
Total Drum Activity = 9.05799E+01mCi
```

```
6.56017E-02
1.43525E-02
0.00000E+00
3.20975E-01
1.28083E-01
2.10403E-01
4.29532E-02
3.79426E-02
1.24617E-01
Activity in Layer = 9.44928E-01mCi
1.61881E-01
0.00000E+00
0.00000E+00
6.67553E-02
0.00000E+00
1.25073E-01
1.30213E-01
1.56430E-02
1.56652E-01
Activity in Layer = 6.56217E-01mCi
2.24097E-01
0.00000E+00
4.04341E-02
0.00000E+00
1.87136E-01
0.00000E+00
7.49142E+01
8.52165E-02
7.41192E-02
Activity in Layer = 7.55252E+01mCi
0.00000E+00
0.00000E+00
2.90683E-02
9.39478E-02
0.00000E+00
1.19243E-01
1.32721E-01
1.17436E-01
1.65963E-01
Activity in Layer = 6.58380E-01mCi
4.83111E-02
0.00000E+00
3.58771E-02
2.10571E-02
0.00000E+00
6.89047E-03
1.54134E-01
5.43617E-02
1.80201E-02
```

```
Activity in Layer = 3.38652E-01mCi
 3.26964E-02
 0.00000E+00
 0.00000E+00
 0.00000E+00
 0.00000E+00
 4.58787E-02
 8.28060E-02
 2.08610E-02
 2.61679E-02
Activity in Layer = 2.08410E-01mCi
Total Drum Activity = 2.39868E+02mCi
```

```
 3.70143E-02
 1.12206E-01
 1.30040E-01
 0.00000E+00
 7.79954E-02
 0.00000E+00
 0.00000E+00
 5.54041E-02
 9.86836E-02
Activity in Layer = 5.11344E-01mCi
 7.15851E-01
 1.80828E-02
 7.25202E+01
 2.03802E-02
 1.46679E-01
 0.00000E+00
 1.63339E-02
 0.00000E+00
 9.98111E-03
Activity in Layer = 7.34475E+01mCi
 3.02327E-02
 1.73755E-01
 5.13995E-02
 5.47682E-02
 3.66012E-02
 0.00000E+00
 0.00000E+00
 4.34637E-02
 3.91554E-01
Activity in Layer = 7.81774E-01mCi
 6.52292E-03
 0.00000E+00
 2.14498E-01
 1.81586E-02
 5.64428E-02
 0.00000E+00
 3.87902E-02
 3.44921E-02
 1.23954E-02
Activity in Layer = 3.81300E-01mCi
 1.06870E-01
 2.15789E-01
 1.83581E-02
 0.00000E+00
 1.01958E-01
 2.00378E-03
 0.00000E+00
 2.39391E-02
 2.60043E-02
```

```
Activity in Layer = 4.94922E-01mCi
 0.00000E+00
 2.85660E-01
 0.00000E+00
 2.50782E-01
 4.92297E-02
 0.00000E+00
 0.00000E+00
 3.58627E-01
 1.61410E-01
Activity in Layer = 1.10571E+00mCi
Total Drum Activity = 5.31368E+02mCi
```

Appendix F

Tabulation of PSRF Symmetry at 0 Degrees Orientation

Appendix F: Tabulation of PSRF Symmetry at 0 Degrees Orientation

This section contains a tabulation of the symmetric properties as used to construct the PSRF matrix used in the evaluation of the source distribution for all experiments. Note, the values in these tables equate to source - detector positions *(i.e. a1,1 translates to detector location A, layer 1, source voxel 1).* Using this symmetry, the number of QAD-CGGP runs was reduced to a manageable number, 150.

Table F.1 PSRF Symmetry for Layer 1 at 0 Degrees Orientation.

Detector	Voxel Number								
Number	1	2	3	4	5	6	7	8	9
a1	a1,1	a1,2	a1,3	a1,4	e1,4	e1,3	e1,2	e1,1	a1,9
b1	b1,1	b1,2	b1,3	b1,4	d1,4	d1,3	d1,2	d1,1	b1,9
c1	c1,1	c1,2	c1,3	c1,4	c1,4	c1,3	c1,2	c1,1	c1,9
d1	d1,1	d1,2	d1,3	d1,4	b1,4	b1,3	b1,2	b1,1	b1,1
e1	e1,1	e1,2	e1,3	e1,4	a1,4	a1,3	a1,2	a1,1	a1,9
a2	a1,10	a1,11	a1,12	a1,13	e1,13	e1,12	e1,11	e1,10	a1,18
b2	b1,10	b1,11	b1,12	b1,13	d1,13	d1,12	d1,11	d1,10	b1,18
c2	c1,10	c1,11	c1,12	c1,13	c1,13	c1,12	c1,11	c1,10	c1,18
d2	d1,10	d1,11	d1,12	d1,13	b1,13	b1,12	b1,11	b1,10	b1,18
e2	e1,10	e1,11	e1,12	e1,13	a1,13	a1,12	a1,11	a1,10	a1,18
a3	a1,19	a1,20	a1,21	a1,22	e1,22	e1,21	e1,20	e1,19	a1,27
b3	b1,19	b1,20	b1,21	b1,22	d1,22	d1,21	d1,20	d1,19	b1,27
c3	c1,19	c1,20	c1,21	c1,22	c1,22	c1,21	c1,20	c1,19	c1,27
d3	d1,19	d1,20	d1,21	d1,22	b1,22	b1,21	b1,20	b1,19	b1,27
e3	e1,19	e1,20	e1,21	e1,22	a1,22	a1,21	a1,20	a1,19	a1,27
a4	a1,28	a1,29	a1,30	a1,31	e1,31	e1,30	e1,29	e1,28	a1,36
b4	b1,28	b1,29	b1,30	b1,31	d1,31	d1,30	d1,29	d1,28	b1,36
c4	c1,28	c1,29	c1,30	c1,31	c1,31	c1,30	c1,29	c1,28	c1,36
d4	d1,28	d1,29	d1,30	d1,31	b1,31	b1,30	b1,29	b1,28	b1,36
e4	e1,28	e1,29	e1,30	e1,31	a1,31	a1,30	a1,29	a1,28	a1,36
a5	a1,37	a1,38	a1,39	a1,40	e1,40	e1,39	e1,38	e1,37	a1,45
b5	b1,37	b1,38	b1,39	b1,40	d1,40	d1,39	d1,38	d1,37	b1,45
c5	c1,37	c1,38	c1,39	c1,40	c1,40	c1,39	c1,38	c1,37	c1,45
d5	d1,37	d1,38	d1,39	d1,40	b1,40	b1,39	b1,38	b1,37	b1,45
e5	e1,37	e1,38	e1,39	e1,40	a1,40	a1,39	a1,38	a1,37	a1,45
a6	a1,46	a1,47	a1,48	a1,49	e1,49	e1,48	e1,47	e1,46	a1,54
b6	b1,46	b1,47	b1,48	b1,49	d1,49	d1,48	d1,47	d1,46	b1,54
c6	c1,46	c1,47	c1,48	c1,49	c1,49	c1,48	c1,47	c1,46	c1,54
d6	d1,46	d1,47	d1,48	d1,49	b1,49	b1,48	b1,47	b1,46	b1,54
e6	e1,46	e1,47	e1,48	e1,49	a1,49	a1,48	a1,47	a1,46	a1,54

Table F.2 PSRF Symmetry for Layer 2 at 0 Degrees Orientation.

Detector	Voxel Number								
Number	10	11	12	13	14	15	16	17	18
a1	a1,10	a1,11	a1,12	a1,13	e1,13	e1,12	e1,11	e1,10	a1,18
b1	b1,10	b1,11	b1,12	b1,13	d1,13	d1,12	d1,11	d1,10	b1,18
c1	c1,10	c1,11	c1,12	c1,13	c1,13	c1,12	c1,11	c1,10	c1,18
d1	d1,10	d1,11	d1,12	d1,13	b1,13	b1,12	b1,11	b1,10	b1,18
e1	e1,10	e1,11	e1,12	e1,13	a1,13	a1,12	a1,11	a1,10	a1,18
a2	a1,1	a1,2	a1,3	a1,4	e1,4	e1,3	e1,2	e1,1	a1,9
b2	b1,1	b1,2	b1,3	b1,4	d1,4	d1,3	d1,2	d1,1	b1,9
c2	c1,1	c1,2	c1,3	c1,4	c1,4	c1,3	c1,2	c1,1	c1,9
d2	d1,1	d1,2	d1,3	d1,4	b1,4	b1,3	b1,2	b1,1	b1,1
e2	e1,1	e1,2	e1,3	e1,4	a1,4	a1,3	a1,2	a1,1	a1,9
a3	a1,10	a1,11	a1,12	a1,13	e1,13	e1,12	e1,11	e1,10	a1,18
b3	b1,10	b1,11	b1,12	b1,13	d1,13	d1,12	d1,11	d1,10	b1,18
c3	c1,10	c1,11	c1,12	c1,13	c1,13	c1,12	c1,11	c1,10	c1,18
d3	d1,10	d1,11	d1,12	d1,13	b1,13	b1,12	b1,11	b1,10	b1,18
e3	e1,10	e1,11	e1,12	e1,13	a1,13	a1,12	a1,11	a1,10	a1,18
a4	a1,19	a1,20	a1,21	a1,22	e1,22	e1,21	e1,20	e1,19	a1,27
b4	b1,19	b1,20	b1,21	b1,22	d1,22	d1,21	d1,20	d1,19	b1,27
c4	c1,19	c1,20	c1,21	c1,22	c1,22	c1,21	c1,20	c1,19	c1,27
d4	d1,19	d1,20	d1,21	d1,22	b1,22	b1,21	b1,20	b1,19	b1,27
e4	e1,19	e1,20	e1,21	e1,22	a1,22	a1,21	a1,20	a1,19	a1,27
a5	a1,28	a1,29	a1,30	a1,31	e1,31	e1,30	e1,29	e1,28	a1,36
b5	b1,28	b1,29	b1,30	b1,31	d1,31	d1,30	d1,29	d1,28	b1,36
c5	c1,28	c1,29	c1,30	c1,31	c1,31	c1,30	c1,29	c1,28	c1,36
d5	d1,28	d1,29	d1,30	d1,31	b1,31	b1,30	b1,29	b1,28	b1,36
e5	e1,28	e1,29	e1,30	e1,31	a1,31	a1,30	a1,29	a1,28	a1,36
a6	a1,37	a1,38	a1,39	a1,40	e1,40	e1,39	e1,38	e1,37	a1,45
b6	b1,37	b1,38	b1,39	b1,40	d1,40	d1,39	d1,38	d1,37	b1,45
c6	c1,37	c1,38	c1,39	c1,40	c1,40	c1,39	c1,38	c1,37	c1,45
d6	d1,37	d1,38	d1,39	d1,40	b1,40	b1,39	b1,38	b1,37	b1,45
e6	e1,37	e1,38	e1,39	e1,40	a1,40	a1,39	a1,38	a1,37	a1,45

Table F.3 PSRF Symmetry for Layer 3 at 0 Degrees Orientation.

Detector	Voxel Number								
Number	19	20	21	22	23	24	25	26	27
a1	a1,19	a1,20	a1,21	a1,22	e1,22	e1,21	e1,20	e1,19	a1,27
b1	b1,19	b1,20	b1,21	b1,22	d1,22	d1,21	d1,20	d1,19	b1,27
c1	c1,19	c1,20	c1,21	c1,22	c1,22	c1,21	c1,20	c1,19	c1,27
d1	d1,19	d1,20	d1,21	d1,22	b1,22	b1,21	b1,20	b1,19	b1,27
e1	e1,19	e1,20	e1,21	e1,22	a1,22	a1,21	a1,20	a1,19	a1,27
a2	a1,10	a1,11	a1,12	a1,13	e1,13	e1,12	e1,11	e1,10	a1,18
b2	b1,10	b1,11	b1,12	b1,13	d1,13	d1,12	d1,11	d1,10	b1,18
c2	c1,10	c1,11	c1,12	c1,13	c1,13	c1,12	c1,11	c1,10	c1,18
d2	d1,10	d1,11	d1,12	d1,13	b1,13	b1,12	b1,11	b1,10	b1,18
e2	e1,10	e1,11	e1,12	e1,13	a1,13	a1,12	a1,11	a1,10	a1,18
a3	a1,1	a1,2	a1,3	a1,4	e1,4	e1,3	e1,2	e1,1	a1,9
b3	b1,1	b1,2	b1,3	b1,4	d1,4	d1,3	d1,2	d1,1	b1,9
c3	c1,1	c1,2	c1,3	c1,4	c1,4	c1,3	c1,2	c1,1	c1,9
d3	d1,1	d1,2	d1,3	d1,4	b1,4	b1,3	b1,2	b1,1	b1,1
e3	e1,1	e1,2	e1,3	e1,4	a1,4	a1,3	a1,2	a1,1	a1,9
a4	a1,10	a1,11	a1,12	a1,13	e1,13	e1,12	e1,11	e1,10	a1,18
b4	b1,10	b1,11	b1,12	b1,13	d1,13	d1,12	d1,11	d1,10	b1,18
c4	c1,10	c1,11	c1,12	c1,13	c1,13	c1,12	c1,11	c1,10	c1,18
d4	d1,10	d1,11	d1,12	d1,13	b1,13	b1,12	b1,11	b1,10	b1,18
e4	e1,10	e1,11	e1,12	e1,13	a1,13	a1,12	a1,11	a1,10	a1,18
a5	a1,19	a1,20	a1,21	a1,22	e1,22	e1,21	e1,20	e1,19	a1,27
b5	b1,19	b1,20	b1,21	b1,22	d1,22	d1,21	d1,20	d1,19	b1,27
c5	c1,19	c1,20	c1,21	c1,22	c1,22	c1,21	c1,20	c1,19	c1,27
d5	d1,19	d1,20	d1,21	d1,22	b1,22	b1,21	b1,20	b1,19	b1,27
e5	e1,19	e1,20	e1,21	e1,22	a1,22	a1,21	a1,20	a1,19	a1,27
a6	a1,28	a1,29	a1,30	a1,31	e1,31	e1,30	e1,29	e1,28	a1,36
b6	b1,28	b1,29	b1,30	b1,31	d1,31	d1,30	d1,29	d1,28	b1,36
c6	c1,28	c1,29	c1,30	c1,31	c1,31	c1,30	c1,29	c1,28	c1,36
d6	d1,28	d1,29	d1,30	d1,31	b1,31	b1,30	b1,29	b1,28	b1,36
e6	e1,28	e1,29	e1,30	e1,31	a1,31	a1,30	a1,29	a1,28	a1,36

Table F.4 PSRF Symmetry for Layer 4 at 0 Degrees Orientation.

Detector	Voxel Number								
Number	28	29	30	31	32	33	34	35	36
a1	a1,28	a1,29	a1,30	a1,31	e1,31	e1,30	e1,29	e1,28	a1,36
b1	b1,28	b1,29	b1,30	b1,31	d1,31	d1,30	d1,29	d1,28	b1,36
c1	c1,28	c1,29	c1,30	c1,31	c1,31	c1,30	c1,29	c1,28	c1,36
d1	d1,28	d1,29	d1,30	d1,31	b1,31	b1,30	b1,29	b1,28	b1,36
e1	e1,28	e1,29	e1,30	e1,31	a1,31	a1,30	a1,29	a1,28	a1,36
a2	a1,19	a1,20	a1,21	a1,22	e1,22	e1,21	e1,20	e1,19	a1,27
b2	b1,19	b1,20	b1,21	b1,22	d1,22	d1,21	d1,20	d1,19	b1,27
c2	c1,19	c1,20	c1,21	c1,22	c1,22	c1,21	c1,20	c1,19	c1,27
d2	d1,19	d1,20	d1,21	d1,22	b1,22	b1,21	b1,20	b1,19	b1,27
e2	e1,19	e1,20	e1,21	e1,22	a1,22	a1,21	a1,20	a1,19	a1,27
a3	a1,10	a1,11	a1,12	a1,13	e1,13	e1,12	e1,11	e1,10	a1,18
b3	b1,10	b1,11	b1,12	b1,13	d1,13	d1,12	d1,11	d1,10	b1,18
c3	c1,10	c1,11	c1,12	c1,13	c1,13	c1,12	c1,11	c1,10	c1,18
d3	d1,10	d1,11	d1,12	d1,13	b1,13	b1,12	b1,11	b1,10	b1,18
e3	e1,10	e1,11	e1,12	e1,13	a1,13	a1,12	a1,11	a1,10	a1,18
a4	a1,1	a1,2	a1,3	a1,4	e1,4	e1,3	e1,2	e1,1	a1,9
b4	b1,1	b1,2	b1,3	b1,4	d1,4	d1,3	d1,2	d1,1	b1,9
c4	c1,1	c1,2	c1,3	c1,4	c1,4	c1,3	c1,2	c1,1	c1,9
d4	d1,1	d1,2	d1,3	d1,4	b1,4	b1,3	b1,2	b1,1	b1,1
e4	e1,1	e1,2	e1,3	e1,4	a1,4	a1,3	a1,2	a1,1	a1,9
a5	a1,10	a1,11	a1,12	a1,13	e1,13	e1,12	e1,11	e1,10	a1,18
b5	b1,10	b1,11	b1,12	b1,13	d1,13	d1,12	d1,11	d1,10	b1,18
c5	c1,10	c1,11	c1,12	c1,13	c1,13	c1,12	c1,11	c1,10	c1,18
d5	d1,10	d1,11	d1,12	d1,13	b1,13	b1,12	b1,11	b1,10	b1,18
e5	e1,10	e1,11	e1,12	e1,13	a1,13	a1,12	a1,11	a1,10	a1,18
a6	a1,19	a1,20	a1,21	a1,22	e1,22	e1,21	e1,20	e1,19	a1,27
b6	b1,19	b1,20	b1,21	b1,22	d1,22	d1,21	d1,20	d1,19	b1,27
c6	c1,19	c1,20	c1,21	c1,22	c1,22	c1,21	c1,20	c1,19	c1,27
d6	d1,19	d1,20	d1,21	d1,22	b1,22	b1,21	b1,20	b1,19	b1,27
e6	e1,19	e1,20	e1,21	e1,22	a1,22	a1,21	a1,20	a1,19	a1,27

Table F.5 PSRF Symmetry for Layer 5 at 0 Degrees Orientation.

Detector	Voxel Number								
Number	37	38	39	40	41	42	43	44	45
a1	a1,37	a1,38	a1,39	a1,40	e1,40	e1,39	e1,38	e1,37	a1, 45
b1	b1,37	b1,38	b1,39	b1,40	d1,40	d1,39	d1,38	d1,37	b1,45
c1	c1,37	c1,38	c1,39	c1,40	c1,40	c1,39	c1,38	c1,37	c1,45
d1	d1,37	d1,38	d1,39	d1,40	b1,40	b1,39	b1,38	b1,37	b1,45
e1	e1,37	e1,38	e1,39	e1,40	a1,40	a1,39	a1,38	a1,37	a1,45
a2	a1,28	a1,29	a1,30	a1,31	e1,31	e1,30	e1,29	e1,28	a1,36
b2	b1,28	b1,29	b1,30	b1,31	d1,31	d1,30	d1,29	d1,28	b1,36
c2	c1,28	c1,29	c1,30	c1,31	c1,31	c1,30	c1,29	c1,28	c1,36
d2	d1,28	d1,29	d1,30	d1,31	b1,31	b1,30	b1,29	b1,28	b1,36
e2	e1,28	e1,29	e1,30	e1,31	a1,31	a1,30	a1,29	a1,28	a1,36
a3	a1,19	a1,20	a1,21	a1,22	e1,22	e1,21	e1,20	e1,19	a1,27
b3	b1,19	b1,20	b1,21	b1,22	d1,22	d1,21	d1,20	d1,19	b1,27
c3	c1,19	c1,20	c1,21	c1,22	c1,22	c1,21	c1,20	c1,19	c1,27
d3	d1,19	d1,20	d1,21	d1,22	b1,22	b1,21	b1,20	b1,19	b1,27
e3	e1,19	e1,20	e1,21	e1,22	a1,22	a1,21	a1,20	a1,19	a1,27
a4	a1,10	a1,11	a1,12	a1,13	e1,13	e1,12	e1,11	e1,10	a1,18
b4	b1,10	b1,11	b1,12	b1,13	d1,13	d1,12	d1,11	d1,10	b1,18
c4	c1,10	c1,11	c1,12	c1,13	c1,13	c1,12	c1,11	c1,10	c1,18
d4	d1,10	d1,11	d1,12	d1,13	b1,13	b1,12	b1,11	b1,10	b1,18
e4	e1,10	e1,11	e1,12	e1,13	a1,13	a1,12	a1,11	a1,10	a1,18
a5	a1,1	a1,2	a1,3	a1,4	e1,4	e1,3	e1,2	e1,1	a1,9
b5	b1,1	b1,2	b1,3	b1,4	d1,4	d1,3	d1,2	d1,1	b1,9
c5	c1,1	c1,2	c1,3	c1,4	c1,4	c1,3	c1,2	c1,1	c1,9
d5	d1,1	d1,2	d1,3	d1,4	b1,4	b1,3	b1,2	b1,1	b1,1
e5	e1,1	e1,2	e1,3	e1,4	a1,4	a1,3	a1,2	a1,1	a1,9
a6	a1,10	a1,11	a1,12	a1,13	e1,13	e1,12	e1,11	e1,10	a1,18
b6	b1,10	b1,11	b1,12	b1,13	d1,13	d1,12	d1,11	d1,10	b1,18
c6	c1,10	c1,11	c1,12	c1,13	c1,13	c1,12	c1,11	c1,10	c1,18
d6	d1,10	d1,11	d1,12	d1,13	b1,13	b1,12	b1,11	b1,10	b1,18
e6	e1,10	e1,11	e1,12	e1,13	a1,13	a1,12	a1,11	a1,10	a1,18

Table F.6 PSRF Symmetry for Layer 6 at 0 Degrees Orientation.

Detector	Voxel Number								
Number	46	47	48	49	50	51	52	53	54
a1	a1,46	a1,47	a1,48	a1,49	e1,49	e1,48	e1,47	e1,46	a1,54
b1	b1,46	b1,47	b1,48	b1,49	d1,49	d1,48	d1,47	d1,46	b1,54
c1	c1,46	c1,47	c1,48	c1,49	c1,49	c1,48	c1,47	c1,46	c1,54
d1	d1,46	d1,47	d1,48	d1,49	b1,49	b1,48	b1,47	b1,46	b1,54
e1	e1,46	e1,47	e1,48	e1,49	a1,49	a1,48	a1,47	a1,46	a1,54
a2	a1,37	a1,38	a1,39	a1,40	e1,40	e1,39	e1,38	e1,37	a1, 45
b2	b1,37	b1,38	b1,39	b1,40	d1,40	d1,39	d1,38	d1,37	b1,45
c2	c1,37	c1,38	c1,39	c1,40	c1,40	c1,39	c1,38	c1,37	c1,45
d2	d1,37	d1,38	d1,39	d1,40	b1,40	b1,39	b1,38	b1,37	b1,45
e2	e1,37	e1,38	e1,39	e1,40	a1,40	a1,39	a1,38	a1,37	a1,45
a3	a1,28	a1,29	a1,30	a1,31	e1,31	e1,30	e1,29	e1,28	a1,36
b3	b1,28	b1,29	b1,30	b1,31	d1,31	d1,30	d1,29	d1,28	b1,36
c3	c1,28	c1,29	c1,30	c1,31	c1,31	c1,30	c1,29	c1,28	c1,36
d3	d1,28	d1,29	d1,30	d1,31	b1,31	b1,30	b1,29	b1,28	b1,36
e3	e1,28	e1,29	e1,30	e1,31	a1,31	a1,30	a1,29	a1,28	a1,36
a4	a1,19	a1,20	a1,21	a1,22	e1,22	e1,21	e1,20	e1,19	a1,27
b4	b1,19	b1,20	b1,21	b1,22	d1,22	d1,21	d1,20	d1,19	b1,27
c4	c1,19	c1,20	c1,21	c1,22	c1,22	c1,21	c1,20	c1,19	c1,27
d4	d1,19	d1,20	d1,21	d1,22	b1,22	b1,21	b1,20	b1,19	b1,27
e4	e1,19	e1,20	e1,21	e1,22	a1,22	a1,21	a1,20	a1,19	a1,27
a5	a1,10	a1,11	a1,12	a1,13	e1,13	e1,12	e1,11	e1,10	a1,18
b5	b1,10	b1,11	b1,12	b1,13	d1,13	d1,12	d1,11	d1,10	b1,18
c5	c1,10	c1,11	c1,12	c1,13	c1,13	c1,12	c1,11	c1,10	c1,18
d5	d1,10	d1,11	d1,12	d1,13	b1,13	b1,12	b1,11	b1,10	b1,18
e5	e1,10	e1,11	e1,12	e1,13	a1,13	a1,12	a1,11	a1,10	a1,18
a6	a1,1	a1,2	a1,3	a1,4	e1,4	e1,3	e1,2	e1,1	a1,9
b6	b1,1	b1,2	b1,3	b1,4	d1,4	d1,3	d1,2	d1,1	b1,9
c6	c1,1	c1,2	c1,3	c1,4	c1,4	c1,3	c1,2	c1,1	c1,9
d6	d1,1	d1,2	d1,3	d1,4	b1,4	b1,3	b1,2	b1,1	b1,1
e6	e1,1	e1,2	e1,3	e1,4	a1,4	a1,3	a1,2	a1,1	a1,9

Appendix G

QAD-CGGP Input Files

Appendix G: QAD-CGGP Input File Examples

This section contains some examples of the input files used by the QAD-CGGP point kernal shielding program. The construction of the input file is outlined in the QAD-CGGP User's Manual, which is referenced in the bibliography. Included in this section is the input file used for the validation procedures and some examples used to calculate the PSRF matrix.

QAD-CGGP Input File 1 - Test Geometry

```
 Detector Response Analysis (CT)  QAD-CG
2   2   2    3   3   1    1   0  1   1  2   0   1   2  1    0
3.7E10   0      0       0       0       0       0
-17.264  -16.764   -16.264
-33.012  -32.512   -32.012
-17.264  -16.764   -16.264
1        1         1
1        1         1
1        1         1
 0    0          QAD-CG CT Assay of Waste Drum
 RCC     1  0.0       0.0        -40.386                          80.772
            27.686
 RCC     2  0.0       0.0        -40.64                           81.28
            27.94
 RCC     3 -22.352    43.18      -32.512   0.0      15.24         0.0
            3.81
 RCC     4 -22.352    43.18      -32.512   0.0      15.24         0.0
            5.08
 RCC     5 -11.176    43.18      -32.512   0.0      15.24         0.0
            3.81
 RCC     6 -11.176    43.18      -32.512   0.0      15.24         0.0
            5.08
 RCC     7  0.0       43.18      -32.512   0.0      15.24         0.0
            3.81
 RCC     8  0.0       43.18      -32.512   0.0      15.24         0.0
            5.08
 RCC     9  11.176    43.18      -32.512   0.0      15.24         0.0
            7.26
 RCC    10  11.176    43.18      -32.512   0.0      15.24         0.0
            5.08
 RCC    11  22.352    43.18      -32.512   0.0      15.24         0.0
            3.81
 RCC    12  22.352    43.18      -32.512   0.0      15.24         0.0
            5.08
 RPP    13 -250.0     250.0      -250.0    250.0    -250.0        250.0
 END
 mat     2     +1
 can     2     +2     -1
 a1i     2     +3
 a1      2     +4     -3
 a2i     2     +5
 a2      2     +6     -5
 a3i     2     +7
 a3      2     +8     -7
 a4i     2     +9
 a4      2     +10    -9
 a5i     2     +11
 a5      2     +12    -11
 air     5     +13    -2     -4     -6     -8     -10    -12
```

```
  END
    1     1     1     1     1     1     1     1     1     1     1     1     1
    1     2     0     3     0     3     0     3     0     3     0     3 1000
   11     7    26    82
AIR  EXP
  0.00125   0.000     0.000
  0.000     7.860     0.000
  0.000     0.000     11.35
  0.662
  0.5627
0.00184
9.7349E-10
 0.661-0.663
    0.662
mev/cm*2-sec            mrem/hr                       (CS fraction)
-22.352    -32.512  53.340    1   0   0    0
-11.176    -32.512  53.340    1   0   0    0
  0.0      -32.512  53.340    1   0   0    0
 11.176    -32.512  53.340    1   0   0    0
 22.352    -32.512  53.340    1   0   0    0
-22.352    -16.256  53.340    1   0   0    0
-11.176    -16.256  53.340    1   0   0    0
  0.0        0.0      0.0       -1   0   0    0
```

QAD-CGGP Input File 2 - Detector A, Level 1, Source Voxel 1

```
 Detector Response Analysis (CT)  QAD-CG
2   2   2     3   3    1     1    0   1   1   2    0   1   2  1    0
3.7E10  0         0         0        0         0        0
-7.825   -7.325   -6.825
-35.95   -35.45   -34.95
17.184   17.684    18.184
1        1         1
1        1         1
1        1         1
 0    0              QAD-CG CT Assay of Waste Drum
 RCC    1  0.0       0.0        -42.545                              85.09
           28.575
 RCC    2  0.0       0.0        -42.799                              85.598
           28.829
 RCC    3  22.86     41.50      -35.45     0.0       20.32       0.0
            2.54
 RCC    4  22.86     41.50      -35.45     0.0       20.32       0.0
            5.08
 RPP    5 -250.0     250.0      -250.0   250.0     -250.0      250.0
 END
 mat    2      +1
 can    2      +2      -1
 ali    2      +3
 al     2      +4      -3
 air    5      +5      -2      -4
 END
   1    1     1    1    1
   1    2     0    3    0
  11    7    26   82
AIR  EXP
  0.00125   0.000     0.000
  0.000     7.860     0.000
  0.000     0.000     11.35
  0.662
  0.5627
0.00184
9.7349E-10
 0.661-0.663
    0.662
mev/cm*2-sec              mrem/hr                    (CS fraction)
 22.86     -35.45  56.769    1   0    0    0
  0.0       0.0       0.0       -1   0    0    0
```

QAD-CGGP Input File 3 - Detector E, Layer 5, Source Voxel 9

```
 Detector Response Analysis (CT)  QAD-CG
2    2    2     3    3    1      1     0   1    1    2    0    1    2  1     0
 3.7E10    0         0          0          0          0        0
-0.5       0.0       0.5
 20.77     21.27     21.77
-0.5       0.0       0.5
 1         1         1
 1         1         1
 1         1         1
 0    0              QAD-CG CT Assay of Waste Drum
 RCC     1  0.0       0.0          -42.545                              85.09
            28.575
 RCC     2  0.0       0.0          -42.799                              85.598
            28.829
 RCC     3 -22.86     41.50        -35.45    0.0        20.32           0.0
            2.54
 RCC     4 -22.86     41.50        -35.45    0.0        20.32           0.0
            5.08
 RPP     5 -250.0     250.0        -250.0   250.0      -250.0         250.0
 END
 mat     2     +1
 can     2     +2     -1
 ali     2     +3
 al      2     +4     -3
 air     5     +5     -2      -4
 END
   1    1    1    1    1
   1    2    0    3    0
  11    7   26   82
AIR  EXP
  0.00125    0.000    0.000
  0.000      7.860    0.000
  0.000      0.000    11.35
  0.662
  0.5627
0.00184
9.7349E-10
 0.661-0.663
    0.662
mev/cm*2-sec          mrem/hr                   (CS fraction)
-22.86     -35.45   56.769    1   0   0    0
  0.0        0.0      0.0      -1   0   0    0
```

Appendix H

QAD-CGGP Output File Examples

Appendix H: QAD-CGGP Output File Examples

This section contains an example of the input files generated by the QAD-CGGP point-kernal shielding program. Note, this is a multi-page fixed format file, and it is for this reason that more examples are not included. The following file was generated for detector A, layer 1, source voxel 1. The input file for this geometry is given in Appendix G, Example 2.

INPUT DATA LIST

```
 Detector Response Analysis (CT)  QAD-CG
2   2   2    3   3   1    1    0   1   1   2   0   1   2  1   0
3.7E10  0        0        0        0        0       0
-7.825  -7.325   -6.825
-35.95  -35.45   -34.95
17.184  17.684   18.184
1        1         1
1        1         1
1        1         1
 0    0            QAD-CG CT Assay of Waste Drum
 RCC    1  0.0     0.0      -42.545                        85.09
           28.575
 RCC    2  0.0     0.0      -42.799                        85.598
           28.829
 RCC    3  22.86   41.50    -35.45   0.0     20.32         0.0
            2.54
 RCC    4  22.86   41.50    -35.45   0.0     20.32         0.0
            5.08
 RPP    5 -250.0   250.0    -250.0   250.0   -250.0        250.0
 END
 mat    2     +1
 can    2     +2     -1
 ali    2     +3
 al     2     +4     -3
 air    5     +5     -2      -4
 END
   1    1    1    1    1
   1    2    0    3    0
  11    7   26   82
AIR  EXP
 0.00125   0.000    0.000
 0.000     7.860    0.000
 0.000     0.000    11.35
 0.662
 0.5627
0.00184
9.7349E-10
 0.661-0.663
   0.662
mev/cm*2-sec            mrem/hr                 (CS fraction)
 22.86     -35.45  56.769   1   0   0   0
  0.0       0.0     0.0      -1   0   0   0
```

```
Detector Response Analysis (CT)  QAD-CG

CONTROL      2      2      2      3      3      1      1      0      1      1      2      0      1      2      1      0
                           0     -8      1     10      0      0      0      0      0      0      0      0      0      0

SOURCE  3.7000E+10  0.0000E-01  0.0000E-01  0.0000E-01  0.0000E-01  0.0000E-01  0.0000E-01

     R -7.8250E+00 -7.3250E+00 -6.8250E+00

     Z -3.5950E+01 -3.5450E+01 -3.4950E+01

   PHI  1.7184E+01  1.7684E+01  1.8184E+01

  F(L)  1.0000E+00  1.0000E+00  1.0000E+00

  F(M)  1.0000E+00  1.0000E+00  1.0000E+00

  F(N)  1.0000E+00  1.0000E+00  1.0000E+00
```

```
QAD-CG CT Assay of Waste Drum

            IVOPT = 0          IDBG = 0


                                                   BODY DATA
RCC    1  0.0000000D+00  0.0000000D+00 -0.4254500D+02  0.0000000D+00  0.0000000D+00  0.8509000D+02    3
          0.2857500D+02
RCC    2  0.0000000D+00  0.0000000D+00 -0.4279900D+02  0.0000000D+00  0.0000000D+00  0.8559800D+02   12
          0.2882900D+02
RCC    3  0.2286000D+02  0.4150000D+02 -0.3545000D+02  0.0000000D+00  0.2032000D+02  0.0000000D+00   21
          0.2540000D+01
RCC    4  0.2286000D+02  0.4150000D+02 -0.3545000D+02  0.0000000D+00  0.2032000D+02  0.0000000D+00   30
          0.5080000D+01
RPP    5 -0.2500000D+03  0.2500000D+03 -0.2500000D+03  0.2500000D+03 -0.2500000D+03  0.2500000D+03   39
END    6  0.0000000D+00  0.0000000D+00  0.0000000D+00  0.0000000D+00  0.0000000D+00  0.0000000D+00   47
NUMBER OF BODIES       5
LENGTH OF FPD-ARRAY   52


                                                   INPUT ZONE DATA
 mat     2       1       0       0       0       0       0       0       0       0  Z  1
 can     2       2      -1       0       0       0       0       0       0       0  Z  2
 ali     2       3       0       0       0       0       0       0       0       0  Z  3
 al      2       4      -3       0       0       0       0       0       0       0  Z  4
 air     5       5      -2      -4       0       0       0       0       0       0  Z  5
 END     0       0       0       0       0       0       0       0       0       0  Z  6
NUMBER OF INPUT ZONES     5
NUMBER OF  CODE ZONES     5
LENGTH OF INTEGER ARRAY  103

CODE ZONE    INPUT ZONE    ZONE DATA LOC.    NO. OF BODIES    REGION NO.    MEDIA NO.
    1            1              36                1               1             1
    2            2              41                2               1             2
    3            3              50                1               1             0
    4            4              55                2               1             3
    5            5              64                3               1             0

   I     KR1(I)     KR2(I)
   1       1          1
   2       2          2
   3       3          3
```

```
4        4          4
5        5          5

      MORSE REGION IN INPUT ZONE(I) ARRAY   MRIZ(I),I=1, 5)

         1    1    1    1    1

      MORSE MEDIA IN INPUT ZONE(I) ARRAY  MMIZ(I),I=1, 5)

         1    2    0    3    0
```

```
 OPTION 0 WAS USED IN CALCULATING VOLUMES, FOR  1 REGIONS
0-SET VOLUMES = 1, 1-CONCENTRIC SPHERES, 2-SLABS, 3-INPUTVOLUMES.

           VOLUMES (CM**) USED IN COLLISIONS DENSITY AND TRACK LENGTH ESTIMATORS.
   REG         1
VOLUME  1.000D+00
```

```
COMP/MAT         N            FE           PB
    1       1.2500E-03   0.0000E-01   0.0000E-01
    2       0.0000E-01   7.8600E+00   0.0000E-01
    3       0.0000E-01   0.0000E-01   1.1350E+01
DATA FOUND:  AIR MEDIUM,  AIR RESPONSE
 GRP/MAT         N            FE           PB

                              NEUTRON REMOVAL CROSS-SECTION
            4.2830E-02   2.1360E-02   1.0260E-02

                              MATERIAL HYDROGEN DENSITY
            0.0000E-01   0.0000E-01   0.0000E-01

                              GAMMA ATTENUATION COEFFICIENT
    1       7.7011E-02   7.2656E-02   1.0525E-01   6.6200E-01
```

***** CONVERSION FACTORS AND BUILD FACTORS

***** BUILDUP FACTORS OF GEOMETRIC-PROGRESSION METHOD ARE USED
***** AIR MEDIUM, AIR RESPONSE

GRP	ENERGY	CONV.	B	C	A	XK	D	
1	5.6270E-01	1.8400E-03	2.3108	1.6141	-0.1146	14.195	0.04592	0.66

GRP	EG	0.5MFP	1.0MFP	2.0MFP	4.0MFP	8.0MFP	10.0MFP	20.0MFP	40.0MFP	60.0MFP
1	0.66	1.565E+00	2.311E+00	4.265E+00	1.003E+01	2.937E+01	4.293E+01	1.439E+02	5.214E+02	1.023E+03

ALBERT-WELTON COEFFICIENTS

7.7200E-09 3.4900E-01 4.2200E-01 6.9800E-01

```
EG-
  6.6200E-01
FE ABS G-
  9.7349E-10
EN-
  1.0000E+01  8.0000E+00  6.0000E+00  5.0000E+00  4.0000E+00  3.0000E+00  2.0000E+00  1.0000E+00  6.7000E-01
  3.3000E-01
FE ABS N-
  2.2500E-15  9.2700E-16  5.4700E-16  4.6800E-16  3.8000E-16  3.0700E-16  2.1600E-16  1.0400E-16  8.3500E-17
  4.6700E-17
WIDTH T-
              0.661-0.663 12.0-0.10

WIDTH G-
                0.662

WIDTH N-
              12.0-9.00   9.00-7.00   7.00-5.50   5.50-4.50   4.50-3.50   3.50-2.50
              2.50-1.50   1.50-0.835  0.835-0.50  0.50-0.10

UNIT G-
              mev/cm*2-sec        mrem/hr              (CS fraction)

UNIT N-
                RAD       WATTS PER   PER HOUR    GRAM      RAD PER  HR
```

COORDINATE TYPE 1 SOURCE INTENSITY OPTION 2

X COORDINATE

	COORDINATE	INTENSITY	COORDINATE	INTENSITY	COORDINATE	INTENSITY	COORDINATE	INTENSITY
1	-7.5750E+00	1.0000E+00	-7.0750E+00	1.0000E+00				

Y COORDINATE

	COORDINATE	INTENSITY	COORDINATE	INTENSITY	COORDINATE	INTENSITY	COORDINATE	INTENSITY
1	1.7434E+01	1.0000E+00	1.7934E+01	1.0000E+00				

Z COORDINATE

	COORDINATE	INTENSITY	COORDINATE	INTENSITY	COORDINATE	INTENSITY	COORDINATE	INTENSITY
1	-3.5700E+01	4.6250E+09	-3.5200E+01	4.6250E+09				

Detector Response Analysis (CT) QAD-CG

RECEIVER NUMBER 1 COORDINATES - X 2.2860E+01 Y 5.6769E+01 Z -3.5450E+01

GEOMETRY PRINT FOR PSEUDO SOURCE POINT AT THE COORDINATE ORIGIN

ZONE	DISTANCE	X	Y	Z
	SOURCE PNT	0.0000E-01	0.0000E-01	0.0000E-01
1	3.3023E+01	1.0674E+01	2.6507E+01	-1.6552E+01
2	2.9354E-01	1.0769E+01	2.6742E+01	-1.6699E+01
0	2.8891E+01	2.0107E+01	4.9932E+01	-3.1181E+01
3	4.2588E+00	2.1483E+01	5.3351E+01	-3.3315E+01
0	4.2588E+00	2.2860E+01	5.6769E+01	-3.5450E+01

Detector Response Analysis (CT) QAD-CG

RCVR 1 X= 2.2860E+01 Y= 5.6769E+01 Z= -3.5450E+01 SOURCE POINT 1 1 1

ZONE	DISTANCE	X	Y	Z
	SOURCE PNT	-7.5750E+00	1.7434E+01	-3.5700E+01
1	1.4063E+01	1.0308E+00	2.8556E+01	-3.5629E+01
2	3.1193E-01	1.2217E+00	2.8803E+01	-3.5628E+01
0	2.7059E+01	1.7780E+01	5.0204E+01	-3.5492E+01
3	4.1506E+00	2.0320E+01	5.3486E+01	-3.5471E+01
0	4.1506E+00	2.2860E+01	5.6769E+01	-3.5450E+01

RCVR 1 X= 2.2860E+01 Y= 5.6769E+01 Z= -3.5450E+01 SOURCE POINT 1 2 1

ZONE	DISTANCE	X	Y	Z
	SOURCE PNT	-7.5750E+00	1.7434E+01	-3.5200E+01
1	1.4063E+01	1.0308E+00	2.8556E+01	-3.5271E+01
2	3.1193E-01	1.2217E+00	2.8803E+01	-3.5272E+01
0	2.7059E+01	1.7780E+01	5.0204E+01	-3.5408E+01
3	4.1506E+00	2.0320E+01	5.3486E+01	-3.5429E+01
0	4.1506E+00	2.2860E+01	5.6769E+01	-3.5450E+01

Detector Response Analysis (CT) QAD-CG

RECEIVER NUMBER 1 COORDINATES - X 2.2860E+01 Y 5.6769E+01 Z -3.5450E+01

GRP NO	MEAN ENERGY MEV	ENERGY GROUP LIMITS MEV	DIRECT BEAM FLUX mev/cm*2-sec	MEAN BUILDUP FACTORS	DOSE RATE mrem/hr DIRECT BEAM	DOSE RATE mrem/hr WITH BUILDUP	HEATING RATES IN IRON (CS fraction) DIRECT BEAM	HEATING RATES IN IRON (CS fraction) WITH BUILDUP
TOTAL	0.6620	0.661-0.663	3.9679E+03	1.4479E+01	7.3009E+00	1.0571E+02	3.8627E-06	5.5928E-05
W/BU	0.6620							
1	0.6620	0.662	3.9679E+03	1.4479E+01	7.3009E+00	1.0571E+02	3.8627E-06	5.5928E-05

Subroutine EXIT has been called. Probably from INPUT.

Appendix I

Tabulation of PSRF Matrix

Table I.1 QAD-CGGP Computed Detector Responses for Layer 1 at 0 Degrees. (photons/sec/mCi)

Detector	Voxel Number								
Number	1	2	3	4	5	6	7	8	9
a1	3967.6	2769.3	840.8	68.86	5761.0	331220.0	559710.0	220.48	113.54
b1	672.18	1047.1	1845.7	413.36	254990.0	332860.0	551010.0	924550.0	17874.0
c1	131410.0	60.69	174.72	254200.0	254200.0	174.72	60.69	131410.0	443470.0
d1	924550.0	551010.0	332860.0	254990.0	413.36	1845.7	1047.1	672.18	17874.0
e1	220,48	559710.0	331220.0	5761.0	68.86	840.8	2769.3	3967.6	113.54
a2	4860.6	3108.6	1014.9	127.99	98.09	1317.2	89.08	1196.7	302.41
b2	1855.1	1526.4	324.62	275.48	12777.0	928.96	65.49	152.31	40.02
c2	258.7	315.28	33.62	3861.9	3861.9	33.62	315.28	258.7	801.47
d2	152.31	65.49	928.96	12777.0	275.48	324.62	1526.4	1855.1	40.02
e2	1196.7	89.08	1317.2	98.09	127.99	1014.9	3108.6	4860.6	302.41
a3	6408.6	3767.0	1484.3	379.4	104.42	167.3	995.28	4626.4	1123.8
b3	4960.8	2735.6	832.41	141.9	47.37	176.09	1012.3	3470.3	563.0
c3	3638.2	1651.1	371.0	55.43	55.43	371.0	1651.1	3638.2	393.08
d3	3470.3	1012.3	176.09	47.37	141.9	832.41	2735.6	4960.8	563.0
e3	4626.4	995.28	167.3	104.42	379.4	1484.3	3767.0	6408.6	1123.8
a4	6944.4	3801.3	2044.5	855.26	528.94	944.79	2969.5	6834.1	2305.7
b4	6735.0	3801.3	1591.2	589.02	423.83	963.96	2946.2	6497.7	1893.5
c4	6478.9	3287.3	1195.0	443.16	443.16	1195.0	3287.3	6478.9	1737.6
d4	6497.7	2946.2	963.96	423.83	589.02	1591.2	3801.3	6735.0	1893.5
e4	6834.1	2969.5	944.79	528.94	855.26	2044.5	3801.3	6944.4	2305.7
a5	6395.2	4258.0	2450.2	1372.0	1127.4	1815.0	3984.8	6850.4	3097.5
b5	6650.4	4158.6	2215.3	1183.0	1047.4	184.03	3926.5	6748.2	2922.7
c5	6660.2	4008.8	1989.0	1066.6	1066.6	1989.0	4008.8	6660.2	2853.1
d5	6748.2	3926.5	184.03	1047.4	1183.0	2215.3	4158.6	6650.4	2922.7
e5	6850.4	3984.8	1815.0	1127.4	1372.0	2450.2	4258.0	6395.2	3097.5
a6	5401.2	3937.1	2605.3	1739.1	1593.5	2290.8	4006.0	5836.1	3320.4
b6	5581.2	3945.3	2509.1	1638.3	1556.1	2320.5	3933.5	5811.9	3272.2
c6	5716.7	3923.2	2402.5	1571.7	1571.7	2402.5	3923.2	5716.7	3251.3
d6	5811.9	3933.5	2320.5	1556.1	1638.3	2509.1	3945.3	5581.2	3272.2
e6	5836.1	4006.0	2290.8	1593.5	1739.1	2605.3	3937.1	5401.2	3320.4

Table I.2 QAD-CGGP Computed Detector Responses for Layer 2 at 0 Degrees. (photons/sec/mCi)

Detector	Voxel Number								
Number	10	11	12	13	14	15	16	17	18
a1	4860.6	3108.6	1014.9	127.99	98.09	1317.2	89.08	1196.7	302.41
b1	1855.1	1526.4	324.62	275.48	12777.0	928.96	65.49	152.31	40.02
c1	258.7	315.28	33.62	3861.9	3861.9	33.62	315.28	258.7	801.47
d1	152.31	65.49	928.96	12777.0	275.48	324.62	1526.4	1855.1	40.02
e1	1196.7	89.08	1317.2	98.09	127.99	1014.9	3108.6	4860.6	302.41
a2	3967.6	2769.3	840.8	68.86	5761.0	331220.0	559710.0	220.48	113.54
b2	672.18	1047.1	1845.7	413.36	254990.0	332860.0	551010.0	924550.0	17874.0
c2	131410.0	60.69	174.72	254200.0	254200.0	174.72	60.69	131410.0	443470.0
d2	924550.0	551010.0	332860.0	254990.0	413.36	1845.7	1047.1	672.18	17874.0
e2	220.48	559710.0	331220.0	5761.0	68.86	840.8	2769.3	3967.6	113.54
a3	4860.6	3108.6	1014.9	127.99	98.09	1317.2	89.08	1196.7	302.41
b3	1855.1	1526.4	324.62	275.48	12777.0	928.96	65.49	152.31	40.02
c3	258.7	315.28	33.62	3861.9	3861.9	33.62	315.28	258.7	801.47
d3	152.31	65.49	928.96	12777.0	275.48	324.62	1526.4	1855.1	40.02
e3	1196.7	89.08	1317.2	98.09	127.99	1014.9	3108.6	4860.6	302.41
a4	6408.6	3767.0	1484.3	379.4	104.42	167.3	995.28	4626.4	1123.8
b4	4960.8	2735.6	832.41	141.9	47.37	176.09	1012.3	3470.3	563.0
c4	3638.2	1651.1	371.0	55.43	55.43	371.0	1651.1	3638.2	393.08
d4	3470.3	1012.3	176.09	47.37	141.9	832.41	2735.6	4960.8	563.0
e4	4626.4	995.28	167.3	104.42	379.4	1484.3	3767.0	6408.6	1123.8
a5	6944.4	3801.3	2044.5	855.26	528.94	944.79	2969.5	6834.1	2305.7
b5	6735.0	3801.3	1591.2	589.02	423.83	963.96	2946.2	6497.7	1893.5
c5	6478.9	3287.3	1195.0	443.16	443.16	1195.0	3287.3	6478.9	1737.6
d5	6497.7	2946.2	963.96	423.83	589.02	1591.2	3801.3	6735.0	1893.5
e5	6834.1	2969.5	944.79	528.94	855.26	2044.5	3801.3	6944.4	2305.7
a6	6395.2	4258.0	2450.2	1372.0	1127.4	1815.0	3984.8	6850.4	3097.5
b6	6650.4	4158.6	2215.3	1183.0	1047.4	184.03	3926.5	6748.2	2922.7
c6	6660.2	4008.8	1989.0	1066.6	1066.6	1989.0	4008.8	6660.2	2853.1
d6	6748.2	3926.5	184.03	1047.4	1183.0	2215.3	4158.6	6650.4	2922.7
e6	6850.4	3984.8	1815.0	1127.4	1372.0	2450.2	4258.0	6395.2	3097.5

Table I.3 QAD-CGGP Computed Detector Responses for Layer 3 at 0 Degrees. (photons/sec/mCi)

Detector	Voxel Number								
Number	19	20	21	22	23	24	25	26	27
a1	6408.6	3767.0	1484.3	379.4	104.42	167.3	995.28	4626.4	1123.8
b1	4960.8	2735.6	832.41	141.9	47.37	176.09	1012.3	3470.3	563.0
c1	3638.2	1651.1	371.0	55.43	55.43	371.0	1651.1	3638.2	393.08
d1	3470.3	1012.3	176.09	47.37	141.9	832.41	2735.6	4960.8	563.0
e1	4626.4	995.28	167.3	104.42	379.4	1484.3	3767.0	6408.6	1123.8
a2	4860.6	3108.6	1014.9	127.99	98.09	1317.2	89.08	1196.7	302.41
b2	1855.1	1526.4	324.62	275.48	12777.0	928.96	65.49	152.31	40.02
c2	258.7	315.28	33.62	3861.9	3861.9	33.62	315.28	258.7	801.47
d2	152.31	65.49	928.96	12777.0	275.48	324.62	1526.4	1855.1	40.02
e2	1196.7	89.08	1317.2	98.09	127.99	1014.9	3108.6	4860.6	302.41
a3	3967.6	2769.3	840.8	68.86	5761.0	331220.0	559710.0	220.48	113.54
b3	672.18	1047.1	1845.7	413.36	254990.0	332860.0	551010.0	924550.0	17874.0
c3	131410.0	60.69	174.72	254200.0	254200.0	174.72	60.69	131410.0	443470.0
d3	924550.0	551010.0	332860.0	254990.0	413.36	1845.7	1047.1	672.18	17874.0
e3	220.48	559710.0	331220.0	5761.0	68.86	840.8	2769.3	3967.6	113.54
a4	4860.6	3108.6	1014.9	127.99	98.09	1317.2	89.08	1196.7	302.41
b4	1855.1	1526.4	324.62	275.48	12777.0	928.96	65.49	152.31	40.02
c4	258.7	315.28	33.62	3861.9	3861.9	33.62	315.28	258.7	801.47
d4	152.31	65.49	928.96	12777.0	275.48	324.62	1526.4	1855.1	40.02
e4	1196.7	89.08	1317.2	98.09	127.99	1014.9	3108.6	4860.6	302.41
a5	6408.6	3767.0	1484.3	379.4	104.42	167.3	995.28	4626.4	1123.8
b5	4960.8	2735.6	832.41	141.9	47.37	176.09	1012.3	3470.3	563.0
c5	3638.2	1651.1	371.0	55.43	55.43	371.0	1651.1	3638.2	393.08
d5	3470.3	1012.3	176.09	47.37	141.9	832.41	2735.6	4960.8	563.0
e5	4626.4	995.28	167.3	104.42	379.4	1484.3	3767.0	6408.6	1123.8
a6	6944.4	3801.3	2044.5	855.26	528.94	944.79	2969.5	6834.1	2305.7
b6	6735.0	3801.3	1591.2	589.02	423.83	963.96	2946.2	6497.7	1893.5
c6	6478.9	3287.3	1195.0	443.16	443.16	1195.0	3287.3	6478.9	1737.6
d6	6497.7	2946.2	963.96	423.83	589.02	1591.2	3801.3	6735.0	1893.5
e6	6834.1	2969.5	944.79	528.94	855.26	2044.5	3801.3	6944.4	2305.7

Table I.4 QAD-CGGP Computed Detector Responses for Layer 4 at 0 Degrees. (photons/sec/mCi)

Detector	Voxel Number								
Number	28	29	30	31	32	33	34	35	36
a1	6944.4	3801.3	2044.5	855.26	528.94	944.79	2969.5	6834.1	2305.7
b1	6735.0	3801.3	1591.2	589.02	423.83	963.96	2946.2	6497.7	1893.5
c1	6478.9	3287.3	1195.0	443.16	443.16	1195.0	3287.3	6478.9	1737.6
d1	6497.7	2946.2	963.96	423.83	589.02	1591.2	3801.3	6735.0	1893.5
e1	6834.1	2969.5	944.79	528.94	855.26	2044.5	3801.3	6944.4	2305.7
a2	6408.6	3767.0	1484.3	379.4	104.42	167.3	995.28	4626.4	1123.8
b2	4960.8	2735.6	832.41	141.9	47.37	176.09	1012.3	3470.3	563.0
c2	3638.2	1651.1	371.0	55.43	55.43	371.0	1651.1	3638.2	393.08
d2	3470.3	1012.3	176.09	47.37	141.9	832.41	2735.6	4960.8	563.0
e2	4626.4	995.28	167.3	104.42	379.4	1484.3	3767.0	6408.6	1123.8
a3	4860.6	3108.6	1014.9	127.99	98.09	1317.2	89.08	1196.7	302.41
b3	1855.1	1526.4	324.62	275.48	12777.0	928.96	65.49	152.31	40.02
c3	258.7	315.28	33.62	3861.9	3861.9	33.62	315.28	258.7	801.47
d3	152.31	65.49	928.96	12777.0	275.48	324.62	1526.4	1855.1	40.02
e3	1196.7	89.08	1317.2	98.09	127.99	1014.9	3108.6	4860.6	302.41
a4	3967.6	2769.3	840.8	68.86	5761.0	331220.0	559710.0	220.48	113.54
b4	672.18	1047.1	1845.7	413.36	254990.0	332860.0	551010.0	924550.0	17874.0
c4	131410.0	60.69	174.72	254200.0	254200.0	174.72	60.69	131410.0	443470.0
d4	924550.0	551010.0	332860.0	254990.0	413.36	1845.7	1047.1	672.18	17874.0
e4	220.48	559710.0	331220.0	5761.0	68.86	840.8	2769.3	3967.6	113.54
a5	4860.6	3108.6	1014.9	127.99	98.09	1317.2	89.08	1196.7	302.41
b5	1855.1	1526.4	324.62	275.48	12777.0	928.96	65.49	152.31	40.02
c5	258.7	315.28	33.62	3861.9	3861.9	33.62	315.28	258.7	801.47
d5	152.31	65.49	928.96	12777.0	275.48	324.62	1526.4	1855.1	40.02
e5	1196.7	89.08	1317.2	98.09	127.99	1014.9	3108.6	4860.6	302.41
a6	6408.6	3767.0	1484.3	379.4	104.42	167.3	995.28	4626.4	1123.8
b6	4960.8	2735.6	832.41	141.9	47.37	176.09	1012.3	3470.3	563.0
c6	3638.2	1651.1	371.0	55.43	55.43	371.0	1651.1	3638.2	393.08
d6	3470.3	1012.3	176.09	47.37	141.9	832.41	2735.6	4960.8	563.0
e6	4626.4	995.28	167.3	104.42	379.4	1484.3	3767.0	6408.6	1123.8

Table I.5 QAD-CGGP Computed Detector Responses for Layer 5 at 0 Degrees. (photons/sec/mCi)

Detector	Voxel Number								
Number	37	38	39	40	41	42	43	44	45
a1	6395.2	4258.0	2450.2	1372.0	1127.4	1815.0	3984.8	6850.4	3097.5
b1	6650.4	4158.6	2215.3	1183.0	1047.4	184.03	3926.5	6748.2	2922.7
c1	6660.2	4008.8	1989.0	1066.6	1066.6	1989.0	4008.8	6660.2	2853.1
d1	6748.2	3926.5	184.03	1047.4	1183.0	2215.3	4158.6	6650.4	2922.7
e1	6850.4	3984.8	1815.0	1127.4	1372.0	2450.2	4258.0	6395.2	3097.5
a2	6944.4	3801.3	2044.5	855.26	528.94	944.79	2969.5	6834.1	2305.7
b2	6735.0	3801.3	1591.2	589.02	423.83	963.96	2946.2	6497.7	1893.5
c2	6478.9	3287.3	1195.0	443.16	443.16	1195.0	3287.3	6478.9	1737.6
d2	6497.7	2946.2	963.96	423.83	589.02	1591.2	3801.3	6735.0	1893.5
e2	6834.1	2969.5	944.79	528.94	855.26	2044.5	3801.3	6944.4	2305.7
a3	6408.6	3767.0	1484.3	379.4	104.42	167.3	995.28	4626.4	1123.8
b3	4960.8	2735.6	832.41	141.9	47.37	176.09	1012.3	3470.3	563.0
c3	3638.2	1651.1	371.0	55.43	55.43	371.0	1651.1	3638.2	393.08
d3	3470.3	1012.3	176.09	47.37	141.9	832.41	2735.6	4960.8	563.0
e3	4626.4	995.28	167.3	104.42	379.4	1484.3	3767.0	6408.6	1123.8
a4	4860.6	3108.6	1014.9	127.99	98.09	1317.2	89.08	1196.7	302.41
b4	1855.1	1526.4	324.62	275.48	12777.0	928.96	65.49	152.31	40.02
c4	258.7	315.28	33.62	3861.9	3861.9	33.62	315.28	258.7	801.47
d4	152.31	65.49	928.96	12777.0	275.48	324.62	1526.4	1855.1	40.02
e4	1196.7	89.08	1317.2	98.09	127.99	1014.9	3108.6	4860.6	302.41
a5	3967.6	2769.3	840.8	68.86	5761.0	331220.0	559710.0	220.48	113.54
b5	672.18	1047.1	1845.7	413.36	254990.0	332860.0	551010.0	924550.0	17874.0
c5	131410.0	60.69	174.72	254200.0	254200.0	174.72	60.69	131410.0	443470.0
d5	924550.0	60.69	332860.0	254990.0	413.36	1845.7	1047.1	672.18	17874.0
e5	220.48	559710.0	331220.0	5761.0	68.86	840.8	2769.3	3967.6	113.54
a6	4860.6	3108.6	1014.9	127.99	98.09	1317.2	89.08	1196.7	302.41
b6	1855.1	1526.4	324.62	275.48	12777.0	928.96	65.49	152.31	40.02
c6	258.7	315.28	33.62	3861.9	3861.9	33.627.0	315.28	258.7	801.47
d6	152.31	65.49	928.96	12777.0	275.48	324.62.0	1526.4	1855.1	40.02
e6	1196.7	89.08	1317.2	98.09	127.99	1014.9	3108.6	4860.6	302.41

Table I.6 QAD-CGGP Computed Detector Responses for Layer 6 at 0 Degrees. (photons/sec/mCi)

Detector	Voxel Number								
Number	46	47	48	49	50	51	52	53	54
a1	5401.2	3937.1	2605.3	1739.1	1593.5	2290.8	4006.0	5836.1	3320.4
b1	5581.2	3945.3	2509.1	1638.3	1556.1	2320.5	3933.5	5811.9	3272.2
c1	5716.7	3923.2	2402.5	1571.7	1571.7	2402.5	3923.2	5716.7	3251.3
d1	5811.9	3933.5	2320.5	1556.1	1638.3	2509.1	3945.3	5581.2	3272.2
e1	5836.1	4006.0	2290.8	1593.5	1739.1	2605.3	3937.1	5401.2	3320.4
a2	6395.2	4258.0	2450.2	1372.0	1127.4	1815.0	3984.8	6850.4	3097.5
b2	6650.4	4158.6	2215.3	1183.0	1047.4	184.03	3926.5	6748.2	2922.7
c2	6660.2	4008.8	1989.0	1066.6	1066.6	1989.0	4008.8	6660.2	2853.1
d2	6748.2	3926.5	184.03	1047.4	1183.0	2215.3	4158.6	6650.4	2922.7
e2	6850.4	3984.8	1815.0	1127.4	1372.0	2450.2	4258.0	6395.2	3097.5
a3	6944.4	3801.3	2044.5	855.26	528.94	944.79	2969.5	6834.1	2305.7
b3	6735.0	3801.3	1591.2	589.02	423.83	963.96	2946.2	6497.7	1893.5
c3	6478.9	3287.3	1195.0	443.16	443.16	1195.0	3287.3	6478.9	1737.6
d3	6497.7	2946.2	963.96	423.83	589.02	1591.2	3801.3	6735.0	1893.5
e3	6834.1	2969.5	944.79	528.94	855.26	2044.5	3801.3	6944.4	2305.7
a4	6408.6	3767.0	1484.3	379.4	104.42	167.3	995.28	4626.4	1123.8
b4	4960.8	2735.6	832.41	141.9	47.37	176.09	1012.3	3470.3	563.0
c4	3638.2	1651.1	371.0	55.43	55.43	371.0	1651.1	3638.2	393.08
d4	3470.3	1012.3	176.09	47.37	141.9	832.41	2735.6	4960.8	563.0
e4	4626.4	995.28	167.3	104.42	379.4	1484.3	3767.0	6408.6	1123.8
a5	4860.6	3108.6	1014.9	127.99	98.09	1317.2	89.08	1196.7	302.41
b5	1855.1	1526.4	324.62	275.48	12777.0	928.96	65.49	152.31	40.02
c5	258.7	315.28	33.62	3861.9	3861.9	33.62	315.28	258.7	801.47
d5	152.31	65.49	928.96	12777.0	275.48	324.62	1526.4	1855.1	40.02
e5	1196.7	89.08	1317.2	98.09	127.99	1014.9	3108.6	4860.6	302.41
a6	3967.6	2769.3	840.8	68.86	5761.0	331220.0	559710.0	220.48	113.54
b6	672.18	1047.1	1845.7	413.36	254990.0	332860.0	551010.0	924550.0	17874.0
c6	131410.0	60.69	174.72	254200.0	254200.0	174.72	60.69	131410.0	443470.0
d6	924550.0	551010.0	332860.0	254990.0	413.36	1845.7	1047.1	672.18	17874.0
e6	220.48	559710.0	331220.0	5761.0	68.86	840.8	2769.3	3967.6	113.54

Table I.7 QAD-CGGP Computed Detector Responses for Layer 1 at 90 Degrees. (photons/sec/mCi)

Detector	Voxel Number								
Number	7	8	1	2	3	4	5	6	9
a1	559710.0	220.48	3967.6	2769.3	840.8	68.86	5761.0	331220.0	113.54
b1	551010.0	924550.0	672.18	1047.1	1845.7	413.36	254990.0	332860.0	17874.0
c1	60.69	131410.0	131410.0	60.69	174.72	254200.0	254200.0	174.72	443470.0
d1	1047.1	672.18	924550.0	551010.0	332860.0	254990.0	413.36	1845.7	17874.0
e1	2769.3	3967.6	220.48	559710.0	331220.0	5761.0	68.86	840.8	113.54
a2	89.08	1196.7	4860.6	3108.6	1014.9	127.99	98.09	1317.2	302.41
b2	65.49	152.31	1855.1	1526.4	324.62	275.48	12777.0	928.96	40.02
c2	315.28	258.7	258.7	315.28	33.62	3861.9	3861.9	33.62	801.47
d2	1526.4	1855.1	152.31	65.49	928.96	12777.0	275.48	324.62	40.02
e2	3108.6	4860.6	1196.7	89.08	1317.2	98.09	127.99	1014.9	302.41
a3	995.28	4626.4	6408.6	3767.0	1484.3	379.4	104.42	167.3	1123.8
b3	1012.3	3470.3	4960.8	2735.6	832.41	141.9	47.37	176.09	563.0
c3	1651.1	3638.2	3638.2	1651.1	371.0	55.43	55.43	371.0	393.08
d3	2735.6	4960.8	3470.3	1012.3	176.09	47.37	141.9	832.41	563.0
e3	3767.0	6408.6	4626.4	995.28	167.3	104.42	379.4	1484.3	1123.8
a4	2969.5	6834.1	6944.4	3801.3	2044.5	855.26	528.94	944.79	2305.7
b4	2946.2	6497.7	6735.0	3801.3	1591.2	589.02	423.83	963.96	1893.5
c4	3287.3	6478.9	6478.9	3287.3	1195.0	443.16	443.16	1195.0	1737.6
d4	3801.3	6735.0	6497.7	2946.2	963.96	423.83	589.02	1591.2	1893.5
e4	3801.3	6944.4	6834.1	2969.5	944.79	528.94	855.26	2044.5	2305.7
a5	3984.8	6850.4	6395.2	4258.0	2450.2	1372.0	1127.4	1815.0	3097.5
b5	3926.5	6748.2	6650.4	4158.6	2215.3	1183.0	1047.4	184.03	2922.7
c5	4008.8	6660.2	6660.2	4008.8	1989.0	1066.6	1066.6	1989.0	2853.1
d5	4158.6	6650.4	6748.2	3926.5	184.03	1047.4	1183.0	2215.3	2922.7
e5	4258.0	6395.2	6850.4	3984.8	1815.0	1127.4	1372.0	2450.2	3097.5
a6	4006.0	5836.1	5401.2	3937.1	2605.3	1739.1	1593.5	2290.8	3320.4
b6	3933.5	5811.9	5581.2	3945.3	2509.1	1638.3	1556.1	2320.5	3272.2
c6	3923.2	5716.7	5716.7	3923.2	2402.5	1571.7	1571.7	2402.5	3251.3
d6	3945.3	5581.2	5811.9	3933.5	2320.5	1556.1	1638.3	2509.1	3272.2
e6	3937.1	5401.2	5836.1	4006.0	2290.8	1593.5	1739.1	2605.3	3320.4

Table I.8 QAD-CGGP Computed Detector Responses for Layer 2 at 90 Degrees. (photons/sec/mCi)

Detector	Voxel Number								
Number	16	17	10	11	12	13	14	15	18
a1	89.08	1196.7	4860.6	3108.6	1014.9	127.99	98.09	1317.2	302.41
b1	65.49	152.31	1855.1	1526.4	324.62	275.48	12777.0	928.96	40.02
c1	315.28	258.7	258.7	315.28	33.62	3861.9	3861.9	33.62	801.47
d1	1526.4	1855.1	152.31	65.49	928.96	12777.0	275.48	324.62	40.02
e1	3108.6	4860.6	1196.7	89.08	1317.2	98.09	127.99	1014.9	302.41
a2	559710.0	220.48	3967.6	2769.3	840.8	68.86	5761.0	331220.0	113.54
b2	551010.0	924550.0	672.18	1047.1	1845.7	413.36	254990.0	332860.0	17874.0
c2	60.69	131410.0	131410.0	60.69	174.72	254200.0	254200.0	174.72	443470.0
d2	1047.1	672.18	924550.0	551010.0	332860.0	254990.0	413.36	1845.7	17874.0
e2	2769.3	3967.6	220.48	559710.0	331220.0	5761.0	68.86	840.8	113.54
a3	89.085	1196.7	4860.6	3108.6	1014.9	127.99	98.09	1317.2	302.41
b3	65.497	152.31	1855.1	1526.4	324.62	275.48	12777.0	928.96	40.02
c3	315.28	258.7	258.7	315.28	33.62	3861.9	3861.9	33.62	801.47
d3	1526.4	1855.1	152.31	65.49	928.96	12777.0	275.48	324.62	40.02
e3	3108.6	4860.6	1196.7	89.08	1317.2	98.09	127.99	1014.9	302.41
a4	995.28	4626.4	6408.6	3767.0	1484.3	379.4	104.42	167.3	1123.8
b4	1012.3	3470.3	4960.8	2735.6	832.41	141.9	47.37	176.09	563.0
c4	1651.1	3638.2	3638.2	1651.1	371.0	55.43	55.43	371.0	393.08
d4	2735.6	4960.8	3470.3	1012.3	176.09	47.37	141.9	832.41	563.0
e4	3767.0	6408.6	4626.4	995.28	167.3	104.42	379.4	1484.3	1123.8
a5	2969.5	6834.1	6944.4	3801.3	2044.5	855.26	528.94	944.79	2305.7
b5	2946.2	6497.7	6735.0	3801.3	1591.2	589.02	423.83	963.96	1893.5
c5	3287.3	6478.9	6478.9	3287.3	1195.0	443.16	443.16	1195.0	1737.6
d5	3801.3	6735.0	6497.7	2946.2	963.96	423.83	589.02	1591.2	1893.5
e5	3801.3	6944.4	6834.1	2969.5	944.79	528.94	855.26	2044.5	2305.7
a6	3984.8	6850.4	6395.2	4258.0	2450.2	1372.0	1127.4	1815.0	3097.5
b6	3926.5	6748.2	6650.4	4158.6	2215.3	1183.0	1047.4	184.03	2922.7
c6	4008.8	6660.2	6660.2	4008.8	1989.0	1066.6	1066.6	1989.0	2853.1
d6	4158.6	6650.4	6748.2	3926.5	184.03	1047.4	1183.0	2215.3	2922.7
e6	4258.0	6395.2	6850.4	3984.8	1815.0	1127.4	1372.0	2450.2	3097.5

Table I.9 QAD-CGGP Computed Detector Responses for Layer 3 at 90 Degrees. (photons/sec/mCi)

Detector	Voxel Number								
Number	25	26	19	20	21	22	23	24	27
a1	995.28	4626.4	6408.6	3767.0	1484.3	379.4	104.42	167.3	1123.8
b1	1012.3	3470.3	4960.8	2735.6	832.41	141.9	47.37	176.09	563.0
c1	1651.1	3638.2	3638.2	1651.1	371.0	55.43	55.43	371.0	393.08
d1	2735.6	4960.8	3470.3	1012.3	176.09	47.37	141.9	832.41	563.0
e1	3767.0	6408.6	4626.4	995.28	167.3	104.42	379.4	1484.3	1123.8
a2	89.08	1196.7	4860.6	3108.6	1014.9	127.99	98.09	1317.2	302.41
b2	65.49	152.31	1855.1	1526.4	324.62	275.48	12777.0	928.96	40.02
c2	315.28	258.7	258.7	315.28	33.62	3861.9	3861.9	33.62	801.47
d2	1526.4	1855.1	152.31	65.49	928.96	12777.0	275.48	324.62	40.02
e2	3108.6	4860.6	1196.7	89.08	1317.2	98.09	127.99	1014.9	302.41
a3	559710.0	220.48	3967.6	2769.3	840.8	68.86	5761.0	331220.0	113.54
b3	551010.0	924550.0	672.18	1047.1	1845.7	413.36	254990.0	332860.0	17874.0
c3	60.69	131410.0	131410.0	60.69	174.72	254200.0	254200.0	174.72	443470.0
d3	1047.1	672.18	924550.0	551010.0	332860.0	254990.0	413.36	1845.7	17874.0
e3	2769.3	3967.6	220.48	559710.0	331220.0	5761.0	68.86	840.8	113.54
a4	89.08	1196.7	4860.6	3108.6	1014.9	127.99	98.09	1317.2	302.41
b4	65.49	152.31	1855.1	1526.4	324.62	275.48	12777.0	928.96	40.02
c4	315.28	258.7	258.7	315.28	33.62	3861.9	3861.9	33.62	801.47
d4	1526.4	1855.1	152.31	65.49	928.96	12777.0	275.48	324.62	40.02
e4	3108.6	4860.6	1196.7	89.08	1317.2	98.09	127.99	1014.9	302.41
a5	995.28	4626.4	6408.6	3767.0	1484.3	379.4	104.42	167.3	1123.8
b5	1012.3	3470.3	4960.8	2735.6	832.41	141.9	47.37	176.09	563.0
c5	1651.1	3638.2	3638.2	1651.1	371.0	55.43	55.43	371.0	393.08
d5	2735.6	4960.8	3470.3	1012.3	176.09	47.37	141.9	832.41	563.0
e5	3767.0	6408.6	4626.4	995.28	167.3	104.42	379.4	1484.3	1123.8
a6	2969.5	6834.1	6944.4	3801.3	2044.5	855.26	528.94	944.79	2305.7
b6	2946.2	6497.7	6735.0	3801.3	1591.2	589.02	423.83	963.96	1893.5
c6	3287.3	6478.9	6478.9	3287.3	1195.0	443.16	443.16	1195.0	1737.6
d6	3801.3	6735.0	6497.7	2946.2	963.96	423.83	589.02	1591.2	1893.5
e6	3801.3	6944.4	6834.1	2969.5	944.79	528.94	855.26	2044.5	2305.7

Table I.10 QAD-CGGP Computed Detector Responses for Layer 4 at 90 Degrees. (photons/sec/mCi)

Detector	Voxel Number								
Number	34	35	38	39	30	31	32	33	36
a1	2969.5	6834.1	6944.4	3801.3	2044.5	855.26	528.94	944.79	2305.7
b1	2946.2	6497.7	6735.0	3801.3	1591.2	589.02	423.83	963.96	1893.5
c1	3287.3	6478.9	6478.9	3287.3	1195.0	443.16	443.16	1195.0	1737.6
d1	3801.3	6735.0	6497.7	2946.2	963.96	423.83	589.02	1591.2	1893.5
e1	3801.3	6944.4	6834.1	2969.5	944.79	528.94	855.26	2044.5	2305.7
a2	995.28	4626.4	6408.6	3767.0	1484.3	379.4	104.42	167.3	1123.8
b2	1012.3	3470.3	4960.8	2735.6	832.41	141.9	47.37	176.09	563.0
c2	1651.1	3638.2	3638.2	1651.1	371.0	55.43	55.43	371.0	393.08
d2	2735.6	4960.8	3470.3	1012.3	176.09	47.37	141.9	832.41	563.0
e2	3767.0	6408.6	4626.4	995.28	167.3	104.42	379.4	1484.3	1123.8
a3	89.08	1196.7	4860.6	3108.6	1014.9	127.99	98.09	1317.2	302.41
b3	65.49	152.31	1855.1	1526.4	324.62	275.48	12777.0	928.96	40.02
c3	315.28	258.7	258.7	315.28	33.62	3861.9	3861.9	33.62	801.47
d3	1526.4	1855.1	152.31	65.49	928.96	12777.0	275.48	324.62	40.02
e3	3108.6	4860.6	1196.7	89.08	1317.2	98.09	127.99	1014.9	302.41
a4	559710.0	220.48	3967.6	2769.3	840.8	68.86	5761.0	331220.0	113.54
b4	551010.0	924550.0	672.18	1047.1	1845.7	413.36	254990.0	332860.0	17874.0
c4	60.69	131410.0	131410.0	60.69	174.72	254200.0	254200.0	174.72	443470.0
d4	1047.1	672.18	924550.0	551010.0	332860.0	254990.0	413.36	1845.7	17874.0
e4	2769.3	3967.6	220.48	559710.0	331220.0	5761.0	68.86	840.8	113.54
a5	89.08	1196.7	4860.6	3108.6	1014.9	127.99	98.09	1317.2	302.41
b5	65.49	152.31	1855.1	1526.4	324.62	275.48	12777.0	928.96	40.02
c5	315.28	258.7	258.7	315.28	33.62	3861.9	3861.9	33.62	801.47
d5	1526.4	1855.1	152.31	65.49	928.96	12777.0	275.48	324.62	40.02
e5	3108.6	4860.6	1196.7	89.08	1317.2	98.09	127.99	1014.9	302.41
a6	995.28	4626.4	6408.6	3767.0	1484.3	379.4	104.42	167.3	1123.8
b6	1012.3	3470.3	4960.8	2735.6	832.41	141.9	47.37	176.09	563.0
c6	1651.1	3638.2	3638.2	1651.1	371.0	55.43	55.43	371.0	393.08
d6	2735.6	4960.8	3470.3	1012.3	176.09	47.37	141.9	832.41	563.0
e6	3767.0	6408.6	4626.4	995.28	167.3	104.42	379.4	1484.3	1123.8

Table I.11 QAD-CGGP Computed Detector Responses for Layer 5 at 90 Degrees. (photons/sec/mCi)

Detector	Voxel Number								
Number	43	44	37	38	39	40	41	42	45
a1	3984.8	6850.4	6395.2	4258.0	2450.2	1372.0	1127.4	1815.0	3097.5
b1	3926.5	6748.2	6650.4	4158.6	2215.3	1183.0	1047.4	184.03	2922.7
c1	4008.8	6660.2	6660.2	4008.8	1989.0	1066.6	1066.6	1989.0	2853.1
d1	4158.6	6650.4	6748.2	3926.5	184.03	1047.4	1183.0	2215.3	2922.7
e1	4258.0	6395.2	6850.4	3984.8	1815.0	1127.4	1372.0	2450.2	3097.5
a2	2969.5	6834.1	6944.4	3801.3	2044.5	855.26	528.94	944.79	2305.7
b2	2946.2	6497.7	6735.0	3801.3	1591.2	589.02	423.83	963.96	1893.5
c2	3287.3	6478.9	6478.9	3287.3	1195.0	443.16	443.16	1195.0	1737.6
d2	3801.3	6735.0	6497.7	2946.2	963.96	423.83	589.02	1591.2	1893.5
e2	3801.3	6944.4	6834.1	2969.5	944.79	528.94	855.26	2044.5	2305.7
a3	995.28	4626.4	6408.6	3767.0	1484.3	379.4	104.42	167.3	1123.8
b3	1012.3	3470.3	4960.8	2735.6	832.41	141.9	47.37	176.09	563.0
c3	1651.1	3638.2	3638.2	1651.1	371.0	55.43	55.43	371.0	393.08
d3	2735.6	4960.8	3470.3	1012.3	176.09	47.37	141.9	832.41	563.0
e3	3767.0	6408.6	4626.4	995.28	167.3	104.42	379.4	1484.3	1123.8
a4	89.08	1196.7	4860.6	3108.6	1014.9	127.99	98.09	1317.2	302.41
b4	65.49	152.31	1855.1	1526.4	324.62	275.48	12777.0	928.96	40.02
c4	315.28	258.7	258.7	315.28	33.62	3861.9	3861.9	33.62	801.47
d4	1526.4	1855.1	152.31	65.49	928.96	12777.0	275.48	324.62	40.02
e4	3108.6	4860.6	1196.7	89.08	1317.2	98.09	127.99	1014.9	302.41
a5	559710.0	220.48	3967.6	2769.3	840.8	68.86	5761.0	331220.0	113.54
b5	551010.0	924550.0	672.18	1047.1	1845.7	413.36	254990.0	332860.0	17874.0
c5	60.69	131410.0	131410.0	60.69	174.72	254200.0	254200.0	174.72	443470.0
d5	1047.1	672.18	924550.0	60.69	332860.0	254990.0	413.36	1845.7	17874.0
e5	2769.3	3967.6	220.48	559710.0	331220.0	5761.0	68.86	840.8	113.54
a6	89.08	1196.7	4860.6	3108.6	1014.9	127.99	98.09	1317.2	302.41
b6	65.49	152.31	1855.1	1526.4	324.62	275.48	12777.0	928.96	40.02
c6	315.28	258.7	258.7	315.28	33.62	3861.9	3861.9	33.62	801.47
d6	1526.4	1855.1	152.31	65.49	928.96	12777.0	275.48	324.62	40.02
e6	3108.6	4860.6	1196.7	89.08	1317.2	98.09	127.99	1014.9	302.41

Table I.12 QAD-CGGP Computed Detector Responses for Layer 6 at 90 Degrees. (photons/sec/mCi)

Detector	Voxel Number								
Number	52	53	46	47	48	49	50	51	54
a1	4006.0	5836.1	5401.2	3937.1	2605.3	1739.1	1593.5	2290.8	3320.4
b1	3933.5	5811.9	5581.2	3945.3	2509.1	1638.3	1556.1	2320.5	3272.2
c1	3923.2	5716.7	5716.7	3923.2	2402.5	1571.7	1571.7	2402.5	3251.3
d1	3945.3	5581.2	5811.9	3933.5	2320.5	1556.1	1638.3	2509.1	3272.2
e1	3937.1	5401.2	5836.1	4006.0	2290.8	1593.5	1739.1	2605.3	3320.4
a2	3984.8	6850.4	6395.2	4258.0	2450.2	1372.0	1127.4	1815.0	3097.5
b2	3926.5	6748.2	6650.4	4158.6	2215.3	1183.0	1047.4	184.03	2922.7
c2	4008.8	6660.2	6660.2	4008.8	1989.0	1066.6	1066.6	1989.0	2853.1
d2	4158.6	6650.4	6748.2	3926.5	184.03	1047.4	1183.0	2215.3	2922.7
e2	4258.0	6395.2	6850.4	3984.8	1815.0	1127.4	1372.0	2450.2	3097.5
a3	2969.5	6834.1	6944.4	3801.3	2044.5	855.26	528.94	944.79	2305.7
b3	2946.2	6497.7	6735.0	3801.3	1591.2	589.02	423.83	963.96	1893.5
c3	3287.3	6478.9	6478.9	3287.3	1195.0	443.16	443.16	1195.0	1737.6
d3	3801.3	6735.0	6497.7	2946.2	963.96	423.83	589.02	1591.2	1893.5
e3	3801.3	6944.4	6834.1	2969.5	944.79	528.94	855.26	2044.5	2305.7
a4	995.28	4626.4	6408.6	3767.0	1484.3	379.4	104.42	167.3	1123.8
b4	1012.3	3470.3	4960.8	2735.6	832.41	141.9	47.37	176.09	563.0
c4	1651.1	3638.2	3638.2	1651.1	371.0	55.43	55.43	371.0	393.08
d4	2735.6	4960.8	3470.3	1012.3	176.09	47.37	141.9	832.41	563.0
e4	3767.0	6408.6	4626.4	995.28	167.3	104.42	379.4	1484.3	1123.8
a5	89.08	1196.7	4860.6	3108.6	1014.9	127.99	98.09	1317.2	302.41
b5	65.49	152.31	1855.1	1526.4	324.62	275.48	12777.0	928.96	40.02
c5	315.28	258.7	258.7	315.28	33.62	3861.9	3861.9	33.62	801.47
d5	1526.4	1855.1	152.31	65.49	928.96	12777.0	275.48	324.62	40.02
e5	3108.6	4860.6	1196.7	89.08	1317.2	98.09	127.99	1014.9	302.41
a6	559710.0	220.48	3967.6	2769.3	840.8	68.86	5761.0	331220.0	113.54
b6	551010.0	924550.0	672.18	1047.1	1845.7	413.36	254990.0	332860.0	17874.0
c6	60.69	131410.0	131410.0	60.69	174.72	254200.0	254200.0	174.72	443470.0
d6	1047.1	672.18	924550.0	551010.0	332860.0	254990.0	413.36	1845.7	17874.0
e6	2769.3	3967.6	220.48	559710.0	331220.0	5761.0	68.86	840.8	113.54

Table I.13 QAD-CGGP Computed Detector Responses for Layer 1 at 180 Degrees. (photons/sec/mCi)

Detector	Voxel Number							
Number	5	6	7	8	1	2	3	4	9
a1	5761.0	331220.0	559710.0	220.48	3967.6	2769.3	840.8	68.86	113.54
b1	254990.0	332860.0	551010.0	924550.0	672.18	1047.1	1845.7	413.36	17874.0
c1	254200.0	174.72	60.69	131410.0	131410.0	60.69	174.72	254200.0	443470.0
d1	413.36	1845.7	1047.1	672.18	924550.0	551010.0	332860.0	254990.0	17874.0
e1	68.86	840.8	2769.3	3967.6	220.48	559710.0	331220.0	5761.0	113.54
a2	98.09	1317.2	89.08	1196.7	4860.6	3108.6	1014.9	127.99	302.41
b2	12777.0	928.96	65.49	152.31	1855.1	1526.4	324.62	275.48	40.02
c2	3861.9	33.62	315.28	258.7	258.7	315.28	33.62	3861.9	801.47
d2	275.48	324.62	1526.4	1855.1	152.31	65.49	928.96	12777.0	40.02
e2	127.99	1014.9	3108.6	4860.6	1196.7	89.08	1317.2	98.09	302.41
a3	104.42	167.3	995.28	4626.4	6408.6	3767.0	1484.3	379.4	1123.8
b3	47.37	176.09	1012.3	3470.3	4960.8	2735.6	832.41	141.9	563.0
c3	55.43	371.0	1651.1	3638.2	3638.2	1651.1	371.0	55.43	393.08
d3	141.9	832.41	2735.6	4960.8	3470.3	1012.3	176.09	47.37	563.0
e3	379.4	1484.3	3767.0	6408.6	4626.4	995.28	167.3	104.42	1123.8
a4	528.94	944.79	2969.5	6834.1	6944.4	3801.3	2044.5	855.26	2305.7
b4	423.83	963.96	2946.2	6497.7	6735.0	3801.3	1591.2	589.02	1893.5
c4	443.16	1195.0	3287.3	6478.9	6478.9	3287.3	1195.0	443.16	1737.6
d4	589.02	1591.2	3801.3	6735.0	6497.7	2946.2	963.96	423.83	1893.5
e4	855.26	2044.5	3801.3	6944.4	6834.1	2969.5	944.79	528.94	2305.7
a5	1127.4	1815.0	3984.8	6850.4	6395.2	4258.0	2450.2	1372.0	3097.5
b5	1047.4	184.03	3926.5	6748.2	6650.4	4158.6	2215.3	1183.0	2922.7
c5	1066.6	1989.0	4008.8	6660.2	6660.2	4008.8	1989.0	1066.6	2853.1
d5	1183.0	2215.3	4158.6	6650.4	6748.2	3926.5	184.03	1047.4	2922.7
e5	1372.0	2450.2	4258.0	6395.2	6850.4	3984.8	1815.0	1127.4	3097.5
a6	1593.5	2290.8	4006.0	5836.1	5401.2	3937.1	2605.3	1739.1	3320.4
b6	1556.1	2320.5	3933.5	5811.9	5581.2	3945.3	2509.1	1638.3	3272.2
c6	1571.7	2402.5	3923.2	5716.7	5716.7	3923.2	2402.5	1571.7	3251.3
d6	1638.3	2509.1	3945.3	5581.2	5811.9	3933.5	2320.5	1556.1	3272.2
e6	1739.1	2605.3	3937.1	5401.2	5836.1	4006.0	2290.8	1593.5	3320.4

Table I.14 QAD-CGGP Computed Detector Responses for Layer 2 at 180 Degrees. (photons/sec/mCi)

Detector	Voxel Number								
Number	14	15	16	17	10	11	12	13	18
a1	98.09	1317.2	89.08	1196.7	4860.6	3108.6	1014.9	127.99	302.41
b1	12777.0	928.96	65.49	152.31	1855.1	1526.4	324.62	275.48	40.02
c1	3861.9	33.62	315.28	258.7	258.7	315.28	33.62	3861.9	801.47
d1	275.48	324.62	1526.4	1855.1	152.31	65.49	928.96	12777.0	40.02
e1	127.99	1014.9	3108.6	4860.6	1196.7	89.08	1317.2	98.09	302.41
a2	5761.0	331220.0	559710.0	220.48	3967.6	2769.3	840.8	68.86	113.54
b2	254990.0	332860.0	551010.0	924550.0	672.18	1047.1	1845.7	413.36	17874.0
c2	254200.0	174.72	60.69	131410.0	131410.0	60.69	174.72	254200.0	443470.0
d2	413.36	1845.7	1047.1	672.18	924550.0	551010.0	332860.0	254990.0	17874.0
e2	68.86	840.8	2769.3	3967.6	220.48	559710.0	331220.0	5761.0	113.54
a3	98.09	1317.2	89.08	1196.7	4860.6	3108.6	1014.9	127.99	302.41
b3	12777.0	928.96	65.49	152.31	1855.1	1526.4	324.62	275.48	40.02
c3	3861.9	33.62	315.28	258.7	258.7	315.28	33.62	3861.9	801.47
d3	275.48	324.62	1526.4	1855.1	152.31	65.49	928.96	12777.0	40.02
e3	127.99	1014.9	3108.6	4860.6	1196.7	89.85	1317.2	98.09	302.41
a4	104.42	167.3	995.28	4626.4	6408.6	3767.0	1484.3	379.4	1123.8
b4	47.37	176.09	1012.3	3470.3	4960.8	2735.6	832.41	141.9	563.0
c4	55.43	371.0	1651.1	3638.2	3638.2	1651.1	371.0	55.43	393.08
d4	141.9	832.41	2735.6	4960.8	3470.3	1012.3	176.09	47.37	563.0
e4	379.4	1484.3	3767.0	6408.6	4626.4	995.28	167.3	104.42	1123.8
a5	528.94	944.79	2969.5	6834.1	6944.4	3801.3	2044.5	855.26	2305.7
b5	423.83	963.96	2946.2	6497.7	6735.0	3801.3	1591.2	589.02	1893.5
c5	443.16	1195.0	3287.3	6478.9	6478.9	3287.3	1195.0	443.16	1737.6
d5	589.02	1591.2	3801.3	6735.0	6497.7	2946.2	963.96	423.83	1893.5
e5	855.26	2044.5	3801.3	6944.4	6834.1	2969.5	944.79	528.94	2305.7
a6	1127.4	1815.0	3984.8	6850.4	6395.2	4258.0	2450.2	1372.0	3097.5
b6	1047.4	184.03	3926.5	6748.2	6650.4	4158.6	2215.3	1183.0	2922.7
c6	1066.6	1989.0	4008.8	6660.2	6660.2	4008.8	1989.0	1066.6	2853.1
d6	1183.0	2215.3	4158.6	6650.4	6748.2	3926.5	184.03	1047.4	2922.7
e6	1372.0	2450.2	4258.0	6395.2	6850.4	3984.8	1815.0	1127.4	3097.5

Table I.15 QAD-CGGP Computed Detector Responses for Layer 3 at 180 Degrees. (photons/sec/mCi)

Detector	Voxel Number								
Number	23	24	25	26	19	20	21	22	27
a1	104.42	167.3	995.28	4626.4	6408.6	3767.0	1484.3	379.4	1123.8
b1	47.37	176.09	1012.3	3470.3	4960.8	2735.6	832.41	141.9	563.0
c1	55.431	371.0	1651.1	3638.2	3638.2	1651.1	371.0	55.43	393.08
d1	141.9	832.41	2735.6	4960.8	3470.3	1012.3	176.09	47.37	563.0
e1	379.4	1484.3	3767.0	6408.6	4626.4	995.28	167.3	104.42	1123.8
a2	98.09	1317.2	89.08	1196.7	4860.6	3108.6	1014.9	127.99	302.41
b2	12777.0	928.96	65.49	152.31	1855.1	1526.4	324.62	275.48	40.02
c2	3861.9	33.62	315.28	258.7	258.7	315.28	33.62	3861.9	801.47
d2	275.48	324.62	1526.4	1855.1	152.31	65.49	928.96	12777.0	40.02
e2	127.99	1014.9	3108.6	4860.6	1196.7	89.08	1317.2	98.09	302.41
a3	5761.0	331220.0	559710.0	220.48	3967.6	2769.3	840.8	68.86	113.54
b3	254990.0	332860.0	551010.0	924550.0	672.18	1047.1	1845.7	413.36	17874.0
c3	254200.0	174.72	60.69	131410.0	131410.0	60.69	174.72	254200.0	443470.0
d3	413.36	1845.7	1047.1	672.18	924550.0	551010.0	332860.0	254990.0	17874.0
e3	68.86	840.8	2769.3	3967.6	220.48	559710.0	331220.0	5761.0	113.54
a4	98.09	1317.2	89.08	1196.7	4860.6	3108.6	1014.9	127.99	302.41
b4	12777.0	928.96	65.49	152.31	1855.1	1526.4	324.62	275.48	40.02
c4	3861.9	33.62	315.28	258.7	258.7	315.28	33.62	3861.9	801.47
d4	275.48	324.62	1526.4	1855.1	152.31	65.49	928.96	12777.0	40.02
e4	127.99	1014.9	3108.6	4860.6	1196.7	89.08	1317.2	98.09	302.41
a5	104.42	167.3	995.28	4626.4	6408.6	3767.0	1484.3	379.4	1123.8
b5	47.37	176.09	1012.3	3470.3	4960.8	2735.6	832.41	141.9	563.0
c5	55.43	371.0	1651.1	3638.2	3638.2	1651.1	371.0	55.43	393.08
d5	141.9	832.41	2735.6	4960.8	3470.3	1012.3	176.09	47.37	563.0
e5	379.4	1484.3	3767.0	6408.6	4626.4	995.28	167.3	104.42	1123.8
a6	528.94	944.79	2969.5	6834.1	6944.4	3801.3	2044.5	855.26	2305.7
b6	423.83	963.96	2946.2	6497.7	6735.0	3801.3	1591.2	589.02	1893.5
c6	443.16	1195.0	3287.3	6478.9	6478.9	3287.3	1195.0	443.16	1737.6
d6	589.02	1591.2	3801.3	6735.0	6497.7	2946.2	963.96	423.83	1893.5
e6	855.26	2044.5	3801.3	6944.4	6834.1	2969.5	944.79	528.94	2305.7

Table I.16 QAD-CGGP Computed Detector Responses for Layer 4 at 180 Degrees. (photons/sec/mCi)

Detector	Voxel Number								
Number	32	33	34	35	28	29	30	31	36
a1	528.94	944.79	2969.5	6834.1	6944.4	3801.3	2044.5	855.26	2305.7
b1	423.83	963.96	2946.2	6497.7	6735.0	3801.3	1591.2	589.02	1893.5
c1	443.16	1195.0	3287.3	6478.9	6478.9	3287.3	1195.0	443.16	1737.6
d1	589.02	1591.2	3801.3	6735.0	6497.7	2946.2	963.96	423.83	1893.5
e1	855.26	2044.5	3801.3	6944.4	6834.1	2969.5	944.79	528.94	2305.7
a2	104.42	167.3	995.28	4626.4	6408.6	3767.0	1484.3	379.4	1123.8
b2	47.37	176.09	1012.3	3470.3	4960.8	2735.6	832.41	141.9	563.0
c2	55.43	371.0	1651.1	3638.2	3638.2	1651.1	371.0	55.43	393.08
d2	141.9	832.41	2735.6	4960.8	3470.3	1012.3	176.09	47.37	563.0
e2	379.4	1484.3	3767.0	6408.6	4626.4	995.28	167.3	104.42	1123.8
a3	98.09	1317.2	89.08	1196.7	4860.6	3108.6	1014.9	127.99	302.41
b3	12777.0	928.96	65.49	152.31	1855.1	1526.4	324.62	275.48	40.02
c3	3861.9	33.62	315.28	258.7	258.7	315.28	33.62	3861.9	801.47
d3	275.48	324.62	1526.4	1855.1	152.31	65.49	928.96	12777.0	40.02
e3	127.99	1014.9	3108.6	4860.6	1196.7	89.08	1317.2	98.09	302.41
a4	5761.0	331220.0	559710.0	220.48	3967.6	2769.3	840.8	68.86	113.54
b4	254990.0	332860.0	551010.0	924550.0	672.18	1047.1	1845.7	413.36	17874.0
c4	254200.0	174.72	60.69	131410.0	131410.0	60.69	174.72	254200.0	443470.0
d4	413.36	1845.7	1047.1	672.18	924550.0	551010.0	332860.0	254990.0	17874.0
e4	68.86	840.8	2769.3	3967.6	220.48	559710.0	331220.0	5761.0	113.54
a5	98.09	1317.2	89.08	1196.7	4860.6	3108.6	1014.9	127.99	302.41
b5	12777.0	928.96	65.49	152.31	1855.1	1526.4	324.62	275.48	40.02
c5	3861.9	33.62	315.28	258.7	258.7	315.28	33.62	3861.9	801.47
d5	275.48	324.62	1526.4	1855.1	152.31	65.49	928.96	12777.0	40.02
e5	127.99	1014.9	3108.6	4860.6	1196.7	89.08	1317.2	98.09	302.41
a6	104.42	167.3	995.28	4626.4	6408.0	3767.0	1484.3	379.4	1123.8
b6	47.37	176.09	1012.3	3470.3	4960.8	2735.6	832.41	141.9	563.0
c6	55.43	371.0	1651.1	3638.2	3638.2	1651.1	371.0	55.43	393.08
d6	141.9	832.41	2735.6	4960.8	3470.3	1012.3	176.09	47.37	563.0
e6	379.4	1484.3	3767.0	6408.6	4626.4	995.28	167.3	104.42	1123.8

Table I.17 QAD-CGGP Computed Detector Responses for Layer 5 at 180 Degrees. (photons/sec/mCi)

Detector	Voxel Number								
Number	41	42	43	44	37	38	39	40	45
a1	1127.4	1815.0	3984.8	6850.4	6395.2	4258.0	2450.2	1372.0	3097.5
b1	1047.4	184.03	3926.5	6748.2	6650.4	4158.6	2215.3	1183.0	2922.7
c1	1066.6	1989.0	4008.8	6660.2	6660.2	4008.8	1989.0	1066.6	2853.1
d1	1183.0	2215.3	4158.6	6650.4	6748.2	3926.5	184.03	1047.4	2922.7
e1	1372.0	2450.2	4258.0	6395.2	6850.4	3984.8	1815.0	1127.4	3097.5
a2	528.94	944.79	2969.5	6834.1	6944.4	3801.3	2044.5	855.26	2305.7
b2	423.83	963.96	2946.2	6497.7	6735.0	3801.3	1591.2	589.02	1893.5
c2	443.16	1195.0	3287.3	6478.9	6478.9	3287.3	1195.0	443.16	1737.6
d2	589.02	1591.2	3801.3	6735.0	6497.7	2946.2	963.96	423.83	1893.5
e2	855.26	2044.5	3801.3	6944.4	6834.1	2969.5	944.79	528.94	2305.7
a3	104.42	167.3	995.28	4626.4	6408.6	3767.0	1484.3	379.4	1123.8
b3	47.37	176.09	1012.3	3470.3	4960.8	2735.6	832.41	141.9	563.0
c3	55.43	371.0	1651.1	3638.2	3638.2	1651.1	371.0	55.43	393.08
d3	141.9	832.41	2735.6	4960.8	3470.3	1012.3	176.09	47.37	563.0
e3	379.4	1484.3	3767.0	6408.6	4626.4	995.28	167.3	104.42	1123.8
a4	98.09	1317.2	89.08	1196.7	4860.6	3108.6	1014.9	127.99	302.41
b4	12777.0	928.96	65.49	152.31	1855.1	1526.4	324.62	275.48	40.02
c4	3861.9	33.62	315.28	258.7	258.7	315.28	33.62	3861.9	801.47
d4	275.48	324.62	1526.4	1855.1	152.31	65.49	928.96	12777.0	40.02
e4	127.99	1014.9	3108.6	4860.6	1196.7	89.08	1317.2	98.09	302.41
a5	5761.0	331220.0	559710.0	220.48	3967.6	2769.3	840.8	68.86	113.54
b5	254990.0	332860.0	551010.0	924550.0	672.18	1047.1	1845.7	413.36	17874.0
c5	254200.0	174.72	60.69	131410.0	131410.0	60.69	174.72	254200.0	443470.0
d5	413.36	1845.7	1047.1	672.18	924550.0	60.69	332860.0	254990.0	17874.0
e5	68.86	840.8	2769.3	3967.6	220.48	559710.0	331220.0	5761.0	113.54
a6	98.09	1317.2	89.08	1196.7	4860.6	3108.6	1014.9	127.99	302.41
b6	12777.0	928.96	65.49	152.31	1855.1	1526.4	324.62	275.48	40.02
c6	3861.9	33.62	315.28	258.7	258.7	315.28	33.62	3861.9	801.47
d6	275.48	324.62	1526.4	1855.1	152.31	65.49	928.96	12777.0	40.02
e6	127.99	1014.9	3108.6	4860.6	1196.7	89.085	1317.2	98.09	302.41

Table I.18 QAD-CGGP Computed Detector Responses for Layer 6 at 180 Degrees. (photons/sec/mCi)

Detector	Voxel Number								
Number	50	51	52	53	46	47	48	49	54
a1	1593.5	2290.8	4006.0	5836.1	5401.2	3937.1	2605.3	1739.1	3320.4
b1	1556.1	2320.5	3933.5	5811.9	5581.2	3945.3	2509.1	1638.3	3272.2
c1	1571.7	2402.5	3923.2	5716.7	5716.7	3923.2	2402.5	1571.7	3251.3
d1	1638.3	2509.1	3945.3	5581.2	5811.9	3933.5	2320.5	1556.1	3272.2
e1	1739.1	2605.3	3937.1	5401.2	5836.1	4006.0	2290.8	1593.5	3320.4
a2	1127.4	1815.0	3984.8	6850.4	6395.2	4258.0	2450.2	1372.0	3097.5
b2	1047.4	184.03	3926.5	6748.2	6650.4	4158.6	2215.3	1183.0	2922.7
c2	1066.6	1989.0	4008.8	6660.2	6660.2	4008.8	1989.0	1066.6	2853.1
d2	1183.0	2215.3	4158.6	6650.4	6748.2	3926.5	184.03	1047.4	2922.7
e2	1372.0	2450.2	4258.0	6395.2	6850.4	3984.8	1815.0	1127.4	3097.5
a3	528.94	944.79	2969.5	6834.1	6944.4	3801.3	2044.5	855.26	2305.7
b3	423.83	963.96	2946.2	6497.7	6735.0	3801.3	1591.2	589.02	1893.5
c3	443.16	1195.0	3287.3	6478.9	6478.9	3287.3	1195.0	443.16	1737.6
d3	589.02	1591.2	3801.3	6735.0	6497.7	2946.2	963.96	423.83	1893.5
e3	855.26	2044.5	3801.3	6944.4	6834.1	2969.5	944.79	528.94	2305.7
a4	104.42	167.3	995.28	4626.4	6408.6	3767.0	1484.3	379.4	1123.8
b4	47.37	176.09	1012.3	3470.3	4960.8	2735.6	832.41	141.9	563.0
c4	55.43	371.0	1651.1	3638.2	3638.2	1651.1	371.0	55.43	393.08
d4	141.9	832.41	2735.6	4960.8	3470.3	1012.3	176.09	47.37	563.0
e4	379.4	1484.3	3767.0	6408.6	4626.4	995.28	167.3	104.42	1123.8
a5	98.09	1317.2	89.08	1196.7	4860.6	3108.6	1014.9	127.99	302.41
b5	12777.0	928.96	65.49	152.31	1855.1	1526.4	324.62	275.48	40.02
c5	3861.9	33.62	315.28	258.7	258.7	315.28	33.62	3861.9	801.47
d5	275.48	324.62	1526.4	1855.1	152.31	65.49	928.96	12777.0	40.02
e5	127.99	1014.9	3108.6	4860.6	1196.7	89.08	1317.2	98.09	302.41
a6	5761.0	331220.0	559710.0	220.48	3967.6	2769.3	840.8	68.86	113.54
b6	254990.0	332860.0	551010.0	924550.0	672.18	1047.1	1845.7	413.36	17874.0
c6	254200.0	174.72	60.69	131410.0	131410.0	60.69	174.72	254200.0	443470.0
d6	413.36	1845.7	1047.1	672.18	924550.0	551010.0	332860.0	254990.0	17874.0
e6	68.86	840.8	2769.3	3967.6	220.48	559710.0	331220.0	5761.0	113.54

Table I.19 QAD-CGGP Computed Detector Responses for Layer 1 at 270 Degrees. (photons/sec/mCi)

Detector	Voxel Number								
Number	3	4	5	6	7	8	1	2	9
a1	840.8	68.86	5761.0	331220.0	559710.0	220.48	3967.6	2769.3	113.54
b1	1845.7	413.36	254990.0	332860.0	551010.0	924550.0	672.18	1047.1	17874.0
c1	174.72	254200.0	254200.0	174.72	60.69	131410.0	131410.0	60.69	443470.0
d1	332860.0	254990.0	413.36	1845.7	1047.1	672.18	924550.0	551010.0	17874.0
e1	331220.0	5761.0	68.86	840.8	2769.3	3967.6	220.48	559710.0	113.54
a2	1014.9	127.99	98.09	1317.2	89.08	1196.7	4860.6	3108.6	302.41
b2	324.62	275.48	12777.0	928.96	65.49	152.31	1855.1	1526.4	40.02
c2	33.62	3861.9	3861.9	33.62	315.28	258.7	258.7	315.28	801.47
d2	928.96	12777.0	275.48	324.62	1526.4	1855.1	152.31	65.49	40.02
e2	1317.2	98.09	127.99	1014.9	3108.6	4860.6	1196.7	89.08	302.41
a3	1484.3	379.4	104.42	167.3	995.28	4626.4	6408.6	3767.0	1123.8
b3	832.41	141.9	47.37	176.09	1012.3	3470.3	4960.8	2735.6	563.0
c3	371.0	55.43	55.43	371.0	1651.1	3638.2	3638.2	1651.1	393.08
d3	176.09	47.37	141.9	832.41	2735.6	4960.8	3470.3	1012.3	563.0
e3	167.3	104.42	379.4	1484.3	3767.0	6408.6	4626.4	995.28	1123.8
a4	2044.5	855.26	528.94	944.79	2969.5	6834.1	6944.4	3801.3	2305.7
b4	1591.2	589.02	423.83	963.96	2946.2	6497.7	6735.0	3801.3	1893.5
c4	1195.0	443.16	443.16	1195.0	3287.3	6478.9	6478.9	3287.3	1737.6
d4	963.96	423.83	589.02	1591.2	3801.3	6735.0	6497.7	2946.2	1893.5
e4	944.79	528.94	855.26	2044.5	3801.3	6944.4	6834.1	2969.5	2305.7
a5	2450.2	1372.0	1127.4	1815.0	3984.8	6850.4	6395.2	4258.0	3097.5
b5	2215.3	1183.0	1047.4	184.03	3926.5	6748.2	6650.4	4158.6	2922.7
c5	1989.0	1066.6	1066.6	1989.0	4008.8	6660.2	6660.2	4008.8	2853.1
d5	184.03	1047.4	1183.0	2215.3	4158.6	6650.4	6748.2	3926.5	2922.7
e5	1815.0	1127.4	1372.0	2450.2	4258.0	6395.2	6850.4	3984.8	3097.5
a6	2605.3	1739.1	1593.5	2290.8	4006.0	5836.1	5401.2	3937.1	3320.4
b6	2509.1	1638.3	1556.1	2320.5	3933.5	5811.9	5581.2	3945.3	3272.2
c6	2402.5	1571.7	1571.7	2402.5	3923.2	5716.7	5716.7	3923.2	3251.3
d6	2320.5	1556.1	1638.3	2509.1	3945.3	5581.2	5811.9	3933.5	3272.2
e6	2290.8	1593.5	1739.1	2605.3	3937.1	5401.2	5836.1	4006.0	3320.4

Table I.20 QAD-CGGP Computed Detector Responses for Layer 2 at 270 Degrees. (photons/sec/mCi)

Detector Number	Voxel Number 12	13	14	15	16	17	10	11	18
a1	1014.9	127.99	98.09	1317.2	89.08	1196.7	4860.6	3108.6	302.41
b1	324.62	275.48	12777.0	928.96	65.49	152.31	1855.1	1526.4	40.02
c1	33.62	3861.9	3861.9	33.62	315.28	258.7	258.7	315.28	801.47
d1	928.96	12777.0	275.48	324.62	1526.4	1855.1	152.31	65.49	40.02
e1	1317.2	98.09	127.99	1014.9	3108.6	4860.6	1196.7	89.08	302.41
a2	840.8	68.86	5761.0	331220.0	559710.0	220.48	3967.6	2769.3	113.54
b2	1845.7	413.36	254990.0	332860.0	551010.0	924550.0	672.18	1047.1	17874.0
c2	174.72	254200.0	254200.0	174.72	60.69	131410.0	131410.0	60.69	443470.0
d2	332860.0	254990.0	413.36	1845.7	1047.1	672.18	924550.0	551010.0	17874.0
e2	331220.0	5761.0	68.86	840.8	2769.3	3967.6	220.48	559710.0	113.54
a3	1014.9	127.99	98.09	1317.2	89.08	1196.7	4860.6	3108.6	302.41
b3	324.62	275.48	12777.0	928.96	65.49	152.31	1855.1	1526.4	40.02
c3	33.62	3861.9	3861.9	33.62	315.28	258.7	258.7	315.28	801.47
d3	928.96	12777.0	275.48	324.62	1526.4	1855.1	152.31	65.49	40.02
e3	1317.2	98.09	127.99	1014.9	3108.6	4860.6	1196.7	89.08	302.41
a4	1484.3	379.4	104.42	167.3	995.28	4626.4	6408.6	3767.0	1123.8
b4	832.41	141.9	47.37	176.09	1012.3	3470.3	4960.8	2735.6	563.0
c4	371.0	55.43	55.43	371.0	1651.1	3638.2	3638.2	1651.1	393.08
d4	176.09	47.37	141.9	832.41	2735.6	4960.8	3470.3	1012.3	563.0
e4	167.3	104.42	379.4	1484.3	3767.0	6408.6	4626.4	995.28	1123.8
a5	2044.5	855.26	528.94	944.79	2969.5	6834.1	6944.4	3801.3	2305.7
b5	1591.2	589.02	423.83	963.96	2946.2	6497.7	6735.0	3801.3	1893.5
c5	1195.0	443.16	443.16	1195.0	3287.3	6478.9	6478.9	3287.3	1737.6
d5	963.96	423.83	589.02	1591.2	3801.3	6735.0	6497.7	2946.2	1893.5
e5	944.79	528.94	855.26	2044.5	3801.3	6944.4	6834.1	2969.5	2305.7
a6	2450.2	1372.0	1127.4	1815.0	3984.8	6850.4	6395.2	4258.0	3097.5
b6	2215.3	1183.0	1047.4	184.03	3926.5	6748.2	6650.4	4158.6	2922.7
c6	1989.0	1066.6	1066.6	1989.0	4008.8	6660.2	6660.2	4008.8	2853.1
d6	184.03	1047.4	1183.0	2215.3	4158.6	6650.4	6748.2	3926.5	2922.7
e6	1815.0	1127.4	1372.0	2450.2	4258.0	6395.2	6850.4	3984.8	3097.5

Table I.21 QAD-CGGP Computed Detector Responses for Layer 3 at 270 Degrees. (photons/sec/mCi)

Detector	Voxel Number								
Number	21	22	23	24	25	26	19	20	27
a1	1484.3	379.4	104.42	167.3	995.28	4626.4	6408.6	3767.0	1123.8
b1	832.41	141.9	47.37	176.09	1012.3	3470.3	4960.8	2735.6	563.0
c1	371.0	55.43	55.43	371.0	1651.1	3638.2	3638.2	1651.1	393.08
d1	176.09	47.37	141.9	832.41	2735.6	4960.8	3470.3	1012.3	563.0
e1	167.3	104.42	379.4	1484.3	3767.0	6408.6	4626.4	995.28	1123.8
a2	1014.9	127.99	98.09	1317.2	89.08	1196.7	4860.6	3108.6	302.41
b2	324.62	275.48	12777.0	928.96	65.49	152.31	1855.1	1526.4	40.02
c2	33.62	3861.9	3861.9	33.62	315.28	258.7	258.7	315.28	801.47
d2	928.96	12777.0	275.48	324.62	1526.4	1855.1	152.31	65.49	40.02
e2	1317.2	98.09	127.99	1014.9	3108.6	4860.6	1196.7	89.08	302.41
a3	840.8	68.86	5761.0	331220.0	559710.0	220.48	3967.6	2769.3	113.54
b3	1845.7	413.36	254990.0	332860.0	551010.0	924550.0	672.18	1047.1	17874.0
c3	174.72	254200.0	254200.0	174.72	60.69	131410.0	131410.0	60.69	443470.0
d3	332860.0	254990.0	413.36	1845.7	1047.1	672.18	924550.0	551010.0	17874.0
e3	331220.0	5761.0	68.86	840.8	2769.3	3967.6	220.48	559710.0	113.54
a4	1014.9	127.99	98.09	1317.2	89.08	1196.7	4860.6	3108.6	302.41
b4	324.62	275.48	12777.0	928.96	65.49	152.31	1855.1	1526.4	40.02
c4	33.62	3861.9	3861.9	33.62	315.28	258.7	258.7	315.28	801.47
d4	928.96	12777.0	275.48	324.62	1526.4	1855.1	152.31	65.49	40.02
e4	1317.2	98.09	127.99	1014.9	3108.6	4860.6	1196.7	89.08	302.41
a5	1484.3	379.4	104.42	167.3	995.28	4626.4	6408.6	3767.0	1123.8
b5	832.41	141.9	47.37	176.09	1012.3	3470.3	4960.8	2735.6	563.0
c5	371.0	55.43	55.43	371.0	1651.1	3638.2	3638.2	1651.1	393.08
d5	176.09	47.37	141.9	832.41	2735.6	4960.8	3470.3	1012.3	563.0
e5	167.3	104.42	379.4	1484.3	3767.0	6408.6	4626.4	995.28	1123.8
a6	2044.5	855.26	528.94	944.79	2969.5	6834.1	6944.4	3801.3	2305.7
b6	1591.2	589.02	423.83	963.96	2946.2	6497.7	6735.0	3801.3	1893.5
c6	1195.0	443.16	443.16	1195.0	3287.3	6478.9	6478.9	3287.3	1737.6
d6	963.96	423.83	589.02	1591.2	3801.3	6735.0	6497.7	2946.2	1893.5
e6	944.79	528.94	855.26	2044.5	3801.3	6944.4	6834.1	2969.5	2305.7

Table I.22 QAD-CGGP Computed Detector Responses for Layer 4 at 270 Degrees. (photons/sec/mCi)

Detector	Voxel Number								
Number	30	31	32	33	34	35	28	29	36
a1	2044.5	855.26	528.94	944.79	2969.5	6834.1	6944.4	3801.3	2305.7
b1	1591.2	589.02	423.83	963.96	2946.2	6497.7	6735.0	3801.3	1893.5
c1	1195.0	443.16	443.16	1195.0	3287.3	6478.9	6478.9	3287.3	1737.6
d1	963.96	423.83	589.02	1591.2	3801.3	6735.0	6497.7	2946.2	1893.5
e1	944.79	528.94	855.26	2044.5	3801.3	6944.4	6834.1	2969.5	2305.7
a2	1484.3	379.4	104.42	167.3	995.28	4626.4	6408.6	3767.0	1123.8
b2	832.41	141.9	47.37	176.09	1012.3	3470.3	4960.8	2735.6	563.0
c2	371.0	55.43	55.43	371.0	1651.1	3638.2	3638.2	1651.1	393.08
d2	176.09	47.37	141.9	832.41	2735.6	4960.8	3470.3	1012.3	563.0
e2	167.3	104.42	379.4	1484.3	3767.0	6408.6	4626.4	995.28	1123.8
a3	1014.9	127.99	98.09	1317.2	89.08	1196.7	4860.6	3108.6	302.41
b3	324.62	275.48	12777.0	928.96	65.49	152.31	1855.1	1526.4	40.02
c3	33.62	3861.9	3861.9	33.62	315.28	258.7	258.7	315.28	801.47
d3	928.96	12777.0	275.48	324.62	1526.4	1855.1	152.31	65.49	40.02
e3	1317.2	98.09	127.99	1014.9	3108.6	4860.6	1196.7	89.08	302.41
a4	840.8	68.86	5761.0	331220.0	559710.0	220.48	3967.6	2769.3	113.54
b4	1845.7	413.36	254990.0	332860.0	551010.0	924550.0	672.18	1047.1	17874.0
c4	174.72	254200.0	254200.0	174.72	60.69	131410.0	131410.0	60.69	443470.0
d4	332860.0	254990.0	413.36	1845.7	1047.1	672.18	924550.0	551010.0	17874.0
e4	331220.0	5761.0	68.86	840.8	2769.3	3967.6	220.48	559710.0	113.54
a5	1014.9	127.99	98.09	1317.2	89.08	1196.7	4860.6	3108.6	302.41
b5	324.62	275.48	12777.0	928.96	65.49	152.31	1855.1	1526.4	40.02
c5	33.62	3861.9	3861.9	33.62	315.28	258.7	258.7	315.28	801.47
d5	928.96	12777.0	275.48	324.62	1526.4	1855.1	152.31	65.49	40.02
e5	1317.2	98.09	127.99	1014.9	3108.6	4860.6	1196.7	89.08	302.41
a6	1484.3	379.4	104.42	167.3	995.28	4626.4	6408.6	3767.0	1123.8
b6	832.41	141.9	47.37	176.09	1012.3	3470.3	4960.8	2735.6	563.0
c6	371.0	55.43	55.43	371.0	1651.1	3638.2	3638.2	1651.1	393.08
d6	176.09	47.37	141.9	832.41	2735.6	4960.8	3470.3	1012.3	563.0
e6	167.3	104.42	379.4	1484.3	3767.0	6408.6	4626.4	995.28	1123.8

Table I.23 QAD-CGGP Computed Detector Responses for Layer 5 at 270 Degrees. (photons/sec/mCi)

Detector	Voxel Number								
Number	39	40	41	42	43	44	37	38	45
a1	2450.2	1372.0	1127.4	1815.0	3984.8	6850.4	6395.2	4258.0	3097.5
b1	2215.3	1183.0	1047.4	184.03	3926.5	6748.2	6650.4	4158.6	2922.7
c1	1989.0	1066.6	1066.6	1989.0	4008.8	6660.2	6660.2	4008.8	2853.1
d1	184.03	1047.4	1183.0	2215.3	4158.6	6650.4	6748.2	3926.5	2922.7
e1	1815.0	1127.4	1372.0	2450.2	4258.0	6395.2	6850.4	3984.8	3097.5
a2	2044.5	855.26	528.94	944.79	2969.5	6834.1	6944.4	3801.3	2305.7
b2	1591.2	589.02	423.83	963.96	2946.2	6497.7	6735.0	3801.3	1893.5
c2	1195.0	443.16	443.16	1195.0	3287.3	6478.9	6478.9	3287.3	1737.6
d2	963.96	423.83	589.02	1591.2	3801.3	6735.0	6497.7	2946.2	1893.5
e2	944.79	528.94	855.26	2044.5	3801.3	6944.4	6834.1	2969.5	2305.7
a3	1484.3	379.4	104.42	167.3	995.28	4626.4	6408.6	3767.0	1123.8
b3	832.41	141.9	47.37	176.09	1012.3	3470.3	4960.8	2735.6	563.0
c3	371.0	55.43	55.43	371.0	1651.1	3638.2	3638.2	1651.1	393.08
d3	176.09	47.37	141.9	832.41	2735.6	4960.8	3470.3	1012.3	563.0
e3	167.3	104.42	379.4	1484.3	3767.0	6408.6	4626.4	995.28	1123.8
a4	1014.9	127.99	98.09	1317.2	89.08	1196.7	4860.6	3108.6	302.41
b4	324.62	275.48	12777.0	928.96	65.49	152.31	1855.1	1526.4	40.02
c4	33.62	3861.9	3861.9	33.62	315.28	258.7	258.7	315.28	801.47
d4	928.96	12777.0	275.48	324.62	1526.4	1855.1	152.31	65.49	40.02
e4	1317.2	98.09	127.99	1014.9	3108.6	4860.6	1196.7	89.08	302.41
a5	840.8	68.86	5761.0	331220.0	559710.0	220.48	3967.6	2769.3	113.54
b5	1845.7	413.36	254990.0	332860.0	551010.0	924550.0	672.18	1047.1	17874.0
c5	174.72	254200.0	254200.0	174.72	60.69	131410.0	131410.0	60.69	443470.0
d5	332860.0	254990.0	413.36	1845.7	1047.1	672.18	924550.0	60.69	17874.0
e5	331220.0	5761.0	68.86	840.8	2769.3	3967.6	220.48	559710.0	113.54
a6	1014.9	127.99	98.09	1317.2	89.08	1196.7	4860.6	3108.6	302.41
b6	324.62	275.48	12777.0	928.96	65.49	152.31	1855.1	1526.4	40.02
c6	33.62	3861.9	3861.9	33.62	315.28	258.7	258.7	315.28	801.47
d6	928.96	12777.0	275.48	324.62	1526.4	1855.1	152.31	65.49	40.02
e6	1317.2	98.09	127.99	1014.9	3108.6	4860.6	1196.7	89.08	302.41

Table I.24 QAD-CGGP Computed Detector Responses for Layer 6 at 270 Degrees. (photons/sec/mCi)

Detector	Voxel Number								
Number	48	49	50	51	52	53	46	47	54
a1	2605.3	1739.1	1593.5	2290.8	4006.0	5836.1	5401.2	3937.1	3320.4
b1	2509.1	1638.3	1556.1	2320.5	3933.5	5811.9	5581.2	3945.3	3272.2
c1	2402.5	1571.7	1571.7	2402.5	3923.2	5716.7	5716.7	3923.2	3251.3
d1	2320.5	1556.1	1638.3	2509.1	3945.3	5581.2	5811.9	3933.5	3272.2
e1	2290.8	1593.5	1739.1	2605.3	3937.1	5401.2	5836.1	4006.0	3320.4
a2	2450.2	1372.0	1127.4	1815.0	3984.8	6850.4	6395.2	4258.0	3097.5
b2	2215.3	1183.0	1047.4	184.03	3926.5	6748.2	6650.4	4158.6	2922.7
c2	1989.0	1066.6	1066.6	1989.0	4008.8	6660.2	6660.2	4008.8	2853.1
d2	184.03	1047.4	1183.0	2215.3	4158.6	6650.4	6748.2	3926.5	2922.7
e2	1815.0	1127.4	1372.0	2450.2	4258.0	6395.2	6850.4	3984.8	3097.5
a3	2044.5	855.26	528.94	944.79	2969.5	6834.1	6944.4	3801.3	2305.7
b3	1591.2	589.02	423.83	963.96	2946.2	6497.7	6735.0	3801.3	1893.5
c3	1195.0	443.16	443.16	1195.0	3287.3	6478.9	6478.9	3287.3	1737.6
d3	963.96	423.83	589.02	1591.2	3801.3	6735.0	6497.7	2946.2	1893.5
e3	944.79	528.94	855.26	2044.5	3801.3	6944.4	6834.1	2969.5	2305.7
a4	1484.3	379.4	104.42	167.3	995.28	4626.4	6408.6	3767.0	1123.8
b4	832.41	141.9	47.37	176.09	1012.3	3470.3	4960.8	2735.6	563.0
c4	371.0	55.43	55.43	371.0	1651.1	3638.2	3638.2	1651.1	393.08
d4	176.09	47.37	141.9	832.41	2735.6	4960.8	3470.3	1012.3	563.0
e4	167.3	104.42	379.4	1484.3	3767.0	6408.6	4626.4	995.28	1123.8
a5	1014.9	127.99	98.09	1317.2	89.08	1196.7	4860.6	3108.6	302.41
b5	324.62	275.48	12777.0	928.96	65.49	152.31	1855.1	1526.4	40.02
c5	33.62	3861.9	3861.9	33.62	315.28	258.7	258.7	315.28	801.47
d5	928.96	12777.0	275.48	324.62	1526.4	1855.1	152.31	65.49	40.02
e5	1317.2	98.09	127.99	1014.9	3108.6	4860.6	1196.7	89.08	302.41
a6	840.8	68.86	5761.0	331220.0	559710.0	220.48	3967.6	2769.3	113.54
b6	1845.7	413.36	254990.0	332860.0	551010.0	924550.0	672.18	1047.1	17874.0
c6	174.72	254200.0	254200.0	174.72	60.69	131410.0	131410.0	60.69	443470.0
d6	332860.0	254990.0	413.36	1845.7	1047.1	672.18	924550.0	551010.0	17874.0
e6	331220.0	5761.0	68.86	840.8	2769.3	3967.6	220.48	559710.0	113.54

Appendix J

MCNP Input File Using a Sample Geometry

Appendix J: MCNP Input File Using a Sample Geometry

```
kla10 *** 950525 air computer tomograph for Kelly L. Ausbrooks ***
c         modified 950526 950531
c     geometry (cell)
1      2 -0.001293       -10       12 -13    $air
2      1 -7.87           -11   10  12 -13    $iron
3      3 -3.67           -41       32 -33    $detector
4      4 -11.35          -42   41  31 -33    $Pb
5      2 -0.0012929      -100  #1 #2 #3 #4   $
6      0                 -101  100           $

c     surface
10     CZ    28.575                $-drum inside
11     CZ    28.829                $-drum outside thickness 0.254cm
12     PZ   -42.545                $BOTTOM of drum
13     PZ    42.545                $top of drum
31     PY    41.529                $shield top
32     PY    56.769                $detector top
33     PY    61.849                $length of NaI 2 in. 5.08cm
c      det. (0. 56.769 -7.09)
41     C/Y    0.    -7.09 2.54     $det. cylinder r=1 in.
42     C/Y    0.    -7.09 5.08     $Pb            r=2 in.
c 41     C/Y   11.43   -7.09 2.54     $det. (11.43 56.769 -7.09)
c 42     C/Y   11.43   -7.09 5.08     $Pb
c 41     C/Y   22.86   -7.09 2.54     $det. (22.86 56.769 -7.09)
c 42     C/Y   22.86   -7.09 5.08     $Pb
c 41     C/Y    0.     -21.27 2.54    $det. ( 0.   56.769 -21.27)
c 42     C/Y    0.     -21.27 5.08    $Pb
c 41     C/Y   11.43   -21.27 2.54    $det. (11.43 56.769 -21.27)
c 42     C/Y   11.43   -21.27 5.08    $Pb
c 41     C/Y   22.86   -21.27 2.54    $det. (22.86 56.769 -21.27)
c 42     C/Y   22.86   -21.27 5.08    $Pb
c 41     C/Y    0.     -35.769 2.54   $det. ( 0.   56.769 -35.769)
c 42     C/Y    0.     -35.769 5.08   $Pb
c 41     C/Y   11.43   -35.769 2.54   $det. (11.43 56.769 -35.769)
c 42     C/Y   11.43   -35.769 5.08   $Pb
c 41     C/Y   22.86   -35.769 2.54   $det. (22.86 56.769 -35.769)
c 42     C/Y   22.86   -35.769 5.08   $Pb
100    SO 1000.
101    SO 1001.

c     material card
M1    26000  1.                              $ Fe 7.87
M2     1000  0.0007199 6000   0.00075846     $atomic fraction(from my
data)
       7000  3.9099    8000   1.0538         $AIR 0.0012929
```

```
M3    11000  0.5      53000  0.5              $NaI  3.67g/cm^3
M4    82000  1.                               $ Pb 11.35
c     source cards
SDEF  ERG=0.662 PAR=2 DIR=D2  WGT=0.0015  $energy, photon, direction,
weight
       POS=  0.          0.      -7.09        $source position   *****
      VEC=  0.         56.769    0.          $vector for cosine
c      det. - source = ( 0.    - 0., 56.769 - 0., -7.09    - (-7.09)) = VEC
c      VEC=  11.43      56.769    0.          $(11.43, 56.769,  -7.09)
c      VEC=  22.86      56.769    0.          $(22.86, 56.769,  -7.09)
c      VEC=  0.         56.769 -14.18         $( 0.   , 56.769, -21.27)
c      VEC=  11.43      56.769 -14.18         $(11.43, 56.769, -21.27)
c      VEC=  22.86      56.769 -14.18         $(22.86, 56.769, -21.27)
c      VEC=  0.         56.769 -28.679        $( 0.   , 56.769, -35.769)
c      VEC=  11.43      56.769 -28.679        $(11.43, 56.769, -35.769)
c      VEC=  22.86      56.769 -28.679        $(22.86, 56.769, -35.769)
SI2    .997  1.     $cos bin 0.997-1  weight=0.003/2
SP2   0.     1.     $probability
c You have to make sure whether the bin include the detector region or
not.
C     tally cards
F14:P  3                             $track length cell=3
**particles/cm^2/s.p.
SD14   102.96                        $ volume of NaI
ft14   inc                           $ to check the number of scattering
fu14   0 1 2 3 4 100 t               $
fq14   e u                           $
F18:P  3                             $pulse height  cell=3
c     tally's response
E0     0.661 0.663
EM0    0.0   1.0
E18    0.000 0.010 0.661 0.663
EM18   0.    0.    0.    1.
c
MODE P                            $photon calculation
PHYS:P  0.663 1 0                 $max. photon energy,  kill TTB
ELPT:P  0.6619 R 0.01  0.6619 R $energy cut off
IMP:P   1.0 4R 0.        $cell importance, It's not available for tally
8.
NPS     20000000         $ the number of history
CTME    1                $min., cpu time (126 min. for most difficult
case)
```

Vita

Kelly Lee Ausbrooks was born in Bowling Green, Kentucky on July 31, 1970. He began his higher education at Western Kentucky University (WKU), where he received a Bachelor of Science degree in Physics in May of 1993. He then began graduate study at the University of Tennessee, Knoxville. Having been awarded the Department of Energy Applied Health Physics Fellowship, he entered into the Nuclear Engineering program in pursuit of a Master of Science degree. He is a founding member and past Treasurer of the University of Tennessee Chapter of the Health Physics Society. Also, he was able to represent the University at the Annual Health Physics Society Meeting, held in Boston, Massachusetts. There, he gave a poster presentation which summarized his research into the area of applied computed tomography for non-destructive assay. He was also fortunate to have interned at the Oak Ridge National Laboratory, managed by Lockheed-Martin Energy Systems, Inc., for the U.S. Department of Energy. Working under Dr. Keith Eckerman, he developed several log-normally based atmospheric transport routines. In December of 1995, he received the Master of Science degree in Nuclear Engineering with a GPA of 3.78.

His research interests include: (1) radioactive waste assay technologies, (2) radioactive waste management strategies, and (3) environmental restoration. His hobbies include antique and classic automobiles, motorsports, hiking, and shooting.